Control of Surfaces in Confined Spaces: Tab-Aileron Control System Development

by

Francois Johannes Rupert

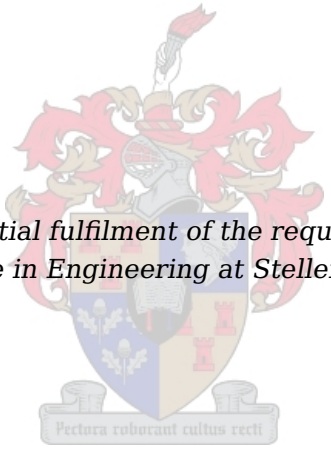

Thesis presented in partial fulfilment of the requirements for the degree Master of Science in Engineering at Stellenbosch University

Supervisor: Mr. JAA Engelbrecht
Dept E&E Engineering

March 2011

Declaration

By submitting this electronically, I declare that the entirety of the work contained therein is my own, original work, that I am the sole author thereof (save to the extent explicitly otherwise stated), that reproduction and publication thereof by Stellenbosch University will not infringe any third party rights and that I have not previously in its entirety or in part submitted it for obtaining any qualification.

Date: March 2011

Abstract

This thesis forms part of the Control Surfaces in Confined Spaces (CoSICS) project conducted at Stellenbosch University. The aim of this project is reduction of control surface actuator footprints on the existing wing structures of commercial airliners such as the Airbus A320 and A330. This is achieved by reducing control surface hinge moments through the application of trailing edge tabs. This results in smaller actuator requirements. The first tier of the project focussed on the geometric optimisation of the tab applied to an aileron. This thesis focusses on the development of dynamic control of the aileron through either tab-only or concurrent tab and aileron actuation.

In the effort to develop dynamic control, a fully coupled generalised dynamic model of the tab and aileron is derived and presented. Through linearisation of this model, linear controllers are developed. Two distinctly different controllers are presented; the first controller makes use of classical methods for control of the tab-only actuated aileron and the second controller makes use of modern control techniques such as full state feedback to facilitate controlled concurrent tab and aileron actuation. Each proposed controller is evaluated in terms of dynamic performance, robustness, disturbance rejection and noise immunity. Based on the controller development, a summary of dynamic actuator requirements is given.

Practical verification of the model and the controller performance is then undertaken. The development of the necessary hardware and software is also presented. The concept of aileron control through tab-only actuation and concurrent tab and aileron actuation is then validated. Conclusion are then drawn about the accuracy of the theoretical model and the practical performance of the controllers.

The thesis is concluded with recommendations for future work to increase the fidelity of the model. Important aspects about the practical implementation of the concept on commercial jetliners are also summarised.

Uitreksel

Hierdie tesis is deel van die Control Surfaces in Confined Spaces[1] projek by Stellenbosch Universiteit. Die doel van hierdie projek behels die verkleining van die aktueerder spasie en ondersteunings struktuur vereistes, op die bestaande vlerk struktuur van kommersiële vliegtuie soos die Airbus A320 en Airbus A330. Dit is bereik deur die vermindering van die beheeroppervlak skarnier se draaimoment met behulp van aerodinamiese hulpvlakke. Kleiner aktueerders word dus benodig. Die eerste stadium van die projek fokus op die geometriese optimisering van die hulpvlak op 'n aileron. Hierdie tesis fokus op die ontwikkeling van dinamiese beheer van die aileron deur middel van hulpvlak aktueering alleenlik of met die gelyktydige aktueering van die hulpvlak en aileron.

In die proses van onwikkeling is 'n volgekoppelde veralgemeende dinamiese model van die hulpvlak en aileron afgelei en voorgelê. Deur middel van linearisasie van die model is linieêre beheerders ontwikkel. Tans is twee verskillende beheerders ontwikkel. Die eerste beheerder is gebaseer op die klassieke metodes en maak staat op die aktueering van die hulpvlak alleenlik. Die tweede beheerder maak gebruik van moderne beheer tegnieke soos vol toestand terugvoer om gelyktydige hulpvlak en aileron aktueering te realiseer. Die beheerders is elk geëvalueer in terme van dinamiese gedrag, robuustheid, versteurings verwerping en ruis verwerping. Die beheerstelsel ontwikkeling lei tot 'n opsomming van die dinamiese aktueerder vereistes.

Dit word gevolg deur praktiese verifikasie van die model en die beheerstelsel gedrag. 'n Opsomming van die ontwikkeling van nodige hardeware en sagteware word voorgelê. In hierdie proses is die konsep van beide hulpvlak alleenlike aktueering en gelyktydige hulpvlak en aileron aktueering bewys. Gevolgtrekkings word gemaak oor die akkuraatheid van die model en die praktiese gedrag van die beheerders.

Die tesis word afgerond met voorstelle vir toekomstige werk wat die model se betroubaarheid kan verbeter. Verder word belangrike punte oor die praktiese aspekte van konsep implementering op kommersiële vliegtuie ook uitgelig.

[1] Beheervlakke in Begrensde Ruimtes

Contents

Declaration **i**

Abstract **ii**

Uitreksel **iii**

Contents **iv**

List of Figures **vii**

List of Tables **x**

Nomenclature **xi**

1 Introduction and Problem Definition **1**
1.1 Background and History 1
1.2 Project Goals 3
1.3 Project Approach and Overview 4
1.4 Previous Research 5
1.5 Thesis Outline 6

2 Modelling **7**
2.1 Tab-Aileron Dynamics 8
2.2 Aerodynamic Hinge Moments 9
2.3 Linearisation of Dynamics 14
2.4 Dynamic Characteristics 20
2.5 Steady-State Characteristics 27
2.6 Actuator Models 29

3 Feedback Control Design **30**
3.1 Dynamic Performance Requirements 31
3.2 Control of Dynamics 31
3.2.1 Successive Loop Closure and Decoupling 32
3.2.2 Full-State Feedback 33

4 Design of Feedback Control for Tab-Only Actuation **35**
4.1 Rate Command Tab Actuator Based Controllers 36
4.1.1 Inner Loop Tab Deflection Control 36
4.1.2 Outer Loop Negative Feedback Aileron Deflection Control 37
4.1.3 Outer Loop Positive Feedback Aileron Deflection Control 42
4.1.4 Disturbance Rejection 46

4.1.5 Noise Suppression . . . 49
4.2 Deflection Command Tab Actuator Based Controllers . . . 51
4.2.1 Negative Feedback Aileron Deflection Control . . . 51
4.2.2 Positive Feedback Aileron Deflection Control . . . 55
4.3 Actuator Requirements . . . 58
4.4 Controller Scaling and Practical Aspects . . . 59

5 Design of Feedback Control for Concurrent Tab and Aileron Actuation 61
5.1 Linear Quadratic Regulation . . . 62
5.2 Power Weighted Linear Quadratic Regulation . . . 64
5.3 Aileron Deflection Command Following . . . 64
5.4 Tab and Aileron Deflection Command Following . . . 68
5.5 Disturbance Rejection . . . 72
5.6 Noise Suppression . . . 75
5.7 Actuator Requirements . . . 78

6 Practical Implementation 82
6.1 Wind Tunnel Parameters . . . 82
6.2 Mechanical Design of the Test Section . . . 84
6.3 Controller Hardware . . . 87
6.3.1 Driver and Interface Unit . . . 87
6.3.2 Actuator Selection . . . 93
6.4 Controller Software . . . 95
6.4.1 Graphic User Interface . . . 95
6.4.2 Controller Implementation . . . 96

7 Model Parameter Determination 98
7.1 Experimental Procedure, Setup and Events . . . 99
7.2 Parameter Estimation Methods . . . 103
7.3 Signal Conditioning . . . 108
7.4 Parameter Estimation Results and Comparison . . . 110
7.4.1 Angle of Attack Effects . . . 118
7.4.2 Velocity Dependent Trends . . . 118
7.4.3 Deflection Range Trends . . . 120
7.4.4 Observed Non-Idealities . . . 121
7.4.5 Model Overview . . . 128
7.5 Actuator Parameter Results . . . 132
7.6 Scalability of Results . . . 133

8 Control Implementation Results 136
8.1 Tab-Only Actuation Test . . . 136
8.2 Aileron-Only Reference Concurrent Tab and Aileron Actuation Test . . . 141
8.3 Results Overview . . . 143

9 Conclusion 145
9.1 Summary . . . 145
9.2 Future Work and Recommendations . . . 146

A 148
A.1 Moment of Inertia Calculation . . . 148
A.2 Correction Factors . . . 149

A.3 Graphic User Interface 150

List of References **153**

List of Figures

1.1 Standard Aircraft Control Surface Locations [1] . . . 1
1.2 Typical Trailing Edge Tab . . . 2
1.3 Dependencies of Project Tasks . . . 4
1.4 Varied Tab Actuation Concepts [2] . . . 5

2.1 Tab and Aileron Mechanics . . . 8
2.2 Deflection, Force and Moment Conventions . . . 10
2.3 Typical Upper and Lower Surface Pressure Distribution from Xfoil . . . 11
2.4 Apparent Airflow . . . 13
2.5 Linearised Hinge Moment Coefficient over Operational Bounds . . . 15
2.6 SISO Aileron Model . . . 18
2.7 Aileron Transfer Function Block Diagram . . . 19
2.8 Eigenvalue Variation due to Tab State . . . 22
2.9 Eigenvalue Variation due to Aileron State . . . 22
2.10 Eigenvalue Variation due to Free-Stream Velocity . . . 23
2.11 Eigenvalue Variation due to Density . . . 24
2.12 Eigenvalue Variation due to Tab Chord Ratio . . . 24
2.13 Eigenvalue Variation for the Aileron Decoupled from the Tab . . . 26
2.14 Tab-Aileron Steady-State Phase Plane and Respective Hinge Moment Coefficients . . . 28
2.15 Actuator Model . . . 29

3.1 Control Approach . . . 30
3.2 Successive Loop Closure Topology . . . 32
3.3 Full-State Feedback Topology . . . 34
3.4 Full-State Feedback Topology for a Servo Problem . . . 34

4.1 Hierarchical Approach to Tab-Only Actuation . . . 35
4.2 Position Inner Loop . . . 36
4.3 Tab-Only Actuation Rate Controlled Topology . . . 37
4.4 Negative Feedback Root Locus at 50 ms^{-1} Airspeed with Rate Actuation . . . 38
4.5 Integrator Loop Root Locus at 50 ms^{-1} Airspeed with Rate Actuation . . . 40
4.6 Negative Feedback Response with Rate Actuator at Airspeed of $30\ ms^{-1}$ and $50\ ms^{-1}$ . . . 40
4.7 Representative Pole Movement . . . 41
4.8 Closed-Loop Bode for Negative Feedback with Rate Actuator . . . 41
4.9 Positive Feedback Deflection Control Dynamics Block Diagram . . . 42
4.10 Positive Feedback Deflection Control Block Diagram . . . 43
4.11 Positive Feedback Root Locus at 50 ms^{-1} Airspeed with Rate Actuation . . . 44

4.12 Integrator Loop Root Locus at 50 ms^{-1} Airspeed with Rate Actuation 44
4.13 Positive Feedback Response with Rate Actuator at Airspeed of $30\ ms^{-1}$ and $50\ ms^{-1}$ 45
4.14 Closed-Loop Bode for Positive Feedback Controller 45
4.15 Motor Output Disturbance 46
4.16 Output Disturbance Representation 47
4.17 SISO Disturbance Sensitivity for Negative Feedback 48
4.18 SISO Disturbance Sensitivity for Positive Feedback 48
4.19 SISO Noise Transmission for Negative Feedback 50
4.20 SISO Noise Transmission for Positive Feedback 50
4.21 SISO Negative Proportional and Rate Feedback Controller Topology 52
4.22 Negative Feedback Root Locus at 50 ms^{-1} Airspeed with Servo Actuation . . 52
4.23 Integrator Loop Root Locus at 50 ms^{-1} Airspeed with Servo Actuation 53
4.24 Negative Feedback Response with Servo Actuator at Airspeed of $30\ ms^{-1}$ and $50\ ms^{-1}$ 54
4.25 Closed-Loop Bode for Negative Feedback Controller with Servo Actuation . . 54
4.26 Positive Feedback Root Locus at 50 ms^{-1} Airspeed with Servo Actuation . . 55
4.27 Integrator Loop Root Locus at 50 ms^{-1} Airspeed with Servo Actuation 56
4.28 Positive Feedback Response with Servo Actuator at Airspeed of $30\ ms^{-1}$ and $50\ ms^{-1}$ 57
4.29 Closed-Loop Bode for Positive Feedback Controller with Servo Actuation . . 57
4.30 Servo Tab Actuator Requirements at $\alpha = 5°$, $V = 50ms^{-1}$ and $10°$ Step Size . 58
4.31 Scaling Effect on Pole Position 60

5.1 Approach to Concurrent Tab and Aileron Actuation 62
5.2 Different Approaches to Concurrent Tab and Aileron Actuation 62
5.3 Simulated Representative Response Before and After Power is Weighed . . . 65
5.4 Reference Input 66
5.5 System Integrator Augmentation 67
5.6 FSF with Feed-Forward and Integrator 68
5.7 Multiple Reference Inputs for FSF 69
5.8 Two Degree of Freedom Phase Plane Trajectories 70
5.9 Twin Reference Input Structure with Integrators and Feedforward 71
5.10 Reference Input Response 71
5.11 MIMO Input Disturbance 72
5.12 Disturbance Sensitivity for an Aileron Reference Only 74
5.13 Disturbance for Concurrent Aileron and Tab References 74
5.14 MIMO Noise 75
5.15 MIMO Noise Transmission for Aileron Reference 76
5.16 MIMO Noise Transmission for Aileron and Tab Reference 77
5.17 FSF Tab and Aileron Actuator Requirements at $\alpha = 5°$, $V = 50ms^{-1}$ and $10°$ Step Size 79
5.18 FSF Tab and Aileron Reference Actuator Requirements at $\alpha = 5°$, $V = 50ms^{-1}$ and $10°$ Step Size 79
5.19 FSF Tab and Aileron Reference Actuator Requirements at $\alpha = 5°$, $V = 50ms^{-1}$ and $10°$ Step Size with Limited Tab Deflection 80
5.20 MIMO FSF Tab and Aileron Actuator Requirements at $\alpha = 5°$, $V = 50ms^{-1}$ and $10°$ Rate Limited Reference 81

6.1 Experimental Setup in Wind Tunnel 86

6.2 Interface PCB . . . 87
6.3 System Interfaces . . . 89
6.4 Current Control Topology . . . 90
6.5 Brushed DC Motor Model . . . 91
6.6 Torque Control Topology . . . 92

7.1 Experimental Setup in Wind Tunnel . . . 100
7.2 Horizontal Setup in Wind Tunnel . . . 101
7.3 Vertical Setup in Wind Tunnel . . . 102
7.4 Response Filtered Derivative . . . 109
7.5 Parameter Estimation Fit Result Airspeed 50 ms^{-1}, 15° Step . . . 111
7.6 Variation of System Parameters with Velocity Dataset 1 . . . 112
7.7 Variation of System Parameters with Airspeed Dataset 2 . . . 113
7.8 Variation of System Parameters with Step Size Dataset 2 . . . 114
7.9 Variation of System Parameters with Velocity Dataset 3 . . . 116
7.10 Variation of System Parameters with Step Size Dataset 3 . . . 117
7.11 Non-Ideal Responses Good vs. Bad fit . . . 121
7.12 Typical Non-Ideal Response Characteristics . . . 122
7.13 Significant Tab Deflection before Aileron Motion is Initiated due to Frictional Break-Away Force . . . 123
7.14 Varying Incremental Aileron Deflection due to Tab Deflection at $\alpha = 5°$ $V = 20ms^{-1}$ . . . 124
7.15 Varying Aileron Deflection due to Tab Deflection . . . 124
7.16 Multiple Stable Aileron Positions . . . 125
7.17 Momentary Loss of Tab Effectiveness $\alpha = 5°$ $V = 30ms^{-1}$ . . . 126
7.18 Drastic Sudden Loss of Tab Effectiveness $\alpha = 5°$ $V = 30ms^{-1}$ . . . 126
7.19 Velocity Root Locus Comaprison . . . 129
7.20 Pole Spread Angles $\leq 15°$ . . . 130
7.21 Pole Spread Angles $\geq 20°$ . . . 131
7.22 Tab Actuator Torque Curve . . . 132
7.23 Aileron Actuator Torque Curve . . . 133
7.24 Tab Pole Identification . . . 134

8.1 Frictional Effect in Case of Steady-State Error and Around Zero Command at $\alpha = 5°$ and $V = 30\ ms^{-1}$ . . . 138
8.2 Frictional Effect in Reproduced in Simulation . . . 138
8.3 Typical Positive Feedback Reponse . . . 139
8.4 Frequency Domain Response Comparison for Tab-Only Actuation Controllers 140
8.5 Typical FSF LQR Controller Response . . . 141
8.6 Frequency Response Comparison . . . 143

A.1 Representation of Moment of Inertia Calculation . . . 148
A.2 GUI Real-Time Plotting Window . . . 150
A.3 GUI Main Control and Interface Window . . . 151
A.4 GUI Gain Import and Adjustment Window . . . 151
A.5 GUI Log and Debug Window . . . 152
A.6 GUI Communication Settings . . . 152

List of Tables

6.1 SUN Wind Tunnel Specifications 83
6.2 SUN Wind Tunnel Operations 83
6.3 Model Physical Characteristics 84
6.4 Actuator Drivers and Sensors 88
6.5 Peak Actuator Torque Requirements 93
6.6 Continuous Actuator Torque Requirements 93
6.7 Actuator Specifications 94

8.1 Testing Matrix for Controllers 136
8.2 Negative Feedback Controller Performance 137
8.3 Positive Feedback Controller Performance 139
8.4 Robust Performance 10° Steps 141
8.5 FSF Controller Performance 142
8.6 Robust Performance of FSF LQR Controller 143

Nomenclature

Greek Letters

α	Angle of attack
δ	Angular deflection
Γ	Discrete control matrix
Λ	Diagonal eigenvalue matrix
ω	Angular velocity
ω_n	Natural frequency
Φ	Discrete state matrix
ρ	Density
σ	Standard deviation
Θ	Model parameter matrix
ζ	Damping ratio

Small Letters

c	Aerodynamic surface chord
$\bar{c}$	Wing chord
k	Stiffness
m	Mass
q	Free-stream dynamic pressure
s	Aerodynamic surface Span
v	Noise function
w	Disturbance function

Capital Letters

B	Damping constant
$\bar{B}$	Damping matrix

C	Capacitance
C_D	Drag coefficient
C_H	Hinge moment coefficient
C_L	Lift coefficient
F	State matrix
G	Control matrix
H	Output matrix
$\bar{G}$	Coupled control matrix
I	Moment of inertia
$\mathbf{I}$	Identity matrix
J	Cost
$\bar{J}$	Coupled moments of inertia matrix
K	Gain
$\bar{K}$	Coupled stiffness matrix
L	Inductance
M	Resultant moment
N	Feedforward gain
P	Pressure
Q	Weighting matrix
R	Resistance
T	Actuator torque
U	Input Vector
V	Airspeed or free-stream velocity
X	State vector
Y	Output vector

Subscripts

∞	Free-stream
0	Linearisation point
a	Aileron
at	Lumped aileron and tab
H	Hinge
I	Integrator

k	$k\Delta T$ time instant
m	Motor
t	Tab

Acronyms

ADC	Analog to digital converter
CAD	Computer aided design
CFD	Computational fluid dynamics
CPUT	Cape Peninsula University of Technology
CoSICS	Control systems in confined spaces
DAC	Digital to analog converter
DC	Direct current
EMF	Electromotive force
FSF	Full-state feedback
GUI	Graphic user interface
ISA	International standard atmosphere
LQR	Linear quadratic regulator
LTI	Linear time-invariant
MIMO	Multi-input multi-output
MSL	Mean sea level
NACA	National Advisory Committee for Aeronautics
NASA	National Aeronautics and Space Administration
PCB	Printed circuit board
PWM	Pulse width modulation
SISO	Single-input single-output
SPI	Serial peripheral interface
SUN	Stellenbosch University
UART	Universal asynchronous receiver/transmitter
UCT	University of Cape Town
USB	Universal serial bus
PC	Personal computer

Chapter 1

Introduction and Problem Definition

1.1 Background and History

In 2008 an agreement was made between Airbus, NACoE[1], CPUT[2] and Stellenbosch University to undertake a project focussed on control surfaces in confined spaces (CoSICS). The CoSICS project is primarily focussed an the reduction of control surface actuator footprints on the existing wing structures of commercial airliners such as the Airbus A320 and A330.

The reduction of actuator footprints has many advantages in terms of aircraft economy. The most obvious and direct result of actuator footprint reduction is the increase in available space, decrease in mass and therefore a more economical aircraft. Further, since the control surfaces are primarily located on the wings and the horizontal and vertical stabilisers, see Figure 1.1, the actuators consequently have to be fitted into the available space of these aerodynamic surfaces. In some cases the actuators protrude from these surfaces and they have to be covered by fairings. The side effect of these fairings is increased drag on the aircraft which in turn has a negative effect on aircraft economy [3].

There are two logical progressions to solving the actuator footprint problem; the actuator requirements can be reduced or a more compact and efficient actuator can be

[1] National Aerospace Centre of Excellence
[2] Cape Peninsula University of Technology

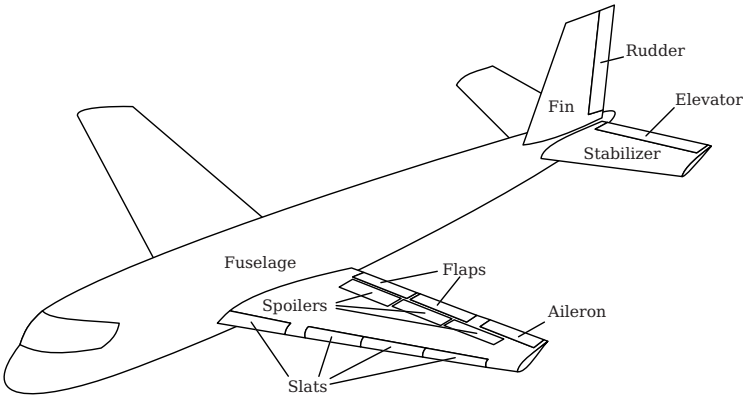

Figure 1.1 – Standard Aircraft Control Surface Locations [1]

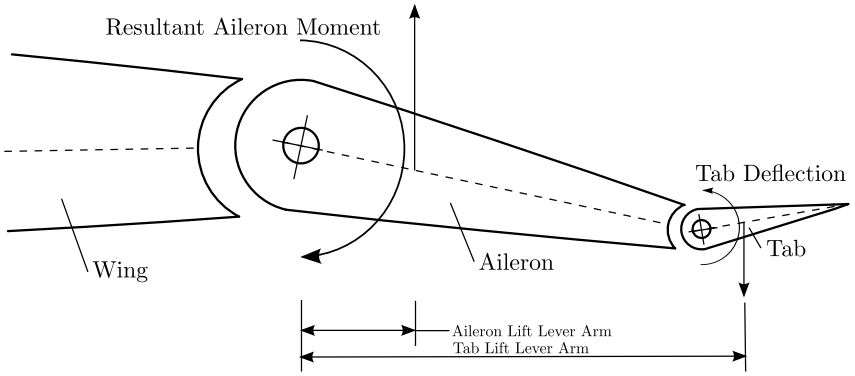

Figure 1.2 – Typical Trailing Edge Tab

developed. The concept of the project is to employ trailing edge tabs to reduce the actuator hinge moment requirements and actuate the control surface through the trailing edge tab. This concept is combined with smart materials aimed at developing more compact and efficient actuators.

The idea of using trailing edge tabs to reduce hinge moment requirements is not a new concept. Early aircraft control surfaces were actuated directly by pilot effort. The progression of aircraft design and development of larger and faster aircraft meant that inherently the stick force needed to move the control surface increased drastically. It came to a point where mechanical advantage became ineffective and cumbersome. This sparked research into trailing edge tabs and many other aerodynamic balancing devices to reduce the control surface hinge moment. Phillips coined this “the quest for reduced control forces” [2].

The concept a trailing edge tab is simple. It was initially developed in the 30’s and 40’s [4]. It is based on the idea that an additional rear hinged part of the control surface operated in the opposite direction of the control surface can result in reduced or even zero control surface hinge moment. Figure 1.2 shows the typical layout of a trailing edge tab along with the control surface and the aerodynamic surface or wing. The lift of each of the independent surfaces can be considered. Specifically, the lift of the tab and control surface can be considered at their respective centres of pressure. The tab lifting force at centre of pressure results in a hinge moment around the tab hinge which is counteracted by the tab actuator. The control surface lift at its centre of pressure results in a hinge moment around the control surface hinge. In conjunction with this, the tab lift also results in a hinge moment around the control surface hinge. The tab lift, which is much smaller, has a mechanical advantage and is in the opposite direction to the control surface lift effect. The correct tab deflection can then result in zero aileron hinge moment. Since both the tab lift and the control surface lift is dependent on their orientations, a specific tab orientation will result in a specific aileron orientation.

In the attempt to apply this concept, it was found that the tab was ineffective at low speeds [4]. It was also found that the two degrees of freedom was prone to flutter [5]. Abzug and Larrabee commented that the advent of hydraulic boost and later hydraulic servos were much simpler to apply than aerodynamic balancing [4]. It avoids potential low-speed control and flutter problems and therefore marked a shift from the aerodynamic balancing methods [4]. The hydraulic actuation of control surfaces has to date remained the standard solution for large aircraft requiring large actuation forces. Planned and unplanned maintenance costs are however major disadvantages to

hydraulic systems [6].

The novelty in the new approach to the trailing edge tab concept is the actuation of both the tab and aileron. This would in theory solve the problems facing the early attempts to implement this concept such as low-speed operation and possibly suppression of control surface oscillations. This is facilitated by development of smart material actuators that could actuate these surfaces.

The development of smart material actuators primarily deals with new actuation methods which makes use of material characteristics to achieve motion. The study of the material characteristics and actuator development is primarily the focus of our research associates at CPUT. Various materials are being investigated. The advantageous traits of each candidate material is being tested and analysed with focus on its application to a trailing edge tab or a control surface.

The control system design for these materials and actuators is undertaken by R.F. Ethlers at Stellenbosch University. Here, various control methods are being evaluated with the focus on tab actuation.

Development of the trailing edge tab configuration was delegated to Stellenbosch University. However, the inherent aerodynamic nature of the problem promoted the inclusion of the University of Witwatersrand (Wits) and the University of Cape Town (UCT) for aerodynamic assistance. The first tier of the problem was initiated by C.D. Jaquet in the study on “The optimisation of trailing edge tabs to reduce control surface hinge moments” [1]. The primary focus was the geometric optimisation of the tab and aileron control surfaces. The focus of the optimisation was on the aileron of an Airbus A330 aircraft. It was concluded that the optimisation of the trailing edge tabs has shown that tab-like structures can be “useful in the endeavour to reduce primary control surface hinge moments” [1]. The development of the control system for the geometrically optimal aileron now remains.

1.2 Project Goals

The focus of this thesis is the control of the optimised tab-aileron control surface combination. The objective is to achieve accurate deflection of the aileron control surface under varying flight conditions.

This entails the development of a parametric model of the tab and aileron based on the available aerodynamic data. Analysis of the model should provide insight into the dynamics and statics of the system. The model must allow for both the tab and aileron control surface to be actuated. The model should then be integrated into a simulation environment ready for the application of control.

To achieve accurate deflection of the control surface a control algorithm has to be proposed. The performance of this control algorithm should match the performance attained by existing control surface actuators used in the Airbus A330. The control algorithm should also be able to achieve the performance across the operating range of the aircraft. Further, simulation of the control algorithm should also provide insight into the actuator requirements of the tab-aileron system.

Finally, the model and control algorithm should be validated through experimentation in a wind tunnel environment. The validation should provide a measure of the accuracy of the model and provide an indication of the controller performance in the wind tunnel environment.

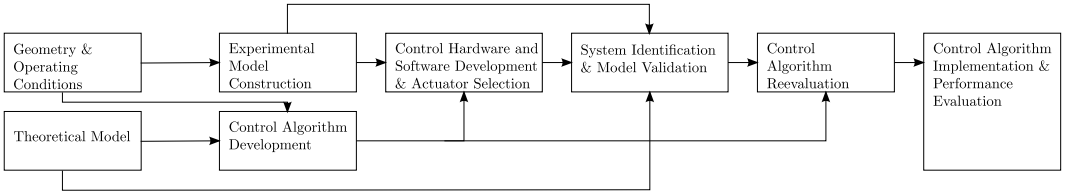

Figure 1.3 – Dependencies of Project Tasks

1.3 Project Approach and Overview

The tasks completed to achieve the ultimate project goal of accurate control over the range of aircraft flight conditions is organised in Figure 1.3 according to their dependency on each other.

The first two tasks of the project, as seen in Figure 1.3, are independent. The development of a parametric theoretical model could be conducted first as a stepping stone for control algorithm development. In parallel to it the geometric and operational constraints of the experimental model needs to be selected. The primary objective of the experimental model would be to confirm the theoretical model and demonstrate the control algorithm. Without the collection of experimental data, it would be hard to provide accurate insight into the accuracy of the theoretical model and therefore the expected control performance. The objective would not be to characterise the aerodynamics of the concept but rather, the aim is to compare the macroscopic behaviour of the experimental setup to that of the theoretical model.

With the available wind tunnel resources it would not be possible to test a full scale and full speed experimental model over the range of flight conditions. It is therefore decided that a low-speed reduced sized model will be constructed and tested to confirm the theoretical model. The control systems would then be tested on the reduced sized model. The notion is that if the model can be confirmed under the conditions for which it is evaluated, it would provide a method for developing a full scale model if all the aerodynamic and geometric data were available.

The consequent task would then be the combination of the geometry and operational conditions with the theoretical model to develop the control algorithm. The geometric data is important in this stage since the dynamics are dependent on the geometry and therefore affect the control algorithm design choices.

The experimental model is then constructed based on the chosen geometry. Along with this, the control hardware would also be designed based on the control requirements identified in the control algorithm development stage. This would be accompanied with the design of adequate control and logging software.

The integration of the experimental model, control hardware and software would then allow system identification to be done. This would then be compared to the theoretical model. Upon completion, the control algorithms would then be revised.

Finally, the control will be implemented on the control hardware and the control algorithms would be tested on the experimental model. The performance of the proposed algorithms would then be evaluated.

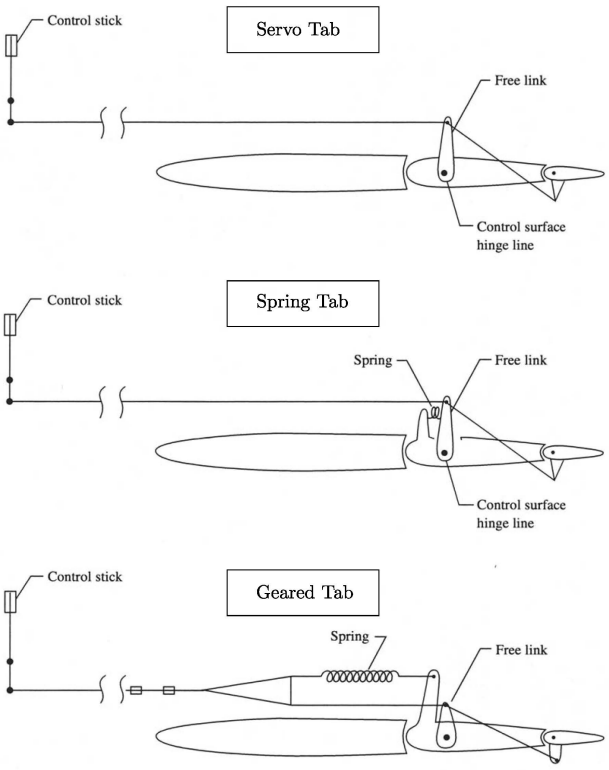

Figure 1.4 – Varied Tab Actuation Concepts [2]

1.4 Previous Research

Most of the publications available on the use of tabs to reduce control surface hinge moments originated from the 1930's and 1940's. The most readily available publications originate from NACA [3] now integrated with NASA [4] where most of the research was conducted. [7] provides a summary of all the data collected on tab actuation at Langley.

Most of the research deals with either servo tab, spring tab or geared tab configurations as presented in Figure 1.4. However, it does not deal with independent actuation of both surfaces. Rather, the surfaces were decoupled from each other and only the tab was actuated or the surfaces were coupled to each other through linkages or springs. Further, the analyses were mostly done statically determining the hinge moments of different tab and control surface orientations. Dynamic investigation came primarily in the form of experimental flutter testing done by Theodorsen and Smith [5][8].

More recently Soinne published a paper touching on some computational fluid dynamics of the spring tab-aileron combination as well as investigating the effect of aileron-wing gap on the stick control force [9]. Further flight dynamic testing was done to test the aircraft roll response in the frequency domain [9]. However, no apparent investigation was made into the tab and aileron dynamics.

[3] National Advisory Committee for Aeronautics
[4] National Aeronautics and Space Administration

Various aircraft employ servo tab or spring tab controls successfully. The more well known example is the Douglas DC-6 and more recently the Saab 2000 and Saab 340A/B. Generally the application of the concept seems to be at airspeeds below Mach 0.5.

1.5 Thesis Outline

The thesis structure is formulated mostly according to the project approach described in §1.3. §2 deals with the development of the theoretical model of the tab-aileron combination. The model derivation, linearisation and analysis is covered. §3, §3 and §5 deals with the control algorithms. The development of the control structures and evaluation of it is presented in these chapters. §6 covers the experimental design and procedure. §7 the process of system identification and the applicable theory behind it. Then, §8 gives analysis of the practical implementation results. Finally, §9 summarises the significant results and give recommendations of what future work would be valuable in further development of the concept.

Chapter 2

Modelling

The primary objectives of adding tabs to control surfaces is to reduce the resultant actuator hinge moment requirements. However, coupled with the reduced hinge moments is the need to understand the dynamics of the tab-aileron concept. The chapter is therefore initiated with the development of a generalised dynamic model of the tab-aileron combination. This however does not yet include the specific aerodynamic and actuator hinge moments.

Therefore, an overview of the aerodynamic model for static control surfaces is given. The synthesis of this static model is based on thin aerofoil theory, Xfoil and PABLO [1] software provided by C. Day [10]. The model aims to provide the hinge moments at the tab and aileron hinge points given a specific subsystem state. The state can be defined as the specific physical configuration, specified angle of attack, tab deflection and aileron deflection. In general, the model is built on a predefined physical configuration which was optimised in terms of the static hinge moments and operation envelope. The optimisation was conducted by Jaquet as part of the CoSICS project [1]. The variable parameters that remain are angle of attack, tab deflection and aileron deflection. For known values of the aforementioned three, the hinge moments can be calculated.

The hinge moment coefficients are then implemented in the dynamic equations. These dynamic equations are then reformulated into an input-output system. The system is then linearised for convenience at later stages of controller design. The dynamic characteristics of the linearised model is further considered and used to predict the model dependence on independent variables such as airspeed, angle of attack, atmospheric conditions and design geometry. It is also shown that the fully coupled system is unstable due to the interaction of the tab and aileron. Additionally, it is shown that the simplified servo tab system is stable if the tab dynamics are suppressed. Lastly, the conditions for applicability of the linearisation is summarised, suggesting that linear control is applicable around a trim condition.

Continuing with the analysis of system characteristics, the steady-state condition is used to develop a static model for the tab-aileron combination. The static model is able to predict the steady-state orientations of the tab and aileron based on a set of design constraints.

To conclude, the different models used for different actuator implementations are summarised giving brief descriptions of the actuator characteristics and their implications in terms of the dynamic model.

[1] Potential flow around Aerofoils with Boundary Layer coupled One-way

2.1 Tab-Aileron Dynamics

This section presents the development of the generalised equations of motion for the tab-aileron system. Firstly, the equations of motion is derived from energy principles and the application of the Euler-Lagrange equation as described in [11]. This then results in equations of motion that contains full inertial coupling.

The first step is to consider the centre of mass and the moment of inertial of the surfaces as described in the Figure 2.1. The sum of the kinetic energy of the surfaces is then given by:

$$E_T = \frac{1}{2}m_a(e_a\dot{\delta_a})^2 + \frac{1}{2}I_a\dot{\delta_a}^2 + \frac{1}{2}m_t(e_{at}\dot{\delta_a} + e_t\dot{\delta_t})^2 + \frac{1}{2}I_t(\dot{\delta_t} + \dot{\delta_a})^2 \tag{2.1.1}$$

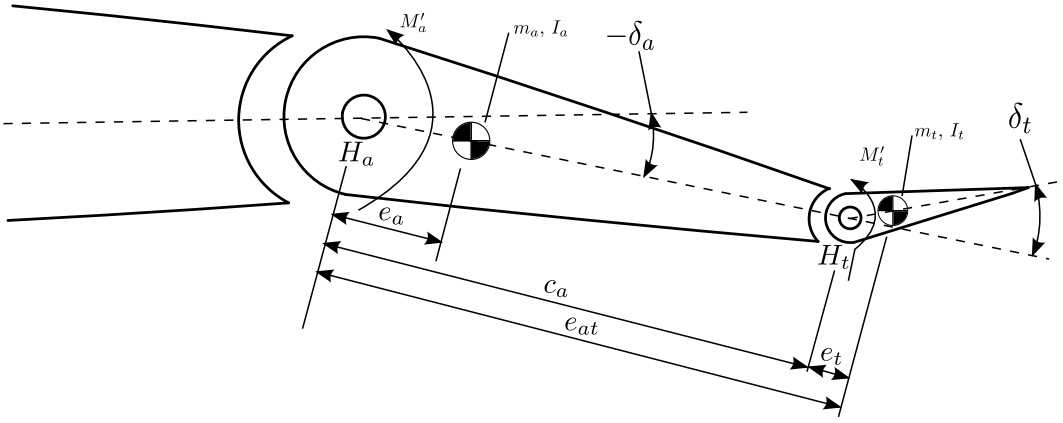

Figure 2.1 – Tab and Aileron Mechanics

The sum of the potential energy of the surfaces are given for the conservative forces only as [11]:

$$E_V = 0 \tag{2.1.2}$$

The Euler-Lagrange equation including external forces is given by:

$$\frac{d}{dt}\left(\frac{\partial E_T}{\partial \dot{\delta}_i}\right) - \frac{\partial E_T}{\partial \delta_i} + \frac{\partial E_V}{\partial \delta_i} = M'_i \tag{2.1.3}$$

Here M'_i is the externally applied moments and non-conservative moments [11]. The partial derivatives are given by:

$$\frac{\partial E_T}{\partial \delta_i} = 0 \tag{2.1.4}$$

$$\frac{\partial E_V}{\partial \delta_i} = 0 \tag{2.1.5}$$

$$\frac{d}{dt}\left(\frac{\partial E_T}{\partial \dot{\delta_t}}\right) = m_t e_t^2\ddot{\delta}_t + m_t e_t e_{at}\ddot{\delta}_a + I_t\ddot{\delta}_t + I_t\ddot{\delta}_a \tag{2.1.6}$$

$$\frac{d}{dt}\left(\frac{\partial E_T}{\partial \dot{\delta_a}}\right) = m_a e_a^2\ddot{\delta}_a + I_a\ddot{\delta}_a + m_t e_{at}^2\ddot{\delta}_a + m_t e_t e_{at}\ddot{\delta}_t + I_t\ddot{\delta}_a + I_t\ddot{\delta}_t \tag{2.1.7}$$

Equation 2.1.3 through Equation 2.1.7 results in:

$$\begin{bmatrix} m_t e_t^2 + I_t & m_t e_t e_{at} + I_t \\ m_t e_t e_{at} + I_t & m_a e_a^2 + m_t e_{at}^2 + I_a + I_t \end{bmatrix} \begin{bmatrix} \ddot{\delta}_t \\ \ddot{\delta}_a \end{bmatrix} = \begin{bmatrix} M_t' \\ M_a' \end{bmatrix} \tag{2.1.8}$$

Equation 2.2.8 describes the generalised dynamics of the tab and aileron with M_t' and M_a' as external moments due to the tab and aileron actuators and the aerodynamics.

2.2 Aerodynamic Hinge Moments

This section focusses on the inclusion of aerodynamics into the generalised tab-aileron dynamics. This is facilitated by first giving a brief overview of important aerodynamic coefficients and conventions. The hinge moment coefficients are then substituted into the generalised dynamics and then the necessary adjustments are made to include the effects of dynamic control surfaces.

The process of determining the lift, drag and hinge moment coefficients of the tab, aileron and wing is mathematically involving. There are various methods for determining these forces and moments resulting from airflow over these surfaces. [12] and [13] provides good theoretical accounts of the calculation of the hinge moment coefficients and lifting forces. The objective is not to redevelop the mathematics but rather use the available data in order to develop a static and dynamic model at a later stage. However, understanding of the assumptions made in the aerodynamic process will provide insight into where the theory might be a weak representation of actuality.

The development of the dynamic model can be based either on theoretical derivation or experimental measurements of lift, drag and hinge moment data. All that is required is a complete set of data in order to determine the resultant forces and moments on the tab and aileron. This is convenient since if more accurate data were obtained, it could be used directly to improve the dynamic model.

The data was primarily provided by our research partners at UCT and necessary adjustments were made by Jaquet [1]. The aerodynamic data is based on thin aerofoil theory which have some inherent assumptions. The assumptions are that the maximum thickness of the foil is small compared to the chord and that airflow is two dimensional in the plane of the aerofoil cross-section. Further, the data provided is only valid for small angles of attack [1]. Furthermore, the theory makes use of inviscid and incompressible flow and is only valid for low Mach numbers less than 0.3.

In aerodynamics, the convention is to represent the forces in their non-dimensional forms thereby generalising the data. The lift, drag and hinge moments are normalised in terms of the dynamic pressure of the free stream, q, and the wing chord, c, giving non-dimensional coefficients. The dynamic pressure is given by the air density, ρ_∞, and free stream velocity, V_∞:

$$q = \frac{1}{2}\rho_\infty V_\infty^2 \tag{2.2.1}$$

The lifting force, L, the drag force, D and the hinge moment, M is then given by:

$$L = qcC_L(\alpha, \delta_t, \delta_a, c_a, c_t) \tag{2.2.2}$$

$$D = qcC_D(\alpha, \delta_t, \delta_a, c_a, c_t) \tag{2.2.3}$$

$$M_a = qc^2C_{Ha}(\alpha, \delta_t, \delta_a, c_a, c_t) \tag{2.2.4}$$

$$M_t = qc^2C_{Ht}(\alpha, \delta_t, \delta_a, c_a, c_t) \tag{2.2.5}$$

The conventions of the moments and forces are presented in Figure 2.2. Positive direction is taken to be the upward displacement of the aileron or tab. Lift is considered the force, resulting from the airflow over the surface, in the perpendicular direction to the airflow and drag the force parallel to the airflow. The parameters of primary importance here are the tab and aileron hinge moment coefficients, C_{Ht} and C_{Ha} respectively. This allows for the static equilibrium orientation to be found. It also allows for development of the angular dynamics based on the hinge moment the tab and aileron will experience at any given orientation, δ_t and δ_a. The hinge moment coefficients are also dependent on the angle of attack, α, and the tab and aileron chord, c_t and c_a respectively.

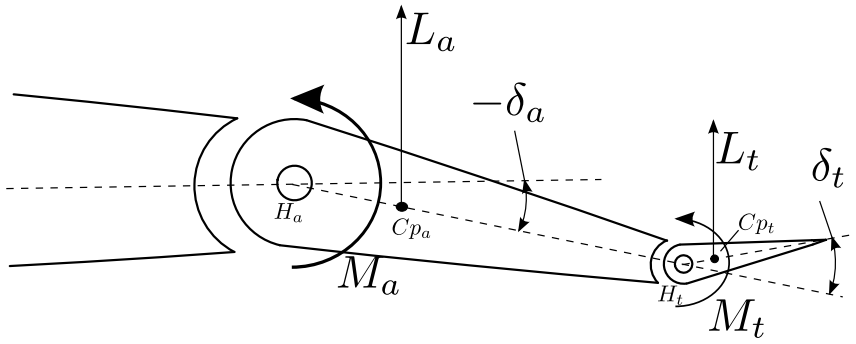

Figure 2.2 – Deflection, Force and Moment Conventions

There are two methods of achieving the same hinge moment coefficients. The intuitive method for determining the moments is to use the lift coefficients and drag coefficients of the wing sections and determining the centres of lift and drag thereby determining the moments around the hinge points. The method through which the centres of lift and lift coefficients are determined is by the integral of the upper and lower pressure distribution along the chambered aerofoil. This leads to a simpler approach of determining the hinge moments. The hinge moments can be found by directly integrating the pressure distribution, for example Figure 2.3, multiplied by the lever arm over the surface. The pressure distribution is easily extracted from Xfoil, thin aerofoil theory or PABLO.

The generalised dynamics presented in Equation 2.2.8 is now combined with the hinge moment coefficients. The moments M_t' and M_a' is now comprised of the aerodynamic hinge moment and the actuator applied moments as seen in Equation **??** Equation 2.2.7. The aerodynamic hinge moments can be expressed in terms of the non-dimentionalised hinge moment coefficients C_{Ht} and C_{Ha} as stated previously.

$$T_t - q\bar{c}^2 C_{Ht}(\delta_t, \delta_a, \alpha, c) = M_t' \tag{2.2.6}$$

$$T_a - q\bar{c}^2 C_{Ha}(\delta_t, \delta_a, \alpha, c) = M_a' \tag{2.2.7}$$

This method for approximating aerodynamic hinge moments is implemented by [11] to model flutter. Equation 2.2.8 then gives the general equation of motion of the tab and aileron combination.

$$\begin{bmatrix} m_t e_t^2 + I_t & m_2 e_t e_{at} + I_t \\ m_2 e_t e_{at} + I_t & m_a e_a^2 + m_t e_{at}^2 + I_a + I_t \end{bmatrix} \begin{bmatrix} \ddot{\delta}_t \\ \ddot{\delta}_a \end{bmatrix} + \begin{bmatrix} q\bar{c}^2 C_{Ht}(\delta_t, \delta_a, \alpha, c) \\ q\bar{c}^2 C_{Ha}(\delta_t, \delta_a, \alpha, c) \end{bmatrix} = \begin{bmatrix} T_t \\ T_a \end{bmatrix} \tag{2.2.8}$$

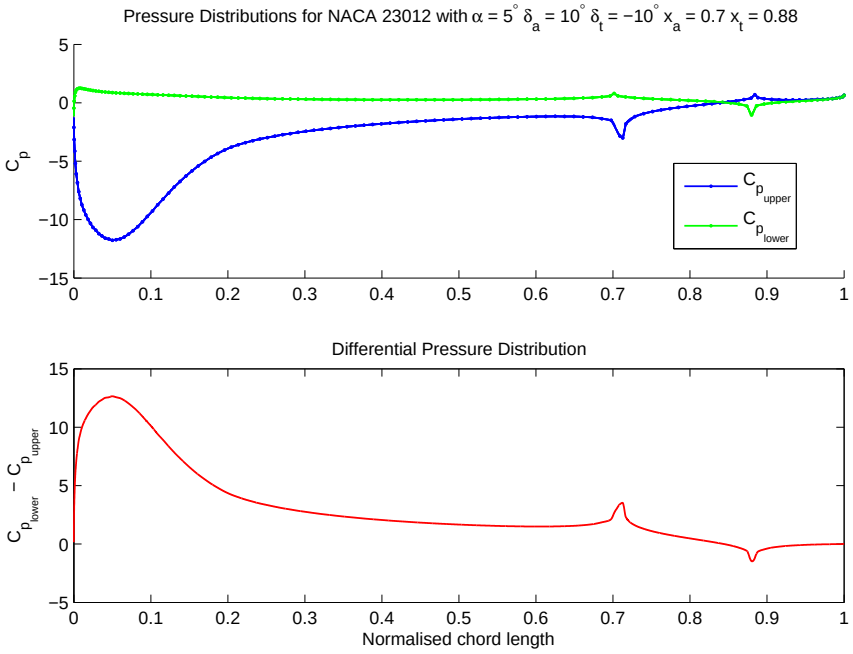

Figure 2.3 – Typical Upper and Lower Surface Pressure Distribution from Xfoil

The next phase is the evaluation of the hinge moment coefficients. The hinge moment coefficient analytical relations are tedious to work with and complicates matters. Furthermore, if data from computational fluid dynamics (CFD), numerical solvers or experimental setups were to be used, a more generic method through which the data can be represented is required. Therefore, a multidimensional Taylor approximation is used to represent the hinge moment coefficient relation as described in Equation 2.2.9 and Equation 2.2.10. The Taylor expansion of the aerodynamic hinge moment relations is used to determine the hinge moment as a function of the current state as shown in Equation 2.2.11. It should be noted in Equation 2.2.9 and Equation 2.2.10 that the dynamics of the tab-aileron configuration, terms such as $\ddot{\delta_a}$, $\dot{\delta_a}$, $\ddot{\delta_t}$ and $\dot{\delta_t}$, do not affect the hinge moment coefficients. The reason for this is that the hinge moment coefficient relations are determined for static surfaces.

$$\begin{aligned} C_{Ht}(X) &= f_{C_{Ht}}(\underline{X}_0) + \nabla f_{C_{Ht}}(\underline{X}_0)^T \times (\underline{X} - \underline{X}_0) + \\ &\quad \frac{1}{2!}(\underline{X} - \underline{X}_0)^T \times \nabla^2 f_{C_{Ht}}(\underline{X}_0) \times (\underline{X} - \underline{X}_0) + \ldots \qquad (2.2.9) \\ C_{Ha}(X) &= f_{C_{Ha}}(\underline{X}_0) + \nabla f_{C_{Ha}}(\underline{X}_0)^T \times (\underline{X} - \underline{X}_0) + \\ &\quad \frac{1}{2!}(\underline{X} - \underline{X}_0)^T \times \nabla^2 f_{C_{Ha}}(\underline{X}_0) \times (\underline{X} - \underline{X}_0) + \ldots \qquad (2.2.10) \end{aligned}$$

$$\underline{X} = \begin{bmatrix} \alpha \\ \delta_t \\ \delta_a \\ \bar{c} \end{bmatrix} \qquad (2.2.11)$$

In simulation it is not necessary to approximate the data and a lookup table may be

used in a numerical simulation process. The objective here is to work towards a model that can be used in control applications not only non-linear simulation.

The method used for determining the effect of the angular rate of the tab and aileron on the hinge moment coefficients is based on the method proposed by Cook to calculate the short period mode damping of an aircraft due to the tailplane [14]. The crux of this approximation is the consideration of the induced angle of attack of the control surface. By translating the angular velocity of the control surface to a tangential velocity at the quarter chord length or centre of lift, the induced normal velocity can be considered a change in angle of attack, see Figure 2.4. It is clear that the tab and aileron are not free surfaces. Consequently, the angle of attack assumption may not be valid due to non-uniform airflow around these surfaces. The centre of lift of the surfaces can also vary significantly over the deflection range of the control surfaces. As the angle of attack increases, the lift contribution of angle of attack effects tend to shift the centre of pressure of the surface forward closer to the quarter chord from the midpoint [14]. To apply these principles to the tab and aileron some assumptions must be made in terms of the flow over the control surfaces. The validity of the assumptions can only be verified once the model parameter identification is done experimentally. The first assumption that must be made in order to apply the principles is that the airflow is unseparated and steady over the tab and aileron. This assumption varies in validity as the angles of deflection of the tab and aileron changes. However, this is an inherent assumption in thin aerofoil theory and therefore it can be carried forward through the modelling process [13]. The assumption of steady airflow may be the largest error introduced in the model since the surface is moving relative to the airflow the flow will not be steady. It can result in significant error in the resultant damping and lift of the surfaces and therefore hinge moment errors.

The second assumption is that the change in angle of attack of the tab aileron configuration can be approximated as a additional aileron or tab deflection or induced angle of attack. This allows evaluation of the resultant hinge moment with the statically determined hinge moment coefficient relations.

The third assumption is that the parallel component of the tangential velocity to the airflow is negligible since the local parallel airflow will be much larger than this component [14]. Thereby, it implies that only the normal component of the tangential velocity has an effect on the angle of attack, Figure 2.4.

Taking the local airflow angle as δ the apparent change in the angle of the local airflow is given by $\Delta\delta$. For small changes in angle, the airflow angle can be approximated as follows:

$$\Delta\delta_a = tan\frac{\frac{1}{4}c_a\dot{\delta_a}}{V} \qquad \approx \frac{\frac{1}{4}c_a\dot{\delta_a}}{V} \tag{2.2.12}$$

$$\Delta\delta_t = tan\frac{\dot{\delta_a}cos(\delta_t)c_a + \frac{1}{4}c_t\dot{\delta_t}}{V} \qquad \approx \frac{\dot{\delta_a}cos(\delta_t)c_a + \frac{1}{4}c_t\dot{\delta_t}}{V} \tag{2.2.13}$$

The adjusted C_{Ht} and C_{Ha} in Equation 2.2.8 can be calculated as before with Equation 2.2.9 and Equation 2.2.10 respectively by adjusting the state, Equation 2.2.16, with Equation 2.2.12 and Equation 2.2.13 as shown in Equation 2.2.17. This constitutes the approximate model of the aileron and tab dynamics.

$$C_{H_{\dot{\delta_a}}}\dot{\delta_a} \approx C_{H_{\delta_a}}\Delta\delta_a \tag{2.2.14}$$

$$C_{H_{\dot{\delta_t}}}\dot{\delta_t} \approx C_{H_{\delta_t}}\Delta\delta_t \tag{2.2.15}$$

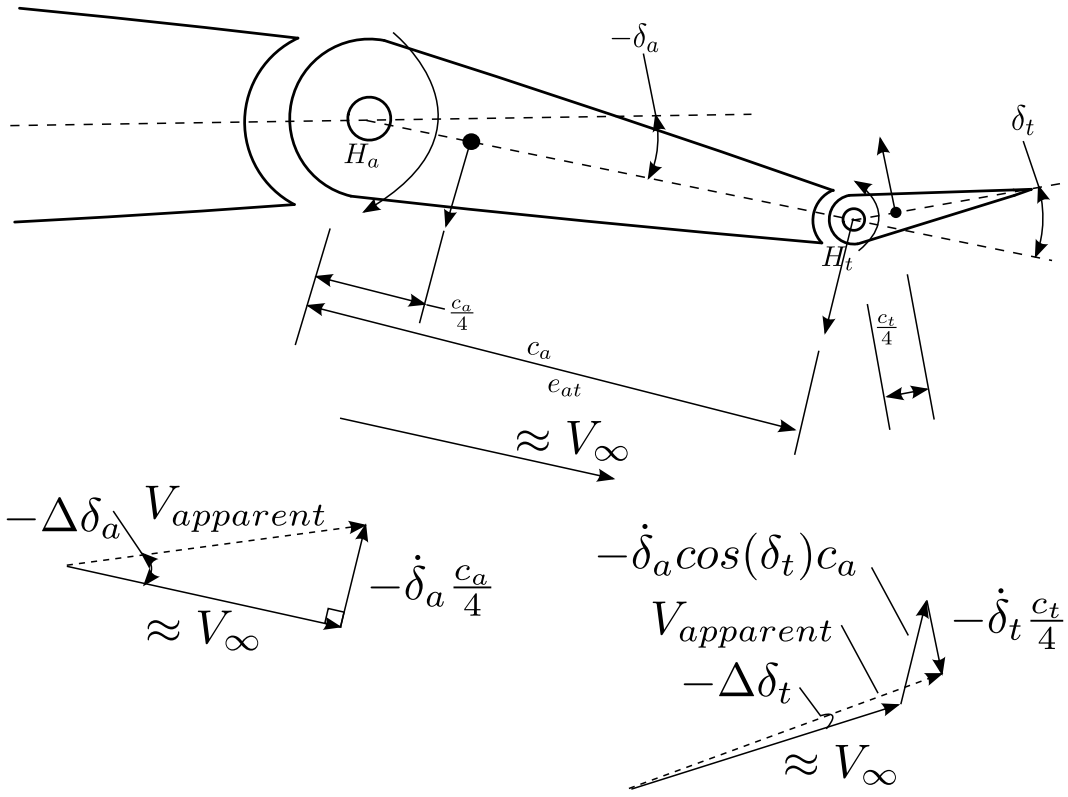

Figure 2.4 – Apparent Airflow

$$\underline{X}_{X+\Delta X} = \begin{bmatrix} \alpha \\ \delta_t + \Delta\delta_t \\ \delta_a + \Delta\delta_a \\ \bar{c} \end{bmatrix} \tag{2.2.16}$$

$$\begin{bmatrix} m_t e_t^2 + I_t & m_2 e_t e_{at} + I_t \\ m_2 e_t e_{at} + I_t & m_a e_a^2 + m_t e_{at}^2 + I_a + I_t \end{bmatrix} \begin{bmatrix} \ddot{\delta}_t \\ \ddot{\delta}_a \end{bmatrix} + \begin{bmatrix} q\bar{c}^2 C_{Ht}(\delta_t + \Delta\delta_t, \delta_a + \Delta\delta_a, \alpha, c) \\ q\bar{c}^2 C_{Ha}(\delta_t + \Delta\delta_t, \delta_a + \Delta\delta_a, \alpha, c) \end{bmatrix} = \begin{bmatrix} T_t \\ T_a \end{bmatrix} \tag{2.2.17}$$

This model developed in this section provides the basis for control systems development and prediction of system dynamics. The model can be based on any dataset sufficiently complete to allow fitting of a Taylor series. The model can be used in the non-linear form for simulation as presented in Equation 2.2.17. The model accuracy is partially dependent on the accuracy of the provided hinge moment coefficient data and the accuracy of the fit of the Taylor series on the dataset. The use of the Taylor series included here facilitates linearisation of the theoretical model.

2.3 Linearisation of Dynamics

The non-linear model derived in the previous section attempts to predict the dynamic behaviour of the system; however, it is not necessarily convenient for control system design. It would not be impossible to derive a non-linear controller for the system. But, it has to be considered whether all the non-linear dynamics are represented in the system model without considering more complex aerodynamic effects and if it was not what the effects would be on the model specific non-linear controller? Furthermore, will the resulting non-linear controller result in the improved performance? Therefore, the approach is to linearise the model, designing a linear model based controller and evaluating whether the performance is sufficient; if it is not, a different route is then justified.

This section therefore deals with the linearisation of the fully coupled non-linear model. The fully coupled linear model is then presented. Following this, a simplification is made to the fully coupled system to indicate the dynamics of a servo tab configuration.

The hinge moment coefficients are not linearly related to the states. But, it may be possible to make a linear assumption within certain bound of operation. If one were to consider the data presented in Figure 2.5, the data seems to be quite linear upon graphical inspection. A linear approximation results in $\pm 5\%$ error over the operational range. This linearisation equates to truncating the Taylor series, Equation 2.2.9 and Equation 2.2.10, to the first order. The result is given by:

$$C_{Ht}(X_{X+\Delta X}) = f_{C_{Ht}}(\underline{X}_0) + \nabla f_{C_{Ht}}(\underline{X}_0)^T \times (\underline{X_{X+\Delta X}} - \underline{X}_0) \tag{2.3.1}$$

$$C_{Ha}(X_{X+\Delta X}) = f_{C_{Ha}}(\underline{X}_0) + \nabla f_{C_{Ha}}(\underline{X}_0)^T \times (\underline{X_{X+\Delta X}} - \underline{X}_0) \tag{2.3.2}$$

The Jacobian, ∇f_{C_H}, in terms of $X_{X+\Delta X}$ is given by:

$$\nabla f_{C_H} = \begin{bmatrix} C_{H_\alpha} \\ C_{H_{\delta_t}} \\ C_{H_{\delta_a}} \\ C_{H_{\delta_c}} \end{bmatrix} \equiv \begin{bmatrix} \frac{\partial C_H}{\partial \alpha} \\ \frac{\partial C_H}{\partial \delta_t} \\ \frac{\partial C_H}{\partial \delta_a} \\ \frac{\partial C_H}{\partial c} \end{bmatrix} \tag{2.3.3}$$

So, Equation 2.3.2 and Equation 2.3.2 combined with Equation 2.2.17 results in:

$$\begin{aligned} &\begin{bmatrix} m_t e_t^2 + I_t & m_2 e_t e_{at} + I_t \\ m_2 e_t e_{at} + I_t & m_a e_a^2 + m_t e_{at}^2 + I_a + I_t \end{bmatrix} \begin{bmatrix} \ddot{\delta}_t \\ \ddot{\delta}_a \end{bmatrix} \\ &+ \begin{bmatrix} q\bar{c}^2 \left(C_{Ht_{\delta_t}}(\delta_t + \Delta\delta_t) + C_{Ht_{\delta_a}}(\delta_a + \Delta\delta_a) \right) \\ q\bar{c}^2 \left(C_{Ha_{\delta_a}}(\delta_a + \Delta\delta_a) + C_{Ha_{\delta_t}}(\delta_t + \Delta\delta_t) \right) \end{bmatrix} \\ &= \begin{bmatrix} T_t + q\bar{c}^2 \left(-\alpha C_{Ht_\alpha} - \bar{c} C_{Ht_{\bar{c}}} - f_{C_{Ht}}(\underline{X}_0) \right) \\ T_a + q\bar{c}^2 \left(-\alpha C_{Ha_\alpha} - \bar{c} C_{Ha_{\bar{c}}} - f_{C_{Ha}}(\underline{X}_0) \right) \end{bmatrix} \end{aligned} \tag{2.3.4}$$

At this point it is important to discuss the profile of the hinge moment coefficient derivatives. Through investigation, not shown here, it was found that the derivatives vary significantly around the zero deflection angles showing that the derivatives have to be evaluated away from this point. This results in smaller hinge moment errors due to linearisation.

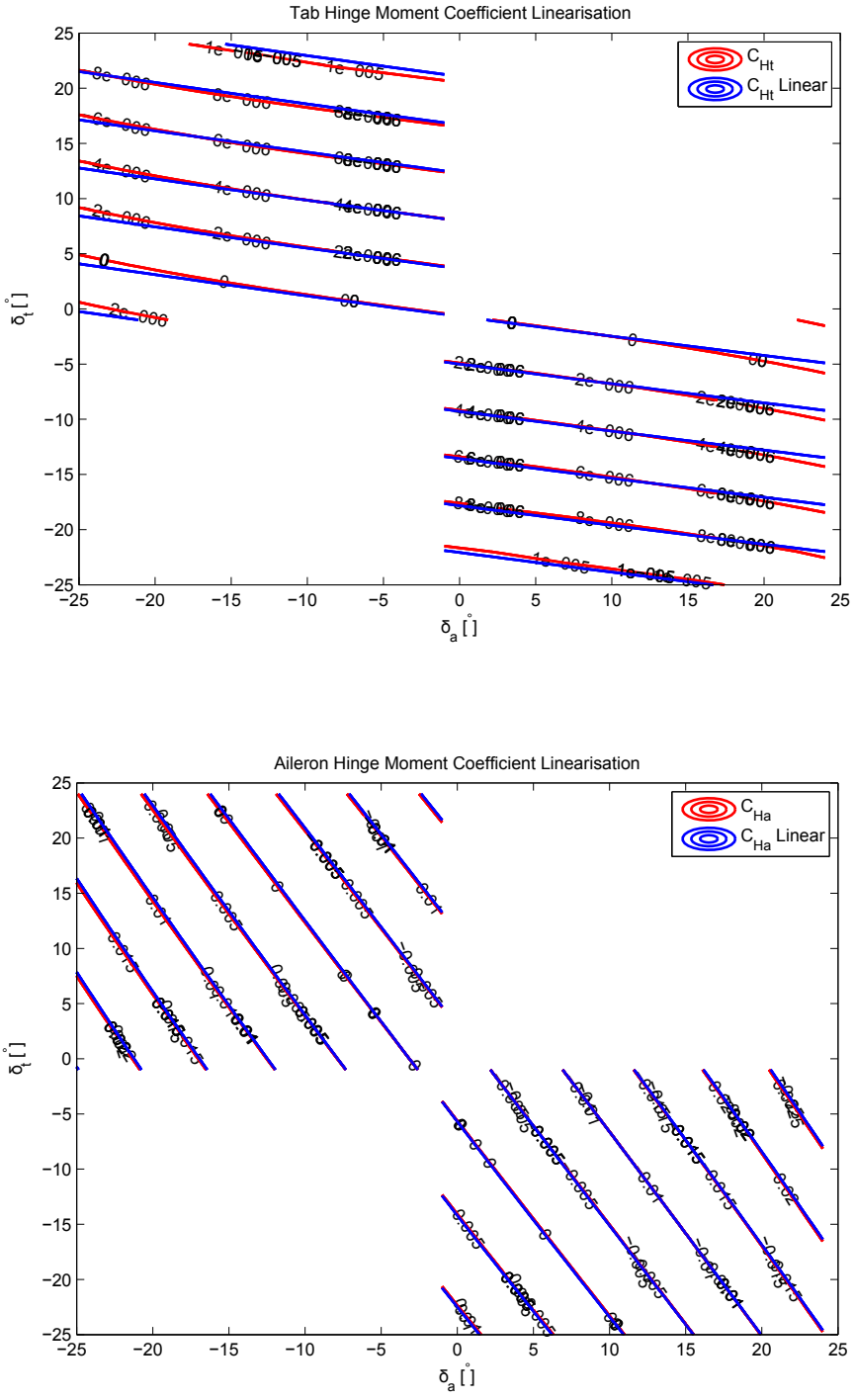

Figure 2.5 – Linearised Hinge Moment Coefficient over Operational Bounds

At this stage only the hinge moment relation has been linearised. The non-linearity that remains is contained in $\Delta\delta_t$ and $\Delta\delta_a$. The linearisation results from Equation 2.3.4 combined with Equation 2.2.12 and Equation 2.2.13 gives:

$$\begin{bmatrix} m_t e_t^2 + I_t & m_2 e_t e_{at} + I_t \\ m_2 e_t e_{at} + I_t & m_a e_a^2 + m_t e_{at}^2 + I_a + I_t \end{bmatrix} \begin{bmatrix} \ddot{\delta}_t \\ \ddot{\delta}_a \end{bmatrix} = \begin{bmatrix} 1 & 0 \\ 0 & 1 \end{bmatrix} \begin{bmatrix} T_t \\ T_a \end{bmatrix}$$
$$+ \begin{bmatrix} q\bar{c}^2 \left(-C_{Ht_{\delta_t}} \left(\frac{\dot{\delta_a} cos(\delta_t)\bar{c_a} + \frac{1}{4}\bar{c}_t\dot{\delta_t}}{V} + \delta_t \right) - C_{Ht_{\delta_a}} \left(\frac{\frac{1}{4}\bar{c}_a\dot{\delta_a}}{V} + \delta_a \right) - \alpha C_{Ht_\alpha} - \bar{c} C_{Ht_{\bar{c}}} - f_{C_{Ht}}(\underline{X}_0) \right) \\ q\bar{c}^2 \left(-C_{Ha_{\delta_a}} \left(\frac{\dot{\delta_a} cos(\delta_t)\bar{c_a} + \frac{1}{4}\bar{c}_t\dot{\delta_t}}{V} + \delta_t \right) - C_{Ha_{\delta_t}} \left(\frac{\frac{1}{4}\bar{c}_a\dot{\delta_a}}{V} + \delta_a \right) - \alpha C_{Ha_\alpha} - \bar{c} C_{Ha_{\bar{c}}} - f_{C_{Ha}}(\underline{X}_0) \right) \end{bmatrix} \tag{2.3.5}$$

The equations are then linearised around a specified trim state.

$$f(X, U, ...) - f(X_0, U_0, ...) \approx \nabla f(X_0, U, ...)(X - X_0) + \nabla f(X, U_0, ...)(U - U_0) \tag{2.3.6}$$

$$\underbrace{\begin{bmatrix} m_t e_t^2 + I_t & m_2 e_t e_{at} + I_t \\ m_2 e_t e_{at} + I_t & m_a e_a^2 + m_t e_{at}^2 + I_a + I_t \end{bmatrix}}_{\bar{J}} \begin{bmatrix} \ddot{\delta}_t - \ddot{\delta}_{t_0} \\ \ddot{\delta}_a - \ddot{\delta}_{a_0} \end{bmatrix}$$
$$= \underbrace{\begin{bmatrix} \frac{\partial F_1}{\partial \dot{\delta_t}} & \frac{\partial F_1}{\partial \dot{\delta_a}} \\ \frac{\partial F_2}{\partial \dot{\delta_t}} & \frac{\partial F_2}{\partial \dot{\delta_a}} \end{bmatrix}}_{\bar{B}_k} \begin{bmatrix} \dot{\delta}_t - \dot{\delta}_{t_0} \\ \dot{\delta}_a - \dot{\delta}_{a_0} \end{bmatrix}$$
$$+ \underbrace{\begin{bmatrix} \frac{\partial F_1}{\partial \delta_t} & \frac{\partial F_1}{\partial \delta_a} \\ \frac{\partial F_2}{\partial \delta_t} & \frac{\partial F_2}{\partial \delta_a} \end{bmatrix}}_{\bar{K}_k} \begin{bmatrix} \delta_t - \delta_{t_0} \\ \delta_a - \delta_{a_0} \end{bmatrix}$$
$$+ \underbrace{\begin{bmatrix} 1 & 0 \\ 0 & 1 \end{bmatrix}}_{\bar{G}_k} \begin{bmatrix} T_t - T_{t_0} \\ T_a - T_{a_0} \end{bmatrix} \tag{2.3.7}$$

The partial derivatives of F_1 and F_2 are determined to be:

$$\frac{\partial F_1}{\partial \delta_t} = -q\bar{c}^2 \left(\frac{-\dot{\delta_{a_0}} sin(\delta_{t_0})\bar{c_a}}{V} + 1 \right) C_{Ht_{\delta_t}} \tag{2.3.8}$$

$$\frac{\partial F_1}{\partial \dot{\delta_t}} = -q\bar{c}^2 \frac{\bar{c}_t}{4V} C_{Ht_{\delta_t}} \tag{2.3.9}$$

$$\frac{\partial F_1}{\partial \delta_a} = -q\bar{c}^2 C_{Ht_{\delta_a}} \tag{2.3.10}$$

$$\frac{\partial F_1}{\partial \dot{\delta_a}} = -q\bar{c}^2 \left(\left(\frac{cos(\delta_{t_0})\bar{c}_a}{V} \right) C_{Ht_{\delta_t}} + \frac{\bar{c}_a}{4V} C_{Ht_{\delta_a}} \right) \tag{2.3.11}$$

$$\frac{\partial F_2}{\partial \delta_t} = -q\bar{c}^2 \left(\frac{-\dot{\delta_{a_0}} sin(\delta_{t_0})\bar{c_a}}{V} + 1 \right) C_{Ha_{\delta_t}} \tag{2.3.12}$$

$$\frac{\partial F_2}{\partial \dot{\delta_t}} = -q\bar{c}^2 \frac{\bar{c}_t}{4V} C_{Ha_{\delta_t}} \tag{2.3.13}$$

$$\frac{\partial F_2}{\partial \delta_a} = -q\bar{c}^2 C_{Ha_{\delta_a}} \tag{2.3.14}$$

$$\frac{\partial F_2}{\partial \dot{\delta_a}} = -q\bar{c}^2 \left(\left(\frac{cos(\delta_{t_0})\bar{c}_a}{V} \right) C_{Ha_{\delta_t}} + \frac{\bar{c}_a}{4V} C_{Ha_{\delta_a}} \right) \tag{2.3.15}$$

With equations Equation 2.3.8 through Equation 2.3.15 substituted into Equation 2.3.7, the instantaneous linearised dynamic equation is determinable for a known trim state, X_0, of the configuration. The state X is defined as:

$$X = \begin{bmatrix} \dot{\delta}_t \\ \ddot{\delta}_t \\ \dot{\delta}_a \\ \ddot{\delta}_a \end{bmatrix} \tag{2.3.16}$$

The dynamic equation can now be restructured into a state-space representation. Consider the generalised notation as follows:

$$\bar{J}\ddot{\bar{\delta}} = \bar{B}\dot{\bar{\delta}} + \bar{K}\bar{\delta} + \bar{G} \tag{2.3.17}$$

The inverse of $\bar{J}$ can then be applied to the equation:

$$\ddot{\bar{\delta}} = \bar{J}^{-1}\bar{B}_k\dot{\bar{\delta}} + \bar{J}^{-1}\bar{K}_k\bar{\delta} + \bar{J}^{-1}\bar{G}_k \tag{2.3.18}$$

with:

$$B' \equiv \bar{J}^{-1}\bar{B}_k \quad K' \equiv \bar{J}^{-1}\bar{K}_k \quad G' \equiv \bar{J}^{-1}\bar{G}_k \tag{2.3.19}$$

The state-space representation then becomes:

$$\underbrace{\begin{bmatrix} \dot{\delta}_t \\ \ddot{\delta}_t \\ \dot{\delta}_a \\ \ddot{\delta}_a \end{bmatrix}}_{\dot{X}} = \underbrace{\begin{bmatrix} 0 & 1 & 0 & 0 \\ K'_{11} & B'_{11} & K'_{12} & B'_{12} \\ 0 & 0 & 0 & 1 \\ K'_{21} & B'_{21} & K'_{22} & B'_{22} \end{bmatrix}}_{F(X_0)} \underbrace{\begin{bmatrix} \delta_t \\ \dot{\delta}_t \\ \delta_a \\ \dot{\delta}_a \end{bmatrix}}_{X} + \underbrace{\begin{bmatrix} 0 & 0 \\ G'_{11} & G'_{12} \\ 0 & 0 \\ G'_{21} & G'_{22} \end{bmatrix}}_{G} \begin{bmatrix} M_t \\ M_a \end{bmatrix} \tag{2.3.20}$$

Equation 2.3.20 represents the linearised state equation in terms of the trim state of the system. The system can be re-linearised at each point in time or a nominal linearisation point can be used as indicative for a specific hypersurface in the four dimensional phase plane. The bounds of validity of the trajectory predicted by the linearisation is dependent on the system. Logically, it follows that the farther from linear the system the smaller the bounds in which linearisation is sufficiently accurate. Sufficiently accurate is also a relative statement since the linearised model might quickly diverge from the non-linear model in terms of response but might still correctly predict the initial state trajectory. Therefore, accuracy will be evaluated in terms of the final controller performance rather than on immediate open loop accuracy of the linear model.

Now that a linear model for the fully coupled model has been developed, a special case of this system can be considered in which only the tab is actuated. This is the classic servo tab configuration. The aileron state space representation can be rewritten with the tab states as the input as seen in Equation 2.3.22. To simplify the scenario it is assumed that the tab moment of inertial is small compared to the aileron moment of inertial and that the tab is effectively mass balanced. The calculated tab moment of inertia for the developed experimental model is about twenty times smaller than the calculated aileron moment of inertia and the calculated centre of mass is less than one millimetre from the hinge point. From Equation 2.3.7, the aileron dynamics become:

$$\underbrace{(m_a e_a^2 + m_t e_{at}^2 + I_a + I_t)}_{I_{at}}\ddot{\delta}_a = \frac{\partial F_2}{\partial \dot{\delta}_t}\dot{\delta}_t + \frac{\partial F_2}{\partial \dot{\delta}_a}\dot{\delta}_a + \frac{\partial F_2}{\partial \delta_t}\delta_t + \frac{\partial F_2}{\partial \delta_a}\delta_a \tag{2.3.21}$$

The state space representation of the aileron dynamics then become:

$$\underbrace{\begin{bmatrix}\dot{\delta_a}\\ \ddot{\delta_a}\end{bmatrix}}_{\dot{X}} = \underbrace{\begin{bmatrix}0 & 1\\ \frac{1}{I_{at}}\frac{\partial F_2}{\partial \delta_a} & \frac{1}{I_{at}}\frac{\partial F_2}{\partial \dot{\delta_a}}\end{bmatrix}_{X_k}}_{F(X_k)}\underbrace{\begin{bmatrix}\delta_a\\ \dot{\delta_a}\end{bmatrix}}_{X} + \underbrace{\begin{bmatrix}0 & 0\\ \frac{1}{I_{at}}\frac{\partial F_2}{\partial \delta_t} & \frac{1}{I_{at}}\frac{\partial F_2}{\partial \dot{\delta_t}}\end{bmatrix}}_{G(X_k)}\begin{bmatrix}\delta_t\\ \dot{\delta}_t\end{bmatrix} \tag{2.3.22}$$

The linearisation validity constraints are the same for the servo tab system as for the fully actuated system. The resultant system is now a single input single output (SISO) system. The transfer function is then derived for a tab deflection input to aileron deflection output as shown in Figure 2.6.

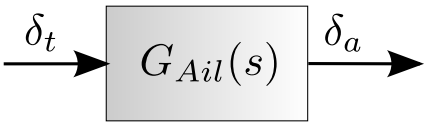

Figure 2.6 – SISO Aileron Model

The model of the tab and aileron configuration is derived in state space form in §2.3.7. The linearised state space model given by Equation 2.3.22. The transfer function from tab deflection to aileron deflection is now derived along with the transfer function from tab rate to aileron deflection as shown in Equation 2.3.24 and Equation 2.3.25 respectively. The resulting complete SISO transfer function is then given by Equation 2.3.28 and is given in terms of the tab-aileron parameters by Equation 2.3.30.

$$\begin{aligned}\begin{bmatrix}\dot{\delta_a}\\ \ddot{\delta_a}\end{bmatrix} &= \underbrace{\begin{bmatrix}0 & 1\\ -\frac{q\bar{c}^2}{I_{at}}C_{Ha_{\delta_a}} & -\frac{q\bar{c}^2}{I_{at}}\left(\left(\frac{cos(\delta_{t_0})\bar{c}_a}{V}\right)C_{Ha_{\delta_t}} + \frac{\bar{c}_a}{4V}C_{Ha_{\delta_a}}\right)\end{bmatrix}}_{F}\begin{bmatrix}\delta_a\\ \dot{\delta_a}\end{bmatrix} +\\ &\quad \underbrace{\begin{bmatrix}0 & 0\\ -\frac{q\bar{c}^2}{I_{at}}\left(\frac{-\dot{\delta_{a_0}}sin(\delta_{t_0})\bar{c_a}}{V}+1\right)C_{Ha_{\delta_t}} & -\frac{q\bar{c}^2}{I_{at}}\frac{\bar{c}_t}{4V}C_{Ha_{\delta_t}}\end{bmatrix}}_{\begin{bmatrix}G_1 & G_2\end{bmatrix}}\begin{bmatrix}\delta_t\\ \dot{\delta}_t\end{bmatrix}\end{aligned} \tag{2.3.23}$$

$$\frac{\delta_a(s)}{\delta_t(s)} = H(sI-F)^{-1}G_1 \tag{2.3.24}$$

$$\frac{\delta_a(s)}{\dot{\delta}_t(s)} = H(sI-F)^{-1}G_2 \tag{2.3.25}$$

$$H = \begin{bmatrix}1\\ 0\end{bmatrix} \tag{2.3.26}$$

for zero initial condition

$$\mathscr{L}(\dot{\delta}_t(t)) = s\delta_t(s) \tag{2.3.27}$$

$$F(s) = \frac{\delta_a(s)}{\delta_t(s)} + s\frac{\delta_a(s)}{\dot{\delta}_t(s)} \tag{2.3.28}$$

$$\begin{aligned}F(s) &= -\frac{\frac{q\bar{c}^2}{I_{at}}\frac{\bar{c}_t}{4V}C_{Ha_{\delta_t}}s + \frac{q\bar{c}^2}{I_{at}}\left(\frac{-\dot{\delta_{a_0}}sin(\delta_{t_0})\bar{c_a}}{V}+1\right)C_{Ha_{\delta_t}}}{s^2 + \frac{q\bar{c}^2}{I_{at}}\left(\left(\frac{cos(\delta_t)\bar{c}_a}{V}\right)C_{Ha_{\delta_t}} + \frac{\bar{c}_a}{4V}C_{Ha_{\delta_a}}\right)s + \frac{q\bar{c}^2}{I_{at}}C_{Ha_{\delta_a}}}\\ &\equiv \frac{\beta_1 s + \beta_0}{s^2 + 2\zeta\omega_n s + w_n^2}\end{aligned} \tag{2.3.29}$$

With respect to Equation 2.3.30 the transfer function as be presented as shown in Figure 2.7.

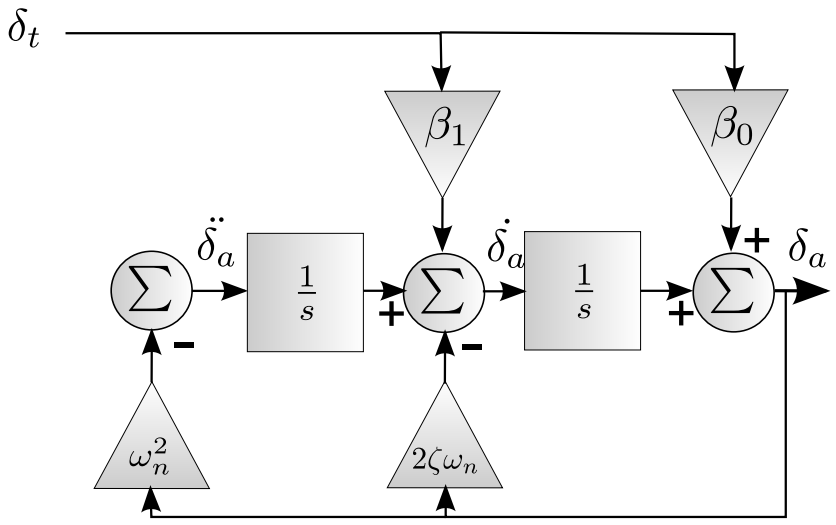

Figure 2.7 – Aileron Transfer Function Block Diagram

Certain aspects about the system transfer function is visible upon initial inspection. The first aspect is that the gain of the system is negative. This is expected since the natural motion of the physical components, tab and aileron, are in opposite directions by modus operandi. This implies that the controller with a negative gain or a positive feedback loop should be used to be equivalent to simple negative feedback. A negative gain controller would be a more elegant option since a positive reference will result in a response in the positive direction. From initial inspection, it is also visible that there are two system poles and one zero.

The zero is shown here to be dependent on the velocity, the effect of the tab on the aileron hinge moment, ratio of the chords, aileron trim rate and tab trim position. It has been found in that this zero is located around -150 to -200 on the real axis. Compared the the dynamics of the system poles, around -15 on the real axis, this zero had little effect.

First, the steady-state gain of deflection from the trim point is given by:

$$K = \frac{\frac{q\bar{c}^2}{I_{at}} C_{Ha_{\delta_t}}}{\frac{q\bar{c}^2}{I_{at}} C_{Ha_{\delta_a}}} \tag{2.3.30}$$

It can also be seen that the natural frequency of the aileron is given by:

$$\omega_n^2 = \frac{q\bar{c}^2}{I_{at}} C_{Ha_{\delta_a}} \tag{2.3.31}$$

As will be shown in §2.4, it is linearly related to velocity, wing chord and to the square root of the hinge moment and density divided by the moment of inertia. Dampening is also shown to be independent of velocity to an extent and that it is partially related to

the ratio between the tab and aileron hinge moment coefficients.

$$\omega_n = V\bar{c}\sqrt{\frac{\rho C_{Ha_{\delta_a}}}{2I_{at}}} \tag{2.3.32}$$

$$2\zeta\omega_n = \frac{q\bar{c}^2}{I_{at}}\left(\left(\frac{cos(\delta_t)\bar{c}_a}{V}\right)C_{Ha_{\delta_t}} + \frac{\bar{c}_a}{4V}C_{Ha_{\delta_a}}\right) \tag{2.3.33}$$

$$\zeta \propto \bar{c}c_a \tag{2.3.34}$$

$$\zeta \propto \sqrt{\frac{\rho C_{Ha_{\delta_a}}}{I_{at}}} \tag{2.3.35}$$

$$\zeta \propto C_{Ha_{\delta_t}}\sqrt{\frac{\rho}{C_{Ha_{\delta_a}}I_{at}}} \tag{2.3.36}$$

It will be shown in §2.4 that there is only weak dependence to the tab and aileron orientation. From the above reaffirmation of the relationship between the transfer function and independent variables above, the linear controller design for the servo tab system only needs to be recalculated based on velocity and atmospheric conditions for a fixed geometry and trim. The dependence on angle of attack is only contained in the variation of the hinge moment derivatives with angle of attack. This now serves as the foundation for the tab-only actuated control scenario further developed in §4.

2.4 Dynamic Characteristics

The model has been developed from the theoretical equations of motion and hinge moment relations; a good feel for the behaviour of the system focusses controller design choices at later stages. Summing up the dynamic behaviour of the system also serves as a check to see if the system behaves as expected. Conversely, it can serve as indication of behaviour that may not be obvious at first glance. This section is therefore focussed on the dynamic characteristics of the system over the operational range. The effect of change in the system independent variables are considered in terms of the non-linearities they introduce. The independent variables includes the effects that are inherent to the operational envelope and design variables; these conditions include air speed, angle of attack, aileron chord ratio and tab chord ratio. The effects of these variables are first analysed with respect to the fully coupled system followed by the simplification to the servo tab configuration.

The first and most obvious way to analyse the system is to evaluate the eigenvalues of the linearised system at different states and atmospheric conditions. It is noted that for a sufficiently smooth linearisable system the linear state matrix will provide a sufficient approximation to the system trajectories within certain bounds [15]. Ideally all the eigenvalues should be on the left of the imaginary axis signifying stable trajectories. This translates to stable open-loop system poles. However, if this is not the case then it would be up to the control system to stabilise the system.

In order to evaluate the effect of the various independent variables on the system eigenvalues, the eigenvalues are evaluated at different values of the independent variables within the operational range. This provides a graphical method of evaluating the dependence of the eigenvalues on each independent variable. A numerical method is used since the fourth order characteristic equation is not readily solvable analytically. The resulting strength of dependence on the independent variable will indicate the degree of linearisability and the bounds of validity of that linearisation.

Initially, consider a specific point in trimmed flight for the system. The model is then linearised at the specific trim altitude, air speed and angle of attack. The geometry is also fixed to the design geometry. The remaining variables are the tab and aileron states. The variation of the eigenvalues of the system can then be evaluated at the different system states. The eigenvalues are found by re-linearising the tab and aileron dynamics at different tab and aileron states. The graphical representation of this is given in Figure 2.8 and Figure 2.9. It can be seen that there is about $1,5\%$ variation of the values with tab state and 10% variation of the values with aileron state over the deflection range. If the controller is robust enough to absorb the variation then system re-linearisation would only be necessary at new trim conditions.

The concave shape of the variation is due to the effect of positive and negative deflections. System states away from the zero deflection state tend to show larger magnitude eigenvalues since larger hinge moments result as the surfaces are deflected. An analogy to this is a larger spring constant in a second order system increasing the eigenvalue/pole magnitude of the system, all else being equal. The relation between the eigenvalues of the system and the outputs, δ_t and δ_a, can be viewed through state variable transformation. The eigenvalue decomposition is given by, see Equation 2.3.7 for notation:

$$F = V\Lambda V^{-1} \tag{2.4.1}$$

Λ is the diagonal eigenvalue matrix and V is the matrix of corresponding eigenvectors. Then apply the state variable transformation into canonical form:

$$\dot{X} = FX + GU \quad Y = CX \tag{2.4.2}$$

$$\bar{X} = VX \tag{2.4.3}$$

$$\dot{\bar{X}} = V^{-1}FV\bar{X} + V^{-1}GU \tag{2.4.4}$$

$$Y = CV\bar{X} \tag{2.4.5}$$

$$\dot{\bar{X}} = \bar{F}\bar{X} + \bar{G}U \tag{2.4.6}$$

$$Y = \bar{C}\bar{X} \tag{2.4.7}$$

$$\bar{C} = CV = \begin{bmatrix} 1 & 0 & 0 & 0 \\ 0 & 0 & 1 & 0 \end{bmatrix} V \tag{2.4.8}$$

$$\bar{F} = \Lambda \tag{2.4.9}$$

$\bar{C}$ then describes the relation between the transformed states and the outputs. These state characteristics are dependent on their respective eigenvalues and are decoupled form each other [16]. It can be noted, when $\bar{C}$ is evaluated, that the tab and aileron are almost equally coupled to all four eigenvalues. This is only a qualitative evaluation of the effects but it suggests that the tab may not be decoupled from the aileron unless the tab can be actuated in a manner which rejects the coupling from the aileron to the tab. This is further discussed in §3.2.1.

The variation of the eigenvalues over range of free-stream velocity and density however results in order changes in eigenvalue over a velocity order change and pressure order change. Both pressure and velocity result in higher eigenvalues as they increase. This is again due to the higher effective aerodynamic restoring moments in the system which is related to dynamic pressure, q. Since the damping ratio in this model contains the term $\frac{q}{V}$, it is expected that damping ratio is linearly related to velocity and density. However, eigenvalue variation in the linearised model shows no damping ratio variation of the eigenvalues due to velocity, Figure 2.10. This could be due to the combination of

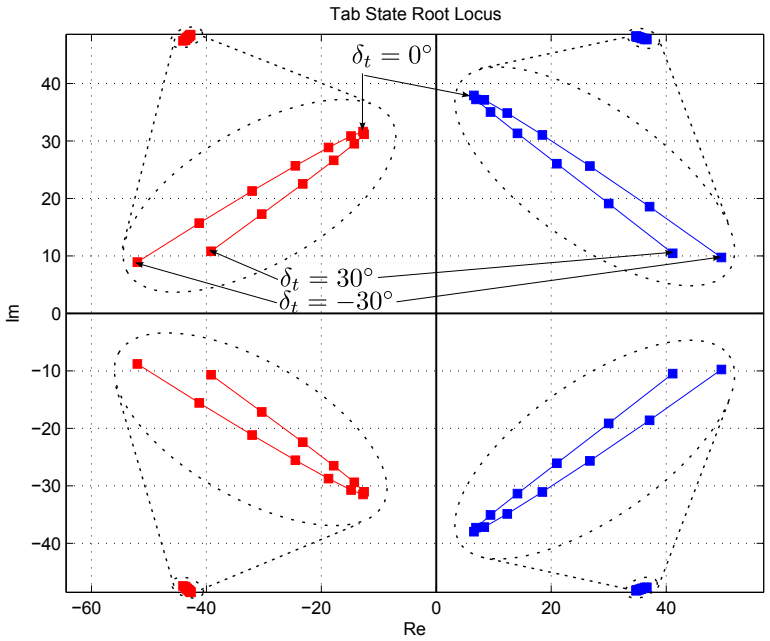

Figure 2.8 – Eigenvalue Variation due to Tab State

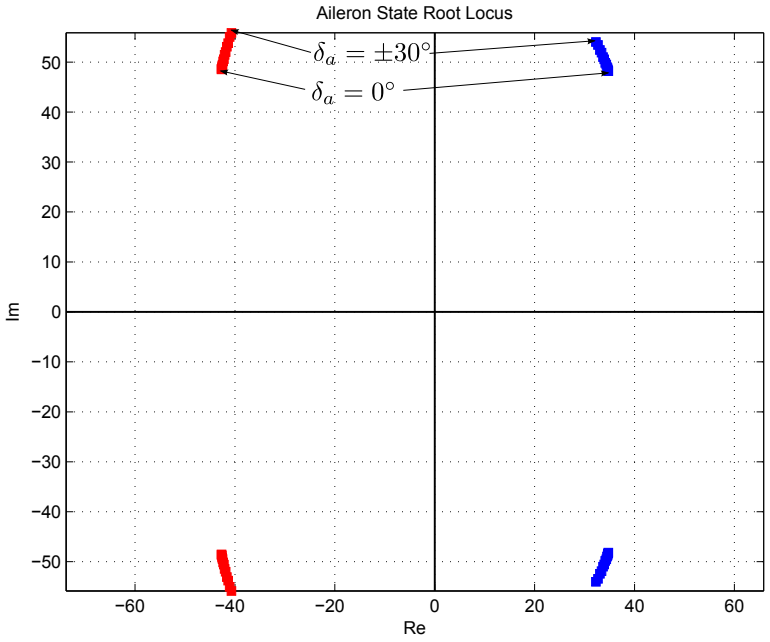

Figure 2.9 – Eigenvalue Variation due to Aileron State

the structure of the model or the linearisation at zero angular velocity. An insignificant amount of damping ratio change is observed due to the density change Figure 2.11. The angle of attack variation also results in no significant variation of the eigenvalues. This means that dynamics would remain the same for the range of angles of attack of the system. This is the case since there is little variation in the hinge moment coefficient derivatives in terms of angle of attack.

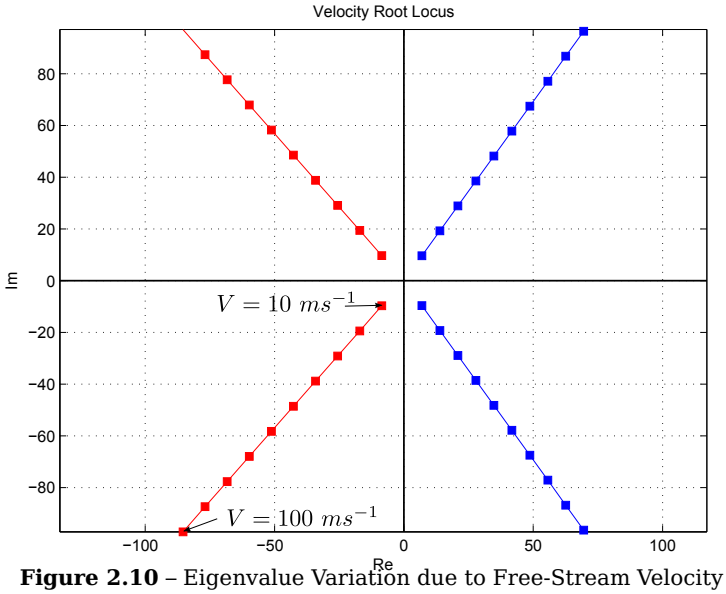

Figure 2.10 – Eigenvalue Variation due to Free-Stream Velocity

Further, variation in terms of design geometry shows that there is no geometric configuration that would result in a open-loop stable system, see Figure 2.12. Here the tab chord ratio is increased from 3% to 47% of the aileron chord. The eigenvalues start with very different magnitudes and as the chord of the tab increases they become closer to the same size suggesting they become more strongly coupled.

The case where the system is operated as a servo tab, the dynamic characteristics vary in the same fashion as the previous case. However, the two eigenvalues are directly related to the aileron poles. Both of these poles are stable since they remain on the left hand side of the imaginary axis throughout as seen in Figure 2.13. The linearised aileron dynamics as presented in Equation 2.3.22 from which some specific characteristics about the tab independent aileron can be determined. The second order dynamic parameters are repeated here for comparison with the numerical results as follows:

$$\omega_n^2 = -\frac{q\bar{c}^2}{I_{at}} C_{Ha_{\delta_a}} \tag{2.4.10}$$

$$\omega_n = V\bar{c}\sqrt{\frac{\rho C_{Ha_{\delta_a}}}{2I_{at}}} \tag{2.4.11}$$

$$2\zeta\omega_n = \frac{q\bar{c}^2}{I_{at}}\left(\left(\frac{cos(\delta_t)\bar{c}_a}{V}\right)C_{Ha_{\delta_t}} + \frac{\bar{c}_a}{4V}C_{Ha_{\delta_a}}\right) \tag{2.4.12}$$

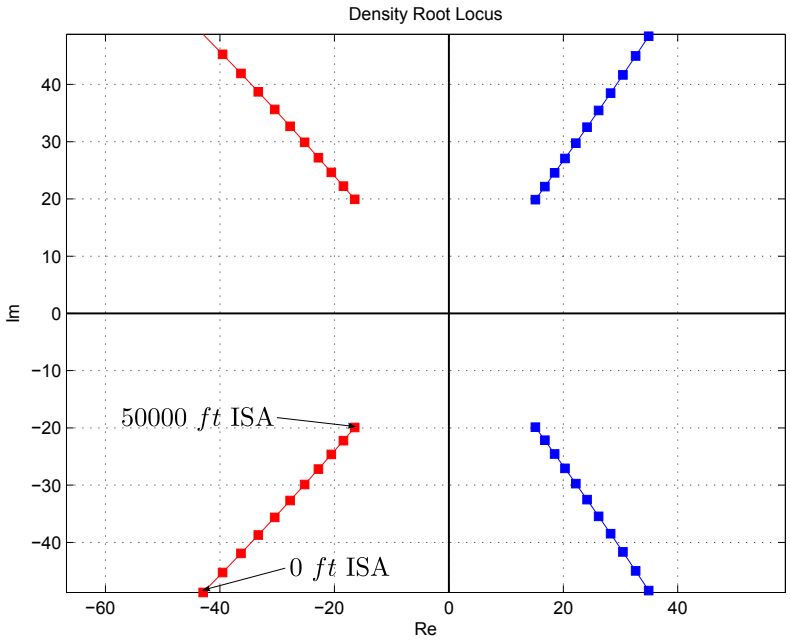

Figure 2.11 – Eigenvalue Variation due to Density

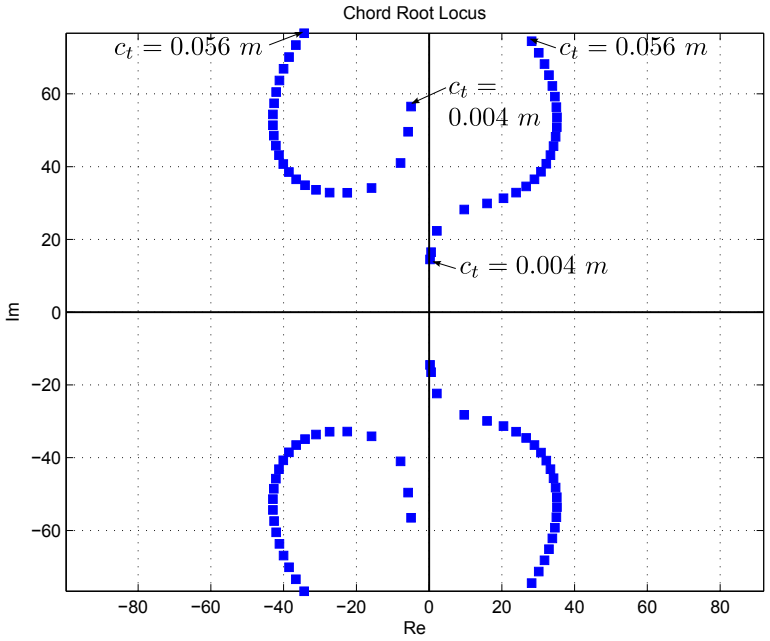

Figure 2.12 – Eigenvalue Variation due to Tab Chord Ratio

$$\zeta \propto \bar{c} c_a \tag{2.4.13}$$

$$\zeta \propto \sqrt{\frac{\rho C_{Ha_{\delta_a}}}{I_{at}}} \tag{2.4.14}$$

$$\zeta \propto C_{Ha_{\delta_t}} \sqrt{\frac{\rho}{C_{Ha_{\delta_a}} I_{at}}} \tag{2.4.15}$$

The steady-state gain of deflection from the trim point is given by:

$$K = \frac{\frac{q\bar{c}^2}{I_{at}} C_{Ha_{\delta_t}}}{\frac{q\bar{c}^2}{I_{at}} C_{Ha_{\delta_a}}} \tag{2.4.16}$$

These trends provides ground for comparison between the theoretical linearised model and the estimated linear time invariant model derived from system identification.

The analysis of the dynamics in terms of the system parameters show that the variation of the eigenvalues in terms of air speed and density is the most predominant. It is therefore required that re-linearisation and control recalculation is needed for the range of pressures and velocities. I would have been convenient to describe this variation in terms of dynamic pressure however the damping coefficient is in this case only related to velocity and not to density. However, the relinearisation points can still be described in terms of dynamic pressure. The variation in terms of angle of attack, tab and aileron states are negligible in terms of the system dynamics. It is therefore not necessary to re-linearise in terms of these variables.

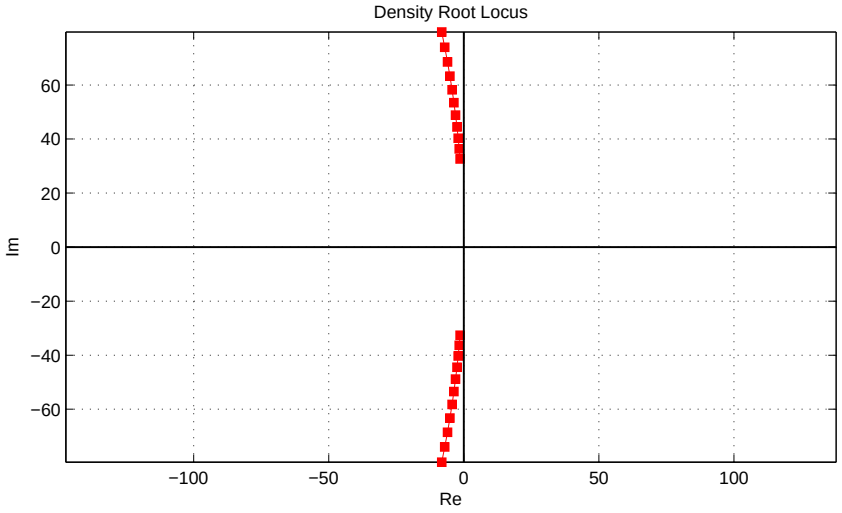

(a) Eigenvalue Variation due to Density

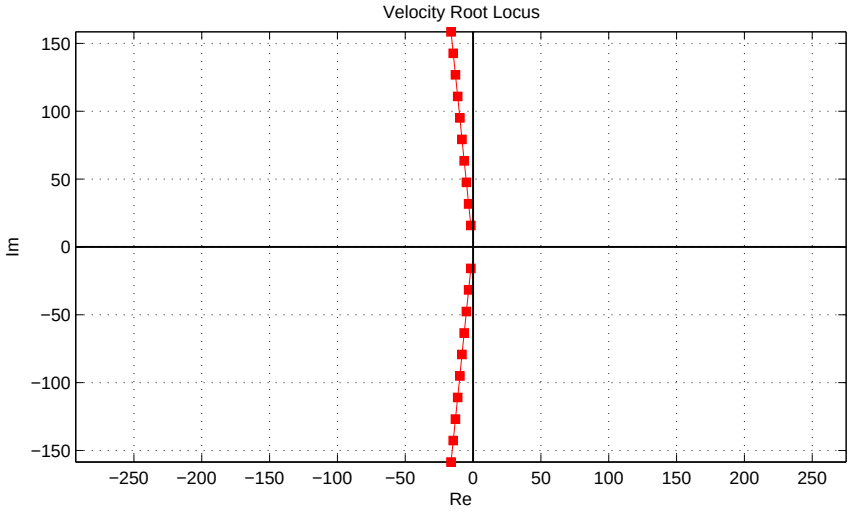

(b) Eigenvalue Variation due to Airspeed

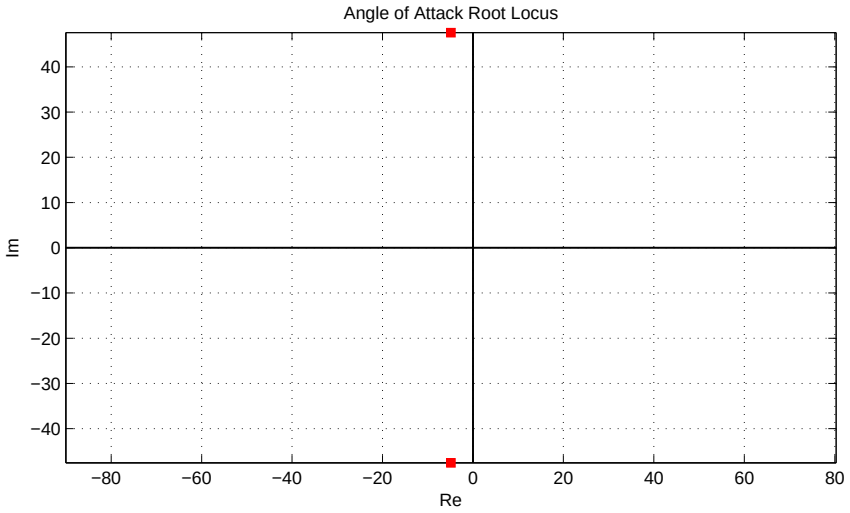

(c) Eigenvalue Variation due to Angle of Attack

Figure 2.13 – Eigenvalue Variation for the Aileron Decoupled from the Tab

2.5 Steady-State Characteristics

The steady-state behaviour of the tab-aileron concept is considered in this section. This provides insight into the final aileron and tab deflections that may be expected depending on the moments applied to the hinges. It also provides insight into the required tab deflection to achieve a desired aileron deflection if zero aerodynamic aileron hinge moment is required.

A static orientation is defined as the state where the resultant hinge moments are zero. Since actuators can be installed on both the tab and aileron hinges, there are at least two degrees of freedom; the hinge moment of the tab and aileron can be anything within the actuator specifications. The static orientation, given the actuator parameters, therefore has a set of solutions rather than a unique one.

The optimisation of the static geometry and lift coefficients is done by Jaquet [1]. This means that only the tab and aileron actuator hinge moments that result in the desired aileron deflection has to be found and the solution is independent of geometry. The objective here is to achieve a desired aileron deflection rather than a specific roll moment. The notion is that the outer loop control systems of the aircraft will command a specific aileron deflection which will result in a specific roll moment on the aircraft. The change in relation between the aileron deflection and roll moment can be adjusted for with a control derivative modification. Jaquet has shown that the roll moment achieved by an unassisted aileron is proportional to the roll moment achieved by a tab assisted aileron [1]. This translates into a control derivative reduction if the total tab-aileron combined chord and span is maintained [1]. To avoid the reduction in control derivative the chord and/or span can be increased resulting in the same control derivative as the unassisted aileron. Alternatively, with a reduced control derivative, the range of deflection has to be increased to achieve the range of roll moments of an equivalent unassisted aileron [1].

To find the hinge moment that must be applied to each hinge point, the equilibrium conditions must be valid as follows:

$$\sum M'_a = 0 = T_a - M_a(\delta_t, \delta_a, \alpha, c_a, c_t) \tag{2.5.1}$$

$$\sum M'_t = 0 = T_t - M_t(\delta_t, \delta_a, \alpha, c_a, c_t) \tag{2.5.2}$$

These are the two simultaneous equations that must be solved for a specific geometry and angle of attack. It can be seen that there are two degrees of freedom if the desired aileron deflection, δ_a, is known. The global constraints on the two simultaneous equations are the tab saturation limits which is defined as:

$$\delta_{t_{min}} \leq \delta_t \leq \delta_{t_{max}} \tag{2.5.3}$$

This still leaves two degrees of freedom if the tab remains unsaturated. Therefore, it is necessary to introduce design constraints. As an example, the ratio between tab and aileron hinge moment can be constrained as follows:

$$r \times |M_t| - |M_a| = 0 \tag{2.5.4}$$

This constraint would equate to the ratio between the maximum allowed tab actuator torque and the maximum allowed aileron actuator torque. An alternate constraint might be that for the unsaturated tab, the aileron actuator should provide zero hinge moment as shown here:

$$T_a = 0 \tag{2.5.5}$$

This would be equivalent to the servo tab concept. If the tab deflection required exceeds the saturation limits, the tab is set to its saturated value and the aileron torque constraint has to be violated to achieve the aileron angle.

Equation 2.5.1, Equation 2.5.1, Equation 2.5.3 and Equation 2.5.4 or Equation 2.5.5 is solved to determine the steady-state deflections of the tab and aileron. The hinge moments are given by:

$$M_t = q\bar{c}^2 C_{H_t} \qquad M_a = q\bar{c}^2 C_{H_a} \tag{2.5.6}$$

In order to facilitate the solving the above equations, the hinge moment coefficients are written in terms of a Taylor series. This results in a quantifiable analytical functions in terms of the independent variables approximated to the nth desirable term. In this specific case the Taylor series is truncated after the fourth term. The truncated multidimensional Taylor series is then given by:

$$C_H(\underline{X}) = C_H(\underline{X}_0) + \nabla C_H(\underline{X}_0)^T \bullet (\underline{X} - \underline{X}_0) + \frac{1}{2!}(\underline{X} - \underline{X}_0)^T \bullet \nabla^2 C_H(\underline{X}_0) \bullet (\underline{X} - \underline{X}_0)$$

where

$$\underline{X} = \begin{bmatrix} \delta_{tab} \\ \delta_{aileron} \end{bmatrix} \tag{2.5.7}$$

The solution to the set of equations can then be found through any one of a number of numerical techniques. These steady-state deflections can be presented on a phase plane as seen in Figure 2.14. Here, examples of the two design constraints are shown. These deflections can then be used as reference inputs for the independent tab and aileron command structure developed later on.

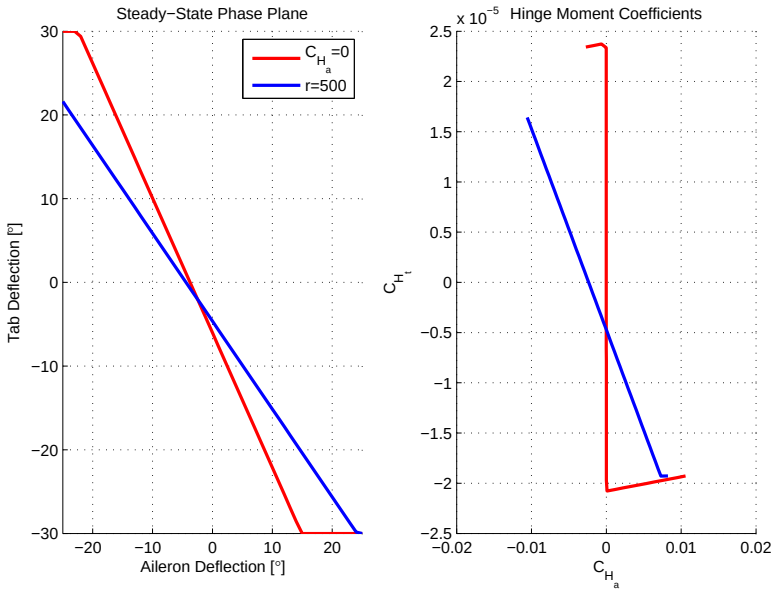

Figure 2.14 – Tab-Aileron Steady-State Phase Plane and Respective Hinge Moment Coefficients

2.6 Actuator Models

The inclusion of actuator dynamics is dependent on the specific mode in which the actuator is operated. The consideration here will concentrate on the macroscopic model of the actuator. That is to say, the actuator will be considered a gain, first or second order actuator.

For the torque actuator it is assumed that it does not contain any dynamics. This assumption is further based on the assumption that the torque dynamics are at least five to ten times faster than the system dynamics and therefore the torque dynamics should be negligible. This condition is ensured during practical implementation. The actual torque, $T(t)$, is then related to the input, $U(t)$, by:

$$T(t) = K_T U(t) \tag{2.6.1}$$

When considering a rate actuator, it is considered a first order response. By extension of the assumption that the torque dynamics are negligible the rate dynamics are given by:

$$I\ddot{\delta}(t) + B\dot{\delta}(t) = K_T U(t) \tag{2.6.2}$$

$$\frac{K}{\tau s + 1} \equiv \frac{\dot{\delta}(s)}{U(s)} = \frac{K_T}{Is + B} \tag{2.6.3}$$

Here $\dot{\delta}$ is the angular rate, T the applied torque, B the damping constant and I the moment of inertia. τ is considered the generalised time constant and K the generalised gain. Extending this to a position actuator is equivalent to the addition of and integrator as follows:

$$\frac{K}{s(\tau s + 1)} \equiv \frac{\delta(s)}{U(s)} = \frac{K_T}{s(Is + B)} \tag{2.6.4}$$

This is summarised by the block diagram provided in Figure 2.15. In some cases po-

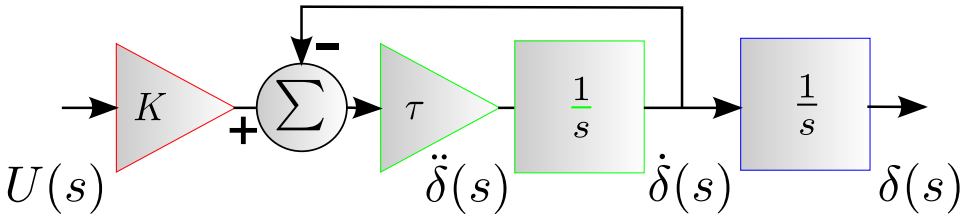

Figure 2.15 – Actuator Model

sition actuator contain internal controller loops which result in the actuator showing primarily first order behaviour. The actuator can then be approximated with ass first order transfer function as shown:

$$\frac{\delta(s)}{U(s)} \equiv \frac{K'}{(\tau' s + 1)} \tag{2.6.5}$$

where K' and τ' have to be characterised. These models are used to include the effect of the actuators in the control systems design phase. The inclusion of torque disturbances are considered at a later stage since it is specific to the type of actuator used in the practical implementation.

Chapter 3

Feedback Control Design

In previous chapters the necessary models for the tab, aileron and actuator dynamics are presented. The dynamic models show varying open-loop performance. To ensure consistent performance of the tab and aileron combination, it is clear that a control system which will tolerate or can be adjusted to the system variation is required. The aim would be to make the minimum amount of changes to the topology of the controller as the operating conditions change. It would also be convenient if the control system gains can be kept constant over a range of system states and possibly trim conditions.

There are various approaches to the control problem such as classical control, modern optimal control and even robust control. The objective of the control system is to satisfy a very specific performance measure; the tab and aileron should at least match the current aileron performance. Since one of the overhead project objectives is the optimisation of the control surfaces and their associate actuator requirements, it would also be convenient to formulate an optimal controller. It was therefore decided to follow the classic control design path at first to build understanding of the control challenges and to follow with a modern optimal control method as signified shown in Figure 3.1. The results of the implemented performance of the controllers will indicate if it is necessary to move towards robust control methods.

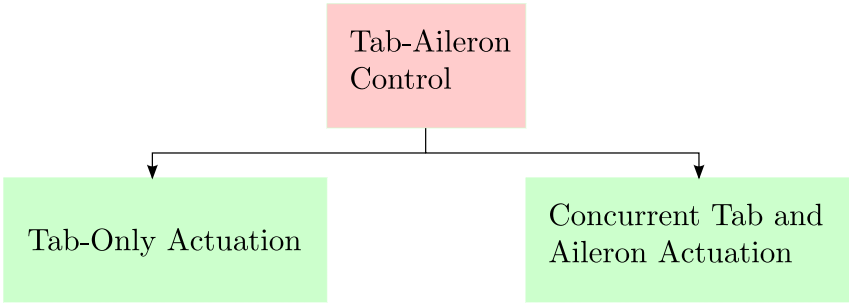

Figure 3.1 – Control Approach

The control design procedure follow two distinct routes as seen in Figure 3.1. The first approach is that of classical control based on s-domain and frequency domain design. Since the methods are primarily focussed at single-input single-output (SISO) control problems and that the classical multi-input multi-output (MIMO) designs are based on

reformulation of these systems into SISO ones [16], it is decided to consider the tab-only actuated system for classical design. In this way the control problem becomes a SISO one, easily dealt with through classical methods. This is also the ideal case in terms of system simplification and actuator footprint reduction. There is however the noted aileron roll performance decrease associated with this approach [1].

The control of the fully coupled system follows a different route since it will facilitate the optimisation of control distribution between actuators by using concurrent tab and aileron actuation. In using a linear quadratic regulator (LQR), the performance can be achieved while considering the input to the system in terms of actuator moments and energy. It optimises not only the steady-state result but also the transient of the response which was not considered in the static characteristics described in §2.5.

3.1 Dynamic Performance Requirements

The dynamic performance requirements have been taken to be equal to that of the standard Airbus simulation model dynamics. Specifically in the Airbus model, the aileron position transfer function is approximated as:

$$G_{Rate}(s) = \frac{\delta(s)}{\delta_{Ref}(s)} = \frac{1}{\tau s + 1} \tag{3.1.1}$$

$$\tau = 0.07 \tag{3.1.2}$$

or a pole position

$$s_p \approx -15 \tag{3.1.3}$$

This equates to a 98% settling time of $0,26\ s$ and a cut-off frequency of $14,3\ rads^{-1}$ This provides a dynamic performance measure for the proposed control systems. Further, it is required that steady-state accuracy is achieved for the aileron deflection. Airbus places an additional constraint on the actuators; a rate limit of $40^{\circ}s^{-1}$ is placed on the actuator reference. This has no real effect on the position dynamics which has to adhere to the aforementioned transfer function but it will be shown later that does affect the peak actuator requirements. The controllers can now be synthesized for the specific actuator types to achieve the current performance specifications.

3.2 Control of Dynamics

In §2.3 the linearised model of the system is presented. This forms the basis of the linear controller design. It is quite apparent at this stage that the model consist of two major dynamic components, tab and aileron. It is clear that the tab and aileron dynamics interact to an extent. The extent of these interactions are made clear in §2.4. On the one hand there is the effect of a tab deflection on the aileron which is desirable and the exact reason for the physical configuration. On the other hand the aileron orientation affects the tab hinge moment which is an undesirable effect since it makes the tab control more complicated. These interaction therefore determine which overhead control topologies will be followed. Two topologies are considered; the first is the decoupling case where just the tab is decoupled from the aileron combined with successive loop closure (SLC). Here, the tab is first stabilised and then the aileron is controlled with the outer loop. The

second topology is based on full-state feedback (FSF) facilitating concurrent actuation of the tab and aileron. Each of these are discussed in terms of their advantages and disadvantages and their applicability in this control problem.

3.2.1 Successive Loop Closure and Decoupling

Successive loop closure (SLC) is a topology where successively larger loops are closed in around the plant as seen in Figure 3.2. This simplifies controller design to a minimum of poles at each stage of loop closure. This results in intuitive placement of the poles by the classical methods or modern control methods such as full state feedback. Other than the design simplification, the additional benefit of SLC is that during the testing phase successive loops can be tested and evaluated. However, there is one condition; each inner loop must be either robust enough to reject the coupling effect of outer loops or the coupling must be insignificant.

The reason why SLC can be applied to the tab-aileron configuration is that intuitively the tab acts as an actuator for the aileron. This suggests the ability to model the tab as an actuator controlled by an inner loop. It is clearly apparent that there is some coupling between the tab and aileron. However, for the moment it is assumed that this coupling can be rejected by the tab actuator.

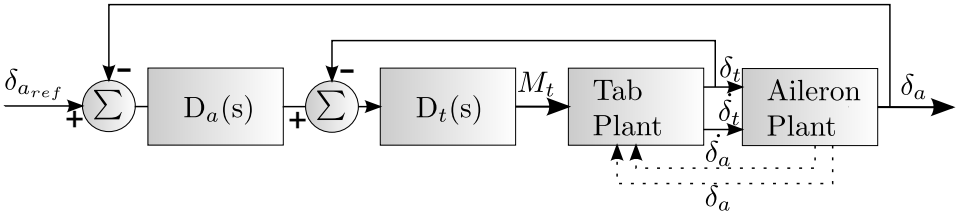

Figure 3.2 – Successive Loop Closure Topology

Figure 3.2 effectively shows that the tab aileron coupling is the sole input to the aileron. This coupling is not necessarily constant and immune to disturbances. Therefore, it is convenient to place a outer feedback loop from the aileron output and a controller $D_a(s)$ to ensure proper reference following. This topology then becomes the servo tab approach with a feedback structure.

There are two methods of achieving desired decoupled dynamics. In the first it is assumed that the dynamics are able to be decoupled by ignoring the cross coupling of dynamics. This is only true if the cross coupling is small. Negligible cross coupling can be tested by evaluating whether Equation 3.2.2 is true.

$$\underbrace{\begin{bmatrix} \frac{\partial F_1}{\partial \delta_t} & \frac{\partial F_1}{\partial \dot{\delta}_t} & \frac{\partial F_1}{\partial \delta_a} & \frac{\partial F_1}{\partial \dot{\delta}_a} \\ \frac{\partial F_2}{\partial \delta_t} & \frac{\partial F_2}{\partial \dot{\delta}_t} & \frac{\partial F_2}{\partial \delta_a} & \frac{\partial F_2}{\partial \dot{\delta}_a} \\ \frac{\partial F_3}{\partial \delta_t} & \frac{\partial F_3}{\partial \dot{\delta}_t} & \frac{\partial F_3}{\partial \delta_a} & \frac{\partial F_3}{\partial \dot{\delta}_a} \\ \frac{\partial F_4}{\partial \delta_t} & \frac{\partial F_4}{\partial \dot{\delta}_t} & \frac{\partial F_4}{\partial \delta_a} & \frac{\partial F_4}{\partial \dot{\delta}_a} \end{bmatrix}_{X_k}}_{F(X_k)} \quad \Rightarrow \quad \begin{bmatrix} A & \vdots & B \\ \dots & + & \dots \\ C & \vdots & D \end{bmatrix} \tag{3.2.1}$$

$$|A||D| \quad \approx \quad \left| \begin{bmatrix} A & B \\ C & D \end{bmatrix} \right| \tag{3.2.2}$$

In some cases Equation 3.2.2 cannot be ensured. In this case $F(X_k)$ varies with time and therefore the determinant varies with time. The decoupling assumption may be invalid at some system states, X_k. Forced decoupling can decouple the tab from theaileron dynamics. Decoupling is achieved by providing some input to the tab states that will negate the input from the aileron states shown in Equation 3.2.3. This is done as in Equation 3.2.4 resulting in Equation 3.2.5. With reference to Equation 3.2.2 decoupling can now be assumed as in Equation 3.2.6. It can now be seen that the tab rates are only dependant on the tab states and the input. Crucially, the aileron states will have to be known to achieve this. Furthermore, variation in the state matrix parameters will adversely affect the response since the expected B' will not match the B in the system.

$$\dot{X} = F(X)X + GU \tag{3.2.3}$$

$$\dot{X} = \begin{bmatrix} A & B \\ C & D \end{bmatrix} X + GU - \begin{bmatrix} 0 & B \\ 0 & 0 \end{bmatrix} X \tag{3.2.4}$$

$$\dot{X} = \begin{bmatrix} A & 0 \\ C & D \end{bmatrix} X + GU \tag{3.2.5}$$

with

$$|A||D| = \left| \begin{bmatrix} A & 0 \\ C & D \end{bmatrix} \right| \tag{3.2.6}$$

Currently, it can be seen that the tab can be modelled as a independent system that can be controlled with any controller of choice. The aileron will then be affected by the tab response since it has not been decoupled from the tab. This is the desired effect however the coupling from the tab to the aileron can not necessarily be ensured to be hundred percent correct at all times. Consider for a moment the case where the cross coupling between the tab and aileron and vice versa is known and that the aileron is also decoupled. This in turn means that all the states have to be known. This effectively results in a FSF scenario which can be handled much more elegantly and effectively with modern control techniques. The only difference is that the controller on each decoupled model can be a higher order controller where FSF only feeds back state information. It can however be achieved through state augmentation in FSF.

The model can now be fully decoupled however it may not be much different from FSF. However, only decoupling the tab from the aileron or assuming this decoupling is valid allows the tab to controlled independently. This then allows for the coupling between the tab and aileron to be used as the aileron actuator. This is effectively a servo tab. To avoid confusion this will be referred to as the tab-only actuation scenario.

3.2.2 Full-State Feedback

An alternative to the decoupled system in which only the tab deflection is used in control is the fully coupled system which can be used to determine full state feedback gain. This allows for the control of the tab and aileron response through actuation of the tab or the combined actuation of the tab and aileron. The advantage of this method is that the coupling in the system, whether large or small, is taken into account. The determination of the feedback gains can be done by either placing the poles where desired or by using linear quadratic regulation.

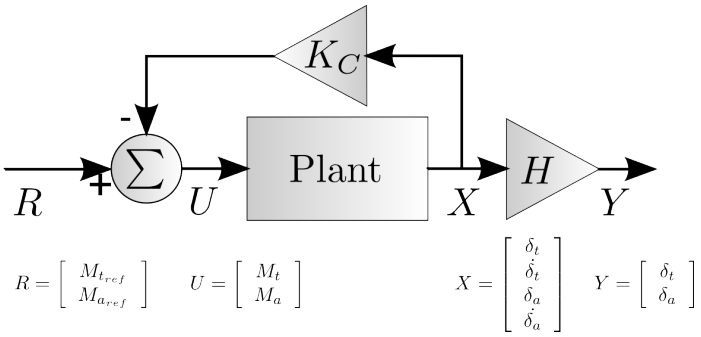

Figure 3.3 – Full-State Feedback Topology

The basic full-state feedback topology can be seen in Figure 3.3. Here, the control signal used is the tab and aileron moment. The the full-state feedback gain K_C will stabilise the plant and H is the output relation to the internal states. It is apparent that the controller will drive the final hinge moment on the tab and aileron to the reference hinge moment values. This is however not the control desired. Rather, the control desired is to deflect the tab and aileron to a desired angle with the controller determining the hinge moments required. The problem is therefore considered a servo or state reference problem and the control topology can be rearranged to reflect this as seen in Figure 3.4.

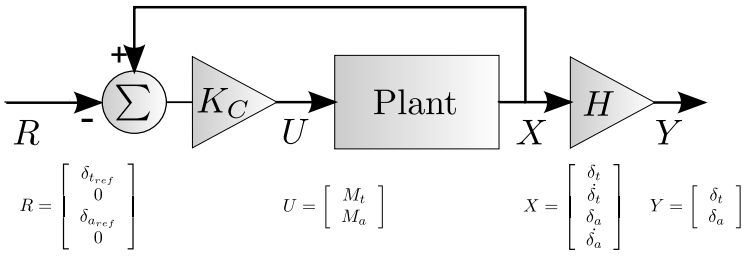

Figure 3.4 – Full-State Feedback Topology for a Servo Problem

In the servo problem the reference signal becomes the tab and aileron deflections, δ_t and δ_a respectively. The reference signal is subtracted form the states thar are fed back. The effect of this is that since there is no reference moment the controller attempts to drive the system to zero error, $X - R = 0$. The accuracy of the steady-state value then depends upon the controller. The poles can be placed or linear quadratic regulation (LQR) can be used to determine these controller gains.

This type of controller can then be further augmented with integrators to ensure steady-state accuracy if needed. Since this type of control takes the complete model into account, it has a better chance of insuring dynamic performance if the system is accurately represented by the model. However if the model accuracy varies performance may be adversely affected.

Chapter 4

Design of Feedback Control for Tab-Only Actuation

Following the conclusion that feedback control is needed to achieve accurate aileron response, the first approach is to investigate the tab-only actuated scenario. The approach to controller design is structured as displayed in Figure 4.1. It is clear that there are two different actuator models that may be used and each actuator model may be used in conjunction with one of two outer loop controller. The two actuator models are both considered since there is a considerable difference in the effect of the inner loop on the outer loop characteristics. The controllers are all based on the application of successive loop closure under the assumption of decoupled tab and aileron dynamics.

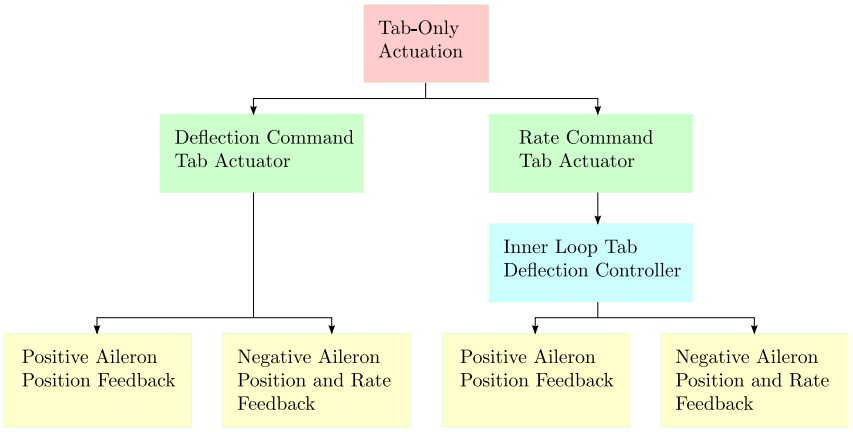

Figure 4.1 – Hierarchical Approach to Tab-Only Actuation

The actuators are based on the models presented in §2.6. The rate command tab actuator is described by a first order transfer function and the deflection command tab actuator here is also described by a first order transfer function. If the position actuator were described by a second order transfer function, the result would be the same as for the rate command tab actuator. However, there would be no control over the inner loop or in other words the tab deflection loop dynamics.

The scenario based on the rate command tab actuator is considered first. The first step is to close the tab position loop and then to apply one of the two outer loop controllers.

The two controllers are then analysed in terms of performance, robustness, disturbance rejection and noise immunity. An overview of the deflection command tab actuator case is then given highlighting the important differences.

4.1 Rate Command Tab Actuator Based Controllers

One example of an actuator, that may be placed on a tab, is a hydraulic actuator. The hydraulic actuator is a rate actuation device functioning primarily by controlling flow rate with valve systems. Hydraulic actuation is a popular choice in current generation aircraft for the high power density and damping provided by the actuator. Applying this type of actuation to a servo tab is therefore a logical step.

This section deals with the implementation these rate command tab actuators for tab-only actuation. This is achieved by first closing a loop around the actuator to give tab position control. The tab position then serves as the input to the aileron transfer function as described in §2.3. Further, to ensure adequate dynamic performance feedback loops are added. A negative aileron deflection and rate feedback topology is proposed along with an alternate positive aileron deflection feedback topology. Then to ensure steady-state accuracy, an integrator and feedforward term is added. The controllers are then evaluated.

4.1.1 Inner Loop Tab Deflection Control

Firstly, the tab-actuator combination is considered. The effect of the tab hinge moment is once again considered a disturbance and therefore the tab and actuator combination can be considered a first order transfer function following a rate command as described in Equation 4.1.1. Then, feeding tab deflection back to the input of the rate actuator results in a zero steady-state error to a step response with a second order transfer function as shown in Equation 4.1.3. The combination is effectively a servo. This now comprises the inner loop of the tab-only actuated system.

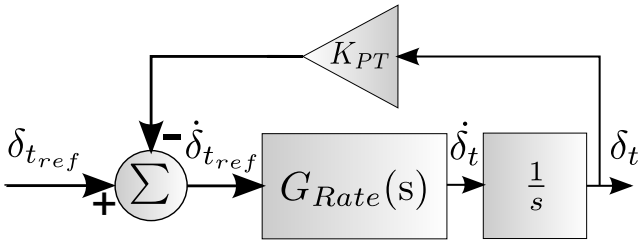

Figure 4.2 – Position Inner Loop

The inner loop feedback gain is determined such that the system poles are optimally damped, $\zeta = 0.707$. The is done by solving the characteristic equation, Equation 4.1.5.

$$G_{Rate}(s) = \frac{\dot{\delta}_{Tab}(s)}{\dot{\delta}_{Ref}(s)} = \frac{1}{\tau s + 1} \tag{4.1.1}$$

$$G_{Deflection}(s) = \frac{\delta_{Tab}(s)}{\delta_{Ref}(s)} = \frac{1}{1 + \frac{K_{PT} G_{Rate}(s)}{s}} \tag{4.1.2}$$

$$G_{IL}(s) \equiv \frac{\delta_{Tab}(s)}{\delta_{Ref}(s)} \tag{4.1.3}$$

$$s = \omega_{n_{IL}} \left(-\frac{1}{\sqrt{2}} \pm \frac{1}{\sqrt{2}} i \right) \tag{4.1.4}$$

$$1 + \frac{K_{PT} G_{Rate}(s)}{s} = 0 \tag{4.1.5}$$

4.1.2 Outer Loop Negative Feedback Aileron Deflection Control

As mentioned before the aileron transfer function input is the tab deflection and the combination of the inner loop and the aileron transfer function comprises the open loop tab-only actuated system. The addition of feedback loops, green in Figure 4.3, around the inner loop and aileron signifies the closed-loop system. This closed-loop system ensures the necessary performance to satisfy the dynamic aileron actuation requirements. However, the steady-state performance is not necessarily ensured since there is no free integrator in the open-loop when considering Equation 4.1.6. Consequently, an integrator loop is added, blue in Figure 4.3, but results in decreased dynamic performance. The solution to this is the addition of a feedforward loop, blue N in Figure 4.3, to negate the integrator dynamics, $\frac{K_I}{s}$ in Figure 4.3. The combination of the three successive loops results in adequate dynamic and steady state response with tolerance to constant disturbances and system gain uncertainty. The block diagram of the the rate actuator, controller and plant is shown in Figure 4.3.

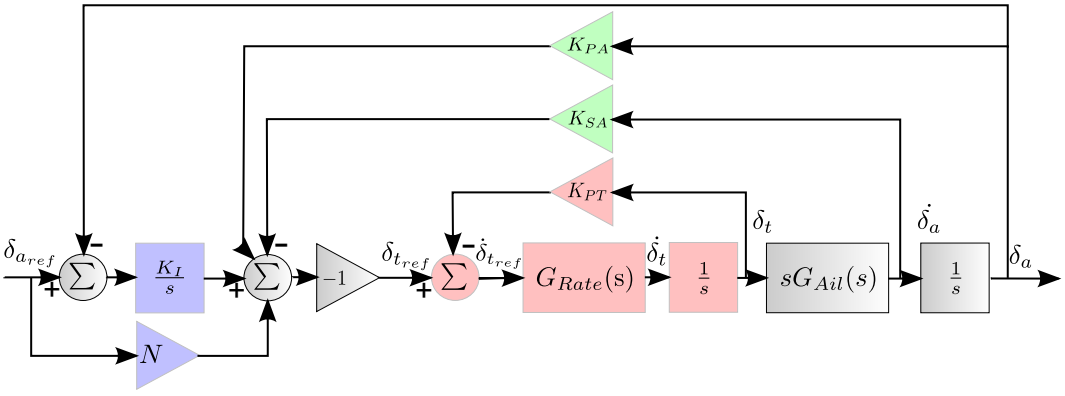

Figure 4.3 – Tab-Only Actuation Rate Controlled Topology

The dynamic constraints of the aileron response can be achieved by adding proportional and rate feedback, K_{PA} and K_{SA} Figure 4.3. The rate feedback and proportional feedback effectively creates an additional transient zero in the closed-loop system, Figure 4.4. The equivalent effect if viewed from the closed loop system is that the system poles are moved from their original location. The gain of the proportional and rate feedback

is calculated by solving the characteristic equation as shown in Equation 4.1.8. It is noted that there is an extra degree of freedom in the characteristic equation. Therefore an additional term has to be fixed. So, the ratio $\frac{K_{PA}}{K_{SA}}$ is fixed to any value preferably constraining the zero close to the origin. This results in adequate dynamic performance.

$$G_{CL}(s) = \frac{G_{IL}(s)G_{Ail}(s)}{1-(K_{SA}s+K_{PA})G_{IL}(s)G_{Ail}(s)} \tag{4.1.6}$$

$$s_p = -15 \tag{4.1.7}$$

$$1-(K_{SA}s_p+K_{PA})G_{IL}(s_p)G_{Ail}(s_p) = 0 \tag{4.1.8}$$

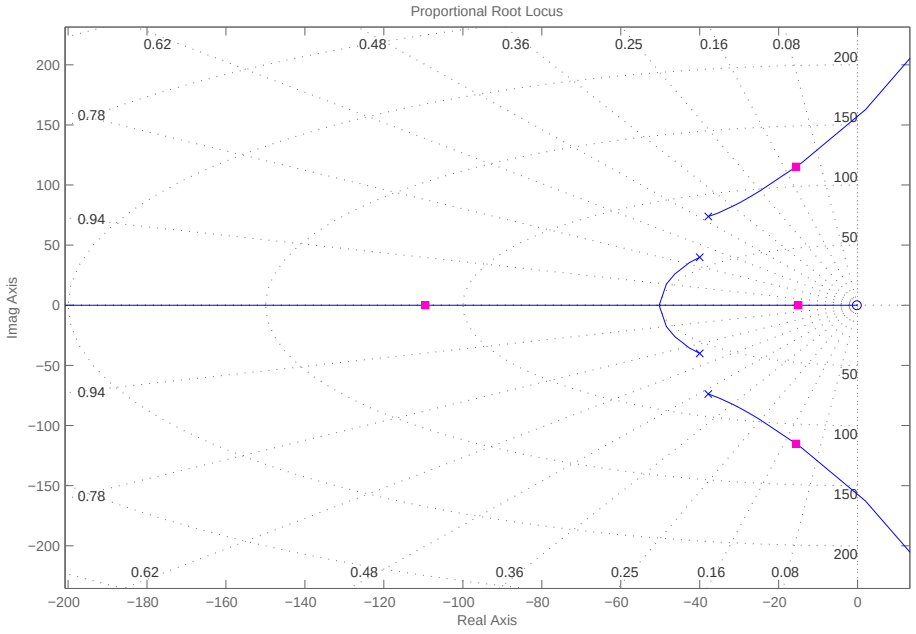

Figure 4.4 – Negative Feedback Root Locus at 50 ms^{-1} Airspeed with Rate Actuation

The steady-state performance is ensured with the addition of the integrator, K_I, with the feedforward, N, negating its dynamic effect, blue in Figure 4.3. The calculation of the required feedforward gain to negate the dynamics is based on the principle that the feedforward gain adds a zero to the closed-loop system. The integrator gain is then chosen for example unity. The size of the integrator gain determines how quickly a disturbance is integrated away however it decreases the stability of the integrator loop as shown by the integrator gain root locus in Figure 4.5. The resulting closed-loop pole position of the open-loop integrator is then calculated with Equation 4.1.10. From the closed-loop integrator transfer function without feedforward using Equation 4.1.6 and Figure 4.3 it is shown that:

$$\frac{\delta_{Ail}(s)}{\delta_{Ail_{Ref}}(s)} = \frac{G_{CL}(s)}{1+\frac{K_I G_{CL}(s)}{s}} \tag{4.1.9}$$

The poles are given by:

$$1 + \frac{K_I G_{CL}(P_I)}{P_I} = 0 \tag{4.1.10}$$

The pole closest to the origin is then the resulting pole due to the integrator addition. Then, the effect of the addition of the feedforward term is apparent when the complete system transfer function with integrator and feedforward is derived:

$$\delta_{Ail}(s) = (\delta_{Ail_{Ref}}(s) - \delta_{Ail}(s))\frac{K_I}{s}G_{CL}(s) + N\delta_{Ail_{Ref}}(s)G_{CL}(s) \tag{4.1.11}$$

$$\delta_{Ail}(s)\left(1 + \frac{K_I}{s}G_{CL}(s)\right) = \delta_{Ail_{Ref}}(s)G_{CL}(s)\left(\frac{K_I}{s} + N\right) \tag{4.1.12}$$

$$\frac{\delta_{Ail}(s)}{\delta_{Ail_{Ref}}(s)} = \frac{G_{CL}(s)\left(\frac{K_I}{s} + N\right)}{1 + \frac{K_I}{s}G_{CL}(s)} \tag{4.1.13}$$

The zero added to the integral loop by N is then placed on the previously calculated integrator closed-loop pole, P_I:

$$\frac{K_I}{s} + N = 0 \tag{4.1.14}$$

$$s = P_I \tag{4.1.15}$$

The stability of the integrator feedback loop has to be ensured. The result of the addition of the integrator is that an additional pole at the origin is added. The resulting root locus is then given by Figure 4.5. It can be seen that the integrator curves the root locus to the right and results in a slow dominant real pole when the integrator gain, K_I, is sufficiently small as shown in Figure 4.3. However, the stability margin is in the order of 1×10^4. As for the feedforward loop its stability is inferred by the stability of the closed-loop system.

From the two typical responses in Figure 4.6, it is apparent that there are some shortcomings of this negative feedback controller. The shortcoming is that the controller cannot adequately reject the undesired dynamics of the aileron. The ripple seen on the response, green in Figure 4.6, is present due to this phenomena but becomes less visible at higher air speed, blue in Figure 4.6. The aileron transients become less apparent at higher airspeed since the poles of the aileron become less dominant as shown in Figure 4.7 representing pole movement with airspeed. This means that the aileron transient behaviour is excited less and dissipates quicker. However, in this system the phenomena presents itself at lower airspeed seemingly insignificant in the full scale airliner application. But, it is the relationship between moment of inertia, lift coefficient and dynamic pressure that determine the point of dominance of the aileron poles. This is discussed further in §4.4.

Further proof of the weakness of the system in terms of rejecting the transient behaviour of the aileron is more visible in the frequency domain depicted in Figure 4.8. The closed-loop bode diagram shows the resonant peak at higher frequencies than the $3\ dB$ cut-off. The partial excitation of this resonant peak occurs during a reference step and this results in the response ripple observed previously.

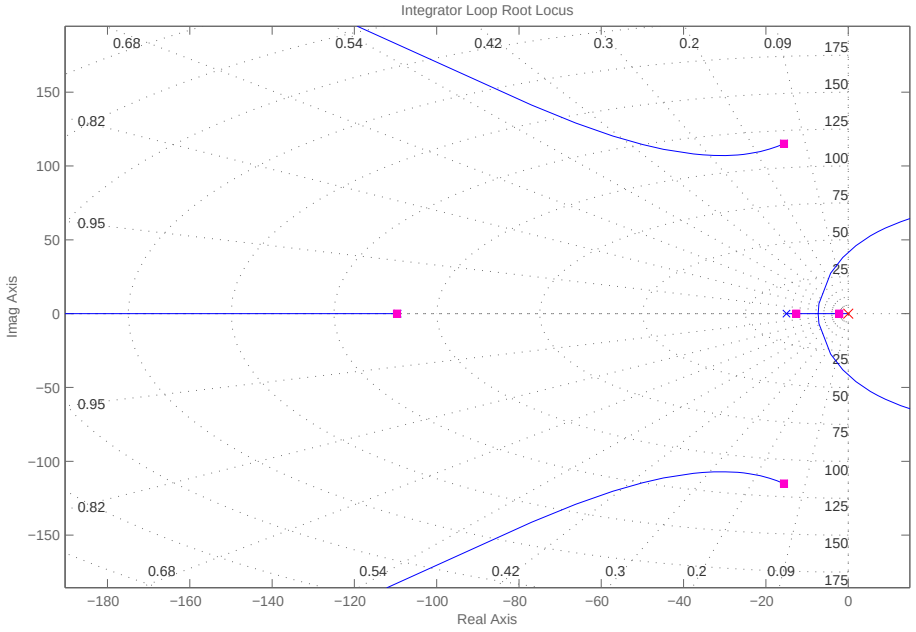

Figure 4.5 – Integrator Loop Root Locus at 50 ms^{-1} Airspeed with Rate Actuation

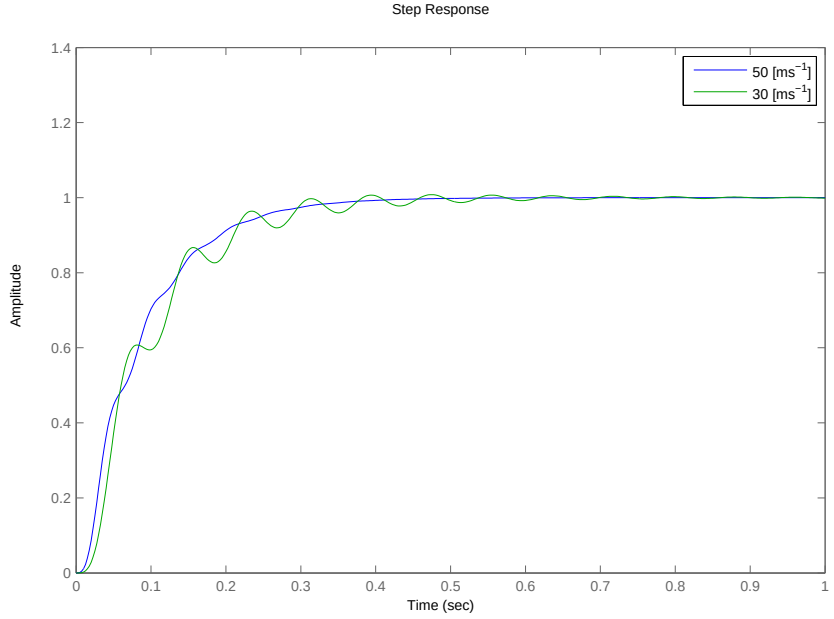

Figure 4.6 – Negative Feedback Response with Rate Actuator at Airspeed of 30 ms^{-1} and 50 ms^{-1}

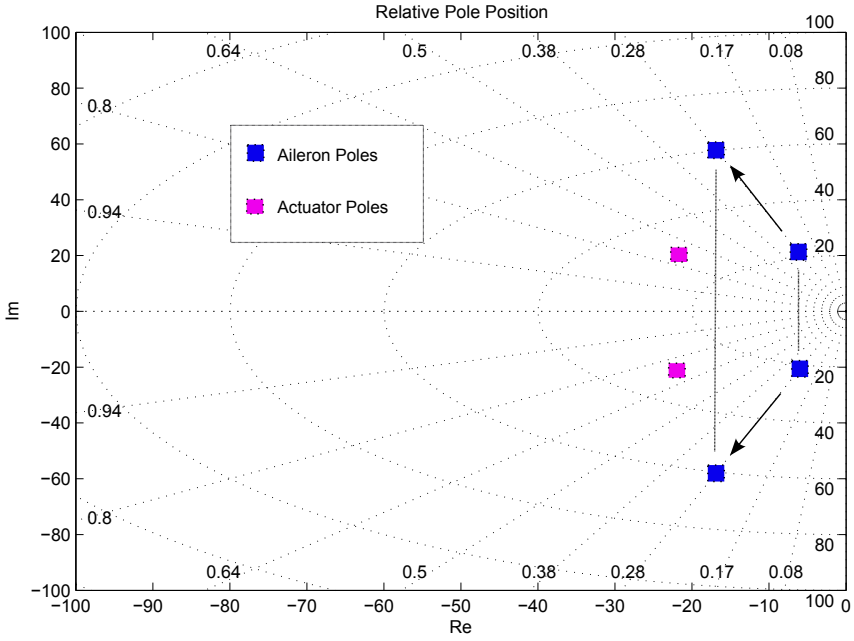

Figure 4.7 – Representative Pole Movement

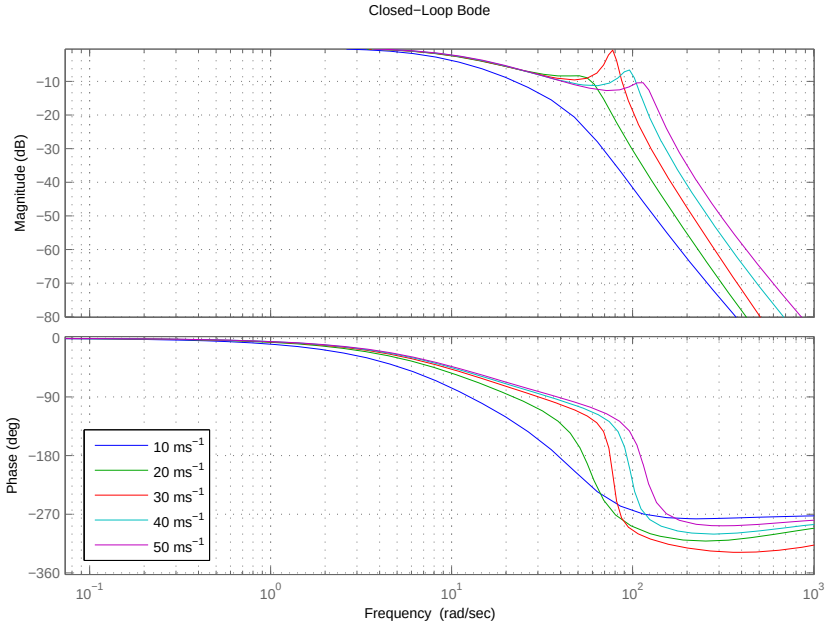

Figure 4.8 – Closed-Loop Bode for Negative Feedback with Rate Actuator

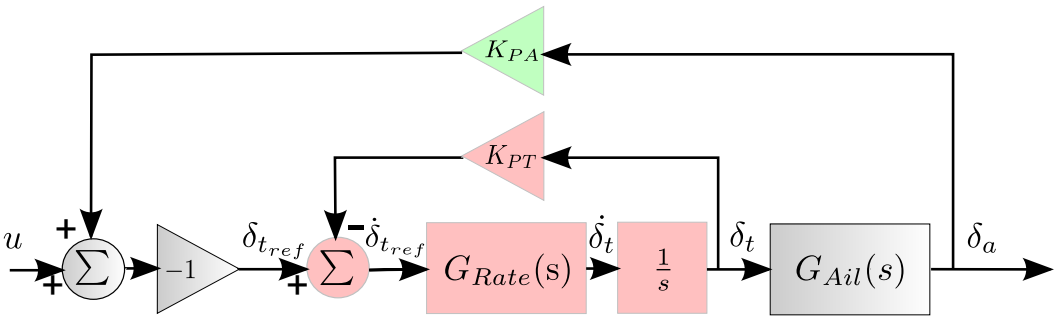

Figure 4.9 – Positive Feedback Deflection Control Dynamics Block Diagram

4.1.3 Outer Loop Positive Feedback Aileron Deflection Control

In order to improve on the proposed negative feedback controller, the new controller must find some way of making the undesired aileron dynamics non-dominant. One way in which to achieve this is to make use of positive feedback indicated by green in Figure 4.9. As can be seen, the block diagram is very similar to that of the negative feedback controller. The only difference is that the proportional feedback is positive and that the rate loop falls away. One way in which to look at the effects of positive feedback is to consider the error dynamics of the tab reference and positive feedback compared to negative feedback. In the negative feedback case, the error dynamics of the tab and aileron, respectively, are as follows:

$$\delta_{t_{ref}}(s) = (K_{SA}s + K_{PA})G_{Ail}(s)\delta_t(s) - u(s) \tag{4.1.16}$$
$$\delta_t(s) = (K_{SA}s + K_{PA})G_{IL}(s)(\delta_a(s) - u(s)) \tag{4.1.17}$$

Since the gain of G_{Ail} is negative, negative feedback has a stabilising effect on the tab since its deflection in the end results in a negative value fed back to it, Equation 4.1.16. The aileron error dynamics however end up having a positive value fed to its input from a positive output and therefore the negative feedback having a destabilising effect on the aileron. For positive feedback the error dynamics become:

$$\delta_{t_{ref}}(s) = -K_{PA}G_{Ail}(s)\delta_t(s) - u(s) \tag{4.1.18}$$
$$\delta_t(s) = K_{PA}G_{IL}(s)(\delta_a(s) + u(s)) \tag{4.1.19}$$

As expected, the converse is true for positive feedback. It has a destabilising effect on the tab and a stabilising effect on the aileron if the same reasoning as before is followed. Another method through which this can be visualised is by comparison of the root loci for the two cases, Figure 4.4 and Figure 4.11. It is shown that in the negative feedback case the tab dynamics are stabilised since its poles move further to the left as the loop gain increases. Effectively it says that more negative feedback or higher gain further stabilises the tab and destabilises the aileron. For the positive feedback scenario the exact opposite is true.

The computation of the positive feedback controller parameters indicated green in Figure 4.10, is similar to that of the negative feedback case. The inner loop is designed

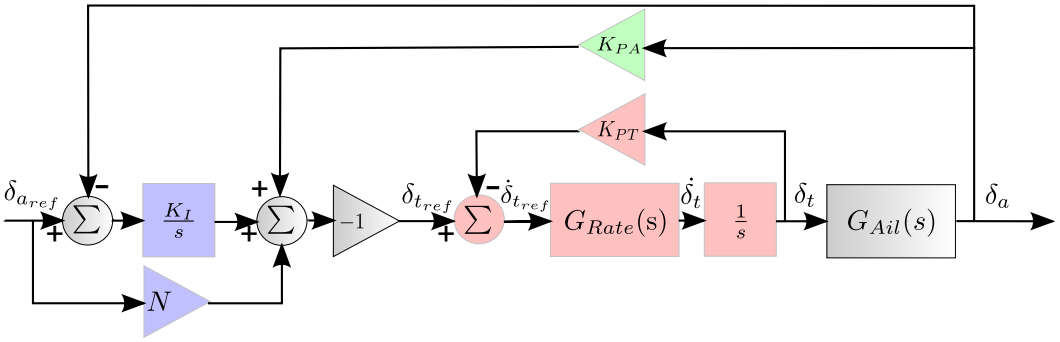

Figure 4.10 – Positive Feedback Deflection Control Block Diagram

as specified in Equation 4.1.1 to Equation 4.1.5 for $\zeta = 0.707$. The closed-loop transfer function is then defined by Equation 4.1.20. The characteristic equation, Equation 4.1.22, is then solved for the specified s_p.

$$G_{CL}(s) = \frac{G_{IL}(s)G_{Ail}(s)}{1 + K_{PA}G_{IL}(s)G_{Ail}(s)} \tag{4.1.20}$$

$$s_p = -15 \tag{4.1.21}$$

$$1 + K_{PA}G_{IL}(s_p)G_{Ail}(s_p) = 0 \tag{4.1.22}$$

The closed loop as with the previous case ensures the dynamic performance of the system but the steady-state performance is still required. It is sensible to follow the same approach as previously to ensure steady-state accuracy. To recap a integrator is added to achieve rejection of constant disturbances and a feedforward term to ensure that the integrator dynamics are not excited shown in blue in Figure 4.10. The calculation follows exactly as in Equation 4.1.9 through Equation 4.1.15. The stability of the integrator loop is easily presented in the root locus depicted in Figure 4.12. It can be seen that as the integrator gain is increased the loop becomes unstable. When comparing the gain margin of this integrator loop with that of the negative feedback controller, there is an obvious difference. In this case it ranges to about 10^2 compared to 10^4 previously. This hints towards difference in robustness of the two controllers discussed in §4.1.4.

The positive feedback controller now ensures both dynamic and steady-state accuracy. The controller is first implemented in simulation verifying its performance shown in Figure 4.13. It can be seen that there is much less of a ripple on the response. This can seen more clearly in the frequency domain diagram shown in Figure 4.14, where the harmonic peaks are suppressed much better. This signifies that the suppression of the undesired aileron dynamics is much better than the negative feedback based controller while maintaining the correct cut-off frequency. The result agrees with the theoretical design. However, the ability of the system to handle model inaccuracies and measurement noise will dictate the applicability of each controller.

Two control topologies based on deflection rate actuators have been presented which exhibit adequate dynamic performance. Also, the design and evaluation procedures are presented in terms of the time domain, s-plane and frequency domain. The response is

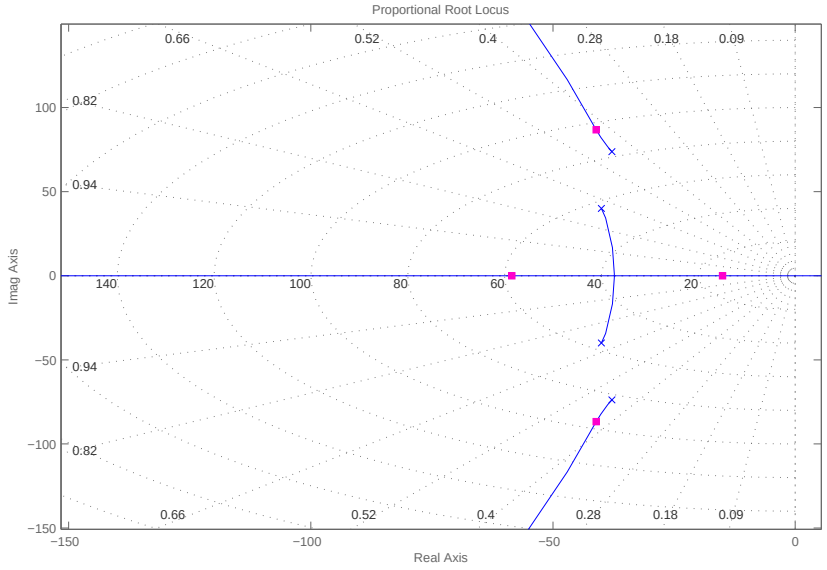

Figure 4.11 – Positive Feedback Root Locus at 50 ms^{-1} Airspeed with Rate Actuation

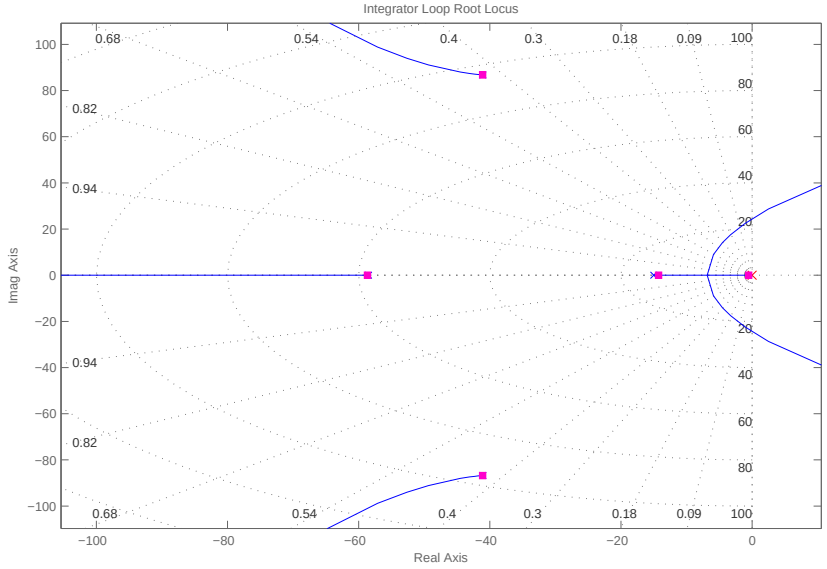

Figure 4.12 – Integrator Loop Root Locus at 50 ms^{-1} Airspeed with Rate Actuation

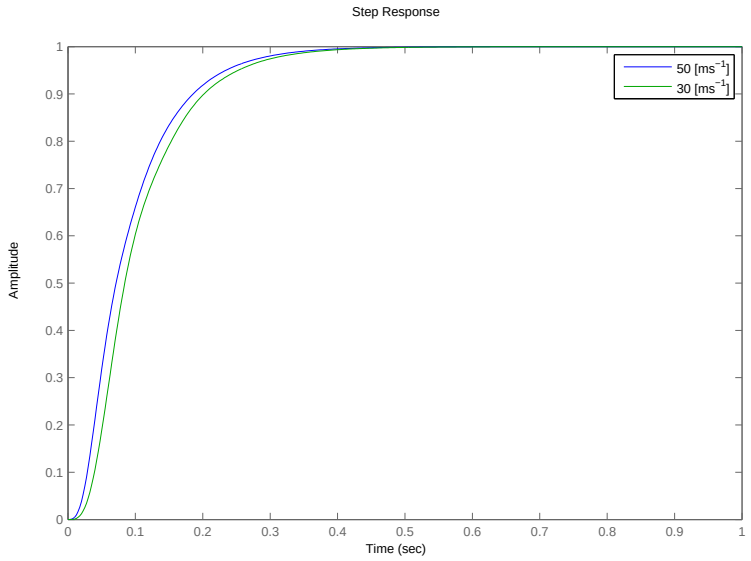

Figure 4.13 – Positive Feedback Response with Rate Actuator at Airspeed of 30 ms^{-1} and 50 ms^{-1}

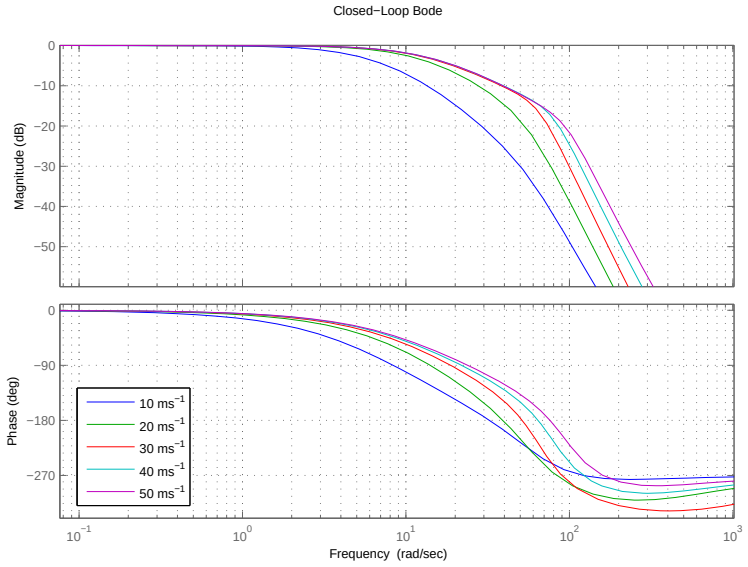

Figure 4.14 – Closed-Loop Bode for Positive Feedback Controller

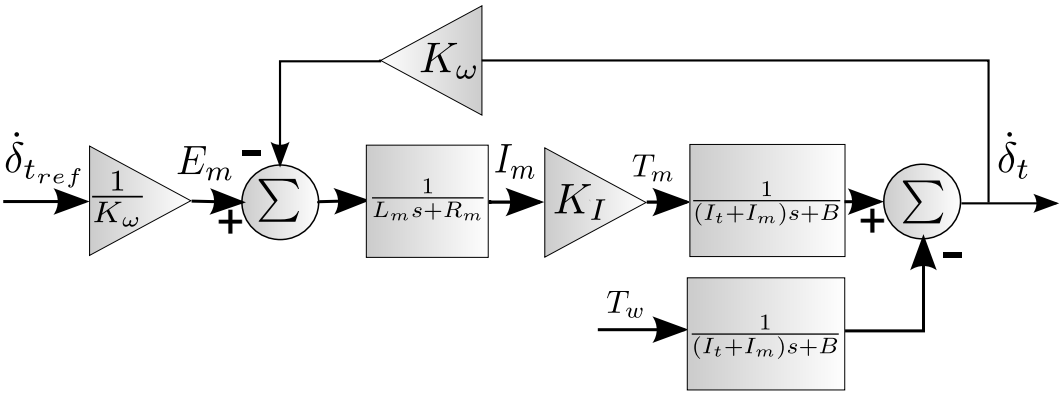

Figure 4.15 – Motor Output Disturbance

verified in simulation and the topologies presented in diagrammatic form. The one controller topology consists of a proportional and rate feedback based controller. But, this control topology does not provide adequate rejection of undesired system dynamics. For this reason an alternate positive proportional feedback topology is proposed. This topology exhibits superior rejection of extraneous dynamics. However, there is a hint of inferior robustness of the controller in terms of parameter variation. Further analysis of the controllers in terms of robustness and noise sensitivity is the determining factor for controller applicability.

4.1.4 Disturbance Rejection

Disturbance rejection and sensitivity is focussed on a specific disturbance that is expected to enter the system. The major disturbances expected in the tab-aileron configuration is hinge moments resulting from extraneous aerodynamic effects. For the full-state control model this corresponds to input disturbances however for the SISO based controllers this corresponds to internal disturbances related to the dynamics of the system through the system structure. The tab dynamics are driven by the motor model where the tab hinge moment and any extraneous hinge moments are considered disturbances. It can be shown that these hinge moments can be translated to a rate output disturbance by shaping the disturbance with the motor-tab combined dynamics, Figure 4.15 [16]. However, It might be more convenient to look at the general case not specific to the motor and consider the disturbances output disturbances as shown by w_t and w_a in Figure 4.16. The sensitivity functions relating the change in tab or aileron transfer function gain to the change in closed loop gain then becomes an indication of the sensitivity to a general disturbance. [16] also shows that this is an indication of the robustness of the system since the aileron or tab transfer function gain variation can be seen as an indirect representation of parameter variation.

It follows that the output disturbance model can be used to determine the sensitivity function of the system. The closed loop transfer function of the SISO rate actuator with rate and proportional feedback control is given by Equation 4.1.9, repeated here:

$$\frac{\delta_{Ail}(s)}{\delta_{Ail_{Ref}}(s)} = \frac{G_{CL}(s)}{1 + \frac{K_I G_{CL}(s)}{s}} \tag{4.1.23}$$

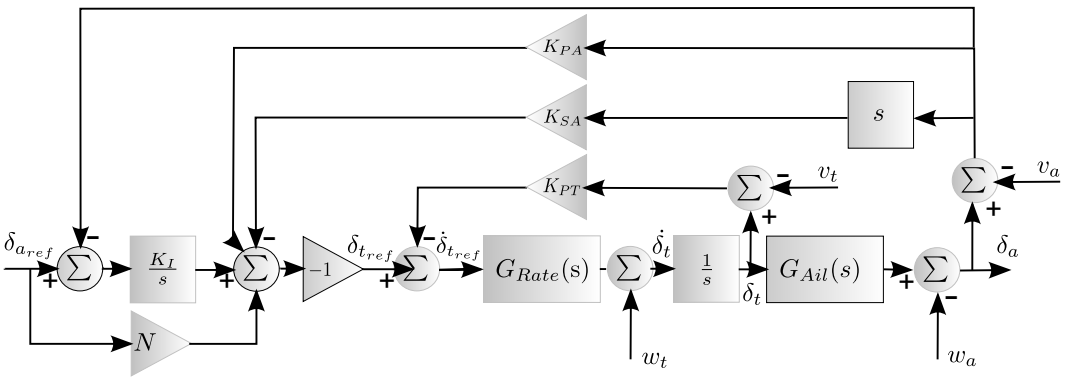

Figure 4.16 – Output Disturbance Representation

The variation of gain versus nominal gain due to variation of the aileron dynamics' gain or an output disturbance in the frequency domain is given by:

$$\frac{dM}{M(s)} = \frac{1}{\left(1 + \frac{K_I G_{CL}(s)}{s}\right)\left(1 - (K_{SA}s_p + K_{PA})G_{IL}(s_p)G_{Ail}(s_p)\right)} \frac{dG_{Ail}}{G_{Ail}} \tag{4.1.24}$$

The sensitivity to tab rate disturbance becomes:

$$\frac{dM}{M(s)} = \frac{1}{\left(1 + \frac{K_I G_{CL}(s)}{s}\right)\left(1 - (K_{SA}s_p + K_{PA})G_{IL}(s_p)G_{Ail}(s_p)\right)\left(1 + \frac{K_{PT}G_{Rate}(s)}{s}\right)} \frac{dG_{Rate}}{G_{Rate}} \tag{4.1.25}$$

The tab rate is sensitive to to the disturbance torque through the motor-tab rate dynamics, assuming that the tab dynamics are dominant, from Figure 4.16 as follows:

$$N(s) = \frac{1}{I_t s + \frac{q\bar{c}^2}{I_t}\frac{\bar{c}_t}{4V}C_{Ht_{\delta_t}}} \tag{4.1.26}$$

The exact same applies for the case where the positive feedback is used and results:

$$\frac{dM}{M(s)} = \frac{1}{\left(1 + \frac{K_I G_{CL}(s)}{s}\right)\left(1 + (K_{PA})G_{IL}(s_p)G_{Ail}(s_p)\right)} \frac{dG_{Ail}}{G_{Ail}} \tag{4.1.27}$$

The sensitivity to tab rate disturbance becomes:

$$\frac{dM}{M(s)} = \frac{1}{\left(1 + \frac{K_I G_{CL}(s)}{s}\right)\left(1 + (K_{PA})G_{IL}(s_p)G_{Ail}(s_p)\right)\left(1 + \frac{K_{PT}G_{Rate}(s)}{s}\right)} \frac{dG_{Rate}}{G_{Rate}} \tag{4.1.28}$$

The sensitivity functions can now be visualised in the frequency domain depicting the effect of disturbances or system gain variation on the system. For sensitivity, the estimated models from 30 to 50 ms^{-1} is presented to show consistency. First the servo tab or SISO configurations are compared. Figure 4.18 shows that the positive feedback is more sensitive to disturbances in the lower frequency regions around the system cut-off frequency. Negative feedback shows higher sensitivity at the system natural frequency of 14 $rads^{-1}$ shown in Figure 4.17. This reinforces the notion that the positive feedback will ensure good rejection of the aileron dynamics and the negative feedback will ensure the system bandwidth to a greater extent. Both these controllers are much more sensitive to aileron disturbances than tab disturbances. Both controllers also show effectively no sensitivity at low frequency due to the addition of the integrators.

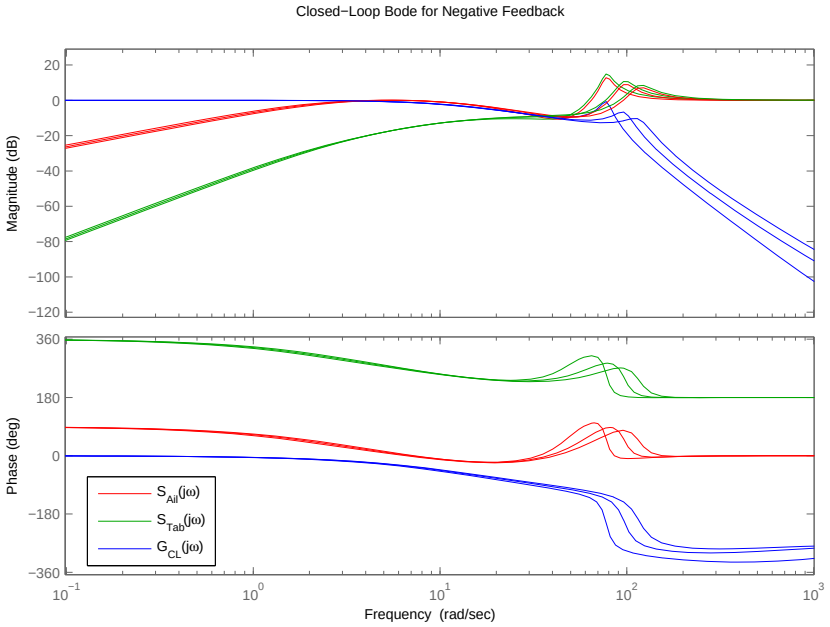

Figure 4.17 – SISO Disturbance Sensitivity for Negative Feedback

.

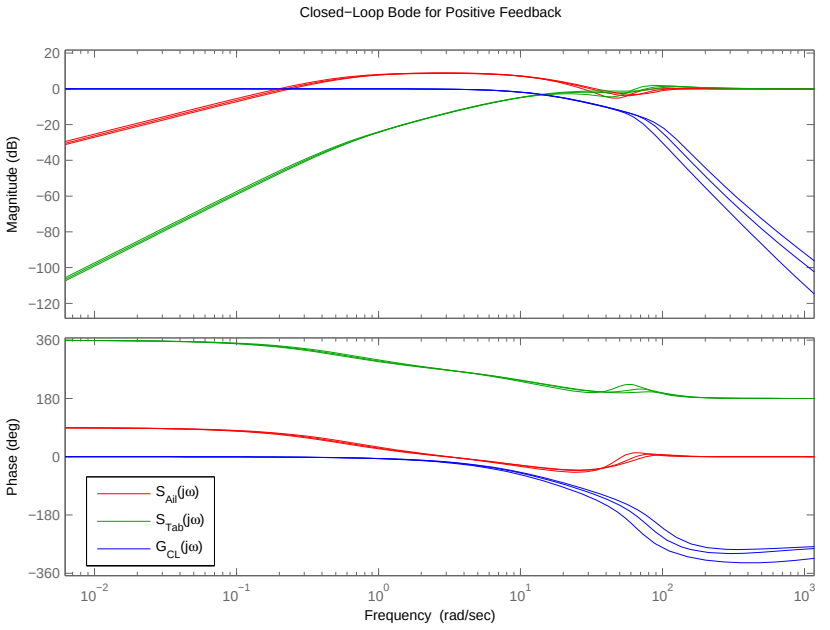

Figure 4.18 – SISO Disturbance Sensitivity for Positive Feedback

.

4.1.5 Noise Suppression

Noise in this control application is primarily resultant from output measurement noise. The outputs are used to reconstruct the system states feeding the noise back into the system. The effect of differentiation to reconstruct the rate states are taken into account where applicable.

Figure 4.16 shows the noise, v_t and v_a, entering the system thought the feedback loops. The tab and aileron sensors each have a different effect on the closed-loop system. The transfer functions from the noise to the output in the position and rate feedback case can then be shown to be:

$$M_{v_a}(s) = \frac{-G_{IL}(s)G_{Ail}(s)\left(K_{SA}s + K_{PA} + \frac{K_I}{s}\right)}{1 - \left(K_{SA}s + K_{PA} + \frac{K_I}{s}\right)G_{IL}(s)G_{Ail}(s)} \tag{4.1.29}$$

$$M_{v_t}(s) = \frac{-G_{IL}(s)G_{Ail}(s)}{1 - \left(K_{SA}s + K_{PA} + \frac{K_I}{s}\right)G_{IL}(s)G_{Ail}(s)} \tag{4.1.30}$$

$$\tag{4.1.31}$$

For the positive proportional positive feedback case it becomes:

$$M_{v_a}(s) = \frac{-G_{IL}(s)G_{Ail}(s)\left(-K_{PA} + \frac{K_I}{s}\right)}{1 - \left(-K_{PA} + \frac{K_I}{s}\right)G_{IL}(s)G_{Ail}(s)} \tag{4.1.32}$$

$$M_{v_t}(s) = \frac{-G_{IL}(s)G_{Ail}(s)}{1 - \left(-K_{PA} + \frac{K_I}{s}\right)G_{IL}(s)G_{Ail}(s)} \tag{4.1.33}$$

$$\tag{4.1.34}$$

The negative positive feedback controller, Figure 4.20, shows good noise rejection at high frequency of about $80\ dB$ per decade. However shows noise sensitivity around the system cut-off frequency. The negative feedback controller, Figure 4.19, only shows about $60\ dB$ per decade aileron sensor noise rejection due to the addition of rate feedback from the derivative of a deflection measurement. It also shows its highest sensitivity to noise at the system resonant peak.

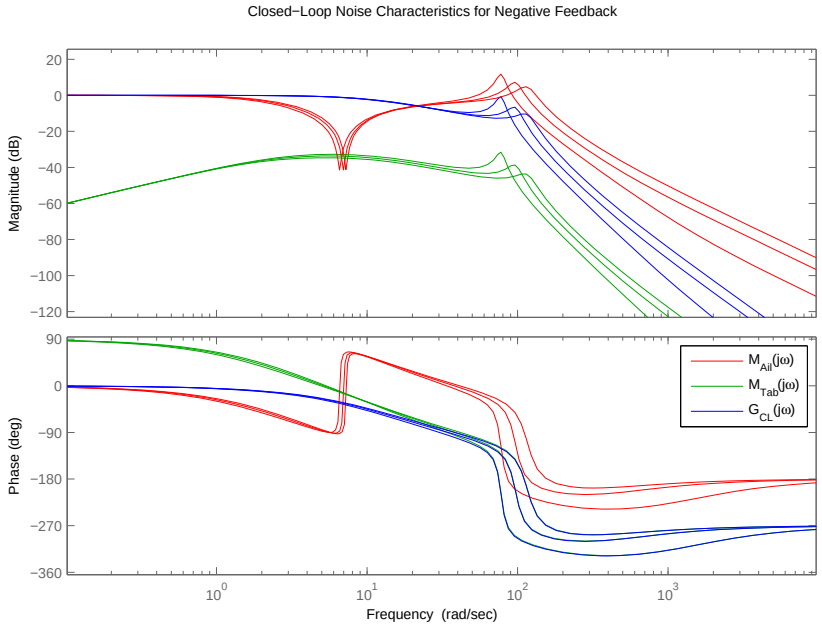

Figure 4.19 – SISO Noise Transmission for Negative Feedback

.

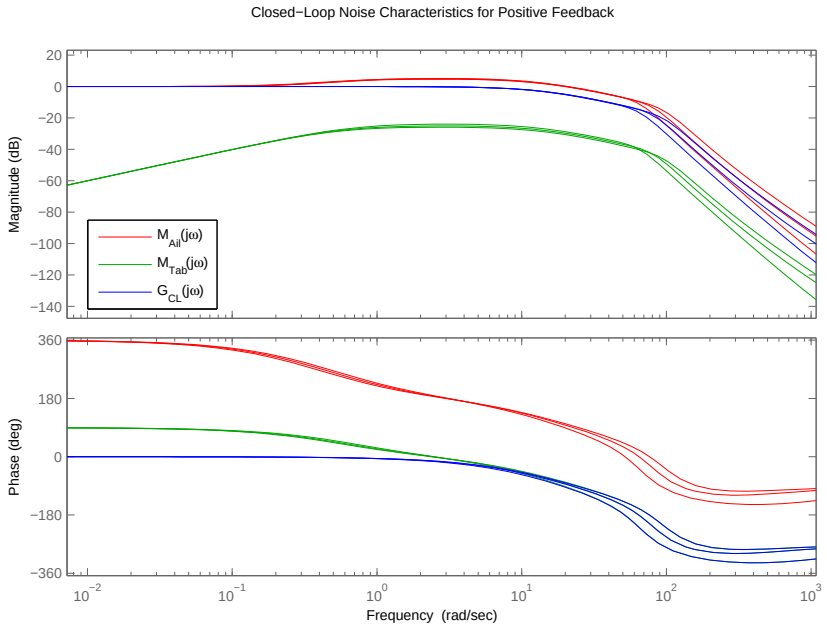

Figure 4.20 – SISO Noise Transmission for Positive Feedback

.

4.2 Deflection Command Tab Actuator Based Controllers

An alternative to a rate actuator is the use of deflection command actuators. These actuators inherently accepts position as an input and responds with a positional output with some dynamic response attributed to the process. So, if it is assumed that any moment applied to the actuator can be considered a disturbance, the addition of a tab to a servo actuator can be ignored. This however is only valid if the servo actuator has sufficient disturbance rejection built into its control loop. Different approximations to servo dynamics can be made. The one is a first order approximation, where it is assumed that the servo actuator and its control consists of a highly dominant real pole. Consequently, the actuator can be approximated to a first order system with an associated gain and time constant. However, if this is not the case the servo has to be modelled as a higher order, usually second order, system. The modelling of the system as a second order system results in the approach being exactly the same as the case where the rate actuator is implemented. With first order modelling, the closed-loop design is marginally different form that of the rate actuator based design.

The modelling of the servo to the first order results in the simplified servo model in Equation 4.2.1. As it can be noted that the gain is usually unity or calibrated to unity. However, the time constant, τ, is actuator dependent.

$$G_{Servo}(s) = \frac{\delta_{Tab}(s)}{\delta_{Ref}(s)} = \frac{1}{\tau s + 1} \tag{4.2.1}$$

4.2.1 Negative Feedback Aileron Deflection Control

The servo actuator is then combined with the aileron transfer function model derived in §2.3, constituting the open-loop model from tab deflection, δ_a, to aileron deflection, δ_a in Figure 4.21. The topology, shown in Figure 4.21, of the closed-loop system is kept similar to that of the rate actuator based design shown in Figure 4.3, with a minor difference. The inner loop, Figure 4.2, is replaced with a servo actuator $G_{Servo}(s)$, shown in red in Figure 4.21. The determination of the feedback gains, green in Figure 4.21, are then done by solving the characteristic equation shown in Equation 4.2.4. As with the rate actuator, there is an additional degree of freedom, so the ratio $\frac{K_{PA}}{K_{SA}}$ is constrained to a value locating the zero close to the origin.

$$G_{CL}(s) = \frac{G_{Servo}(s)G_{Ail}(s)}{1 - (K_{SA}s + K_{PA})G_{Servo}(s)G_{Ail}(s)} \tag{4.2.2}$$

$$s = -15 \tag{4.2.3}$$

$$1 - (K_{SA}s + K_{PA})G_{Servo}(s)G_{Ail}(s) = 0 \tag{4.2.4}$$

The closed-loop root locus that results is shown in Figure 4.22. It can be seen that there is an infinite gain margin. The dominant pole is then located at $s = -15$ as designed. The closed-loop design now ensures adequate dynamic performance for this aileron model.

The steady-state performance is once again, as with the rate actuator, ensured by adding the integral loop, $\frac{K_I}{s}$, and the feedforward term, N, blue in Figure 4.21. The integral insures steady state accuracy and the feedforward insures that the integrator dynamics are not excited. The feedforward gain calculation method and the choice of the integrator gain is covered by Equation 4.1.10 through Equation 4.1.15. The stability of the integrator loop is confirmed by the root locus in Figure 4.23.

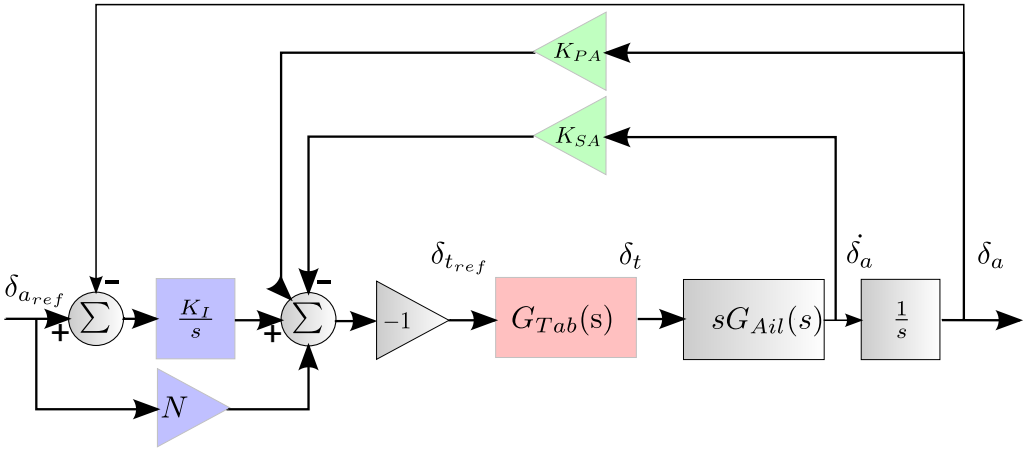

Figure 4.21 – SISO Negative Proportional and Rate Feedback Controller Topology

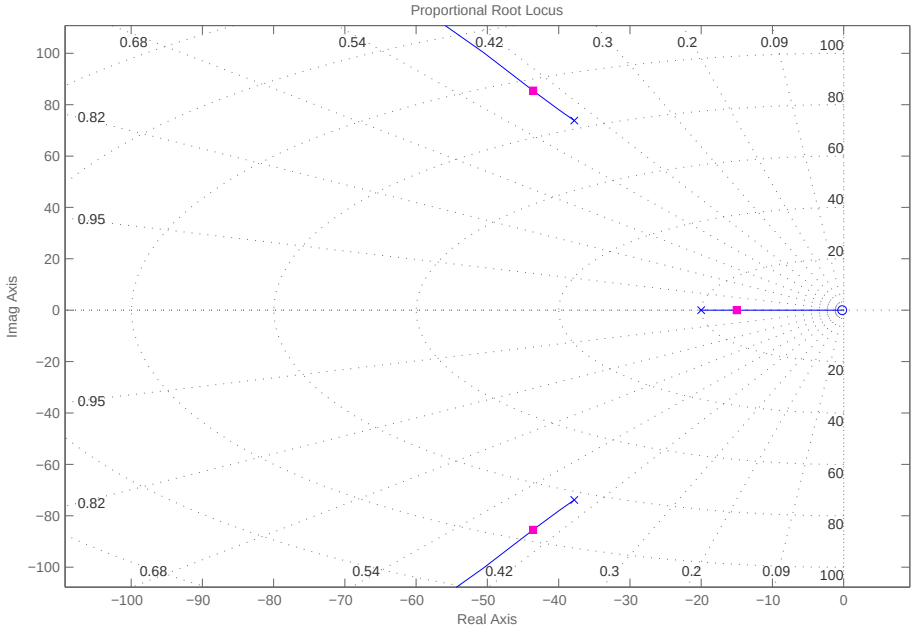

Figure 4.22 – Negative Feedback Root Locus at 50 ms^{-1} Airspeed with Servo Actuation

Previously, when the rate actuator was used the response showed a transient ripple resulting from the aileron dynamics. This ripple is not present to a large degree in this response which is shown by the frequency domain analysis in Figure 4.25 since there is proper rejection of the aileron resonant dynamics. The primary reason is that the actuator only has a single dominant pole resulting in the ability to damp the aileron very well. The position and rate feedback topology is sufficient in its rejection of the aileron dynamics. The proportional and rate feedback results in infinite gain margin in

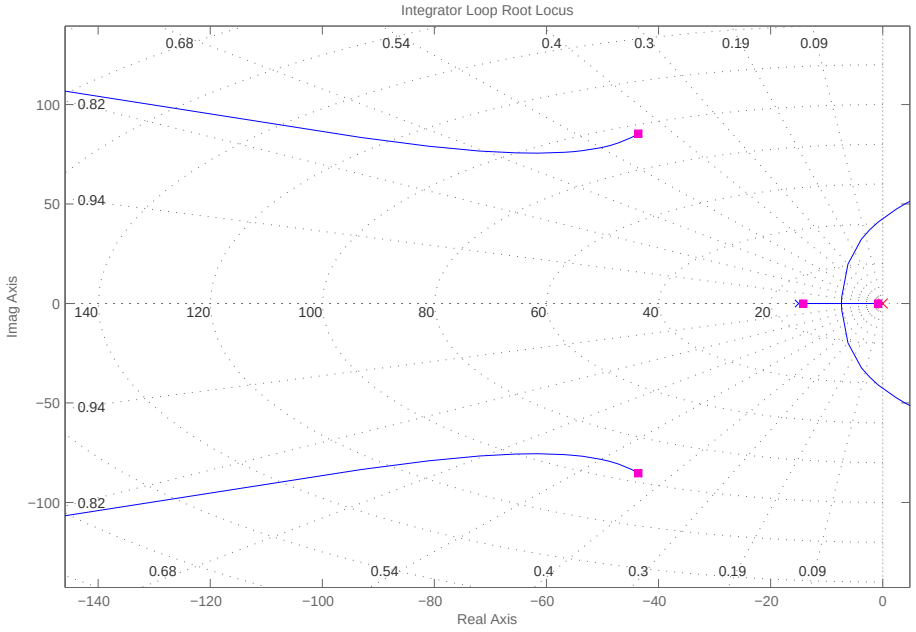

Figure 4.23 – Integrator Loop Root Locus at 50 ms^{-1} Airspeed with Servo Actuation

the inner loop, however the bode plot, Figure 4.29, shows that the closed-loop system has a gain margin due to the addition of the integrator.

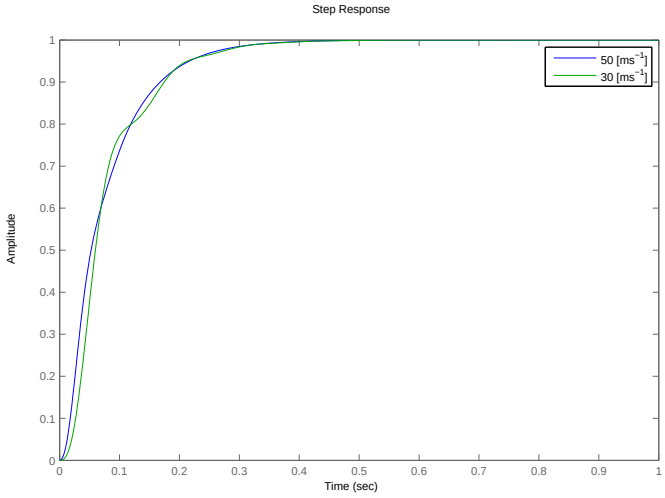

Figure 4.24 – Negative Feedback Response with Servo Actuator at Airspeed of $30\ ms^{-1}$ and $50\ ms^{-1}$

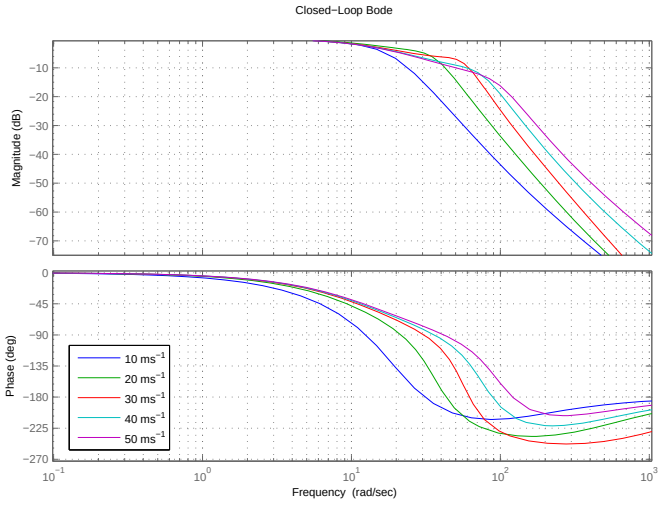

Figure 4.25 – Closed-Loop Bode for Negative Feedback Controller with Servo Actuation

4.2.2 Positive Feedback Aileron Deflection Control

The positive feedback topology allows for proportional only feedback to achieve the desired dynamic performance. The positive feedback scenario has the same beneficial characteristics as presented with the rate actuator. The error dynamics are very similar to those described by Equation 4.1.16 through Equation 4.1.19. The only difference is that the inner loop or tab actuator dynamics now only contain one pole and not two. The effects of this is discussed when considering the root locus at a later stage.

The calculation of the feedback gain is done as explained in Figure 4.1.20 through Equation 4.1.22. The inner loop however is just replaced by the servo dynamics as follows:

$$G_{CL}(s) = \frac{G_{Servo}(s)G_{Ail}(s)}{1 + K_{PA}G_{Servo}(s)G_{Ail}(s)} \tag{4.2.5}$$

$$s_p = -15 \tag{4.2.6}$$

$$1 + K_{PA}G_{Servo}(s_p)G_{Ail}(s_p) = 0 \tag{4.2.7}$$

This results in a dominant pole at s=-15. The degree of dominance however is subject to the aileron transfer function's, $G_{Ail}(s)$, pole positions. The weaker the damping of the aileron open loop poles the less dominant the the resulting real pole will be since the amount the open loop poles have to be moved to achieve adequate response is greater. This is shown by the root locus in Figure 4.26. It is once again apparent from the root locus that the tab actuator pole becomes unstable as the gain is increased as predicted by the error dynamics in §4.1.3.

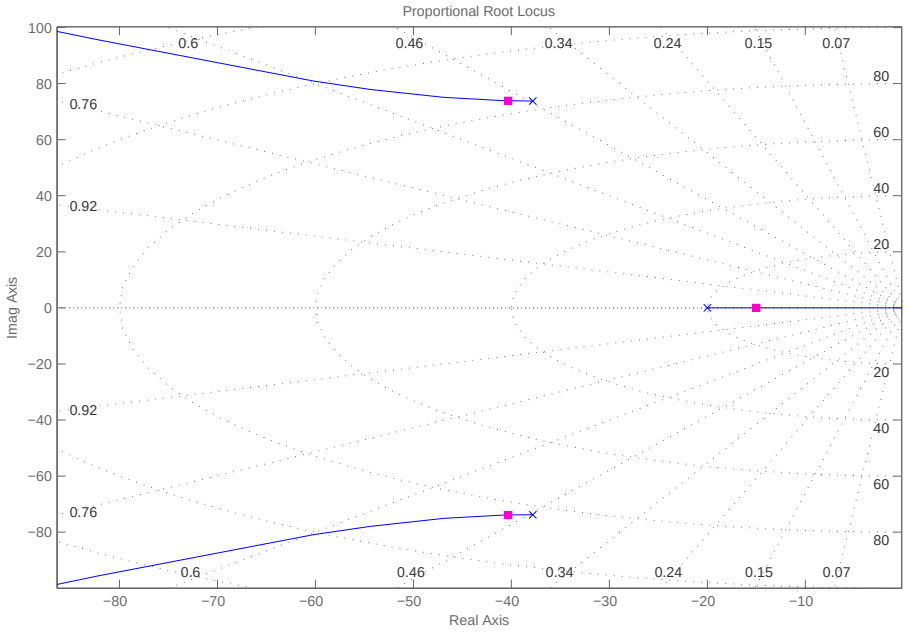

Figure 4.26 – Positive Feedback Root Locus at 50 ms^{-1} Airspeed with Servo Actuation

The steady-state accuracy is then once again ensured with the feedforward and integrator combination. The resulting root locus of the integrator loop is presented in Figure 4.27 showing stability. From the response of the closed loop system Figure 4.28, it can be seen that the dynamics of the negative feedback and positive feedback control appear to be very similar. The frequency domain, Figure 4.25 and Figure 4.29, also shows similar gain margins for the system, between $10\ dB$ and $20\ dB$ depending on the air speed. From the root loci in Figure 4.22 and Figure 4.26, it can however be seen more clearly that the positive feedback controller results in relatively better damping of the aileron as the gain is increased.

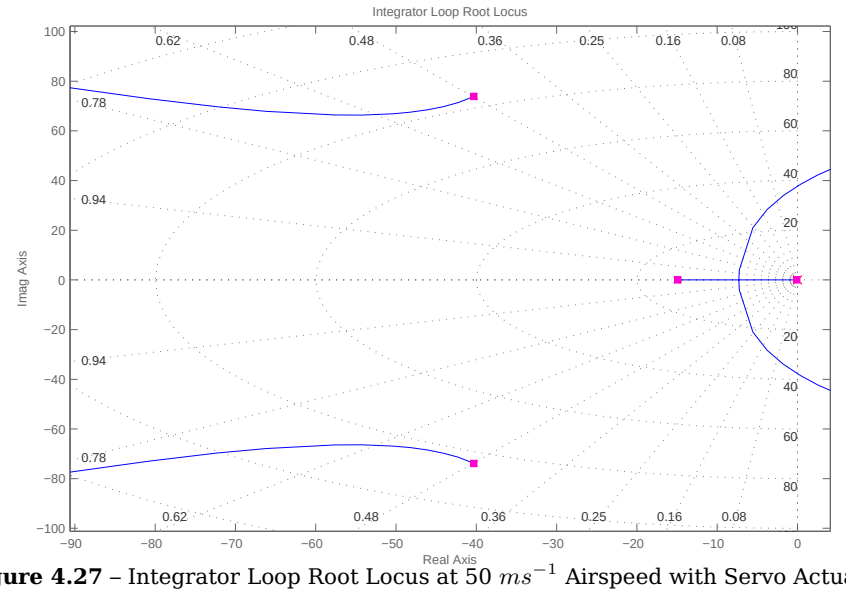

Figure 4.27 – Integrator Loop Root Locus at 50 ms^{-1} Airspeed with Servo Actuation

The proposed control topologies presented in §4.1 is adapted for the case where a servo actuator is used by the tab. The topologies are presented diagrammatically and similarities with the rate actuation process is presented. Further, the modifications in the parameter evaluation procedure is summarised. The performance of the controllers are checked in simulation and it is once again found that the ability of the position and rate feedback controller to reject the unwanted aileron dynamics is limited. The positive feedback controller once again results in superior performance but is subject to reduced robustness. The robustness, disturbance sensitivity and noise immunity is not analysed for the deflection actuator scenario. It is expected to be much the same as the rate actuator scenario since it is based based on the same outer loop dynamics.

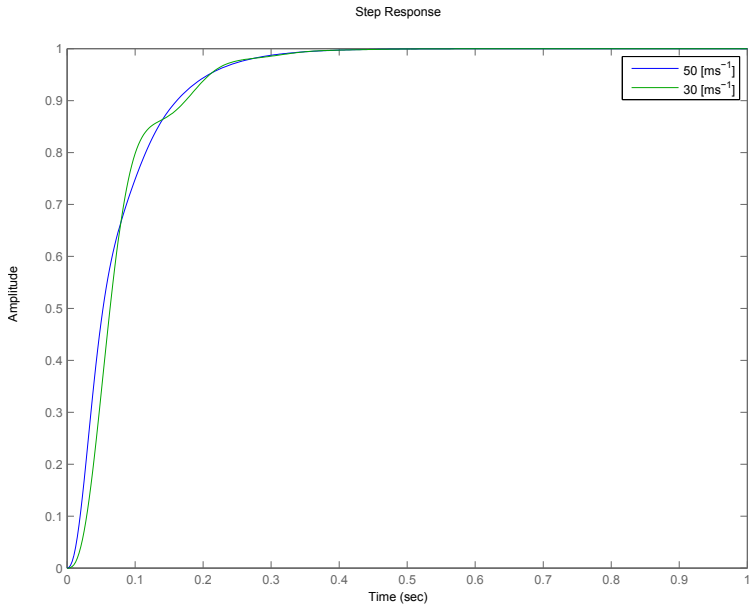

Figure 4.28 – Positive Feedback Response with Servo Actuator at Airspeed of 30 ms^{-1} and 50 ms^{-1}

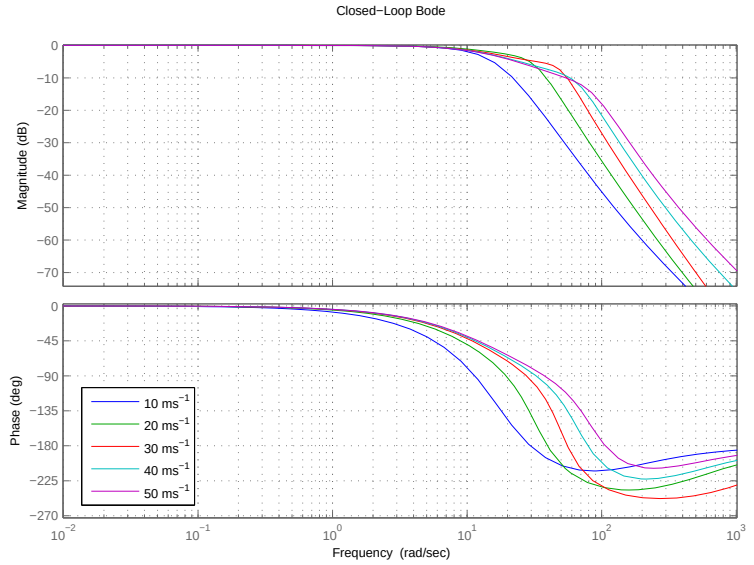

Figure 4.29 – Closed-Loop Bode for Positive Feedback Controller with Servo Actuation

4.3 Actuator Requirements

A natural result of the control process is the understanding of the dynamic actuator requirements. This in actuality may be very different from the static optimal solutions provided by §2.5 and Jaquet's work [1]. Qualitatively there is the notion that in order to affect motion in the tab and aileron there should be an excess in toque applied to the surface relative the aerodynamic hinge moment. The extent off excess is dependent on the dynamic requirements of the response. This in turn is a result of the controllers used.

In the tab-only actuation scenario, the control is only applied to the tab and classical control is used. The result is that there are no strict input considerations in the control design. Qualitatively the input is considered by the designer when synthesizing the controller. Statement like not attempting to drive the actuator beyond its bandwidth and attempting to maintain optimal damping helps these considerations. Noted, the damping in this case was chosen to be much higher than unity and therefore extra control input will be needed to coax the system into responding in this way.

Since the scenarios are dependent on the surface chord and span, airspeed, angle of attack and density as well as the dynamic requirements, short of simulating every possible scenario it would be difficult to provide a complete dataset of the requirements. However, considering following the presented scenario will provide great insight into the actuator requirements of each controller. The tab actuation torque command is depicted in Figure 4.30. It is apparent from the plot of the input to the tab servo that the peak torque is approximately $25\times$ larger than the steady-state torque for the negative feedback controller. The positive feedback controller input indicates a maximum of about $12\times$ the steady-state actuator torque over the observed responses. Through

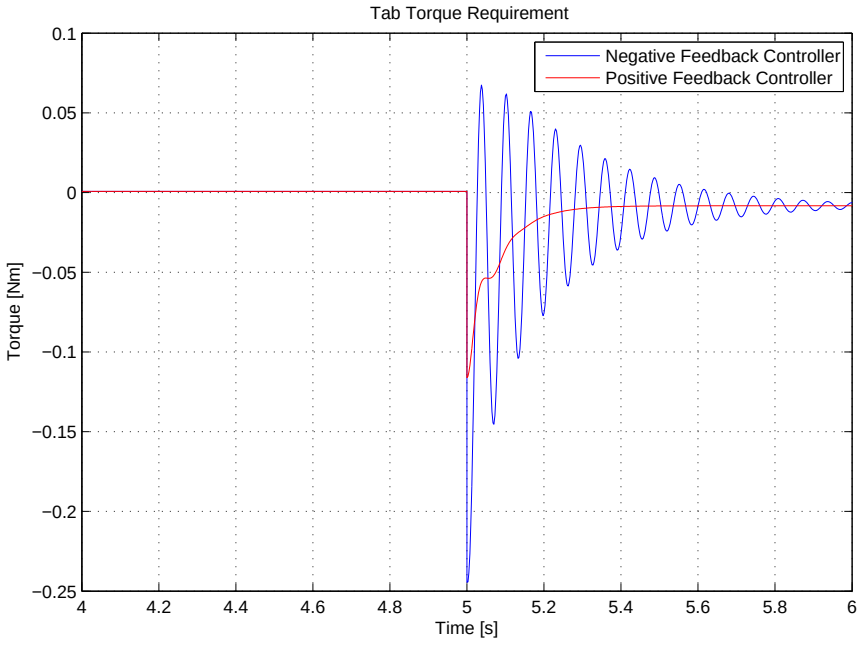

Figure 4.30 – Servo Tab Actuator Requirements at $\alpha = 5°$, $V = 50ms^{-1}$ and $10°$ Step Size

inspection, this is shown to be the general case for the positive and negative feedback controllers. This is however the theoretical result due to a step command showing the massive initial peak since actuator saturation is intentionally not shown here. A rate limited step is expected to show a considerably smaller initial peak.

4.4 Controller Scaling and Practical Aspects

Up to this point, the control topologies, implementation, performance and actuator requirements have been discussed at length. The direct implications and applicability of these control systems on a general scenario is discussed here. The aspects of the system that are changeable is considered here. A general overview of the important aspects of the tab-only actuation scenario is given based on the expected changes when scaling this system.

The velocity, moment of inertia, chord ratio and span all affect the natural frequency of the tab and aileron dynamics. For the moment, the gain and effectiveness of the tab is considered to have been optimised and the controller requirement is considered relative to the dynamics that result from the optimised system. §2.4 shows that there is a linear relationship between velocity and natural frequency and an inverse relation to moment of inertia. Further, the natural frequency is related linearly to the cord and to the square root of the span. The hinge moment is then a complex function of the geometry of the tab and aileron but is considered to be the same for the same tab-aileron chord ratios. Consider the worst case scenario where very low damping is present and the maximum performance of the available actuators is limited. The direct impact is that the poles of the aileron would probably end up at (1) blue in Figure 4.31. Now consider an airliner such as an A330, compared to the setup tested the cruising velocity is probably about five times the tested velocities however the total wing chord at the location of the aileron is about four times the experimental setup's chord [17]. Additionally, the moment of inertia of the surfaces would be expected to be much larger. The resultant natural frequency can therefore not truly be predicted without the final mechanical structure. Two specific scenarios are possible one where the natural frequency of the system is smaller than the desired final pole and one where it has a larger natural frequency.

Consider the case where the poles are very slow, slower than the desired final dominant pole, and very badly damped as shown by (2) blue in Figure 4.31. The only controller that seems to be effective in achieving a better damped and fast as possible response in this case is the proportional and rate feedback controller. It effectively actively damps the aileron dynamics as depicted by (2) red in Figure 4.31. Consequently, in these cases the dynamics of the system would be limited to those of the aileron. This makes sense since the dynamics of the system is limited by aerodynamics and the ability of the tab to create a resultant hinge moment on the aileron. It would therefore probably be impossible to drive the system much faster than the aerodynamic limitations will allow. Even though the linear model will allow for the inputs the tab would probably saturate. The input requirements of this condition therefore has to be considered since the actuator will have to do a considerable amount of work to actively damp the aileron poles. This damping can be achieved by mechanical means as well removing the need for the actuator to do all the work. This would then mean that no real control is necessary to control the dynamics maybe only an integrator and some feedforward to ensure accurate following.

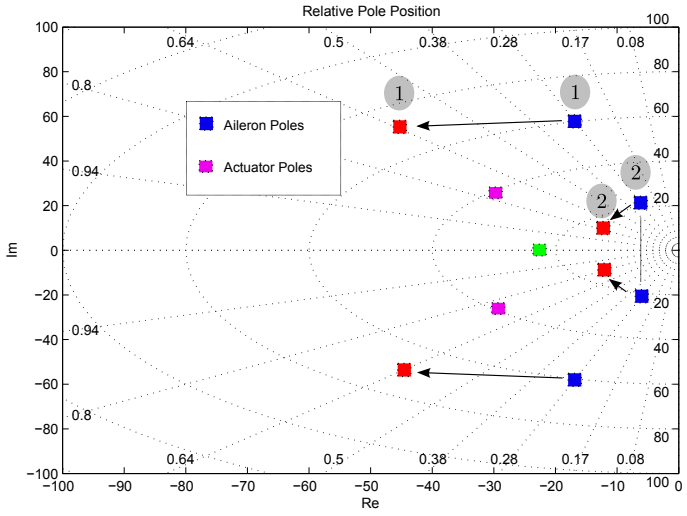

Figure 4.31 – Scaling Effect on Pole Position

The other scenario is where the natural frequency of the system is considerably larger than the desired pole location and thereby the poles can be located more favourably. The most attractive controller for achieving this is the positive feedback controller. Here the positive feedback controller succeeds in damping the aileron poles and improving the dynamic response considerably (1) red in Figure 4.31. This has also been shown in the practical implementation where the aileron dynamics have been rejected properly by the positive feedback controller. The resultant actuator pole indicated by green in Figure 4.31 will then be dominant.

The damping can be done in a mechanical method which will result in a structure which is much more controllable and would not require much control at all as before. The mention of mechanical damping appears to nullify the need for active control. However, under changing flight conditions the required mechanical damping would have to change or design would have to be done at nominal values. This in turn would mean a less than ideal response. The convenience with active control is that adapting it is as simple as changing a gain.

The ability of the active control to dampen the aileron poles is dependent on the excess actuator bandwidth. The bandwidth of the actuator should be in the order of the poles it is attempting to dampen, preferably larger. This then allows for active damping otherwise not much can be done in terms of damping the aileron poles. On the other hand when the dynamics become much faster than the actuator poles, even if they are badly damped they will tend not to be excited by the reference commands. The only risk is that this resonant behaviour will be excited by disturbances which can lead an control surface oscillation. It is therefore imperative to dampen the aileron poles at least enough to avoid this condition.

Chapter 5

Design of Feedback Control for Concurrent Tab and Aileron Actuation

In the previous approach to control of the tab and aileron combination, the system is solely controlled by tab actuation. This implies that in the design stage it must be ensured that the tab must always be able to affect the necessary aileron performance. However, consider a case where this is not acceptable and the operating region of the tab cannot be insured. It is therefore necessary to attain some other method of aileron actuation. The only choice is an aileron actuator. Conveniently it has been shown [1] that the size of the aileron actuator would be significantly reduced.

The model is formulated to be actuated by a resultant actuator torque. This is contrary to the technique used previously where torque is considered a disturbance and the actuator rejects it. Attempting to place two position or rate actuators on the tab and aileron would mean that the actuators will have to be able to reject the interacting aerodynamic hinge moments. Decoupling of the hinge moments can be attempted but resultant hinge moment requirements have to be translated into position and rate commands for the actuators. Furthermore, as the actuators start to operate closer and closer to their torque limits the ability to reject additional disturbances of cross coupling would become less. Getting this right becomes an iterative process and not necessarily dynamically efficient, since there is no direct consideration of dynamic actuator torque requirements.

Another option to attempt would be frequency separation or frequency domain decoupling between the tab-aileron coupling and the aileron actuator. However, since the tab-aileron coupling is already close to the required dynamics performance there is no space in the frequency domain to place the aileron actuator. Since the aim is to keep the aileron actuator as small as possible, placing it at a higher frequency means that a large actuator is required anyway to achieve the deflection initially while the tab is still responding at a slower rate.

Keeping the model in its purest form by actuating it with torque actuators, the requirements of the actuators can be controlled by the designer rather than it being the result of an iterative process. This then leads directly to optimal control methods allowing the designer to weigh between different aspects of the response as needed. The weights can be modified to ensure dynamic performance while still considering input requirements. This section therefore deals primarily with the application of LQR and consequently FSF methods to control the tab and aileron to the desired final orientation.

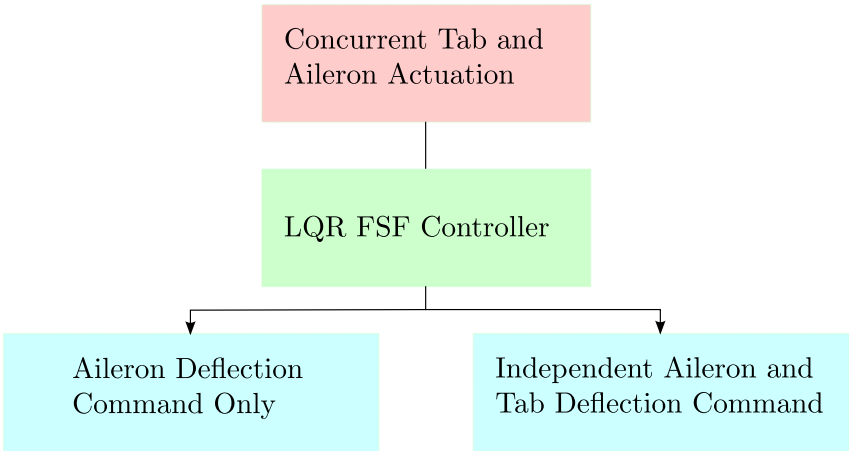

Figure 5.1 – Approach to Concurrent Tab and Aileron Actuation

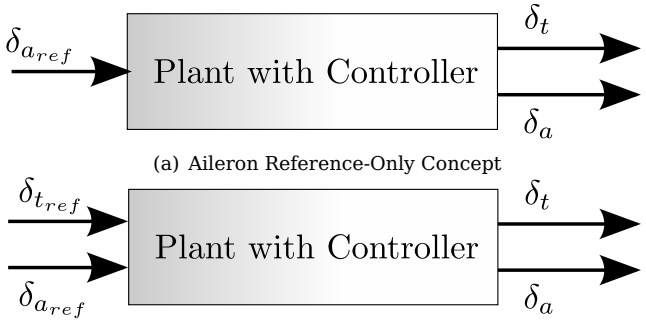

(a) Aileron Reference-Only Concept

(b) Tab and Aileron Reference Concept

Figure 5.2 – Different Approaches to Concurrent Tab and Aileron Actuation

The application of concurrent tab and aileron actuation is presented in two forms as shown in Figure 5.1. The first approach is formulated such that the system ensures accurate following of an aileron deflection command as shown in Figure 5.2. In this case only an aileron reference angle is given to the system. The second method is to ensure the tab and aileron both follow their respective reference commands as shown in Figure 5.2. Therefore, the section first presents the LQR controller and then applies it to both approaches.

5.1 Linear Quadratic Regulation

Linear quadratic regulation (LQR) is a specific result of optimal control applied to a variety of problems. It is used when direct control of poles is not needed. It results in optimal controllers for the weights specified by the designer. This need for designer input means that some insight is needed in the meaning of the optimised cost function. The cost function generally used in LQR is given in Equation 5.1.1. The cost function weights input in terms of its magnitude and the states in terms of its magnitude.

$$J = \int_0^\infty X^T Q_1 X + U^T Q_2 U dt \tag{5.1.1}$$

The weights Q_1 and Q_2 of the states, X, and the inputs, U, respectively can be chosen such that a desired response can be achieved. Q_1 and Q_2 are positive symmetric matrices, important in the solution, and X and U are vectors. Effectively the Q_1 term weights the square of the state. By adjusting its relative size compared to the input weights, Q_2, the state sizes can be regulated and vice-versa. This occurs due to the optimisation process resulting in gains that will cause the cheaper of U or X to be larger.

One way to choose the magnitudes of the diagonal terms of the weighing matrix is to use the Pincer Method [18]. This method uses an approximation for the settling time of the system in order to determine the necessary ratio between the weights. An alternate is to normalise the percentage change contribution by each state and input to the change in cost and to use the output matrix, H, to consider only the states that must be regulated [18]. To accommodate this, the cost functions is then modified to the form in Equation 5.1.2. The the normalisation of the states and inputs is done in terms of their full scale values $x_{1_{max}}$ and $u_{1_{max}}$ respectively. Further, an additional relative weighting can be multiplied by the weighing matrix Q_1 to make it $Q_1' = \rho_1 Q_1$ allowing for relative importance to be put on input and state following.

$$J = \int_0^\infty X^T H^T Q_1' H X + U^T Q_2 U dt \tag{5.1.2}$$

$$Q_1 = \begin{bmatrix} \frac{1}{x_{1_{max}}^2} & 0 & 0 & \cdots & 0 \\ 0 & \frac{1}{x_{2_{max}}^2} & 0 & \cdots & 0 \\ 0 & 0 & \frac{1}{x_{3_{max}}^2} & \cdots & 0 \\ \vdots & \vdots & \vdots & & \vdots \\ 0 & 0 & 0 & \cdots & \frac{1}{x_{n_{max}}^2} \end{bmatrix} \tag{5.1.3}$$

$$Q_2 = \begin{bmatrix} \frac{1}{u_{1_{max}}^2} & 0 & 0 & \cdots & 0 \\ 0 & \frac{1}{u_{2_{max}}^2} & 0 & \cdots & 0 \\ 0 & 0 & \frac{1}{u_{3_{max}}^2} & \cdots & 0 \\ \vdots & \vdots & \vdots & & \vdots \\ 0 & 0 & 0 & \cdots & \frac{1}{u_{n_{max}}^2} \end{bmatrix} \tag{5.1.4}$$

The solution to the LQR problem is based on FSF control in which the input U is given by:

$$U = -KX \tag{5.1.5}$$

The system model is a dynamic constraint in the cost function:

$$\dot{X}(t) = FX(t) + GU(t) \tag{5.1.6}$$

The cost function can then be solved through the use of a Lagrange multiplier and Ricatti equation or Hamiltonian [19]. The solution is not shown here since it is readily available in literature. The use of the solution is more interesting and it is calculated with the MATLAB lqr.m function. All the necessary conditions such as positive semi-definiteness of the weighting matrices and controllability of the states are ensured. This allows for the optimal feedback gains to be calculated for the specified weights and implemented in a FSF topology.

5.2 Power Weighted Linear Quadratic Regulation

Now, an addition is made to the linear regulator in order to include a power weighting in the cost function. The result of this should be a energy optimal control input for the chosen weights since the cost function contains the time integral of power. Take the simple linear quadratic regulator and include the cross terms of the control input and states as shown in Equation 5.2.1. Since rate information is included in the states of the system and the actuator moment is considered the input of the system, Q_3 can be chosen so that the cross term results in the instantaneous actuator power consumption. In the specific case where only the tab is actuated, it will result in Equation 5.2.2. When the aileron is also actuated, Equation 5.2.3 results. The power can then be weighted further with a relative term $Q_3' = \rho_3 Q_3$ allowing importance to be placed on the power consumption.

$$X^T Q_3 U \tag{5.2.1}$$

$$\begin{bmatrix}\delta_{t_k} & \dot{\delta}_{t_k} & \delta_{a_k} & \dot{\delta}_{a_k}\end{bmatrix} \begin{bmatrix}0\\1\\0\\0\end{bmatrix} M_t(t) \tag{5.2.2}$$

$$\begin{bmatrix}\delta_{t_k} & \dot{\delta}_{t_k} & \delta_{a_k} & \dot{\delta}_{a_k}\end{bmatrix} \begin{bmatrix}0 & 0\\1 & 0\\0 & 0\\0 & 1\end{bmatrix} \begin{bmatrix}M_t(t)\\M_a(t)\end{bmatrix} \tag{5.2.3}$$

The cost function can now be modified as described in Equation 5.2.4 [19].

$$J = \int_0^\infty X^T H^T Q_1' H X + U^T Q_2 U + 2X^T Q_3' U dt \tag{5.2.4}$$

The cost function can then be solved through the use of a Lagrange multiplier and Ricatti equation or Hamiltonian [19]. The solution is not shown here since it is available in literature. The MATLAB lqr.m function is once gain used to calculate the steady-state control gain of the optimal controller.

The example in Figure 5.3 shows the reduction in energy resulting from weighing the cross terms as shown in Equation 5.2.4 by $2X^T Q_3 U$. It can be seen that there is no significant change in the system performance however a 10% reduction in energy is achieved by choosing the power weight correctly. The weights Q_1, Q_2 and ρ_1 is as described in Equation 5.3.11, Equation 5.3.11 and Equation 5.3.14.

5.3 Aileron Deflection Command Following

Full-state feedback control results in control over the poles of the fully coupled system. This combined with the optimal control methods such as LQR, see §5.1, provides the adequate input and output dynamics of the system. These dynamics are controlled by the gains resulting from the state and input weights and can be chosen to satisfy input constraints as well as the output constraints. However, the steady-state response of the controller is not necessarily guaranteed under conditions of constant disturbances. To ensure steady steady performance some modifications to the input structure has to be made.

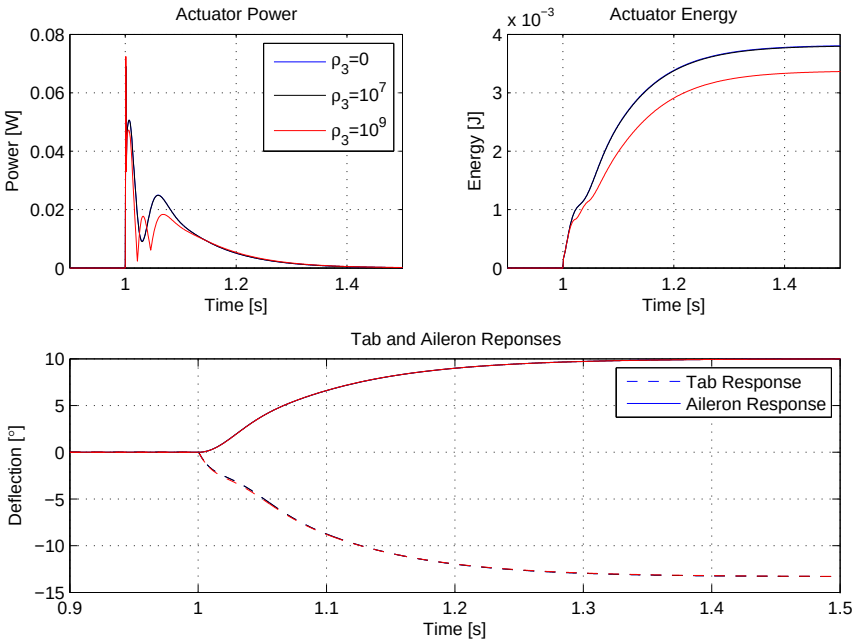

Figure 5.3 – Simulated Representative Response Before and After Power is Weighed

The weighting matrices are chosen through the normalisation method as described in §5.1. In this specific case there are two inputs and four states. The normalisation is done such that the tab deflection is not weighted. This effectively allows as much tab deflection as required by the control system. The tab rate however is weighted since it is the equivalent of more damping. The aileron rate is weighed equally to the tab rate since about the equal amount of damping is required. The aileron final value is weighed heavily to ensure there is accurate command following. Further, for the inputs it is known that the hinge moments are in the order of $0.5\ Nm$ for the aileron and $0.05\ Nm$ for the tab so they are normalised in this region. It was found however that the relative size of the tab moment and the aileron moment had to be increased so that aileron hinge moment is about twenty times more expensive than the tabmoment. This results in primarily the use of the tab actuator to achieve the response. It was found that there is a great deal of weight adjustment necessary for this problem to give a desirable response. This is somewhat an indication that the natural motion of the system has to be forced to move in the desired manner. Another factor indicating this is the large ratio used between input and state weight $\rho = 10$.

The first step is to introduce a reference input to the closed-loop system. As shown in [18] is achieved through the addition of two gains; the state command, N_X, and the steady-state control input, N_U indicated in red in Figure 5.4. The state command perturbs the system state to force the controller to drive the state error, $X - N_X \delta_{Ail_{Ref}}$, to zero. But, the controller consisting only of gains cannot drive the state error to zero if there is no open loop integrator present in the system. It is necessary to introduce a steady-state input to ensure proper command following. This input is introduced through $N_U \delta_{Ail}$. It is just a matter of determining the correct gains in order to ensure steady-state accuracy.

To calculate the command and steady-state input gains N_X and N_U, respectively, steady-

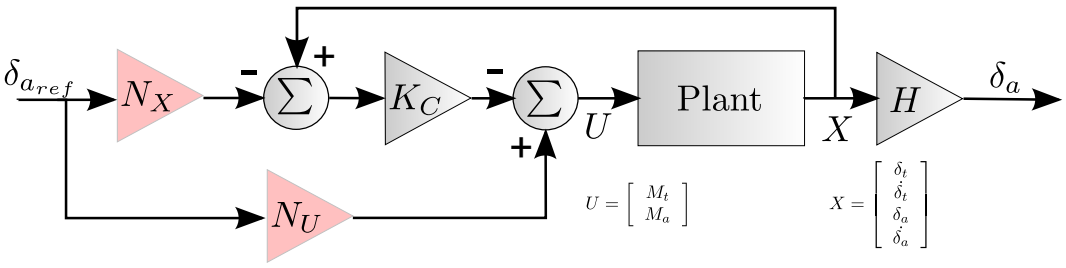

Figure 5.4 – Reference Input

state conditions are considered [18]:

$$X - N_X \delta_{Ail_{Ref}} = 0 \tag{5.3.1}$$

$$HX = \delta_{Ail_{Ref}} \tag{5.3.2}$$

$$U_{SS} = N_U \delta_{Ail_{Ref}} \tag{5.3.3}$$

which gives

$$HN_X = I \tag{5.3.4}$$

This combined with the steady-state condition for the continuous model is then:

$$\dot{X_{SS}} = FX_{SS} + GU_{SS} = 0 \tag{5.3.5}$$

$$FN_X \delta_{Ail_{Ref}} + GN_U \delta_{Ail_{Ref}} = 0 \tag{5.3.6}$$

$$FN_X + GN_U = 0 \tag{5.3.7}$$

The Equation 5.4.4 and Equation 5.4.7 can then be solved simultaneously:

$$\begin{bmatrix} F & G \\ H & \underline{0} \end{bmatrix} \begin{bmatrix} N_X \\ N_U \end{bmatrix} = \begin{bmatrix} \underline{0} \\ I \end{bmatrix} \tag{5.3.8}$$

This method of introducing a reference input ensured steady-state accuracy and is independent from the controller gain. Under conditions where disturbances are present in system and a degree of model uncertainty, this method of introducing a reference input will not necessarily ensure accuracy. To rectify this specific problem, the steady-state input gain can be replaced with an integrator. The integrator would result in the ability to reject constant disturbances and follow the reference command [18].

The addition of an open-loop integrator is effectively reducing the error, $\delta_{Ail} - \delta_{Ail_{Ref}}$, to zero and can be considered as a variable N_U, green in Figure 5.5. The feedforward term N_X will command the response and the integrator will effectively result in the cancellation of the constant disturbances and model uncertainties. The integrator gain is determined by augmenting the full state feedback model with an integrator:

$$\begin{bmatrix} \dot{X} \\ \dot{x}_I \end{bmatrix} = \begin{bmatrix} F & 0 \\ H_I & 0 \end{bmatrix} \begin{bmatrix} X \\ x_I \end{bmatrix} + \begin{bmatrix} G \\ 0 \end{bmatrix} U + \begin{bmatrix} \underline{0} \\ 1 \end{bmatrix} \delta_{Ail_{Ref}} \tag{5.3.9}$$

with

$$U = \begin{bmatrix} M_t \\ M_a \end{bmatrix} \qquad H_I = \begin{bmatrix} 0 & 0 & -1 & 0 \end{bmatrix} \tag{5.3.10}$$

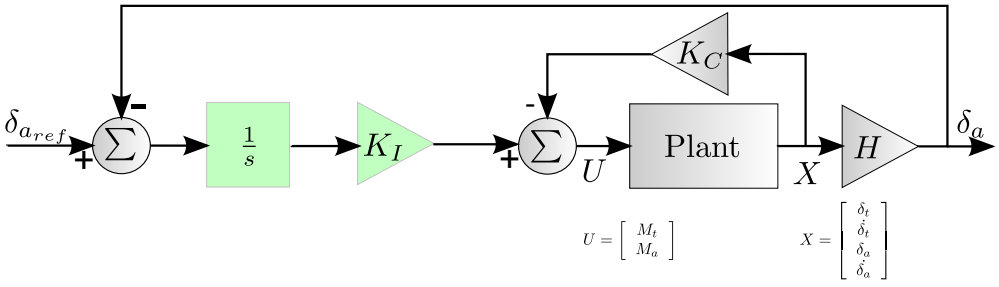

Figure 5.5 – System Integrator Augmentation

The controller gain can then be calculated for the augmented system with the weights remaining the same as in the absence of the integrator. An additional weight has to be added for the integrator. It is weighed equally to the aileron state. The exact weighting can be debated but generally, the integrator must have a small enough weight to result in a large enough integrator gain to quickly remove the constant disturbances and model uncertainties. The new state weighting matrices are given by:

$$Q_{1_I} = \begin{bmatrix} Q_1 & \underline{0} \\ \underline{0} & Q_{1_{(3,3)}} \end{bmatrix} = \begin{bmatrix} \frac{1}{10^2} & 0 & 0 & 0 & 0 \\ 0 & \frac{1}{0.05^2} & 0 & 0 & 0 \\ 0 & 0 & \frac{1}{0.001^2} & 0 & 0 \\ 0 & 0 & 0 & \frac{1}{0.02^2} & 0 \\ 0 & 0 & 0 & 0 & \frac{1}{0.001^2} \end{bmatrix} \tag{5.3.11}$$

$$Q_2 = \begin{bmatrix} \frac{1}{0.02^2} & 0 \\ 0 & \frac{1}{0.001^2} \end{bmatrix} \tag{5.3.12}$$

$$H = \begin{bmatrix} 0 & 0 & 0 & 0 & 0 \\ 0 & 1 & 0 & 0 & 0 \\ 0 & 0 & 1 & 0 & 0 \\ 0 & 0 & 0 & 1 & 0 \\ 0 & 0 & 0 & 0 & 1 \end{bmatrix} \tag{5.3.13}$$

$$\rho_1 = 10 \tag{5.3.14}$$

The gain can then be recalculated with the standard LQR algorithm, §5.1. This results in a feedback gain which can be broken into its constituents as follows:

$$K_{(2\times5)} = \begin{bmatrix} K_{C_{(2\times4)}} & K_{I_{(2\times1)}} \end{bmatrix} \tag{5.3.15}$$

It can be seen from Figure 5.5 that the system dynamics will be affected by the integrator. It is therefore convenient to add a feedforward term that will cancel the dynamics of the integrator, blue in Figure 5.6. The total effect of the integrator is not cancelled however the feedforward stops the integrator from being excited by commands [18]. It can be shown that the feedforward term adds a zero at the location $s = -\frac{K_I}{N}$, shown in Equation 4.1.14. The resulting closed-loop pole added by the integrator can therefore be cancelled by placing the zero on it. First, the closed-loop pole is found:

$$\left[\lambda I - (F - GK_C)\right] = 0 \tag{5.3.16}$$

(5.3.17)

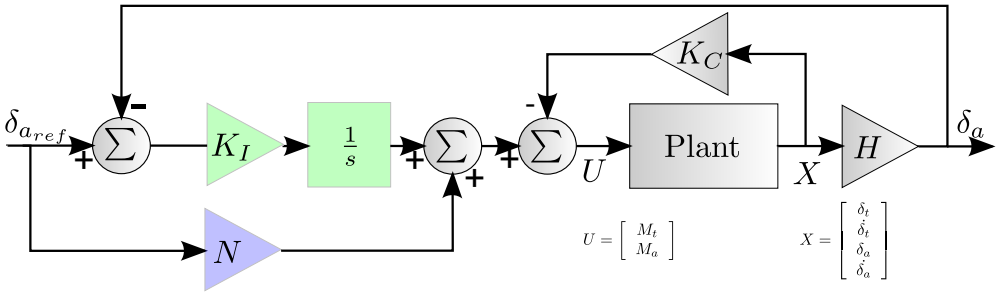

Figure 5.6 – FSF with Feed-Forward and Integrator

The real pole, λ_i, closest to the origin originates from the integrator. The zero can then be placed on it:

$$N = -\frac{K_I}{\lambda_i} \tag{5.3.18}$$

It is clear that in order to ensure dynamic performance and command constraints the controller is designed with the LQR method. However, it has been shown that in order to achieve the steady-state requirements the system needs to be augmented with an integrator and a feedforward. The reference input gains, N_X and N_U, are therefore rejected since they do allow for adequate compensation under conditions of model uncertainty and constant disturbances.

5.4 Tab and Aileron Deflection Command Following

In the previous section a controller has been derived which allows for dual actuator implementation and control force optimisation. However, it does not yet allow the tab to be actuated in the saturation region. Therefore, as the tab coupling to the aileron becomes weaker, the integrator will attempt to apply more tab to compensate for this effect. This may help but if the coupling has completely saturated, there will be very little effect on the aileron from the tab. This results in a very slow wind-up of the integrator.

One method which was attempted was to make a switching controller to switch off the tab actuation dominated integrator used in §5.3. Then, it is switched to an integrator only applying additional aileron hinge moment when the tab has exceeded a known critical angle where the tab is observed to become ineffective. However, in this process the switched integrator dynamics are not easily cancelled by a feedforward meaning that the dynamics are affected. Furthermore, the integrators have to be reloaded with initial conditions when moving in and out of these regions making it a highly condition based controller.

Alternatively, the command structure used in Equation 5.3.1 through Figure 5.3.3 presented in Figure 5.7 can be modified for multiple reference inputs. The state reference matrix, N_X is modified as presented in Equation 5.4.1 and the steady-state input matrix, N_U, is modified as in Equation 5.4.3. The solution to Equation 5.4.8 then evaluates N_X and N_U [18]. There are then multiple outputs shown by Equation 5.4.9. This is applied as shown in Figure 5.7.

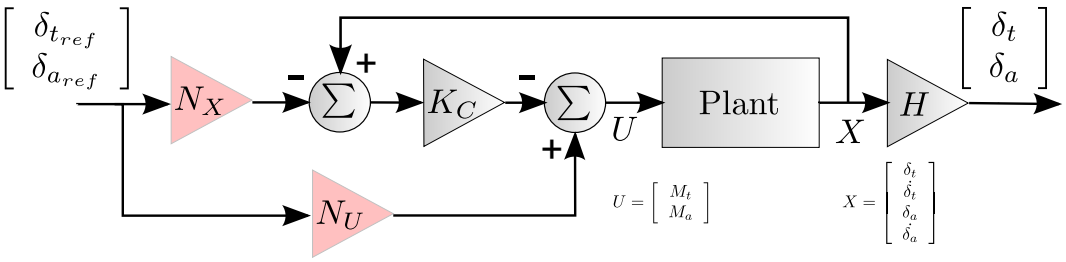

Figure 5.7 – Multiple Reference Inputs for FSF

$$X - N_X \begin{bmatrix} \delta_{Tab_{Ref}} \\ \delta_{Ail_{Ref}} \end{bmatrix} = 0 \tag{5.4.1}$$

$$HX = \begin{bmatrix} \delta_{Tab_{Ref}} \\ \delta_{Ail_{Ref}} \end{bmatrix} \tag{5.4.2}$$

$$U_{SS} = N_U \begin{bmatrix} \delta_{Tab_{Ref}} \\ \delta_{Ail_{Ref}} \end{bmatrix} \tag{5.4.3}$$

giving,

$$HN_X = I \tag{5.4.4}$$

combined with the steady-states,

$$\dot{X_{SS}} = FX_{SS} + GU_{SS} = 0 \tag{5.4.5}$$

$$FN_X \begin{bmatrix} \delta_{Tab_{Ref}} \\ \delta_{Ail_{Ref}} \end{bmatrix} + GN_U \begin{bmatrix} \delta_{Tab_{Ref}} \\ \delta_{Ail_{Ref}} \end{bmatrix} = 0 \tag{5.4.6}$$

$$FN_X + GN_U = 0 \tag{5.4.7}$$

sovling by

$$\begin{bmatrix} F & G \\ H & \underline{0} \end{bmatrix} \begin{bmatrix} N_X \\ N_U \end{bmatrix} = \begin{bmatrix} \underline{0} \\ I \end{bmatrix} \tag{5.4.8}$$

where

$$H = \begin{bmatrix} 1 & 0 & 0 & 0 \\ 0 & 0 & 1 & 0 \end{bmatrix} \tag{5.4.9}$$

The controller can be calculated with the same weights as before but the integrator augmentation is not done. This will result in a MIMO system that will follow the two inputs as long as the model is accurate. However, if there were disturbances or small model errors, the model will not produce completely accurate reference following. Therefore, it is convenient to augment both inputs with integrators as shown in Figure 5.9 in green. The integrators are combined with feedforward terms, $\bar{N}$, to minimise the effect of the integrator dynamics on the system bandwidth [18]. Here the N_U and N_X terms effectively decoupled the two commands meaning that the two integrators do not coupled into each other simplifying the feedforward calculation. The feedforward terms can be

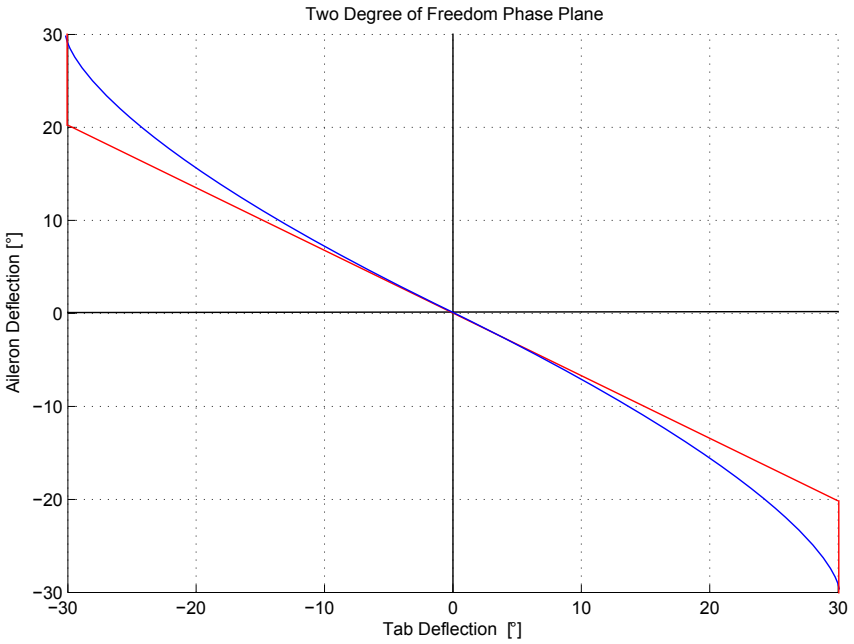

Figure 5.8 – Two Degree of Freedom Phase Plane Trajectories

calculated by considering the independent transfer function models of the two paths or it can be adjusted by the designer to give adequate dynamic response.

The advantage of the MIMO system that will follow two independent references is that the tab can now be commanded to its maximum angle and the aileron can be commanded to an angle larger than that resulting with previous controllers while the tab remains at the maximum angle. The result is that the static aileron and tab optimal orientations can now be used as input to the system. Consider the simplified form of the system phase plane by reducing the hyperplane of fourth order to the second order. This is achieved by applying the steady-state conditions $\dot{\delta}_a$ and $\dot{\delta}_t$ set to zero. Now only δ_t and δ_a remain as the two degrees of freedom which can be controlled. The steady state phase plane can therefore be shaped as desired according to actuator usage or static ratio §2.5. The system effectively becomes a variable ratio geared tab system. Considering Figure 5.8, any one of the desired trajectories can be followed by the controller. Previously a weight chosen in the optimal controller resulted in a single one of the trajectories for a design weight but when the tab saturated, the controller could not compensate. Now the predefined optimal trajectory defines the controller behaviour at tab saturation.

An example of an dynamic response of the system is shown in Figure 5.10. It can be seen that the tab and aileron can be commanded freely from each other the only effect being change in hinge moment.

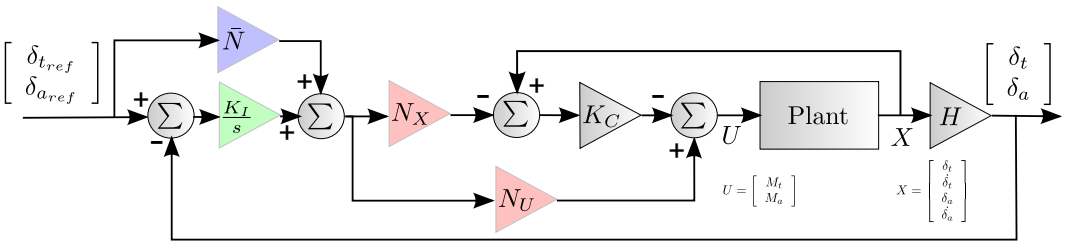

Figure 5.9 – Twin Reference Input Structure with Integrators and Feedforward

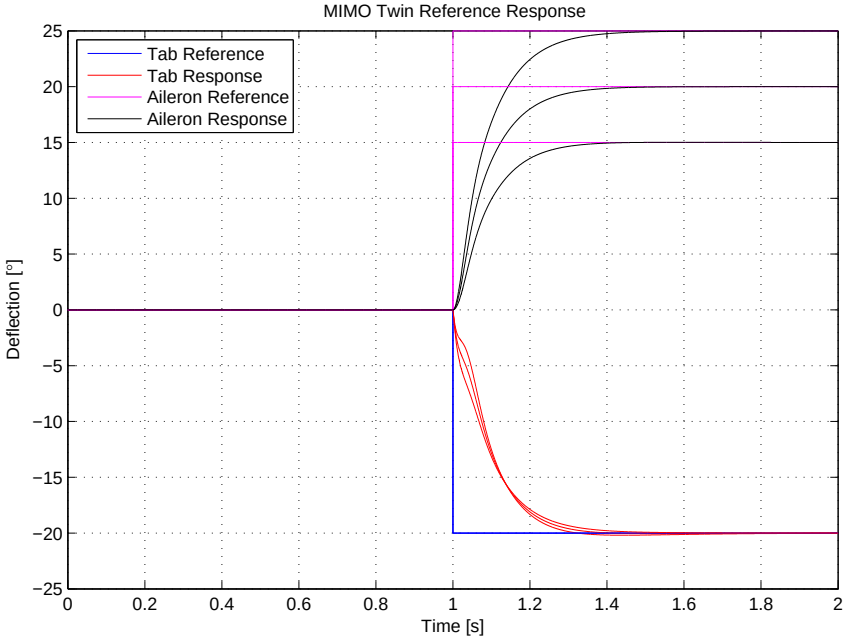

Figure 5.10 – Reference Input Response

5.5 Disturbance Rejection

Disturbance rejection and sensitivity is focussed on a specific disturbance that is expected to enter the system. The major disturbances expected in the tab-aileron configuration is hinge moments resulting from extraneous aerodynamic effects. For the full-state control model this corresponds to input disturbances.

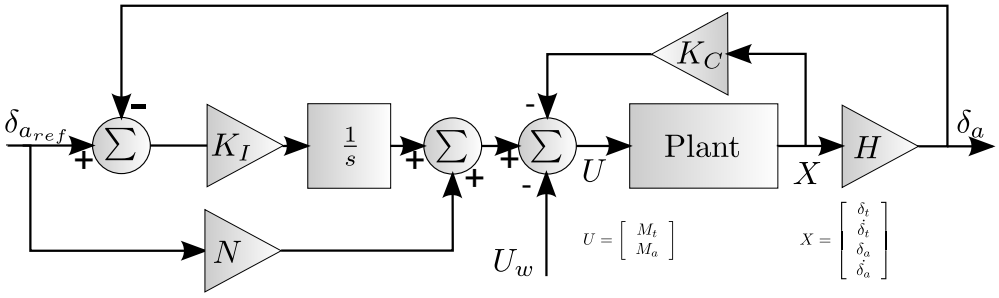

Figure 5.11 – MIMO Input Disturbance

For the MIMO case with a single reference, it can be shown that the sensitivity due to input disturbances, Figure 5.11, is described by rewriting in the s-domain as follows for a tab moment disturbance:

$$S_{input}(s) = \frac{H(sI - F + GK)^{-1}G_{W_t}}{1 + \frac{H(sI-F+GK)^{-1}GK_I}{s}} \tag{5.5.1}$$

$$G_{W_t} = \begin{bmatrix} 0 \\ \frac{1}{I_t} \\ 0 \\ 0 \end{bmatrix} \tag{5.5.2}$$

For an aileron moment disturbance, it is given by:

$$S_{input}(s) = \frac{H(sI - F + GK)^{-1}G_{W_a}}{1 + \frac{H(sI-F+GK)^{-1}GK_I}{s}} \tag{5.5.3}$$

$$G_{W_a} = \begin{bmatrix} 0 \\ 0 \\ 0 \\ \frac{1}{I_{at}} \end{bmatrix} \tag{5.5.4}$$

and for an output disturbance:

$$S_{output}(s) = \frac{1}{1 + \frac{H(sI-F+GK)^{-1}GK_I}{s}} \tag{5.5.5}$$

The case where two reference inputs are given the system can be considered two separate transfer functions and the sensitivity functions can be considered through the

following matrices derived form the matrices defined in §5.4:

$$H_t = \begin{bmatrix} 1 & 0 & 0 & 0 \end{bmatrix} \tag{5.5.6}$$

$$H_a = \begin{bmatrix} 0 & 0 & 1 & 0 \end{bmatrix} \tag{5.5.7}$$

$$\begin{bmatrix} N_{U_t} & N_{U_a} \end{bmatrix} \equiv NU \tag{5.5.8}$$

$$\begin{bmatrix} N_{X_t} & N_{X_a} \end{bmatrix} \equiv NX \tag{5.5.9}$$

For the case where tab an aileron references are introduced, the two hinge moment disturbance sensitivity functions are then broken up into tab coupling to tab, tab coupling to aileron, aileron coupling to tab and aileron coupling to aileron:

$$S_{input_{Tab2Tab}}(s) = \frac{H_t(sI - F + GK)^{-1}G_{W_t}}{1 + \frac{H_t(sI-F+GK)^{-1}G(N_{U_t}+KN_{X_t})K_{It}}{s}} \tag{5.5.10}$$

$$S_{input_{Tab2Ail}}(s) = \frac{H_a(sI - F + GK)^{-1}G_{W_t}}{1 + \frac{H_a(sI-F+GK)^{-1}G(N_{U_a}+KN_{X_a})K_{Ia}}{s}} \tag{5.5.11}$$

$$S_{input_{Ail2Tab}}(s) = \frac{H_t(sI - F + GK)^{-1}G_{W_a}}{1 + \frac{H_t(sI-F+GK)^{-1}G(N_{U_t}+KN_{X_t})K_{It}}{s}} \tag{5.5.12}$$

$$S_{input_{Ail2Ail}}(s) = \frac{H_a(sI - F + GK)^{-1}G_{W_a}}{1 + \frac{H_a(sI-F+GK)^{-1}G(N_{U_a}+KN_{X_a})K_{Ia}}{s}} \tag{5.5.13}$$

The sensitivity functions can now be visualised in the frequency domain depicting the effect of disturbances on the system. For sensitivity, the estimated models form 30 to $50\ ms^{-1}$ is presented to show consistency.

For the aileron-only reference controller the system output, δ_a, seems to be sensitive to tab moment disturbances much more that aileron moment disturbances, Figure 5.12. The maximum sensitivity is also located around the system cut-off frequency similar the positive feedback scenario seen in the tab only control. The FSF controller however has the advantage that it shows low sensitivity at both high and low frequencies. The FSF controller with concurrent tab and aileron reference inputs show the lowest overall sensitivity over all the regions as well as having low sensitivity at high and low frequencies, Figure 5.13.

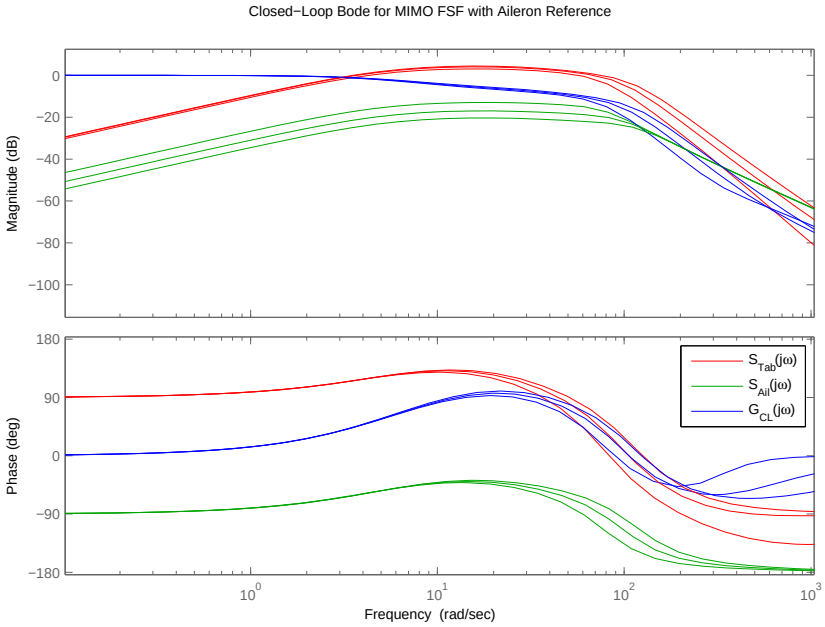

Figure 5.12 – Disturbance Sensitivity for an Aileron Reference Only

.

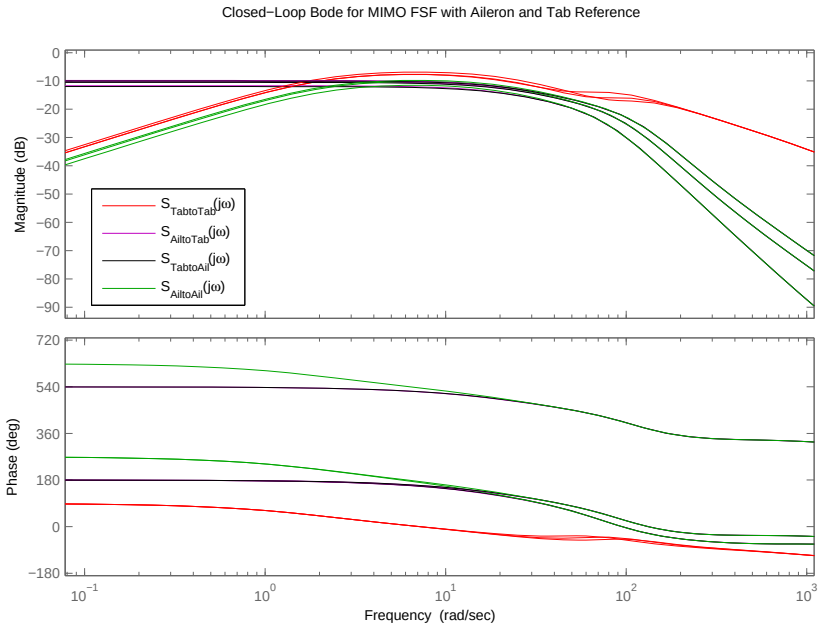

Figure 5.13 – Disturbance for Concurrent Aileron and Tab References

.

5.6 Noise Suppression

Noise in this control application is primarily resultant from output measurement noise. These outputs are used to reconstruct the system states feeding the noise back into the system. The effect of differentiation to reconstruct the rate states are taken into account.

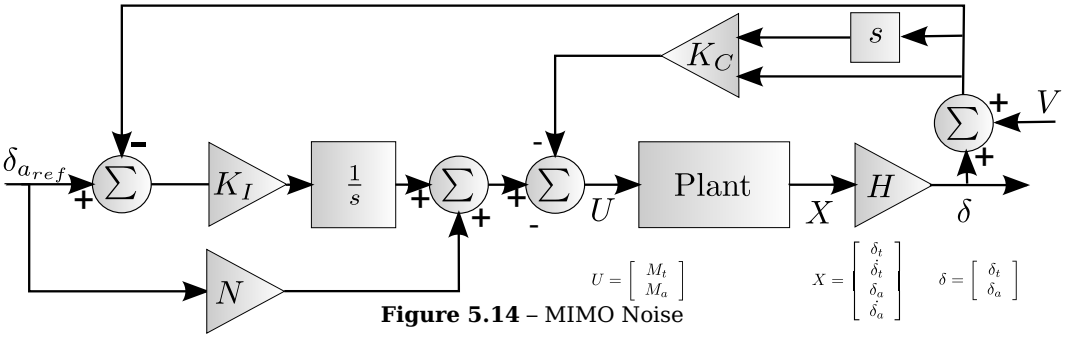

Figure 5.14 – MIMO Noise

The FSF noise analysis is somewhat more involved. Consider noise entering on the states as in Figure 5.14. It follows that:

$$\dot{X} = (F - GK)(X + V) \tag{5.6.1}$$

$$Y = HX \tag{5.6.2}$$

The transfer function equivalent then becomes:

$$\frac{Y(s)}{V(s)} = H(sI - F + GK)^{-1}(F - GK) \tag{5.6.3}$$

Then since the angular position is differentiated:

$$V(s) = \begin{bmatrix} 1 & 0 \\ s & 0 \\ 0 & 1 \\ 0 & s \end{bmatrix} \begin{bmatrix} v_t(s) \\ v_a(s) \end{bmatrix} \tag{5.6.4}$$

The the effect of each noise on the tab and aileron response can then be considered independently by substituting H with H_t or H_a. There are four distinct effects; the sensitivity of the tab to tab noise, the sensitivity of the tab to aileron noise, the sensitivity of the aileron to tab noise and the sensitivity of the aileron to aileron noise. In the more specific case when the augmented integrator is used, the augmented states can be used to determine the noise suppression characteristics. In the case of the multi reference inputs, an integrator can be added around the tab or aileron response considering one output and one noise source at a time. The output then becomes:

$$\begin{aligned} Y(s) &= H_t(sI - F + GK)^{-1}(F - GK)V(s) \\ &+ H_t(sI - F + GK)^{-1}G(N_{U_t} + KN_{X_t})\frac{(R(s) - Y(s))K_{It}}{s} \end{aligned} \tag{5.6.5}$$

since R the reference is independent of noise and the second term of Equation 5.6.5 is a scalar transfer function of Y if H_t or H_a is used:

$$Y(s)\left(1 + H_t(sI - F + GK)^{-1}G(N_{U_t} + KN_{X_t})\frac{Y(s)K_{It}}{s}\right)$$
$$= H_t(sI - F + GK)^{-1}(F - GK)V(s) \tag{5.6.6}$$
$$Y(s) = \frac{H_t(sI - F + GK)^{-1}(F - GK)V(s)}{1 + H_t(sI - F + GK)^{-1}G(N_{U_t} + KN_{X_t})\frac{Y(s)K_{It}}{s}} \tag{5.6.7}$$

The exact same applies for the aileron noise if H_a, N_{U_a}, N_{X_a} and K_{Ia} is substituted in the above equation.

The FSF controllers were generally less sensitive to disturbances however seem to show more noise sensitivity here. It can be seen that for the FSF aileron reference-only case in Figure 5.15, the system has little noise rejection characteristics due to rate feedback from derived aileron and tab deflection measurements. If the rates were measured, the system would have shown $40\ dB$ per decade cut-off in noise. The concurrent tab and aileron reference MIMO case seen in Figure 5.16, shows initially good noise suppression but does not show the rejection at high frequency due to the derived sensor measurement as noted for the aileron reference-only case. The cross coupled noise states from tab to aileron and aileron to tab tend to show the $40\ dB$ per decade rejection.

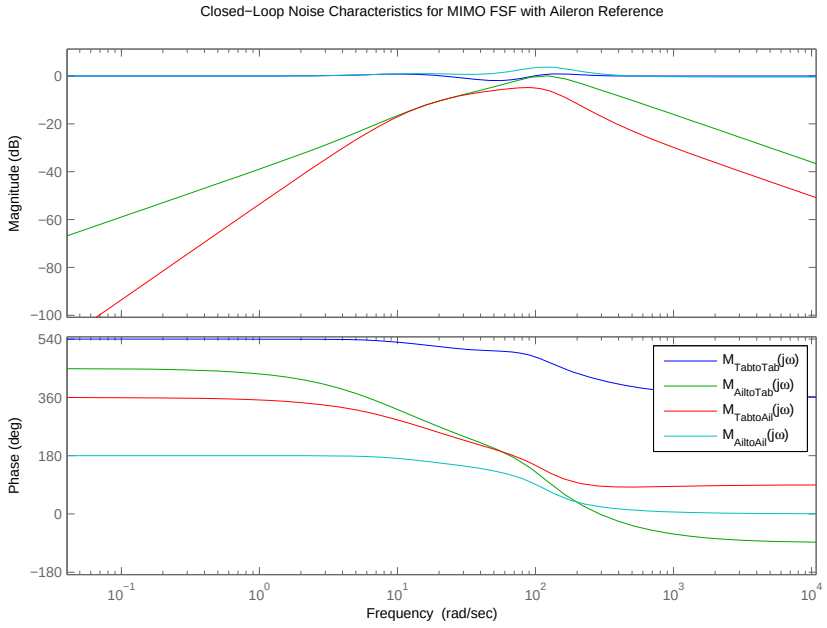

Figure 5.15 – MIMO Noise Transmission for Aileron Reference

.

Typically, there is a trade-off between noise immunity and disturbance rejection since disturbance rejection is generally achieved by high loop gains ensuring low sensitivity to disturbances. Conversely, high loop gains feed noise back and increasing its gain

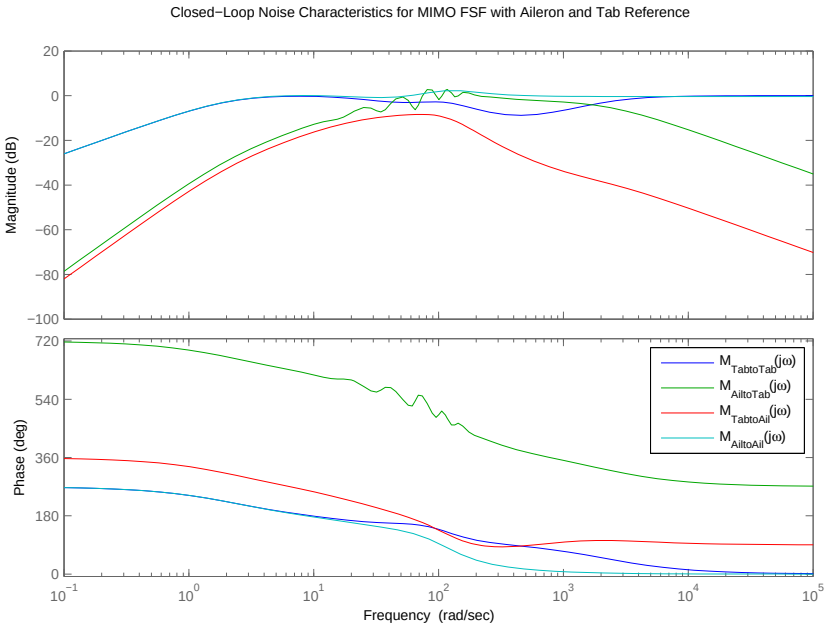

Figure 5.16 – MIMO Noise Transmission for Aileron and Tab Reference

.

resulting in poor noise rejection, [16]. Seen here, the FSF controllers tend to only have about $40\ dB$ per decade noise rejection even if the rates were not derived. Whereas the classical controllers tend to show high cut-off of up to $80\ dB$ per decade.

5.7 Actuator Requirements

The input requirements were considered in the FSF LQR control design. However, it was found that some inventive tweaking of the weights was necessary in order to achieve an acceptable response. The result is that the response is not optimal in the global sense when considering input and state error. It can be considered more an optimal for the desired response. From the point where the desired response is achieved, additional relative weighting can now be used if it were desired to reduce input requirements but at the detriment of the response quality.

The actuator requirements for the concurrent tab and aileron reference inputs is a more complicated scenario. Consider, the case when the tab remains effective and is commanded in such a way that the resultant aileron hinge moment is zero. This is the same scenario as the tab-only actuation scenario. The difference is that the dynamics are controlled by the FSF controller and this means that there will be transient actuator requirements. The non-optimal case when the tab is saturated or becomes ineffective, the aileron actuator will need to apply a great deal of torque. This has definite aileron actuator implications. Additionally, the dynamic torque also needs to be provided. The true extent of the torque requirement in this case is determined by the effective tab range and the required aileron range.

For the FSF LQR case where the tab and aileron are actuated, the actuator currents are presented in Figure 5.17 for a representative step. The consideration of the theoretical data showed that the dynamic torque requirements for the tab are of the order of 300% more than the steady-state torque much like those of the negative feedback controller in the tab only actuation scenario. The dynamic requirements for the aileron are much larger, in the order of 700%, and it is mostly dependent on the weighting chosen for tab and aileron inputs in the LQR process. If dynamic performance is sacrificed the dynamic torque requirements can be reduced even further.

The controller based on the FSF controller with concurrent tab and aileron reference inputs are considered according to the two scenarios below. The first scenario the steady-state optimal orientations are used defined by the orientation of tab that will result in zero aileron hinge moment for a desired aileron deflection. Figure 5.18 shows the command and the response of the controller with reference commands for the tab and aileron. Through simulation, it became apparent that depending on the magnitude of the feedforward term and the step size the tab actuator will tend to saturate instantaneously on the initial peak however putting a saturation limit in shows no apparent decrease in the performance. The saturation is a numerical anomaly due to the step command. In the case where the tab is limited to an angle smaller that required to make the aileron hinge moment zero, the applied torque can be seen in Figure 5.19. It is clear that the amount of excess aileron hinge moment required is dependent on the integrator gain and therefore choosing a larger integrator gain and smaller feedforward will reduce the excess aileron hinge moment required above the steady state value. Further, it is visible that the required aileron steady-state hinge moment is an order larger than when the tab was effectively reducing the hinge moment. The direct implication is that the feedforward and integrator gains can be chosen such that the aileron hinge moment maximum is equal to the steady-state value.

An important additional constraint on the actuators is that they must be able to provide the necessary hinge moment at the maximum deflection rate which is dependent on the step command size. It seems to be common practice to limit the aileron rate in the provided AIRBUS models to 40° per second and therefore the step command can

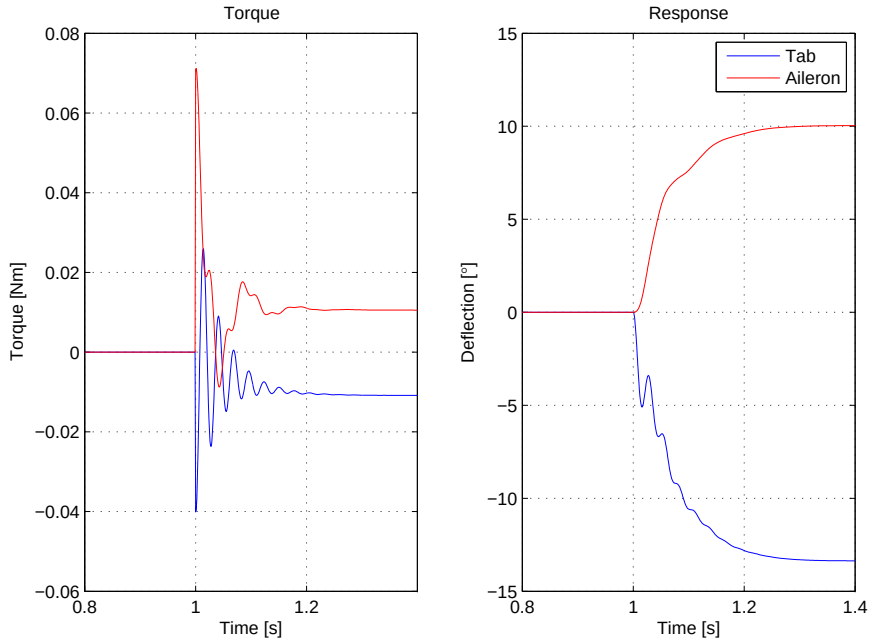

Figure 5.17 – FSF Tab and Aileron Actuator Requirements at $\alpha = 5°$, $V = 50ms^{-1}$ and $10°$ Step Size

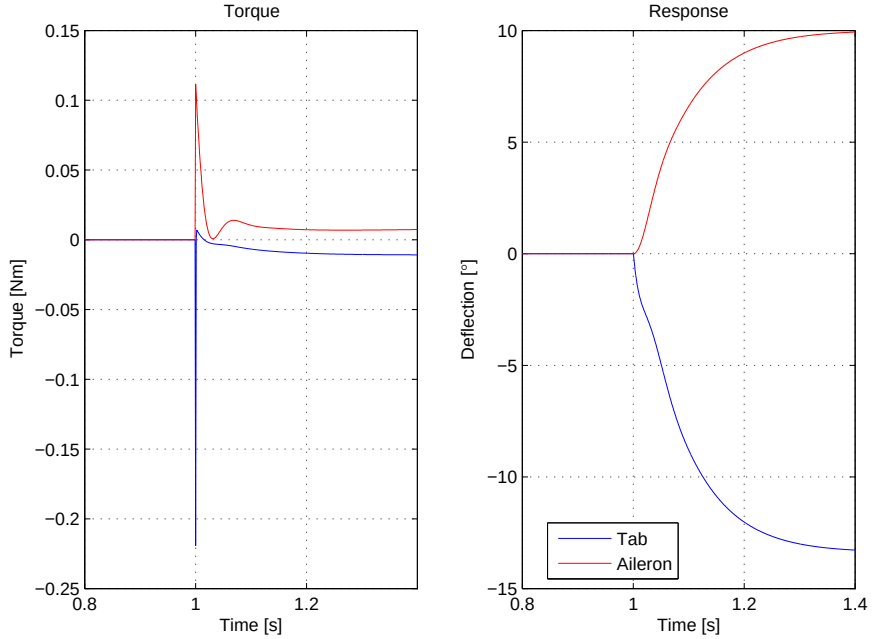

Figure 5.18 – FSF Tab and Aileron Reference Actuator Requirements at $\alpha = 5°$, $V = 50ms^{-1}$ and $10°$ Step Size

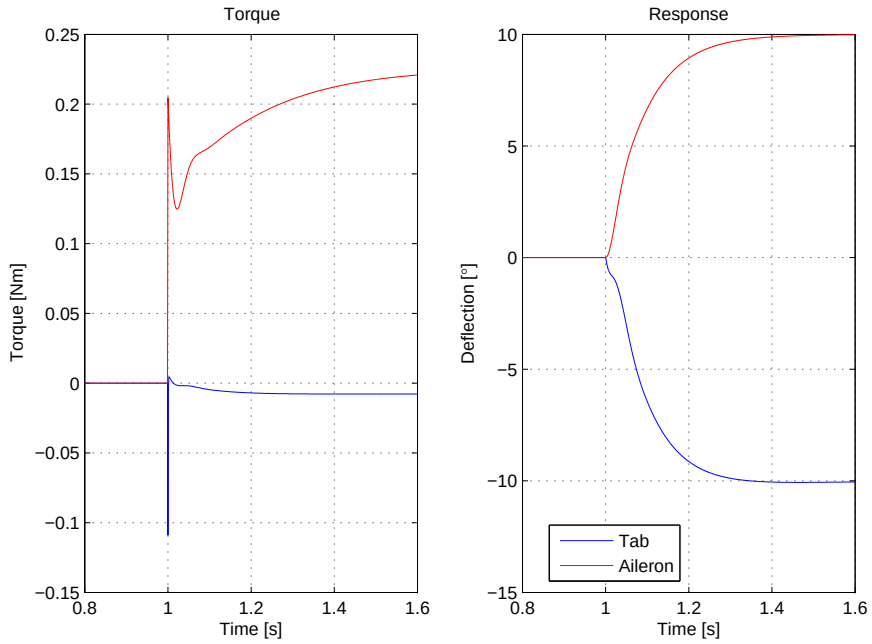

Figure 5.19 – FSF Tab and Aileron Reference Actuator Requirements at $\alpha = 5°$, $V = 50ms^{-1}$ and $10°$ Step Size with Limited Tab Deflection

be considered a rate limited reference. This mitigates the initial peak observed when a step command is given. The response to a rate limited reference is shown in Figure 5.20. It can be seen that the initial peak torque requirement is significantly reduced for the aileron actuator and mitigated for the tab actuator. Clearly the steady-state torque is maintained the same as presented in Figure 5.18.

When considering the dynamic limitations of the system, in the FSF LQR case the dynamic limitations are subject to actuator limitations. The dynamics can be made as quick as desired based on the actuator moment allowance and performance. Therefore, the dynamic response is only limited by the allowed aileron and tab actuator power profile. The power is the limiting factor since the torque must be available at the correct angular rates. The designer can therefore constrain the actuator torque by weighing the system inputs in the LQR calculation process as required. The actuator requirements can range anywhere between only a tab actuator being used to the other end of the spectrum where only an aileron actuator is used. The reason why nearly any dynamic performance can be achieved is that both the aileron and tab is actuated. The limitation to the response is no longer the aerodynamic factors and therefore the tab to aileron transfer function but it is the aileron and tab actuators. But, the optimal control method provides an objective method for weighing between the extremes.

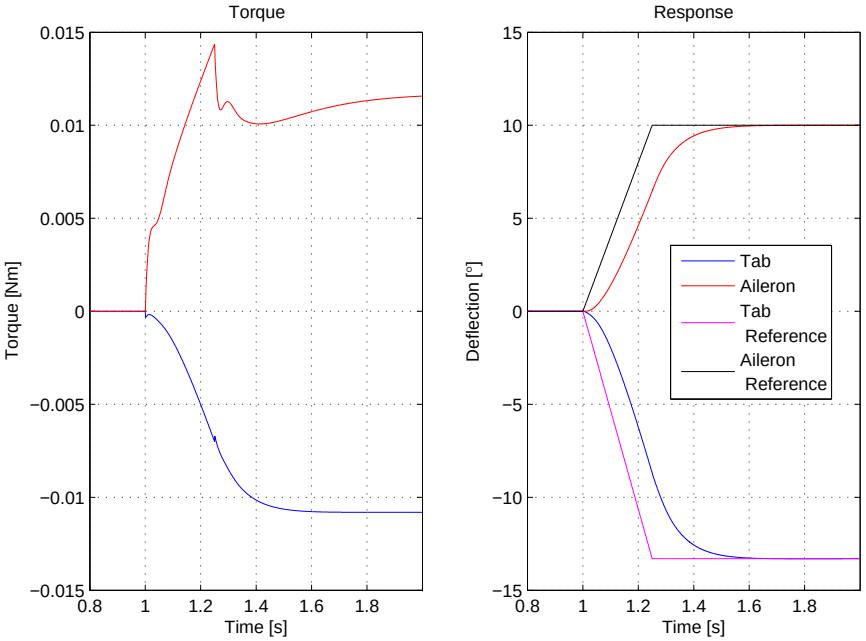

Figure 5.20 – MIMO FSF Tab and Aileron Actuator Requirements at $\alpha = 5°$, $V = 50ms^{-1}$ and $10°$ Rate Limited Reference

Chapter 6

Practical Implementation

Data on dynamic behaviour of tab assisted control surfaces are not freely available in a generalised format. It is therefore imperative that at least a qualitative evaluation of the model and control is necessary. The objective is to measure the macroscopic characteristics of the model and controller.

The characteristics are measured from a model constructed and placed in a simulated environment such as wind tunnel. The model will provide an indication if the method through which the theoretical model is determined is adequate for predicting system behaviour. The experimental setup and limitations are discussed taking into account available resources.

To ensure the model characteristics are captured accurately, data logging and sensing is implemented. The data collection and logging are also summarised and implications thereof are discussed. The data logged forms the basis for the linear models developed in §7. The hardware required for each controller implementation is also discussed followed by the selection and implementation of this hardware. The hardware is supported by the necessary software developed specifically for this application. The chapter is then concluded with an overview of the hardware and software development process.

6.1 Wind Tunnel Parameters

This section discusses the limiting factors of the wind tunnel and gives an overview of its capabilities. The geometric limitations imposed by the wind tunnel on the model is derived from the wind tunnel parameters. The model dimensions are therefore based on the wind tunnel limitations rather than specific scaling requirements. The model does not match any specific Reynolds number of an Airbus A330 wing model or the exact dimensions. The model is based on the same aileron chord ratio as optimised by Jaquet [1] and the NACA 23012 foil profile. The model does also not take into account the three dimensional airflow effects but will rather consider the section two dimensional and mitigate three dimensional effects. This is convenient since this condition is assumed in the aerodynamic data used in the theoretical model development. As mentioned previously, the primary objective of the experimental setup is to confirm the theoretical model characteristics for this setup thereby allowing at least partial extension to other geometries.

The logical testing environment for the setup is a wind tunnel since it is available. There are however certain practical considerations when doing a wind tunnel test. The

wind tunnel is a low-speed, atmospheric, non-circulating model with the specifications described in Table 6.1.

Wind Tunnel Specs	
Height	1,2 [m]
Width	1,0 [m]
Cross Sectional Area	1,2 [m^2]
Airspeed	0 - 100 [ms^{-1}]
Density	Atmospheric
Flow Blockage Tolerance	8 %

Table 6.1 – SUN Wind Tunnel Specifications

The parameters of the wind tunnel restricts the maximum size of the model and the range of angle of attack that can be achieved. Firstly, the increase in maximum camber and the forward projected area when increasing angle of attack increases blockage which limits the chord and/or span of the setup. Further, the airspeed is a limitation on the testing range but the primary limitation is the actuator capabilities. The density of the flow can also not be controlled so the dynamic pressure range is limited by the ambient conditions of the testing day. The resulting model characteristics are presented in Table 6.2.

Wind Tunnel Operation	
Blocked Area	0,096 [m^2]
Model Span	0,6 [m]
Max Camber	0,08 [m]
Max Chord (NACA 23012)	0,4 [m]
Max Angle of Attack	10°
ρ_{air}	Atmospheric
R_e	$\approx 9,3 \times 10^6$

Table 6.2 – SUN Wind Tunnel Operations

The geometric dimensions resulting are small due the limits in blockage. Thereby, the span of the model is limited in order to allow the necessary chord to ensure the setup is manufacturable. This limited span will most likely result in increased inaccuracy since the effects of the end plates could be more noticeable on a smaller span.

Further, some aspects of the wind tunnel are non-ideal since the flow is restricted to a limited cross section. However, this effect of horizontal buoyancy, otherwise known as solid blockage, is generally negligible when working with wing aerofoils [20]. A summary of the correction factors associated with two dimensional wind tunnel testing is summarised in §A.2. It is advantageous to use a very small wing chord to tunnel height ratio in order to maintain uncorrected effects as small as possible. By using rough estimates of solid blockage and wake blockage from lift and drag coefficient in the correct order of magnitude the velocity correction comes to around 1%. This is the convenient result of using a small wing chord removing the need for adjustment of the results. With the wind tunnel limitations considered, the model parameters are fixed and further stages of experimental design is conducted.

6.2 Mechanical Design of the Test Section

This section focuses on the construction, geometry and layout of the test section placed in the wind tunnel. The construction techniques used for the tab-aileron model is summarized and an overview of the mechanical layout is given, see Figure 6.1. Furthermore, the effect of non-idealities is discussed in this context. In tandem, the geometric layout is also explained and mention is made of the limitations imposed on it due the wind tunnel characteristics. A brief account of the construction methods and materials used is also given.

Maximum limitations are imposed on the experimental setup due to the wind tunnel operational characteristics, summarised in Table 6.2. Minimum limitations are imposed by the available construction techniques and the minimum size of each section that can be made accurately.

As far as construction methods are concerned, the wing is constructed of expanded polystyrene foam core with a composite E-glass epoxy outer skin, see Table 6.3. Along with this, stringers are placed inside the core to ensure adequate strength and rigidity of the model as shown in Figure 6.1. This construction method is used since the lead time of construction is relatively short and the computer numerically controlled (CNC) foam cutting process is cost and time effective compared to multi-axis CNC milling.

Skin	E-Glass: 1 layer of 105 g/m^2 & 1 layer of 205 g/m^2 Ampreg 21 Epoxy Resin System
Stringers	Steel 1080 Cold Drawn ⌀8 mm
Core	Sagex 32 kgm^{-3} expanded polystyrene foam

Table 6.3 – Model Physical Characteristics

When considering the limitations of the construction process, it is found that the minimum surface that can be made is limited in span to chord ratio. The process of lamination with E-glass is dependent on the rigidity of the foam core. A long, thin foam core cannot maintain shape while being laminated and a greater risk of warping is present. The tab dimensions are therefore increased from the optimal geometry which was presented by Jaquet [1]. The tab size is specified to be 3,0 % of the total chord. This value is practical when designing for a full-scale commercial craft however on this scale it is not practical. The model tab chord ratio is therefore extended to 7,5 % of total chord. This gives more practical dimensions for construction. The implications of the larger tab is that the tab would be more effective at moving the aileron to the desired final position however there would be a loss in total lift of the aileron. This does not drastically affect the model since the theoretical model comparison will be done for the adjusted model instead of the geometrically optimal model.

Structural rigidity is an important aspect the manufacturing process since it affects the modes of motion of the model. It is important to construct the model as stiffly as possible limiting the mechanical deformation of the surfaces due to the aerodynamic forces. Even more detrimental would be flutter of the model since the structural vibration or oscillation of the surfaces will affect the aerodynamic characteristics. Generally, the flutter of a scale model would be at higher frequency than that of a full scale model due to its smaller dimensions and therefore shorter fundamental wavelength. There are various other factors that affect flutter such as geometric cross section, lift distribution etc. It is ensured that the model does not flutter by increasing the model stiffness with

the steel stringers and a thick composite layer. The investigation of structural flutter and the flutter conditions are not the primary concern and it is mitigated on an ad-hoc basis.

The actuators selected in §6.3.2 are embedded into the wing and aileron. These provide actuation through the connection rods and servo horns minimising the extraneous aerodynamic effects as seen in Figure 6.1. The actuation points are placed at the centre of the aerodynamic surfaces in order to minimise the mechanical deformation due to the application of the hinge moment at a single point.

The strengthening stringers are placed in the main wing section and serves as attachments to the end plates. The aileron and tab are supported by a four point and a three point hinge respectively. The hinges are plain bearings. The tab hinge axis is carbon fibre and the aileron hinge axis is hardened mild steel. The hinges are not ball bearing based due to the limitations in space and the need to maintain a simple design to promote better manufacturability. The adverse effect of these hinges are that their friction is strongly coupled to the radial forces. This in turn results in dynamic changes in friction as the aileron and tab is deflected. The deflections causes increased lift and drag on the surfaces increasing the radial force and therefore friction. This friction may be hard to characterise and will be loosely angular position dependant. The friction would also change with dynamic pressure as the total resultant aerodynamic forces increase. These effects will become apparent when the practical model is compared to the theoretical model in §7.4.

With a fixed aerodynamic design, the control system hardware can be selected and the necessary model adaptations made. The final actuator selection can be done based on the hinge moment requirements as discussed in §6.3.2.

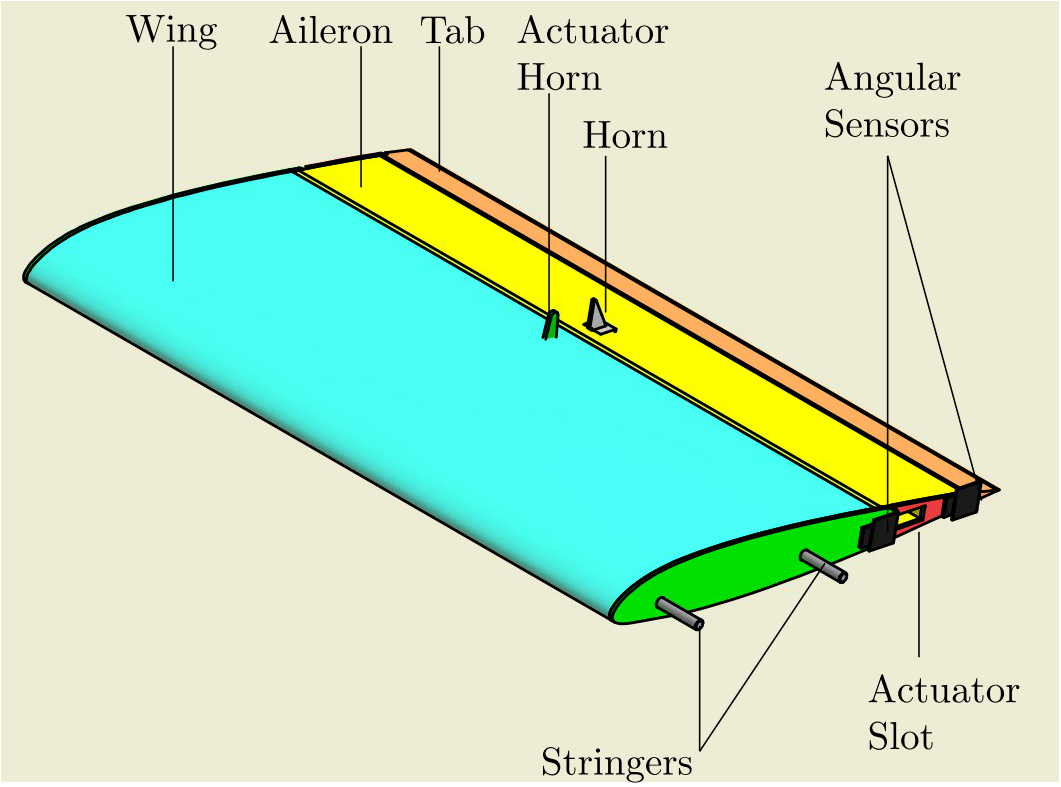

(a) Three-Dimensional CAD Model

(b) Manufactured Model

Figure 6.1 – Experimental Setup in Wind Tunnel

6.3 Controller Hardware

This section gives an overview of the hardware development aimed at the implementation of system identification and control. First, the design of the interface and driver unit is overviewed. This covers the individual interfaces which are briefly explained along with an overview of the necessary actuator drivers. This is then followed by the selection of the appropriate actuators which will be adequate for system identification and control.

6.3.1 Driver and Interface Unit

Throughout, the system sensor data is used as feedback for control which makes is convenient to design a single set of hardware which can satisfy all the logging and control requirements. The controller hardware and an overview of the development process is discussed here. This process of development is undertaken by first identifying the interfaces needed for the actuators and logging after which the correct components are selected for each interface. The interfaces are then integrated onto a single printed circuit board (PCB) with a micro-controller controlling these interfaces as shown in Figure 6.2. Furthermore, the control algorithm was implemented on the hardware. A general overview of this integration process with important considerations is also given.

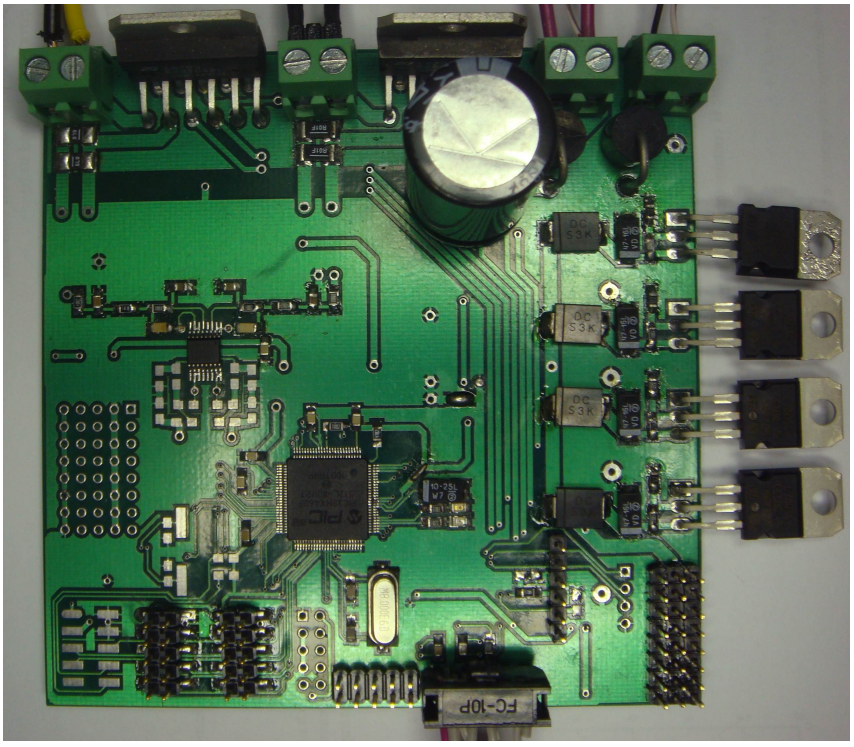

Figure 6.2 – Interface PCB

For the three control strategies, there are three different actuator outputs required. The first method of servo actuation relies on the built in hardware of the servo actuator and therefore the interface must comply with that of the servo. Therefore a pulse-width

modulation (PWM) channel is allocated to the servo control method which acts as the angular reference to the servo. Additionally, a regulated power supply is required for the servo and it was also allocated. The regulated supply and the PWM channel allows the controller to command the tab to the desired angle and the servo hardware will ensure that the angle is reached.

To achieve deflection rate control, motor voltage control is done over the servo motor. This is effectively a first order rate actuator. The voltage control also needs to be bipolar in order to achieve bidirectional actuation. The most convenient interface is therefore a H-bridge driver. The bridge can be switched in either unipolar or bipolar mode depending on the voltage following characteristics required. In short for capacitive and inductive load the bipolar switching would result in quicker mean voltage following. Details are discussed in [21]. The H-bridge driver is all that is needed in order to achieve rate actuation.

Torque control on the other hand requires motor current control. Motor current control is achieved indirectly through motor voltage control and current feedback. The voltage can therefore be controlled with the H-bridge with the addition of current sensing to close the current loop. This could not be done in an open-loop fashion from current required to voltage command, since the additional rate feedback or back electromotive force (EMF) would result in inaccurate and varying current following characteristics. For all intent and purpose, the current loop is considered at least ten times as fast as the fastest system pole and is therefore neglected in controller design, detail of which is discussed later on. The current sensor and the H-bridge combination therefore acts as the current source required for torque control.

For an H-bridge two to four PWM channels are needed each. The current sensing capabilities require an analog-to-digital converter (ADC) to interface with the microcontroller. The total for actuator interfaces are summarised in Table 6.4.

In order to achieve control and system state logging, sensing of the system states are needed. For the controllers, it is important that all states are known since full-state feedback as well as rate feedback is used. There are various transducer/sensor combinations for sensing angular displacement and rate. These include optical encoder, resistive angular sensors, hall-effect sensors and rate gyros. It was found that the most accurate, simple and cost effective solution is the hall-effect sensors. The sensor uses serial peripheral interface (SPI) bus and has an angular resolution of twelve bits. With a sample rate of 1 kHz to 11 kHz and a noise standard deviation of $0.03°$, the angular rate measurement can be derived from the angular position measurement. This removes the need for a second set of sensors to sense angular rate. A SPI interface will therefore suffice for the sensing of the angular states of the tab and aileron.

Specification	Torque control		Deflection Control	Rate Control	Total Interfaces
	Tab	Aileron	Tab	Tab	
Driver	H-Bridge 5A-6V 2×PWM	H-Bridge 2A-6V 2×PWM	Supply 1.4A-6V 1×PWM	H-Bridge 2A-6V 2×PWM	2×H-Bridge 2A- & 5A- 6V 4×PWM
Current Sensor	1×ADC	1×ADC	1×ADC	1×ADC	2×ADC
Angle Sensor	SPI Hall Effect Sensor	SPI Hall Effect Sensor	SPI Hall Effect Sensor	SPI Hall Effect Sensor	2×SPI Hall Effect Sensor

Table 6.4 – Actuator Drivers and Sensors

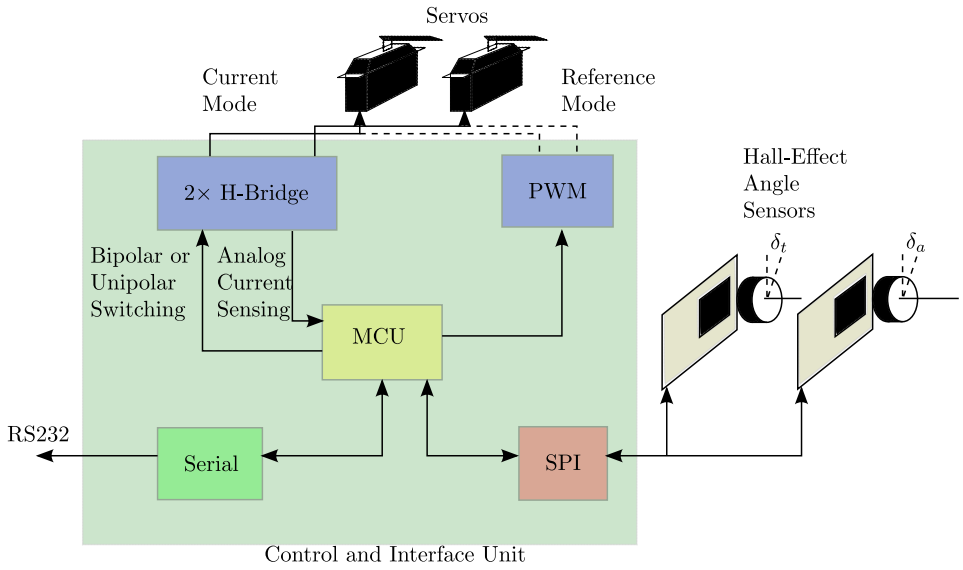

Figure 6.3 – System Interfaces

The high level schematic of the control hardware is displayed in Figure 6.3. From this it can be seen that the microprocessor interfaces with a personal computer (PC) through a serial interface at 1 MBaud. This is sufficient to log all system commands at 1kHz. This however required non-standard serial communications interface with the PC since the high baud rates are not supported by the Microsoft Windows based PCs. A FTDI [1] based serial to USB dongle was used and the graphic user interface (GUI) is coded to interface through the system drivers rather that virtual comport drivers.

Furthermore, the current is monitored in shunt with the actuators allowing for accurate bidirectional current measurement. The current sensor measurements are buffered by third order active Butterworth filters meaning the PWM frequency current oscillations are filtered out. It also acts as an anti-aliasing filter for the ADC.

The PWM channels are interfaced directly with the H-bridge discrete packages allowing for both bipolar and unipolar switching. The PWM signals are also connected for optional use as reference to the tab servo in servo based control mode. The PWM bridge is switched at 10 kHz to ensure good frequency separation between the voltage control and the rest of the system dynamics.

The hall-effect sensors are connected to the SPI bus. Two chip select lines are carried along with the SPI bus to alternately select the angle transducers that must be polled.

The controllers are implemented on the hardware and is coded in C. The control hardware accepts a series of commands from the Windows based GUI enabling and disabling the controllers. Additionally some physical command limitations are coded on the hardware such as deflection angle limitations, maximum voltage limitations and maximum current limitations.

Within the general outer control structure there are some necessary inner loops not considered part of the overall control design. These loops are considered part of the hardware implementation and they are relatively specific to the actuator type. These

[1] Future Technology Devices International Inc.

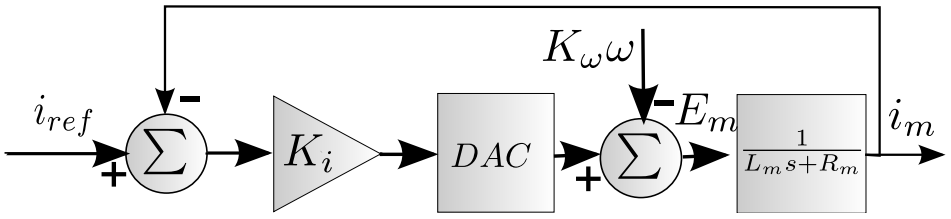

Figure 6.4 – Current Control Topology

loops have been mentioned in terms of the actuation interfaces and they are voltage control, current control, rate control and torque control.

Voltage control is achieved by using the basic concept of pulse width modulation. In brief the pulse width is varied to vary the mean voltage. This is implemented with an H-bridge in conjunction with a RC filter circuitry in order to smooth the pulsed voltage to the mean value. The RC filter is not the most efficient method of achieving this, but it was used since the minimum pulsed voltage was double the maximum servo voltage, 12 V, which caused excessive current in the motor coils. The voltage control is primarily open-loop and is calibrated to provide accurate voltage output. The voltage control is effectively a digital-to-analog converter (DAC).

Current control is achieved by adding a secondary loop to the voltage output. The current sensing is used as the feedback loop for the current control. The loops are realised with a high gain proportional controller. Figure 6.4 shows the feedback of current measurements to the current reference with a proportional controller. The motor is a permanent magnet DC brush motor and the standard model is used for the motor partially shown in Figure 6.4 [16]. The resultant motor current relation is given by:

$$\frac{I_m(s)}{E_m(s)} = \frac{1}{L_m s + R_m} \tag{6.3.1}$$

The only addition to the motor model is the RC filter used to filter the PWM supply coming from the H-bridge. The transfer function for the first order RC filter is easily shown to be:

$$E_m(s) = \frac{1}{RCs+1} E_{DAC}(s) \tag{6.3.2}$$

The DAC voltage is then:

$$E_{DAC} = (i_{ref} - i_m)K_i + K_\omega\omega \tag{6.3.3}$$

The only assumptions are that the RC constant of the filter and the $\frac{L}{R}$ constant of the motor is sufficiently small that it can be neglected in terms of the control dynamics of the system. Firstly, the RC constant can be chosen to be at around 1 kHz and the LC constant is measured and found to be at least of the order of 10^{-4}. This provides fast non-dominant current control of the actuator.

Rate control is achieved by applying a voltage to the actuator causing it to settle at a specific angular velocity, Figure 6.5. As seen previously, the torque is directly related to the motor current. In turn, the angular velocity is related to the torque through the

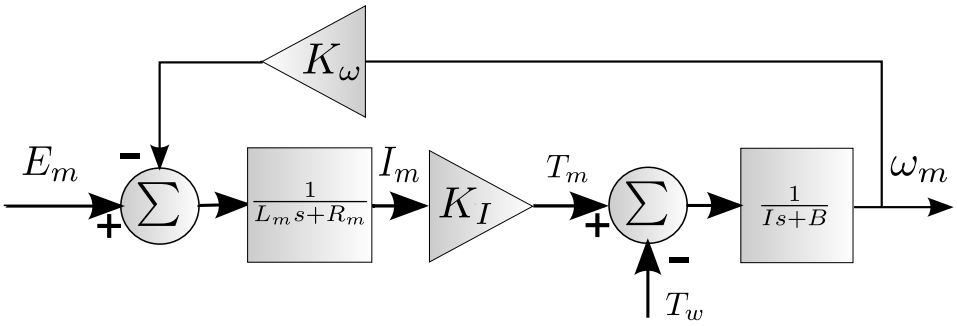

Figure 6.5 – Brushed DC Motor Model

kinematics of the mechanical system, simply:

$$T = I\dot{\omega} + B\omega \tag{6.3.4}$$

$$\frac{\omega(s)}{T(s)} = \frac{1}{Is+B} \tag{6.3.5}$$

Here I designates the equivalent moment of inertia of the mechanical system and B designates the damping coefficient of the system. The resultant torque is designated by T. The combination of the kinematics, the torque dynamics and the back EMF, see Figure 6.5, results in the complete motor dynamics as follows:

$$\omega_m(s) = (\omega_m(s)k_\omega + E_m(s))\left(\frac{1}{L_m s+R_m}\frac{1}{Is+B}\right)K_T \tag{6.3.6}$$

$$\frac{\omega_m(s)}{T_w(s)} = \frac{\left(\frac{1}{L_m s+R_m}\frac{1}{Is+B}\right)K_T}{1+\frac{K_T K_\omega}{L_m s+R_m}\frac{1}{Is+B}} \tag{6.3.7}$$

$$\frac{\omega_m(s)}{E_m(s)} = \frac{K_T}{(L_m s+R_m)(Is+B)+K_T K_\omega} \tag{6.3.8}$$

but with negligible inductance as noted previously [16],

$$\frac{\omega_m(s)}{E_m(s)} = \frac{K_T}{R_m(Is+B)+K_T K_\omega} \tag{6.3.9}$$

$$\frac{\omega_m(s)}{E_m(s)} = \frac{\frac{K_T}{R_m B+K_T K_\omega}}{\frac{R_m I}{R_m B+K_T K_\omega}s+1} \tag{6.3.10}$$

The angular rate response $\omega(s)$ is approximately a first order function of the voltage applied over the motor terminals, E_m. This is the origin of the first order approximation assumed in §2.6. One important omission of this model is the disturbance torque T_w, in which it is assumed that the system is robust enough to reject the disturbance. Consider for a moment the disturbance torque is present. Any discrepancy in the angular rate will result in a change in back EMF, $K_\omega\omega_m$ which will result in a change in motor current and therefore torque. This partially compensates for the disturbance torque. This built in feedback loop therefore automatically suppresses torque disturbances. This can be shown by the transfer function from disturbance torque $T_w(s)$ to motor torque is, ω_m by, Figure 6.5. Now consider Equation 6.3.7 and the sensitivity function is given by [16]:

$$S(s) = \frac{1}{1+\frac{K_T K_\omega}{L_m s+R_m}\frac{1}{Is+B}} \tag{6.3.11}$$

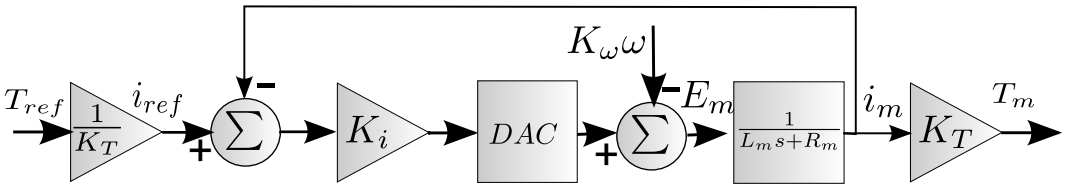

Figure 6.6 – Torque Control Topology

It can be seen from the transfer function that the terms that would increase the denominator and not the numerator is primarily the torque constant, K_T, and the rate constant, K_ω. This would result in better disturbance rejection.

Torque control is an open-loop extension of current control. Since torque is directly related to the motor current, by controlling the current with the previously described curent loop, the motor torque can be controlled directly. It is clear from Figure 6.5 that the motor torque is related to current through the torque constant, K_T. So, by adjoining the current control loop, K_T, and applying a gain correction at the input, $\frac{1}{K_T}$, the moment control topology in Figure 6.6 results. As noted, the open loop control is only acceptable if accurate information about K_T is available. This is generally the case since the motor can be properly characterised. The linearity of the torque-current relationship can be checked during this characterisation process. It was found that the actuator torque constant, K_T, is constant for the operational range, Figure **??**. Consequently, the current loop and actuator characterisation combination facilitates adequate torque control.

As a whole, the control hardware contains all the necessary components to facilitate accurate control and data logging. Throughout the hardware design process the control implications were considered and all hardware effect are kept to a minimum in terms of the higher level control algorithm. The current control and voltage control subsystems were kept non-dominant. Furthermore, the sensor sampling rates and noise was designed or selected in order to mitigate extraneous effects. The outcome is that the hardware can adequately control the system without introducing significant additional dynamics and non-idealities.

6.3.2 Actuator Selection

This section covers the actuator selection process for testing purposes. Initially, the actuator requirements are determined from simulated responses for each control topology. Actuators that satisfy the requirements are then selected based on published data. The actuators are then characterised in terms of its operating modus. Two characterisations are carried out, namely torque and response characterisation. Finally, specific considerations are made in terms of the operating range of the actuators.

For this experimental setup, hobby servos are used as actuators. The reason for this is that these components can provide the necessary bandwidth and torque in a compact form factor. These units are then placed inside the aerofoil sections, as mentioned, in order to actuate the control surfaces. The maximum torque requirements for each controller setup are determined from simulation of the maximum deflection at the extrema of the operating envelope. The three controller setups are torque control, angular deflection control and angular rate control. The maximum and steady-state values for the tab is presented in Table 6.5 and Table 6.6. For the aileron, the simulation is done as if the tab was not present this allows for the absolute maximum hinge moment to be determined, Table 6.6. It can be seen that the hinge moments are orders larger compared to tab hinge moments. The maximum and steady state values with the tab present are presented in Table 6.5 and Table 6.6. All the simulations are at maximum airspeed, 100 $ms^{-}1$, which results in maximum hinge moments.

Alpha	Aileron Deflection	Peak Actuator Torque Requirement [Nm]					
		Torque control		Deflection Control		Rate Control	
		Tab	Aileron	Tab	Aileron	Tab	Aileron
10°	-25°			-0,0764	-	-0,764	-
10°	25°			0,125	-	0,124	-
-5°	-25°			-0,108	-	-0,108	-
-5°	25°			0,0929	-	0,0929	-

Table 6.5 – Peak Actuator Torque Requirements

Alpha	Aileron Deflection	Continuous Actuator Torque Requirement [Nm]						
		Torque control			Deflection Control		Rate Control	
		Tab	Aileron	Aileron Only	Tab	Aileron	Tab	Aileron
10°	-25°	0,0805	0,00	-10,8	-0,0764	-	-0,764	-
10°	25°	-0,0880	5,25	17,9	0,125	-	0,124	-
-5°	-25°	0,0952	-1,75	-16,0	-0,108	-	-0,108	-
-5°	25°	-0,0945	0,00	13,3	0,0929	-	0,0929	-

Table 6.6 – Continuous Actuator Torque Requirements

From Table 6.6 it can be seen that the range of torque required is too large for a standard sized hobby servo. Since the hobby servos are based on DC motors, the main limitations in torque is due to the limitation of motor current and power dissipation. Therefore the applied current is limited to a fraction of the specified stall torque depending on the specific DC motor implemented in the servo. It follows that the maximum range of deflection will not be achievable over the range of angles of attack. The torques of $-1,75\ Nm$ at $-5°$ angle of attack and $5,25\ Nm$ at $10°$ angle of attack are

not achievable with modified analog servos, discussed below, given that the maximum attainable torque is about $\pm 1\ Nm$ at 50% stall torque.

The control strategies require three setups; a moment actuator setup, a deflection actuator setup and angular rate actuator setup. These three setups can be achieved with different hobby servo types. The angular deflection actuator can be achieved with a digital hobby servo with integrated PI controller. For this application, the analog hobby servos will not suffice since it does not have adequate command following. This is true since its feedback loop only has a proportional component. The rate actuator can however be achieved with an analog servo by removing the proportional feedback loop. The voltage controlled motor is therefore a first order rate actuator as shonw in §6.3.1. The servo then effectively becomes voltage controlled for which a feedback loop can be closed to become rate controlled. The moment actuator can be achieved by removing the internals of the analog servo and effectively controlling the current through the servo and thereby directly controlling the moment §6.3.1.

The choices of servos and their specifications are presented in Table 6.7.

Specification	Torque control		Deflection Control		Rate Control	
	Tab	Aileron	Tab	Aileron	Tab	Aileron
Manufacturer	HuiDa RC	HuiDa RC	HuiDa RC	-	HuiDa RC	-
Model	HD-1501MG	HD-1160A	HD-2213MG	-	HD-1160A	-
No-Load Period $[\frac{s}{60^\circ}]$	0,14	0,12	0.16	-	0,12	-
No-Load Velocity $[^\circ s^{-1}]$	429	500	375	-	500	-
Stall Troque [Nm]	1,70	0,27	0,46	-	0,27	-
Nominal Voltage [V]	6,0	6,0	6,0	-	6,0	-
Dimensions $(h \times w \times l)$ [mm]	$40.7 \times 20.5 \times 39.5$	$29 \times 11.7 \times 30.2$	$22.8 \times 12 \times 29.4$	-	$29 \times 11.7 \times 30.2$	-
Mass [g]	60	16	15.8	-	16	-
Misc	Metal Gears	Metal Gears	Metal Gears	-	Metal Gears	-

Table 6.7 – Actuator Specifications

The actuators are supplied with internal driving circuitry which could not be used due some fundamental limitations. The circuitry relies on a $50\ Hz$ pulse width modulated reference signal. The inherent problem with this is that at minimum the delay between the command and the reference signal changing is $20\ ms$. The result is that the internal servo circuitry can only be used for the characterisation of the aileron dynamics in which there are no control requirements. A design of a controller can be done taking into account the delay however this will affect the performance of the inner loop. It is better just to implement the inner loop with a custom controller. This finally results in effectively creating a rate loop as shown inFigure 6.5 and then closing a second position loop around it as shown in Figure 4.2. Consequently this results in the same topology as the rate controlled system. It can be recalled that the rate control inner loop has two poles, whereas the deflection control actuator has one pole. It is therefore decided just to test the rate actuation controller with the optimally damped, $\zeta = 0,707$, inner

loop rather than tuning the loop to have one slower dominant real pole and one faster non-dominant real pole.

The modifications made to the servos consists of removing the original driver and driving the DC motor directly from the H-bridge. The control hardware, as presented in §6.3.1, can then control motor voltage or current depending on the operation mode. The control of motor current further allows for torque characterisation of the actuator. This is done in order to realise torque control. The voltage control facilitates the rate loop of the actuator. The two drive modes can now be achieved without changing actuators during testing.

6.4 Controller Software

This section covers the development of the necessary custom software to facilitate the control of the interface and driver unit. First an overview of the software capabilities is given and then the logging and communication specifications are described. This is followed by a description of the emulation methods used for the hardware control implementation.

6.4.1 Graphic User Interface

The hardware designed for the experimental setup required a user interface in order to control test runs. The user interface is intended to minimise the amount of wind tunnel time required by expediting the data collection process and test run turnaround time. The user interface also provides a control platform for systems testing before any test run was initiated.

The user interface is custom PC based software written in C++ and compiled with Qt© Development Frameworks. The graphic user interface (GUI) performed a set of functions in data collection and control process. Screenshots of the software is provided in §A.3. The software includes the following features:
Control

- Gain uploading to hardware: The graphic user interface provided the necessary one click functionality to upload control gain data from the specified input file generated by the MATLAB controller gain calculation script.
- Simulation command importation and execution: Functionality is provided to import a time based command vector from a text file. At the specific times the commands are then transmitted to the hardware.
- Manual command execution: A facility is provided to input custom tab and aileron commands.
- System shut-down/start-up, safety check and error logging capability: All hardware driver stages, modes and control algorithms can be initiated and stopped form the GUI. Further, a debugging window is provided indicating system automated actions.

Logging

- Graphical display: The graphic user interface included real-time graphical plotting of selectable system states such as command, orientations, driver currents and controller commands on customisable scales. This facilitates on-line debugging and fault detection.
- State monitor: A tab is provided for display of current state, command, driver current and reference values to aid in initial calibration and monitoring of system responses.
- State logging: A raw and ASCII[2] based logging function is included for logging of current state, command, driver current and reference values at rate of reception. The logging includes the controller modes at the point of reception of the data from the hardware.

The PC hardware interface is based on a 1 Mbaud serial interface passing through a high-speed FTDI serial to USB device. Since standard operating systems to not support high speed serial the GUI was directly interfaces with system drivers in order to achieve the desired speed for data logging. Thereby, it is possible to do data logging at 1 kHz. Further, data interface between the hardware and GUI was done in raw mode to minimise the packet data size.

Each packet of data logged contains the following information:

- Tab and aileron deflection: The deflection measured by the angular sensors
- Tab and aileron command: The input variable to the respective actuator either commanded voltage or current
- Tab and aileron actuator current: The measured actuator current
- Control mode: Specifies open-loop tab reference, servo tab mode, tab and aileron control mode or tab sinusoidal excitation
- Driver mode: Specifies current control or voltage control mode

The logging system allows continuous automated testing. The command vector is uploaded to the GUI, the simulation started and logging is initiated. The command vector consists of a set of tab and aileron commands at specified times stored in an data file. The simulation process requires no user input and runs its course until completed.

6.4.2 Controller Implementation

In §3 through §5 the controllers are designed in the continuous domain. The controllers could be redesigned in the same topology in the discrete domain through the z-transform or emulation methods could be used. It was decided that emulation methods would be used since the control recalculation and sample time was set well above the system dynamic frequencies. The system response dynamics was expected to reach 20 Hz at maximum and the controller sample time was set to 2 kHz. Further, sensor sampling times were all synchronised with the controller sample time. The primary reason for the high sampling rate was to allow oversampling of the tab and aileron angular position for filtering and differentiation as explained in §7.3.

[2] American Standard Code for Information Interchange

For the emulation method the backwards Euler method for calculation of integrals and derivatives were used as shown:

$$\dot{\delta}_t(k) = \frac{\delta_t(k) - \delta_t(k-1)}{T} \tag{6.4.1}$$

$$\int_0^{kT} (\delta_{t_{ref}}(t) - \delta_t)(t)dt = \sum_{i=0}^{i=k} (\delta_{t_{ref}}(i) - \delta_t(i))T \tag{6.4.2}$$

Here T is the controller sampling time. The same applies for the aileron derivatives and integrals. The derivatives are then filtered with a first order low-pass filter to ensure rejection of noise resulting from the derivative in the rate calculation. The filter cut-off frequency was set to $500\ rads^{-1}$ and implemented digitally with a first order filter expansion:

$$\tau_f = 1/500 \tag{6.4.3}$$

$$\dot{\delta}_t(k+1) = \left(1 - \frac{T}{\tau_f}\right)\dot{\delta_t(k)} + \left(1 - \frac{T}{\tau_f}\right)\frac{T}{\tau_f}\frac{\delta_t(k) - \delta_t(k-1)}{T} \tag{6.4.4}$$

$$\tag{6.4.5}$$

Once again the same is applied for the aileron filtered derivative.

The simple Euler approximations are adequate as long as the sampling frequency is around 5-10 times the dominant pole frequency [22]. This recommended sampling rate is well below the controller sampling rate and therefore very little effect of sampling should be observed. This provides the necessary integral and derivative states to allow continuous gains to be used in the control algorithm.

Chapter 7

Model Parameter Determination

This section overviews the process of practical model identification. The experimental setup, procedure and events are summarised. Further, the different model identification methods are considered in terms of its case specific practicality. Then, parameter estimation from step input responses is used to determine a practical data based model for comparison with the theoretical model.

Theoretical models often do not provide complete or realistic insight into the behaviour of a system. It is therefore necessary to compare with practical results as far as practical. The difficulty however in practical results is that it is sometimes hard to attribute certain behaviour to specific aspects of the system. The system response characteristics may become ambiguous in whether it is a specific effect of the setup or a general characteristic of the system. It is further complicated by the occurrence of multiple effects at the same instance. The logical attempt would be to isolates the effect from each other but this is not always possible. In such a case an alternate way in which to determine the system model has to be found. This is done by either making do with approximate models and factoring it in when designing a controller or by estimating the effects as a system phenomenological model. However, this makes it difficult to extrapolate to models much different from the test model. However, even if it does not provide direct parametric insight into a generalised model, it does provide valuable insight into its behaviour and a basis for the controller design approach.

The simplest approach to determining the response of a system given its inputs is using a linear time-invariant (LTI) system approach but it has limitations. Usually, a first or second order transfer function is used and the parameters of this transfer function is derived from an impulse, step or ramp response. This is easily done through the use of overshoot, damped frequency, gain, rise time and sometimes settling time. However, if the input is not as clearly defined, the response will not be easily related to specific transfer function models. This is the reason why, in this specific case, a step command based parameter estimation route is taken. The parameter estimation results in a model parameters based on a arbitrary input.

Alternatively, the model can be identified using a frequency response analysis. However, there are two drawbacks to frequency analysis. The first is that if little is known about the system there is a risk of exciting unknown dynamics and this could sometimes result in system failure. This could be mitigated by a careful approach to the system characterisation. Further, the process of data collection can be very time consuming and many methods of excitation design has been developed to attempt to minimise this

[23]. It was decided to use the step command based identification for the simplicity of estimating the results from the method.

7.1 Experimental Procedure, Setup and Events

This section covers the testing conditions, setup and procedure followed during testing. The data collected is summarised in §7.4 and §8.

There are three major components to the experimental setup; a personal computer (PC) for logging through a graphic user interface, the control hardware for interfacing and control of the tab-aileron system and the experimental model with a wing section, aileron and tab. The aileron and tab include relevant actuators to realise the three control algorithms. An image of the experimental setup is presented in Figure 7.1.

The first setup was done in the horizontal sense since the initial intention was to evaluate the system with gravitational effect included. Horizontal mounting is the most accurate for a aileron simulation since it is the orientation it primarily occurs in an aircraft. In this case, the additional effect of gravity and weight of the surface is present. Figure 7.2 shows the setup with a Plexiglass side to allow monitoring of the system. The objective of the first wind tunnel run was to do general system identification to allow controller adjustment and gain calculation. This would be followed at a later stage by the second wind tunnel run which was intended for control systems testing on the identified system in the first run. However, after inspection of the first set of results, it was decided that all the extraneous effects should be mitigated to first allow more accurate characterisation of the aerodynamic effects which seemed erratic, reasons for which is discussed in §7.4. With the horizontal model setup it was found that this increased the friction on the hinges, which has plain bearings. The alternate vertical orientation relieves this problem however it has no gravitational coupling. Luckily, the effect of gravity is very predictable in the realm of operation and it can be added to the aerodynamic model by simple superposition. Figure 7.3 shows the vertical wing setup. Since the setup was changed a new identification run had to be completed. However during an identification run at $70\ ms^{-1}$ a oscillatory tab mode was excited and the vibration caused the upper hinge to shift out of position due to excess play. This resulted in the aileron and tab being blown out. Needless to say, the aileron and actuators were destroyed. Consequently, the aileron had to be reconstructed as quick as possible; the result was not ideal. Once reconstruction was complete, the setup was once again done in the wind tunnel and another identification run was done.

The results of the identification run that the system behaved very different from the second set of data, see §7.4. However, since the allocated time for the wind tunnel infrastructure was running out, it was decided to proceed with the control tests on the badly performing model to at least get a qualitative performance indication of the controllers.

As far as the test conditions are concerned, the atmospheric conditions are not controllable in the Stellenbosch University wind tunnel. Therefore, all tests were done at equivalent international standard atmosphere conditions at sea level (ISA). Standard mean sea level (MSL) temperature is $15°C$ and standard MSL pressure is $1013.25\ hPa$. The standard MSL density is $1.225\ kgm^{-3}$ The Pitot tube pressure differential was therefore calculated for these conditions and maintained on testing days ensuring consistent dynamic pressure, q, between tests. The dynamics pressure below mach 0.3 is given by

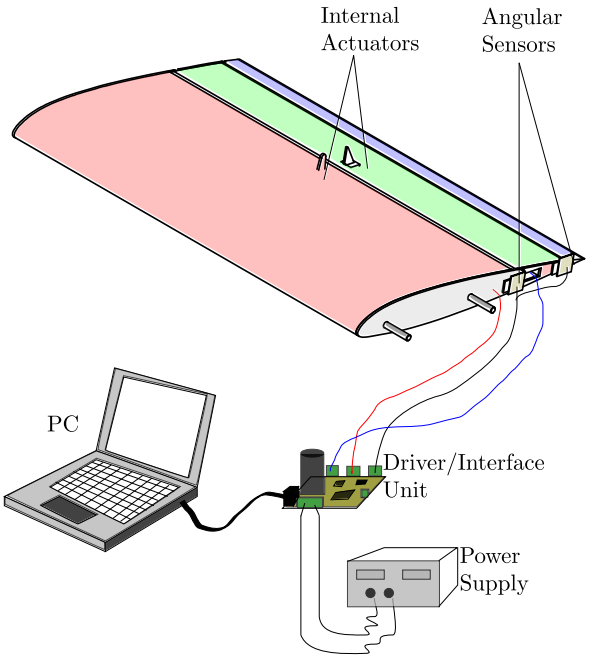

(a) Diagramatic Overview of the Setup

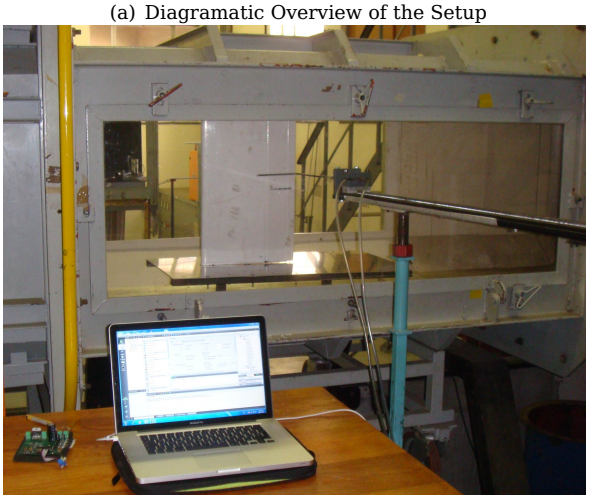

(b) Image of the Setup

Figure 7.1 – Experimental Setup in Wind Tunnel

[24]:

$$q = \Delta P = \frac{1}{2}\rho V^2 \tag{7.1.1}$$

The Pitot tube was located in the free stream in the wind tunnel. It was first placed midway between the test section in the wind tunnel and moved closer and further away from the test section until the free stream zone where velocity is independent form position is found. It was then rotated and pitched until maximum dynamic pressure is measured. The differential pressure sensor showed no fluctuation in the airflow to the displayed precision of a pascal during testing at speeds up to $40\ ms^{-1}$. However, at speeds of $50\ ms^{-1}$ and above some fluctuation was evident to a maximum of $\pm 5\ Pa$ corresponding to $\pm 0,2\ ms^{-1}$.

(a) Horizontal Setup Front View

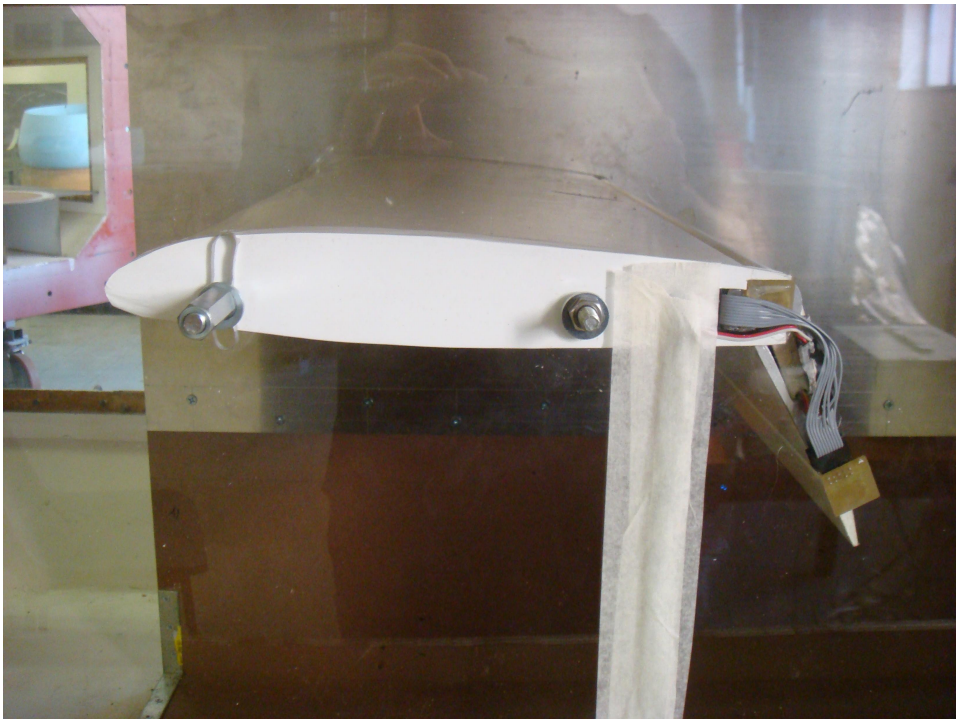

(b) Horizontal Setup Side View

Figure 7.2 – Horizontal Setup in Wind Tunnel

(a) Vertical Setup Quarter View

(b) Vertical Setup Side View

Figure 7.3 – Vertical Setup in Wind Tunnel

The tab and aileron angles are calibrated to zero position. The zero position is strictly chosen as the shape of the undeformed aerofoil. This was approximated by aligning the profile with a scale printed profile. This allowed re-calibration between runs and shutdowns.

Once the test setup was completed and calibrated, the tunnel was turned on and testing was done at velocity increments initiating an automated test cycle at each velocity and then continuing on to the next velocity. It would have been convenient to run multiple identifications at each velocity to get an idea of the statistical spread of performance however wind tunnel time was limited. Some runs were repeated due to logging errors and qualitatively, the responses seemed repeatable outside the regions where friction seemed to dominate, discussed in §7.4.

The experimental testing setup time was the major component in the testing and little time remained each time for data collection before the scheduled time was over. A major component of time pressure resulted form the failure of the aileron and therefore negatively impacted the amount of testing that could be done. With less time constraints and armed with the collected data and post mortem an improved setup could provide much more predictable results. The improved setup would require more complex manufacturing techniques similar to that used in the aeroplane industry and more detailed design to mitigate the non-idealities.

7.2 Parameter Estimation Methods

The concept driving the estimation process is the general notion that if both the input and output of the system is known then a n-th order model can be fitted to the system dynamics. The chosen procedure for fitting the data to the model is presented in this section. The fitting of the data take into account a certain degree of prior knowledge of the system structure under investigation. Conveniently, since the theoretical model has been established this knowledge is available. Furthermore, the efficacy of the estimation method is discussed in terms of the parameter accuracy. The parameters are verified post estimation through a final simulated response comparison with recorded data. Rooted in the response comparison, a qualitative discussion of the non-idealities apparent from the recorded data is given. The estimation finally provides crucial data about practical system behaviour upon which the controller design is based.

The parameter estimation process is done much like a linear estimation process. The chosen process is undertaken in the time domain. The standard process is based on the relationship Equation 7.2.1. This makes it possible to reconstruct or estimate the states, X, from the measurements, Y, given that the states are observable.

$$Y = H \times X \tag{7.2.1}$$

The key is to rewrite the parameter matrix in a form suitable to linear estimation. The first step is to identify the output matrix, relating the model parameters Θ to the outputs, the measured states, as shown in Equation 7.2.2. It is clear however that this is not a linear estimation process since the output matrix is dependent on the current model states and inputs, X and U respectively, Equation 7.2.2. The set of state relations, Equation 7.2.3 can be rewritten in terms of its partial derivatives of each state derivative in terms of the parameters as in an extended Kalman filter (EKF). Θ then

becomes the estimation states and the measurements become the outputs $\dot{X}$. The noticeable disadvantage of this is however that the derivative of the system states, $\dot{X}$, need be known or the integral of both sides have to be taken to determined in which case only the states have to be known, Equation 7.2.4.

$$\dot{X}(t) = H\left(X(t), U(t)\right)\Theta \tag{7.2.2}$$

$$\dot{X}(t) = FX(t) + GU(t) \tag{7.2.3}$$

$$\int_0^t \dot{X}(t)dt = \int_0^t H\left(X(t), U(t)\right)\Theta dt \tag{7.2.4}$$

$$H \equiv \frac{\partial \dot{X}}{\partial \Theta} \tag{7.2.5}$$

$$\begin{bmatrix} \dot{x}_1 \\ \dot{x}_2 \\ \vdots \\ \dot{x}_n \end{bmatrix} = \begin{bmatrix} \frac{\partial x_1}{\partial \theta_1} & \frac{\partial x_1}{\partial \theta_2} & \cdots & \frac{\partial x_1}{\partial \theta_n} \\ \frac{\partial x_2}{\partial \theta_2} & \frac{\partial x_2}{\partial \theta_2} & \cdots & \frac{\partial x_2}{\partial \theta_n} \\ \vdots & & & \\ \frac{\partial x_n}{\partial \theta_1} & \frac{\partial x_n}{\partial \theta_2} & \cdots & \frac{\partial x_n}{\partial \theta_n} \end{bmatrix} \begin{bmatrix} \theta_1 \\ \theta_2 \\ \vdots \\ \theta_n \end{bmatrix} \tag{7.2.6}$$

However, the continuous version of the estimation process is not entirely applicable when only sampled data is available. This means that the discrete state relations are more useful, Equation 7.2.7. The result is that the output matrix can be rewritten as Equation 7.2.8. This now means that only the states themselves have to be measured in order to determine the system parameters. This can be further reduced to only the original system outputs but the parameters have to be chosen in such a way that will ensure that they are all observable from the system outputs as with any standard estimation problem. It is important to notice that if either the input or the current state becomes zero the matrix H will be badly conditioned or in other words have bad observability of the states. The implication is that the system must be continually actuated otherwise the there will be no improvement in the estimated parameters due to the specific measurements taken.

$$X(k+1) = \Gamma X(k) + \Phi U(k) \tag{7.2.7}$$

$$H \equiv \frac{\partial X_{k+1}}{\partial \Theta} \tag{7.2.8}$$

$$X_{k+1} = H(X_k, U_k)\Theta \tag{7.2.9}$$

At this point only a linear relationship is known between the parameter and the outputs. It is preferable that the structure is linear since estimation methods to be used generally only guarantee convergence under linear conditions, [25]. It is therefore preferable to write Equation 7.2.8 in the form of Equation 7.2.9. Here $H(X_k, U_k)$ is not a function of the parameters but only the states. For a linear system as described in Equation 7.2.7, Equation 7.2.9 becomes a set of linear equations and with an adequate amount of input, U_k, and output, X_k, samples the linear equations can be solved.

The process of solving the linear equations is the so-called estimation process. Since more information or samples are available than required, a cost function based minimisation process is used to find the parameters that satisfy the set of linear equations the best. This estimation process can then be conducted in a multitude of ways. Three of which are least-squares estimation (LSE), weighted least-squares estimation (WLSE) and recursive weighted least-squares estimation (RWLSE). Here LSE and WLSE are

batch processes. Variants of least-square estimation is used since the square cost function has a simple analytical solution; for more on estimation see [26]. The minimum solution to these cost functions can also be found through standard optimization algorithms however as aforementioned it would not provide any improvement on the analytic solution. However, if the cost function were modified it would have merit.

One optimisation method used to solve the output error minimisation problem is the steepest descent method [27]. It was used to determine the optimal parameters of a predefined model structure by minimising the output error. This is done by firstly identifying the cost function, Equation 7.2.10. Here N defines the total number of samples, Y the output and $\hat{Y}_\Theta$ is the response of the model defined by the estimated parameters.

$$J = \sum_{k=0}^{k=N} \left(Y(k) - \hat{Y}_\Theta(k) \right) \tag{7.2.10}$$

The system step response, Y(t) or Y(k), can be determined analytically in terms of the system parameters. The cost function can then be written as a function of the system parameters and measurements. The Jacobian in terms of the parameters then has to be found which indicates the steepest descent direction. To find the Jacobian, differentiation can be done or small perturbation theory can be used [27]. This method was done solely for verification purposes and was found to be computationally expensive compared to RWLSE.

Using the aforementioned parameter estimation methods the parameters of the model can be determined at different set points. There are two approaches to the tab-aileron model. The fist approach is though assuming a decoupled tab model. In doing so the coupling from the aileron to the tab is ignored allowing a tab model to be parametrized independently. This results in two estimation processes. The tab estimation Equation 7.2.12 is derived from the tab state equation Equation 7.2.11 for which the input is tab moment, M_{Tab} and the states are the tab angular position δ_{Tab} and rate $\dot{\delta}_{Tab}$.

$$X_{k+1} = \Gamma_{Tab} X_k + \Phi_{Tab} M_{Tab_k} \qquad X_k = \begin{bmatrix} \delta_{Tab_k} \\ \dot{\delta}_{Tab_k} \end{bmatrix} \tag{7.2.11}$$

$$\begin{bmatrix} \delta_{Tab_{k+1}} \\ \dot{\delta}_{Tab_{k+1}} \end{bmatrix} = \underbrace{\begin{bmatrix} \delta_{Tab_k} & \dot{\delta}_{Tab_k} & 0 & 0 & T_{Tab_k} & 0 \\ 0 & 0 & \delta_{Tab_k} & \dot{\delta}_{Tab_k} & 0 & T_{Tab_k} \end{bmatrix}}_{H_{Tab_k}} \underbrace{\begin{bmatrix} \Gamma_{11} \\ \Gamma_{12} \\ \Gamma_{21} \\ \Gamma_{22} \\ \Phi_{11} \\ \Phi_{21} \end{bmatrix}}_{\Theta_{Tab}} \tag{7.2.12}$$

However, the model for the tab and aileron can also be derived from the reference input tab deflection, δ_{Ref}, to the output of the tab, δ_{Tab}, see Equation 7.2.13. This is the method in which the tab is characterised when the tab actuation is done by a servo which already has internal control loops present. Importantly here the macroscopic model of the tab is estimated which includes the tab actuator.

$$X_{k+1} = \Gamma_{Tab} X_k + \Phi_{Tab} \delta_{Ref_k} \qquad X_k = \begin{bmatrix} \delta_{Tab_k} \\ \dot{\delta}_{Tab_k} \end{bmatrix} \tag{7.2.13}$$

$$\begin{bmatrix}\delta_{Tab_{k+1}}\\ \dot{\delta}_{Tab_{k+1}}\end{bmatrix} = \underbrace{\begin{bmatrix}\delta_{Tab_k} & \dot{\delta}_{Tab_k} & 0 & 0 & \delta_{Ref_k} & 0\\ 0 & 0 & \delta_{Tab_k} & \dot{\delta}_{Tab_k} & 0 & \delta_{Ref_k}\end{bmatrix}}_{H_{Tab_k}} \underbrace{\begin{bmatrix}\Gamma_{11}\\ \Gamma_{12}\\ \Gamma_{21}\\ \Gamma_{22}\\ \Phi_{11}\\ \Phi_{21}\end{bmatrix}}_{\Theta_{Tab}} \tag{7.2.14}$$

Furthermore, the aileron model can then be derived as a response to the tab deflection. This estimation process is described as follows:

$$X_{k+1} = \Gamma_{Ail} X_k + \Phi_{Ail}\delta_{Tab_k} \qquad X_k = \begin{bmatrix}\delta_{Ail_k}\\ \dot{\delta}_{Ail_k}\end{bmatrix} \tag{7.2.15}$$

$$\begin{bmatrix}\delta_{Ail_{k+1}}\\ \dot{\delta}_{Ail_{k+1}}\end{bmatrix} = \underbrace{\begin{bmatrix}\delta_{Ail_k} & \dot{\delta}_{Ail_k} & 0 & 0 & \delta_{Tab_k} & 0\\ 0 & 0 & \delta_{Ail_k} & \dot{\delta}_{Ail_k} & 0 & \delta_{Tab_k}\end{bmatrix}}_{H_{Ail_k}} \underbrace{\begin{bmatrix}\Gamma_{11}\\ \Gamma_{12}\\ \Gamma_{21}\\ \Gamma_{22}\\ \Phi_{11}\\ \Phi_{21}\end{bmatrix}}_{\Theta_{Ail}} \tag{7.2.16}$$

These are however not the only way in which to represent the tab and aileron estimation problem. The output matrix, previously H, can be rewritten in any set of partial derivatives of any set of parameters, Θ. This was done in terms of the natural frequency, damping and gain as a comparison to this method and cross-checking parameter agreement. With the two decoupled models the ground work has been done for tab-only actuation control.

However, for full-state feedback control a full-state model is needed. This is achieved either by combining the two decoupled models into a single full state model or by creating a full-state estimation process. The full-state estimation process entails estimating all system parameters simultaneously. Notably, for the full state model the inputs are no longer tab deflection or tab reference but rather the tab and aileron applied moment.

The problem can be structured exactly as described in the previous cases. The only difference is that there are more parameters that are estimated simultaneously. Intuitively this means more data is needed to estimate more parameters and convergence would take longer. Looking at the specifics of this estimation process, it can be seen that there are a total of twenty-four parameters that have to be estimated. The number of parameters can be reduced since many of the parameters are already known when looking at a standard discretised fourth order theoretical model. However, since a recursive method is used the covariance of the initial guess of those known parameters are set to very small values this means that the parameter update gain, which is related to the inverse of covariance, would be near zero.

$$X_{k+1} = \Gamma X_k + \Phi \begin{bmatrix}M_t\\ M_a\end{bmatrix} \qquad X_k = \begin{bmatrix}\delta_{Tab_k}\\ \dot{\delta}_{Tab_k}\\ \delta_{Ail_k}\\ \dot{\delta}_{Ail_k}\end{bmatrix} \tag{7.2.17}$$

$$X_{k+1} = \underbrace{\begin{bmatrix} X'_k & \underline{0} & \underline{0} & \underline{0} & U'_k & \underline{0} & \underline{0} & \underline{0} \\ \underline{0} & X'_k & \underline{0} & \underline{0} & \underline{0} & U'_k & \underline{0} & \underline{0} \\ \underline{0} & \underline{0} & X'_k & \underline{0} & \underline{0} & \underline{0} & U'_k & \underline{0} \\ \underline{0} & \underline{0} & \underline{0} & X'_k & \underline{0} & \underline{0} & \underline{0} & U'_k \end{bmatrix}}_{H_k} \underbrace{\begin{bmatrix} \Gamma_{11} \\ \Gamma_{12} \\ \Gamma_{13} \\ \Gamma_{14} \\ \Gamma_{21} \\ \vdots \\ \Gamma_{44} \\ \Phi_{11} \\ \vdots \\ \Phi_{14} \\ \Phi_{21} \\ \vdots \\ \Phi_{24} \end{bmatrix}}_{\Theta} \tag{7.2.18}$$

$$X_k = \begin{bmatrix} \delta_{Tab_k} \\ \dot{\delta}_{Tab_k} \\ \delta_{Ail_k} \\ \dot{\delta}_{Ail_k} \end{bmatrix} \quad U_k = \begin{bmatrix} T_t \\ T_a \end{bmatrix} \tag{7.2.19}$$

It has been mentioned that the RWLSE method was used to estimate the system parameters. The reason why the recursive method was used is that the batch processes are limited by the maximum matrix size that can be handled during the numerical calculations. The derivation of the RWLSE methods is readily available in literature and results in [18]:

$$Q_{k+1} = \left(Q_k^{-1} + H_k^T R^{-1} H_k\right)^{-1} \tag{7.2.20}$$

$$\hat{\Theta}_{k+1} = \hat{\Theta}_k + Q_k H_k^T R^{-1}(X_k - H_k \hat{\Theta}_k) \tag{7.2.21}$$

with the initial conditions

$$Q_0 = 10^6 \mathbf{I}_{n\times n} \tag{7.2.22}$$

$$R_0 = 10^{-6} \mathbf{I}_{N\times N} \tag{7.2.23}$$

$$\Theta_0 = [\bar{0}]_{n\times 1} \tag{7.2.24}$$

where

$$X_k = \begin{bmatrix} \vdots \end{bmatrix}_{N\times 1} \tag{7.2.25}$$

$$\Theta = \begin{bmatrix} \vdots \end{bmatrix}_{n\times 1} \tag{7.2.26}$$

Here, the notations have been reformulated to fit the specific estimation problems mentioned previously. The estimation of the parameters can then be concluded by recursively evaluating the covariance update given by Equation 7.2.20 and the estimated parameter update given by Equation 7.2.21. Here the update gain is recalculated at each instance since the matrix $H(X_k)$ changes with time. Each estimation process is

first tested with simulation data generated with a known model allowing one to compare the estimated parameter with actual parameters.

In totality, each of the required models of the system in question is formulated into a simple linear estimation problem to be solved with the RWLSE method once the necessary test data is available. Furthermore, the recursive method is used for its computational efficiency. The estimation procedure consequently allows any set of input and output data of a system that holds the forms of Equation 7.2.11, Equation 7.2.13 or Equation 7.2.17 to be translated into time invariant system parameters. The experimentally logged data is therefore used to determine the most appropriate aileron and tab models.

7.3 Signal Conditioning

The theoretical form of linear RWLSE process is presented in the previous section which is the basis for the model verification process. The estimation process is facilitated by state measurements and these state measurements will contain some degree of noise. Proper conditioning of the measurements is important in insuring that the observed dynamics is directly represented by the state measurements. This section gives an overview of the considerations when conditioning the state measurements along with the general filtering architecture implemented.

The system states consist of the tab and aileron angular positions and rate. These states have to be measured or estimated somehow to facilitate the parameter estimation process. In terms of measuring the four states, strictly four sensors are required. However, if position information is available the rate can be derived or estimated. This reduces the measurements to two states. For estimation of the states a system model is required or a kinematic model has to be used. Consider using an optimal filtering technique with an incorrect system model, this could introduce estimator dynamics into the measurements. If the kinematic model were used the optimal filter would not necessarily provide much improvement over a well chosen low pass filter and derivative. Additionally there is increased complexity of adding an estimator to the process and having to choose the weighting matrices. The simpler choice where the outcome is more predictable is the use of a n-th order filter.

The state variables sampling frequency is $1\ kHz$. This value is limited partially by the hall effect angular sensor, see §6.3.1 an partially by the maximum serial baud rate. However, this sampling frequency is much higher than the system natural frequencies which are in the order of tens of hertz, derived from the theoretical model initially. The noise has a specific form since it is already digitally sampled by the hall effect transducer. It can also be seen in any of the responses that the noise is quantised to a large extent. Investigation into the power spectral density of the noise showed that it is definitely not white noise. The manufacturer quotes the noise values as having a specific variance but they do not specify the characteristics of the noise.

In general this amount of noise is not a problem in terms of the angular position measurement for control and estimation. However, since the position is differentiated to determine the angular rate, the noise at higher frequencies are amplified. Noise at 100 rad/s will be amplified 40 dB and the noise at 1000 rad/s 60 dB since there is 20 dB per decade amplification by a derivative. These figures result in noise peaks on the angular rate in excess of the nominal system angular rate. Since the sampling is done at a much higher frequency than the system dynamics, low pass filtering of this signal

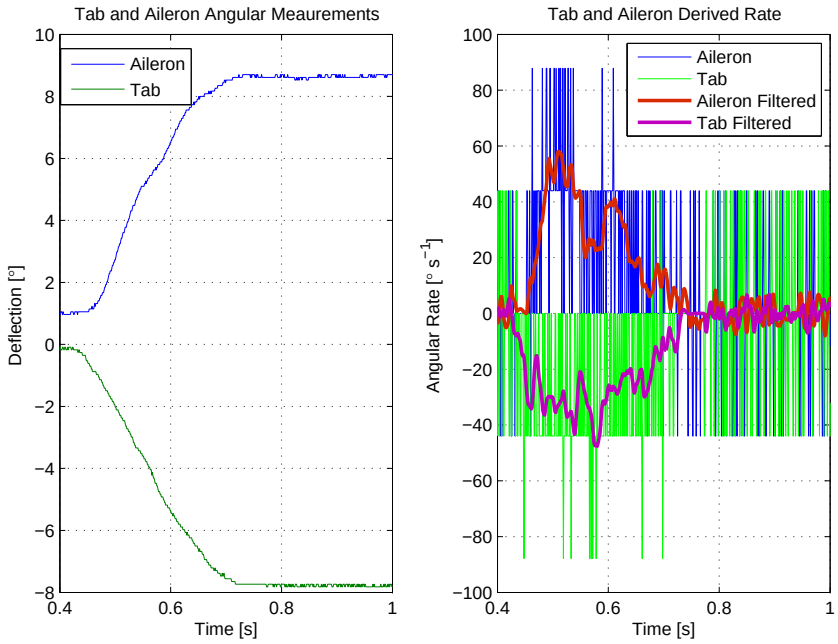

Figure 7.4 – Response Filtered Derivative

effectively results in a oversampling topology. The filter used must therefore be at least a order higher than the derivative. This means that the minimum a second order filter is required. A third order filter is chosen to ensure that the system higher frequency noise is attenuated by at least 40 dB per decade. The cut-off frequency is chosen at the minimum acceptable value where it will not affect the result in the estimation process. The rule of thumb for a control system design is that a non-dominant pole's dynamics can be ignored as long as the pole is located a half to a full decade away from the system poles. The result is that a cut-off frequency of around 500 rad/s will maintain the system dynamic information and reject high frequency noise.

The effect of choosing the filter incorrectly is that the system parameters tend to become distorted. Consider a case where the cut-off is selected at a lower frequency too close to the system dynamics. The result is that higher frequency responses of the faster system poles are attenuated. The parameters will then be estimated for the incorrect dynamic data in which the degree of dominance of the higher frequency behaviour is incorrect. In the alternate case where the filter frequency is chosen excessively high and noise passes through, the RWLSE process will tend to estimate the parameters incorrectly since it would become difficult to discern between noise and the response.

Figure 7.4 shows a typical aileron response with the angular rate derived from the response. It is quite apparent that the noise standard deviation is in the same order of magnitude as the system rate values. The filtered and then differentiated rate information in red can be seen to contain much less noise.

Through making use of the oversampled data, the conditioning of the signal can be achieved with a third order Butterworth filter. This results in an adequately noise free response to facilitate the estimation process. It is also noted that both excessively high and low filter cut-off frequencies will result in inaccurate parameter estimation. The

ability to evaluate a more accurate state vector means that the estimation process is more accurate.

7.4 Parameter Estimation Results and Comparison

In §7.2, the method for parameter estimation using the experimental data collected as explained in §6 is presented. The necessary preprocessing of the data is highlighted in §7.3. The wind tunnel data collected is summarised in terms of velocity or airspeed, angle of attack and step size. The primary parameters that are estimated and presented are the ones relating to the aileron dynamics. The estimation of a full-state model is also discussed in terms of its feasibility at this stage.

To recap, there are three distinct setups for which the parameters were estimated. They correspond to three different wind tunnel runs. The details of the hardware is provided in §6. The first wind tunnel setup was primarily intended for model identification and parameter estimation to allow further model development. The wing profile was mounted in the horizontal sense as shown in Figure 7.2. The test runs were done as described in §7.1. A set of tab steps were executed at each angle of attack interval and velocity interval. The tab steps were controlled by the internal servo control loop and there was no aileron feedback. The data was then extracted from the log files and run thought the estimation process for aileron model identification as described in Equation 7.2.15. Then, for each angle of attack and velocity test point a LTI model results from the estimation process. The LTI model is then used in simulation to confirm its response matches the experimental data. An example is presented in Figure 7.5. The final parameter sanity check is then done by a graphical inspection of goodness of fit. Rather than using error to check the quality of fit which has already been minimised by the RWLS estimation process, the characteristic performance measures of the response is checked. The main reasoning for this is that in some responses exhibit discontinuous trajectories; an example is given in Figure 7.12. Since the LTI model response does not have any discontinuities, these discontinuities in the experimental response will introduce errors in the estimated parameters. The observed non-idealities are discussed further in §7.4.4.

Figure 7.6 shows the data collected in terms of the system parameters estimated through the RWLSE process. ζ signifies the damping ratio most representative of the response at that velocity. Gain signifies the ratio between resultant aileron deflection and the tab deflection. ω_n signifies the natural frequency of the best fit LTI model. The dashed line represents a negative deflection of the aileron and the solid line represents a positive deflection. For the first set, data of 10° tab steps were taken and the LTI parameters were derived. The velocity was varied in increments of $10\ ms^{-1}$ and angle of attack was varied in increments of 5°.

In order to remove any extraneous effects the second setup was done in the vertical sense as seen in Figure 7.2. Furthermore, all attempts were made to eliminate frictional effects which are discussed in §7.4.4. This meant that the system identification had to be repeated since the model changed. The data from the second set was collected at a fixed angle of attack in order to reduce the required wind tunnel time. From theory was also apparent that the angle of attack should have no effect on the hinge moment coefficient derivatives in these velocities and atmospheric conditions [28]. The data was once again collected at $10\ ms^{-1}$ increments and 5° step intervals in both directions up to 25°. This allows the investigation of the effects of the tab deflection and velocity on

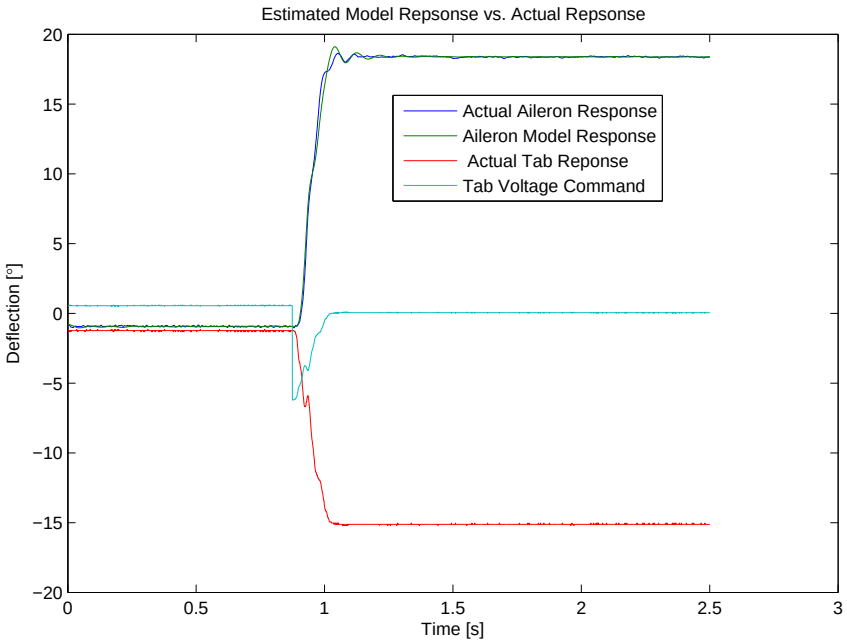

Figure 7.5 – Parameter Estimation Fit Result Airspeed 50 ms^{-1}, 15° Step

the aileron dynamics. The data was once again preprocessed and the LTI parameters estimated as before. This data is presented in terms of velocity in Figure 7.7 and in terms of step size in Figure 7.8.

However, during the system identification run a tab oscillation was inadvertently excited and underwent high frequency oscillations. The tab servo loop could not reject these oscillations resulting in failure of the upper hinge. The aileron was blown out and resulted in its destruction. The causes are discussed in §7.4.4. The effect was that data collected in the second run would be of no use in control testing since the model was destroyed. Since the first model had a considerable lead time, it was decided to redo the construction in-house. The original manufacturing methods as described in §**??** were not available so a moulding technique was used. This resulted in some inaccuracies in the profile of the new aileron. Further, as a risk prevention strategy additional hinges were added.

After the reconstruction, a third parameter estimation run was done. However, it was found that the performance was not nearly as good as the second parameter estimation run. Various methods were attempted to improve performance however the only culpable reason for the reduced performance seemed to be the increased clearance between the aileron and wing profile, discussed later on. The additional clearance was a result of the additional hinges and the inaccuracies in the new aileron profile. Further, the inaccuracies in the overall shape of the aileron could have contributed to the extent of decrease in performance.

Due to the limited time available for testing and infrastructure use, it was decided to continue and demonstrate the concept of control irrespective of the tab performance. Since the second setup had shown that the tab can indeed function desirably, the continued testing is done to investigate the control concepts. These system identification

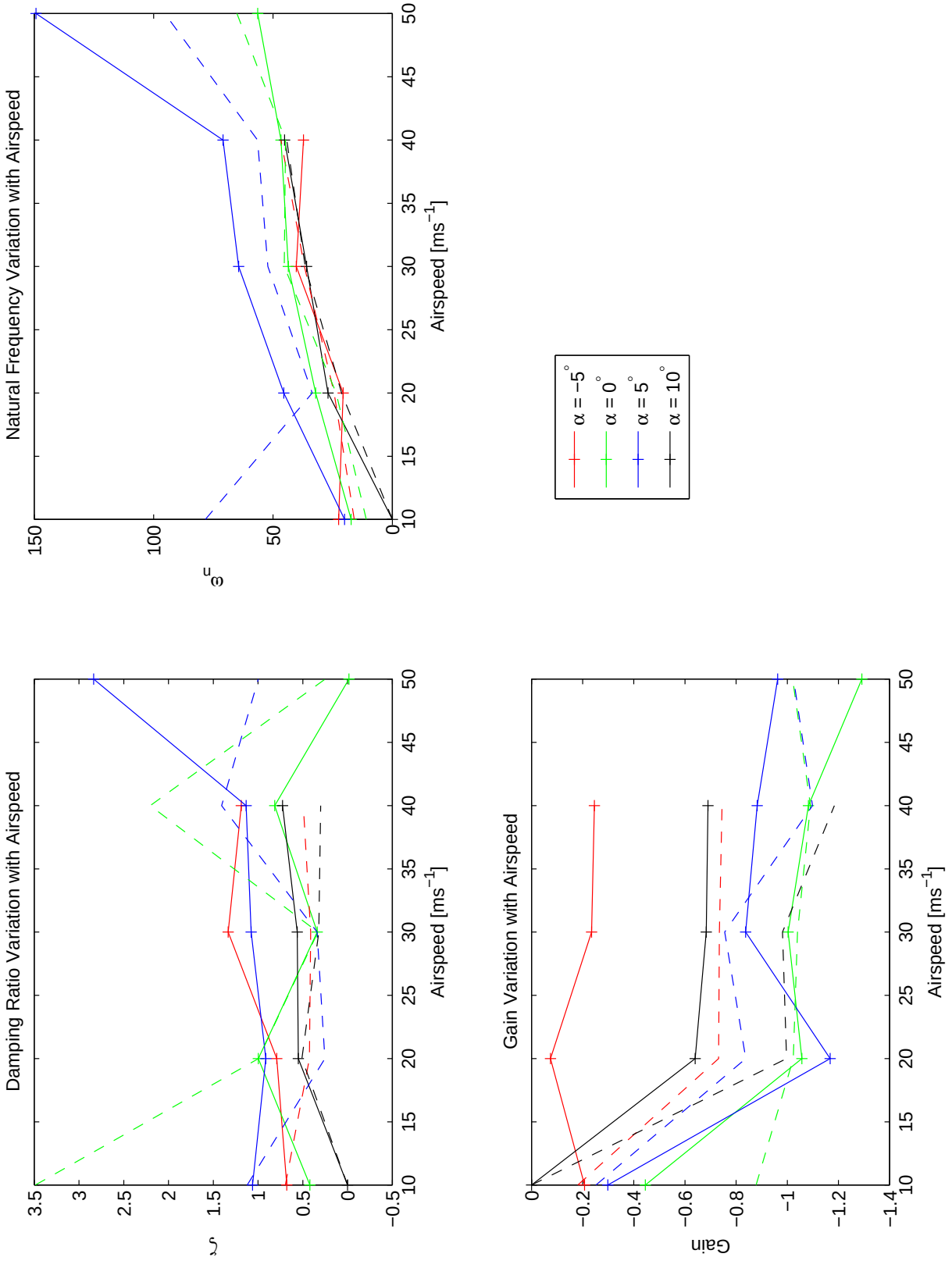

Figure 7.6 – Variation of System Parameters with Velocity Dataset 1

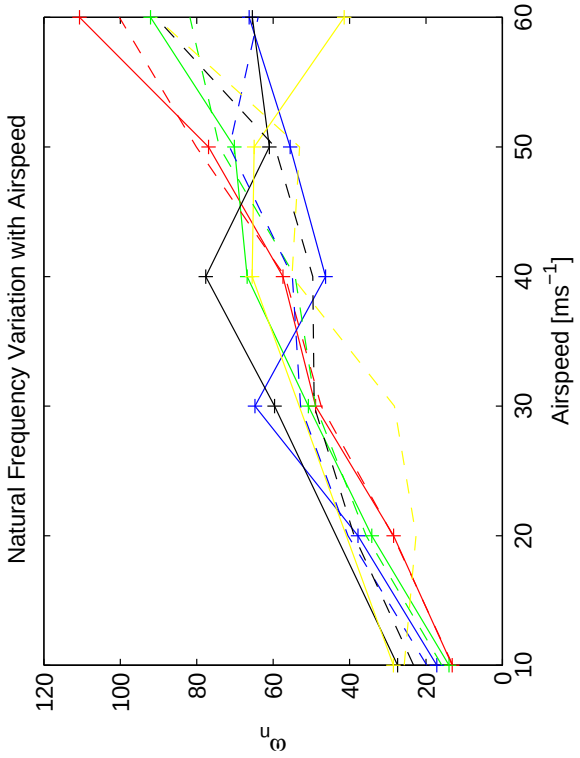

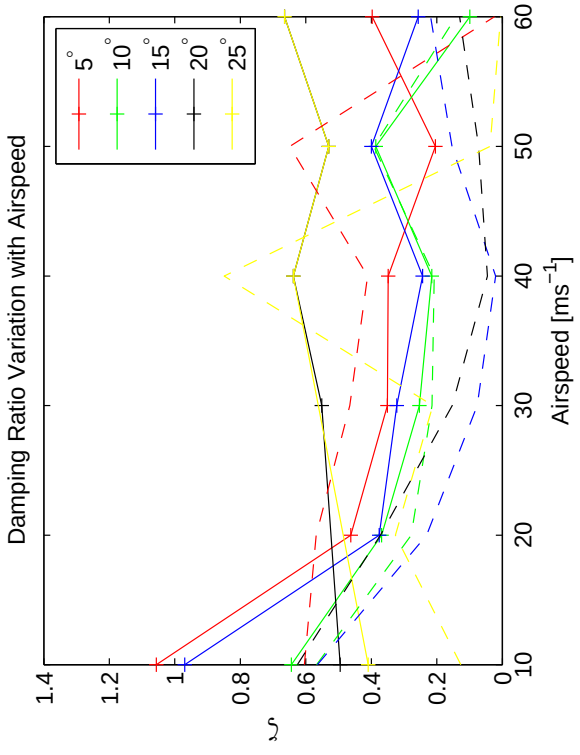

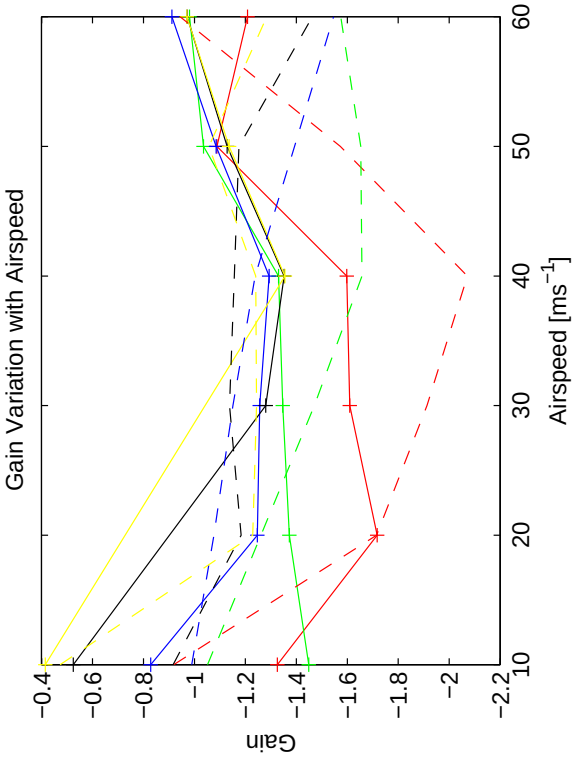

Figure 7.7 – Variation of System Parameters with Airspeed Dataset 2

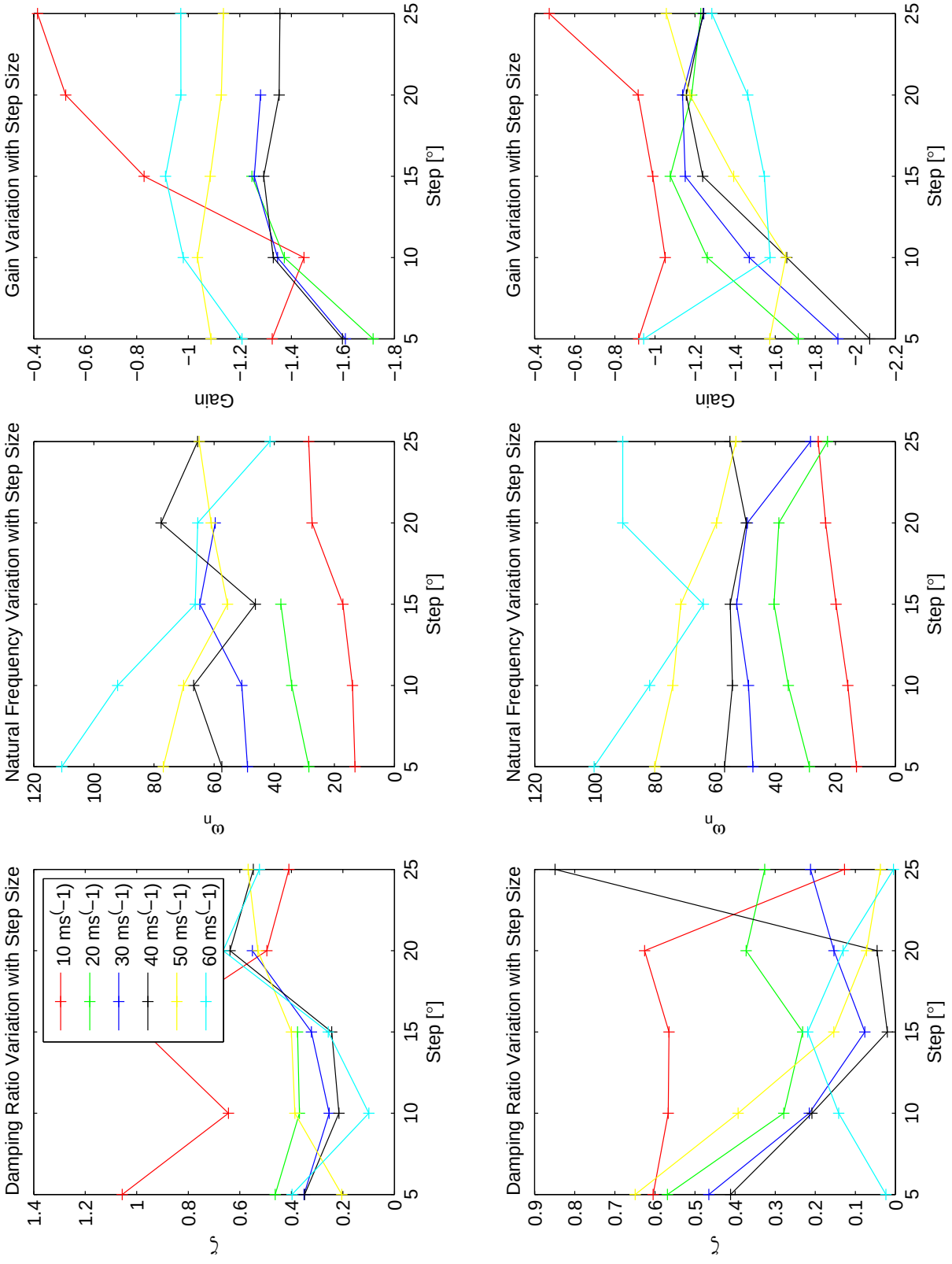

Figure 7.8 – Variation of System Parameters with Step Size Dataset 2

results are presented in Figure 7.9 in terms of velocity and in Figure 7.10 in terms of step size.

The collected data provides insight into the dynamics of the aileron and provides meaningful comparison for the theoretical model. The comparisons can be drawn in terms of the system variation as a function of the independent variables or conditions; angle of attack, velocity and final tab and aileron state. Additional effects not predicted by the theoretical model can also be observed. The focus however remains not to completely characterise the aerodynamics of the tab-aileron but rather to get an approximate model on which to base the control design.

Initially there was hope that the data would provide a chance to estimate the full state model of the system in terms of the moment inputs as explained in §7.2 in Equation 7.2.17. However, when this was attempted it was found that the estimation continually resulted in parameters which could not reproduce the system response with the given inputs. After a reasonable amount of investigation, it was found that the constant moments applied against friction resulting in no state changes resulted in system parameters which did not represent the data. It was therefore decided to use the tab-aileron transfer functions resulting from estimation and combining it with the linearised theoretical tab dynamics to reconstruct the full state model. Conveniently, the system input matrix was easily attainable from the moment of inertia properties. The crucial part in the model is the tab coupling to the aileron states and this was available.

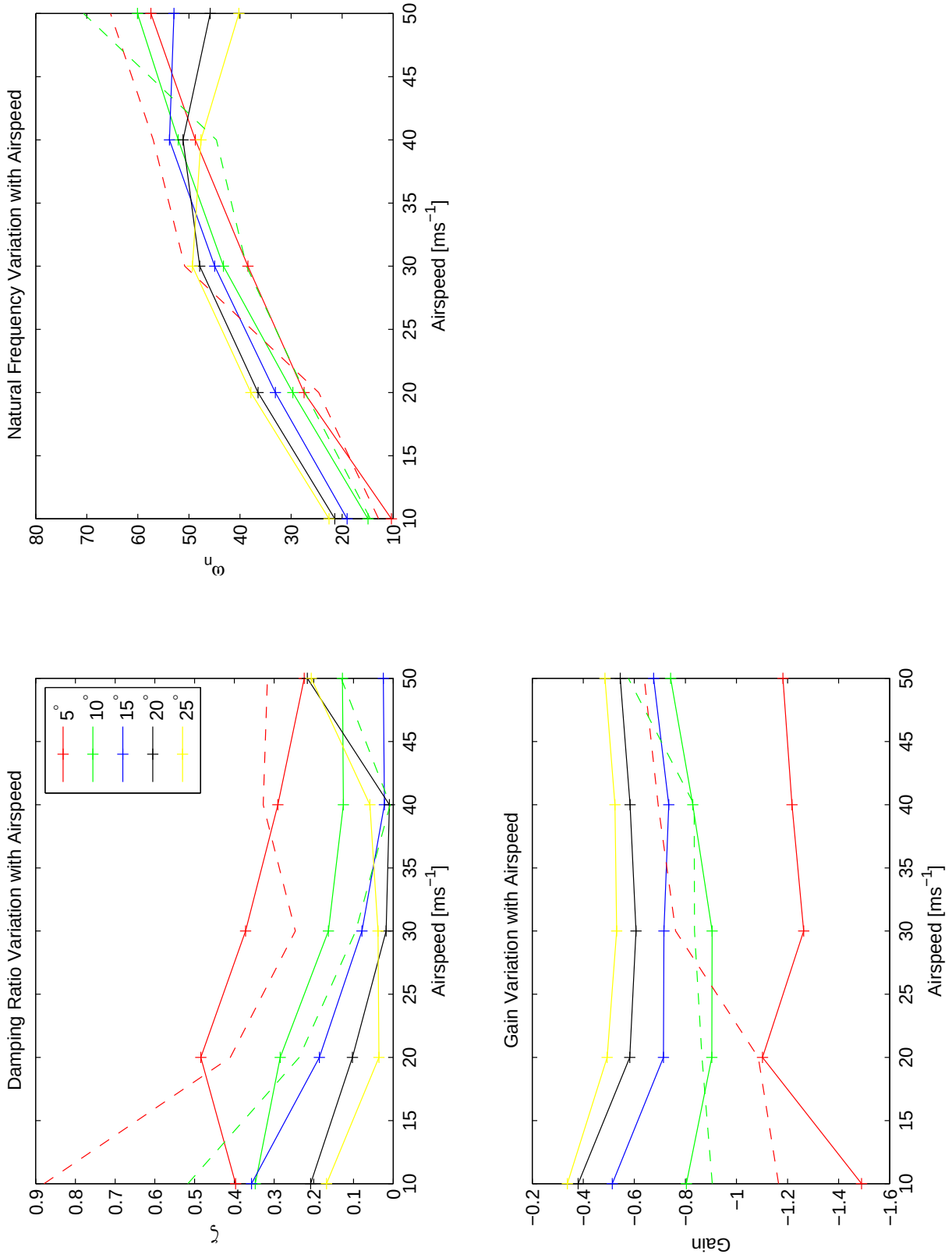

Figure 7.9 – Variation of System Parameters with Velocity Dataset 3

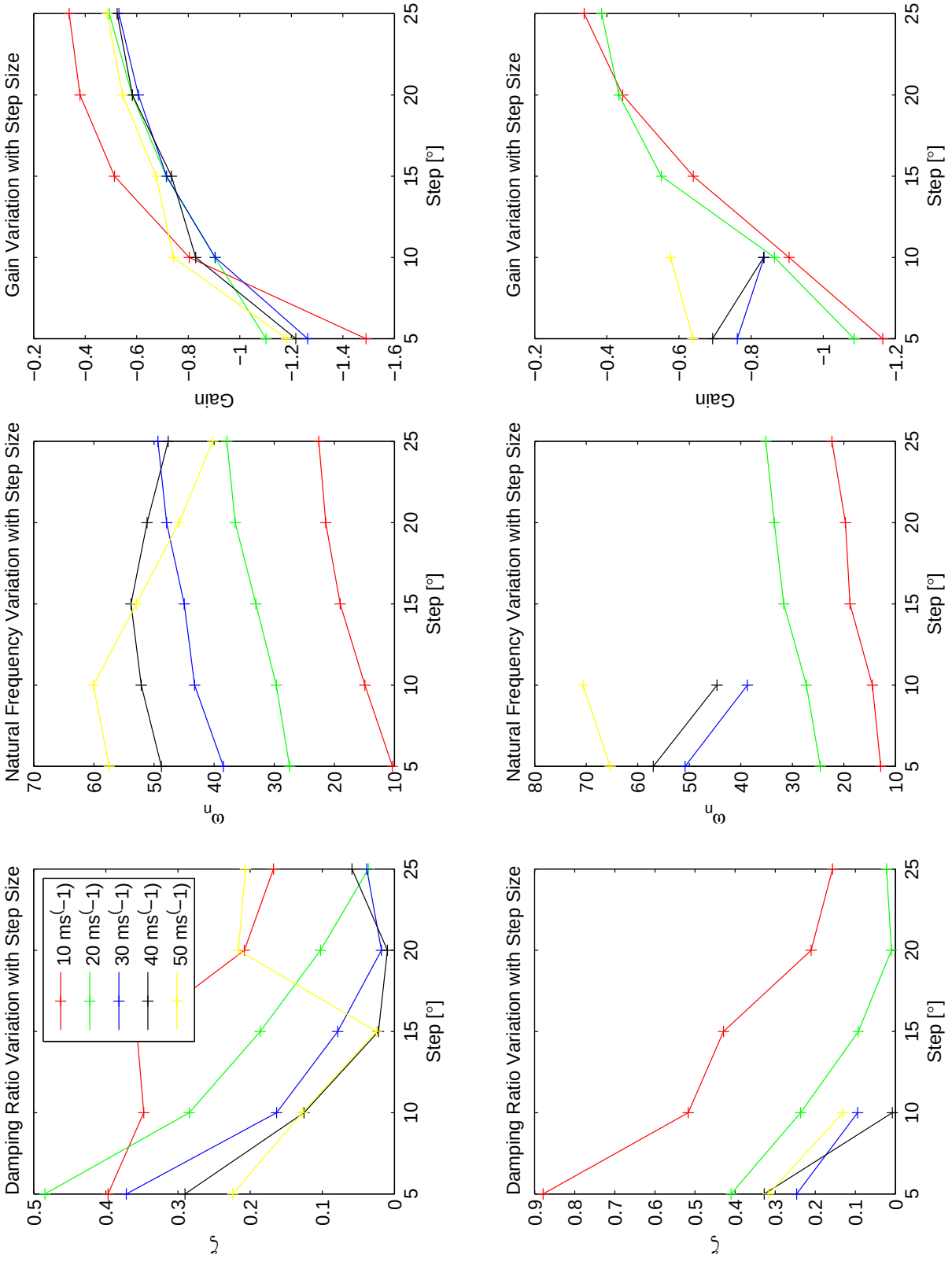

Figure 7.10 – Variation of System Parameters with Step Size Dataset 3

7.4.1 Angle of Attack Effects

The primary data concerning the angle of attack effect is derived from the first wind tunnel run. The data is represented in Figure 7.6. The theoretical effect to be expected from angle of attack variation is presented in Figure 2.13.

The theoretical data suggests that there should be no variation in the tab-aileron model due to the variation of the angle of attack. The model is primarily dependent on the aileron hinge moment coefficient derivative in terms of tab deflection, $\frac{\partial C_{H_a}}{\partial \delta_t}$ or $C_{H_{\delta_t}}$, and aileron hinge moment coefficient derivative in terms of aileron deflection, $\frac{\partial C_{H_a}}{\partial \delta_a}$ or $C_{H_{\delta_a}}$, which shows little variation over the operating angle of attack region of -5° to 10°, see §2.2. The static tests done by Ragallo also showed very linear behaviour in terms of the hinge moment coefficients [28] for a sealed aileron but also contributed that the effect of aileron ventilation does in fact adversely affect these derivatives.

The measured data however show that there is a trend related to angle of attack. The gain shows peak values between 5° and 0° angle of attack. It also shows that the damping is higher at the the extrema of the angles of attack -5°. Further, the natural frequency of the setup at 5° angle of attack is significantly higher over the range of velocities than the other angle of attack setups. It is also visible that for the extrema of angles of attack there is a larger difference between the positive and negative step responses. However, zero angle of attack data shows little difference in gain between positive and negative deflections.

The difference in positive and negative deflections at the extrema due to angle of attack is most probably caused by flow disturbance over the surfaces. In qualitative analysis of available experimental data, Crandall and Murray noted that the tab efficiency became “discontinuous” and that the tab effectiveness decreased towards the extrema of angle of attack as well as the positive and negative directional effectiveness of the tab differing [7]. These results are confirmed various times with different aerofoil shapes. For example, [29] who attributed it to increased boundary layer thickness due to airflow through the aileron-wing gap. The trend in the region between -5° and 10° angle of attack clearly contradicts the theoretical model since no irregular hinge moment effects are visible in the theoretical hinge moment data. This is noted and the effect on the controller is checked practically in a robustness test against angle of attack variation discussed in §8.

No conclusive answer can be given as to the reason for the effect of angle of attack based on the available data. Flow visualisation techniques could provide some valuable insight into the effects and would provide more conclusive answers. The observed effects are shown to not be unique to this setup which is cause for the robustness tests in terms of angle of attack during controller evaluation.

7.4.2 Velocity Dependent Trends

The velocity dependent trends are visible in all the parameter estimation data. The trend can be most readily observed in the parameter plots against velocity, Figure 7.6, Figure 7.7 and Figure 7.9 of wind tunnel run one, two and three respectively. The trends can be compared to the theoretical trends and observations made in §2.4.

The theoretical linearised analysis predicts that the damping should be constant over the velocity range since it is not velocity dependent, see Equation 2.4.13 through Equation 2.4.15. The linear model also predicts that the natural frequency of the system

should increase linearly with the velocity, see Equation 2.4.10. Thirdly the gain should remain constant throughout the velocity range, see Equation 2.4.16. The prediction is based on the linearised hinge moment and the linearised coupling dynamics.

The parameter estimation results, primarily considering Figure 7.7, indeed does show that the natural frequency of the equivalent LTI system does increase very roughly, linearly with velocity. However, the data seems to show large spread and dependency on step size, discussed in §7.4.3. The gain however does not remain constant. This could be due to any range of reasons. A possible reason is that thin aerofoil theory does not correctly predict the hinge moments and that they are in fact not linear. This is most probably the case, the reason being that the practical aspects of the aerofoil such as flow leakage between moving surfaces and boundary layer effects are not taken into account. Mechanical aspects such as friction, discussed in §7.4.4, are also not taken into account. There may be a multitude of other less obvious reasons why the parameters do not exactly match.

The effects of velocity and therefore Reynolds number is considered by Crandall and Murray in [7]. The trends are primary attributed to boundary layer effects. Initially, it is said that the boundary layer thins due to increased Reynolds number after which it thickens again since the transition point moves forward. Thus, the boundary layer over the trailing edge control surfaces become thicker. It is noted that one would initially expect improved performance due to the thinning of the boundary layer however there is greater sensitivity to surface roughness effects. As Reynolds number increases the performance is then expected to decrease at some point. These boundary layer effects could effect both tab an aileron and may possibly result in changing behaviour in the dynamics of the aileron and the performance of the tab.

Further, it can be seen that the damping ratio ranges between less than 0.1 and 0.8 at the middle range velocities. It however has to be said that at low speeds the frictional effects on the hinges played a dominant role sometimes causing the system not to respond to small tab deflections. Again, at higher velocities the damping seemed to increase possibly an effect of increased radial forces on the hinge plain bearings and therefore more friction. The small variations are possibly due to these effects but for example at $60\ ms^{-1}$ the damping varies erratically signifying aerodynamic effects rather than frictional or mechanical effects.

Some data at lower airspeeds, 20 and $30\ ms^{-1}$ where large deflections, $20°$ and $25°$ were given was omitted from the data presented since a linear model could not be fitted to it. These effects are discussed in §7.4.4. These responses showed sudden losses of gain and abrupt changes in aileron position to lower deflections.

When considering Figure 7.9, it can be seen that the natural frequency range is similar to that of Figure 7.7 which indicate that $\frac{\partial C_{H_a}}{\partial \delta_a}$ has remained approximately the same. However, the gain does not show the same behaviour and is about half of that shown previously but varies less over the range of velocities for a given step size. This could be a result of the effects that caused erratic data in the second set occurring more readily. Further since the aileron natural frequency has remained similar the tab performance is most probably to blame. The data for the negative deflections larger than $10°$ is not displayed since the data did not show linearity and parameters for the data could not be derived. The reason was the same as the reason in the second set except that the phenomena occurred more readily. The gains in the third run decreased so much at $15°$ step size that the tab is almost saturated.

Primarily, information taken form the velocity parameter estimation is that there is an increase in system bandwidth linearly with airspeed and that the aileron natural frequency seemed to be reasonably repeatable under the slight changes in geometry and clearances explained previously. Further the damping is mostly underdamped with the damping ratio ranging from $0,1$ to about $0,8$. Furthermore, that the gain is subject to non-ideal effects in this particular setup. The gains in the third run, which would be used for controller testing, is so low that without aileron actuation the controllers will not be able to achieve more than $15°$ aileron angle. With the setup used in the second wind tunnel run, it would have been possible to achieve the full aileron angle without an aileron actuator and therefore the tab-only actuated system would have been sufficient.

7.4.3 Deflection Range Trends

The tab deflection angle effect on the aileron is displayed in Figure 7.8 and Figure 7.10. The parameter estimation data is the same data as presented previously but the independent variable is the tab deflection.

The linearised model once again showed little variation, less than $0,5\%$, in terms of tab position since once again the basic aerodynamic theory does not show large variation of the hinge moment coefficient derivatives, see §2.3. On the contrary the derived parameters showed large variations of the aileron dynamics with the tab deflection as seen in Figure 7.8. It seems that the natural frequency of the aileron is affected greatly by tab position causing on about 30% to 50%, one case more than 60%, change in natural frequency and up to 60% change in the gain of the tab to aileron. At low velocities it shows an increase in the natural frequency with tab step size and at high velocities it shows decreasing natural frequency with step size. There seems to be a confluence of the natural frequencies at the higher angles between 30 and 60 rad, s^{-1}. However the third data set, Figure 7.10, shows contradictory results with increasing natural frequency as step size is increased by up to 25%. After more investigation it was found that the data in the third set fit the LTI models better, with less error, than the data for large tab angles in the second set. The reason for this seems to be that even though the second set shows larger gains an better performance than the third set the onset of non-linearities at the large deflecion angles are more prominant. Whereas, the third set had more consistent nonidealities.

The gains also show confluence at large tab deflections at much lower values of between $0,3$ and $0,6$ for the third test run and mostly 1 and $1,4$ for the second test run. The decreased tab effectiveness is also noted by Crandall [7], who suggests that the aileron position affects the tab performance. Therefore, the effect is probably due to the aileron deflection affecting the tab and not the large tab deflection itself. Further there is a downward trend in damping in nearly all cases except for the damping in positive displacements in the second wind tunnel run.

A very general trend is that the system bandwidth is greatly decreased by large tab deflections, greater than $10°$ at velocities larger than 20 ms^{-1}. The system damping is equally affected decreasing to low damping values below 0,4 in all but one case. Further, gain in the third set is reduced to a point where the tab is nearly ineffective. The second dataset however still shows larger than unity gain.

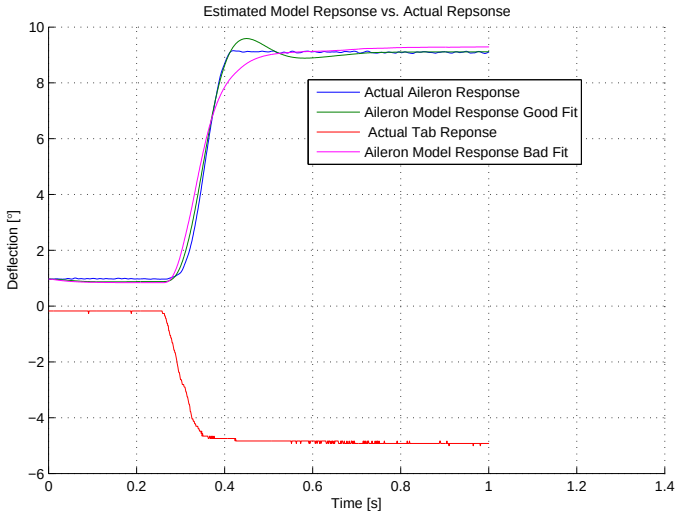

Figure 7.11 – Non-Ideal Responses Good vs. Bad fit

7.4.4 Observed Non-Idealities

Throughout the evaluation of the collected data some aspects were noticed which are not predicted by the theoretical model. These aspects are discussed in this section in terms of their qualitative behaviour. Also, some indicative evidence for the origin of the behaviour is given.

The example in Figure 7.12, shows the typical two discontinuities observed in the experimental measurements. Through continuous observation of the estimation outputs, it was found that the discontinuities tend to affect settling time the most and therefore tend to overestimate the damping in the system and underestimate the overshoot. Therefore, the graphical check was done mainly to ensure that the rise rate or rise time and overshoot is represented by the parameters. Figure 7.11 shows a comparison between two estimation results one fitting correctly and the other not. In terms of the estimation process there is not much that can be done to correct a bad fit other than manually adjusting the parameters until the fit represents the overshoot and rise rate more accurately or discarding the data point. This inherently means that the response is not linear and that a LTI mod can probably not be fitted to it.

The only real option that will result in accurate LTI parameter estimation is if the non-idealities or non-linearities are also estimated. Since there is suspicion that the non-idealities are discontinuous, such as friction, it would be difficult to include the effect in the estimation process. This is dependent on whether the friction is described by a continuous function. Further, even if the continuous models of friction such as the LuGre or Bliman-Sorine models [30] is used, the parameter estimator complexity increases significantly without ensuring that the friction model used accurately represents the actual discontinuity.

The reason why the discontinuities are considered to be friction is, if you were to consider Figure 7.13, that even when the tab has undergone considerable deflected the aileron remains stationary. However, there should be a resultant aerodynamic moment on the aileron hinge according to the theoretical model. This effects was also visually

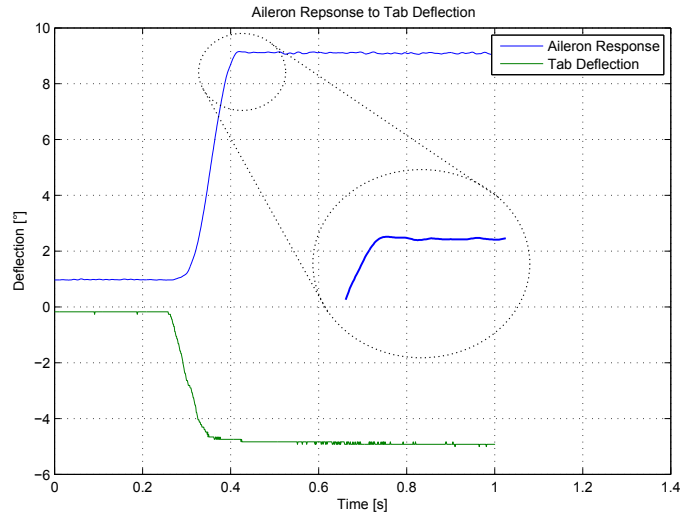

(a) Sticking at Low Angular Rate with No Overshoot $\alpha = 5°$ $V = 20ms^{-1}$

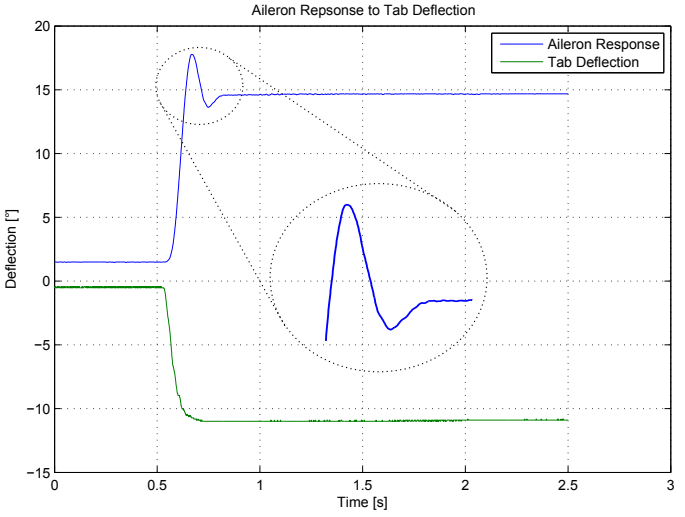

(b) Sticking at Low Angular Rate Mid-Oscillation $\alpha = 5°$ $V = 20ms^{-1}$

Figure 7.12 – Typical Non-Ideal Response Characteristics

very apparent during the wind tunnel tests at low airspeeds where the aileron would under some circumstances not respond to a tab deflection. This is reinforced by low gain values estimated for low airspeeds and small tab deflections, Figure 7.6. It seems that, in these cases, the resultant moment is less or only barely more than the break-away frictional torque [30]. The response visible in Figure 7.12 shows the response ceasing as the resulting excess torque becomes less than the frictional torque. The problem of friction is considered once again in later stages when the controller performance is evaluated. At this point in time, since this is the first iteration of the dynamic model, the approximate linear model will be estimated and the frictional effects are considered disturbances in the model. The implications of this is that the controller will have to be able to reject the frictional effects not represented in the LTI model.

An important effect, which could have a significant impact on the tab operation, is the significant drop in gain from tab to aileron deflection experienced at higher tab deflections and lower velocities. If Figure 7.14 is analysed, it can be seen that the

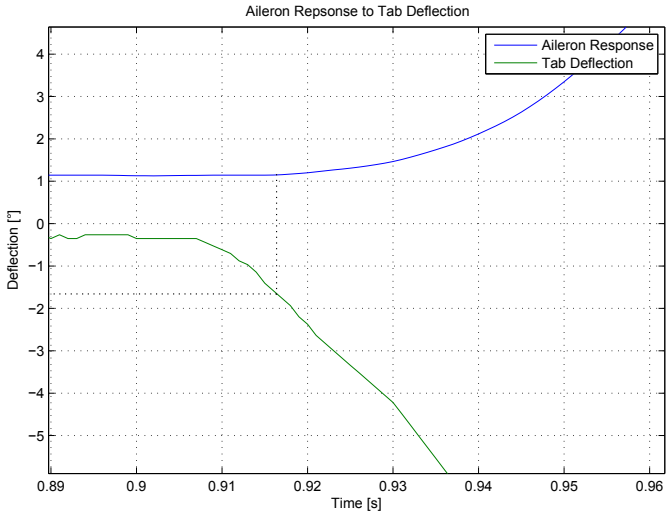

Figure 7.13 – Significant Tab Deflection before Aileron Motion is Initiated due to Frictional Break-Away Force

additional tab deflection from $15°$ to $20°$ results in a drop in total aileron deflection. This coincides with what seems like large peak overshoot values which was found through practical experience to be be rarely fittable with a LTI model. This suggests a maximum usable tab angle. This discontinuity seems to shift depending on velocity, moving to larger tab angles as velocity increases Figure 7.7. Figure 7.7 shows that the larger the velocity the higher the absolute gains are for larger step sizes. As shown in Figure 7.14, the effect is more prevalent in the negative deflection direction. This is possibly a result of the angle of attack and camber causing different flow conditions when comparing a positive deflection with a negative deflection.

One very interesting effect noticed in the responses is that the same tab deflection could result in different aileron deflections. The difference seems to be the tab path to the final tab deflection. It was found that if the tab was ramped slowly to the final deflection, the aileron would settle at a higher angle than that observed when one large tab step is given. In Figure 7.15 it can be seen that initially $25°$ tab steps result in $12°$ aileron responses. However, if the tab is stepped to $20°$ and the to $25°$ a $30°$ aileron deflection results. A similar effect was observed by Ragallo when static tests were conducted. He collected data for aileron hinge moment variation with tab angle [28]. As a secondary effect in the data it was observed that there could be as much as three points on the hinge moment curve for a specific large tab deflection that would result in zero aileron hinge moment. This data is also confirmed on another aerofoil shape, NACA 65-012, by [31]. However, this effect was not prevalent when the gap between the aileron and wing profile was sealed [28].

Extrapolating form this data into the dynamic scenario, it is expected that the system could settle at the stable zero aileron hinge moment points for a given tab deflection. Figure 7.16 shows a conceptual representation of the data found by Ragallo [28]. The points 1 and 2 are stable due to the hinge moment around those points acting as returning moments. The point 2 is unstable since any perturbation from that point would cause a moment and therefore a deflection toward one of the other two points. Further

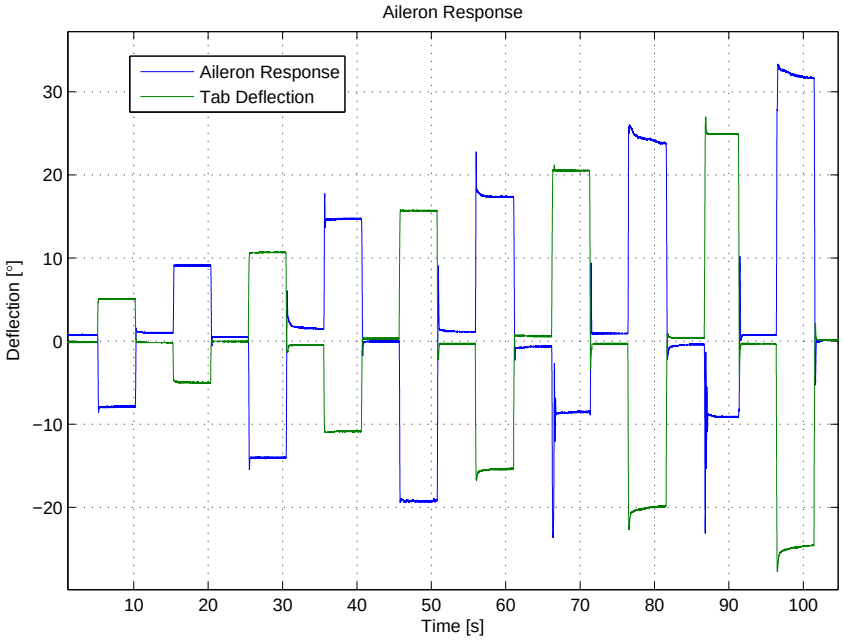

Figure 7.14 – Varying Incremental Aileron Deflection due to Tab Deflection at $\alpha = 5^\circ$ $V = 20ms^{-1}$

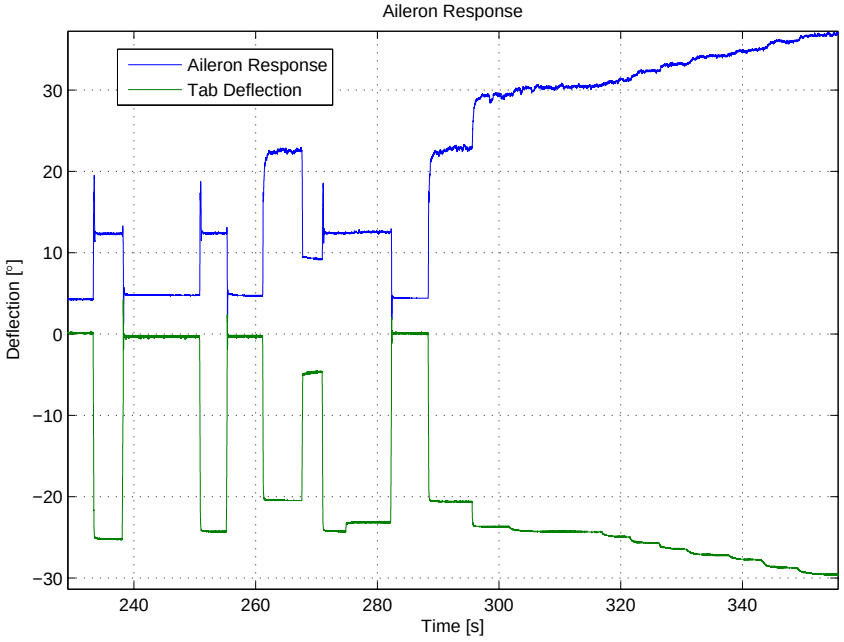

Figure 7.15 – Varying Aileron Deflection due to Tab Deflection

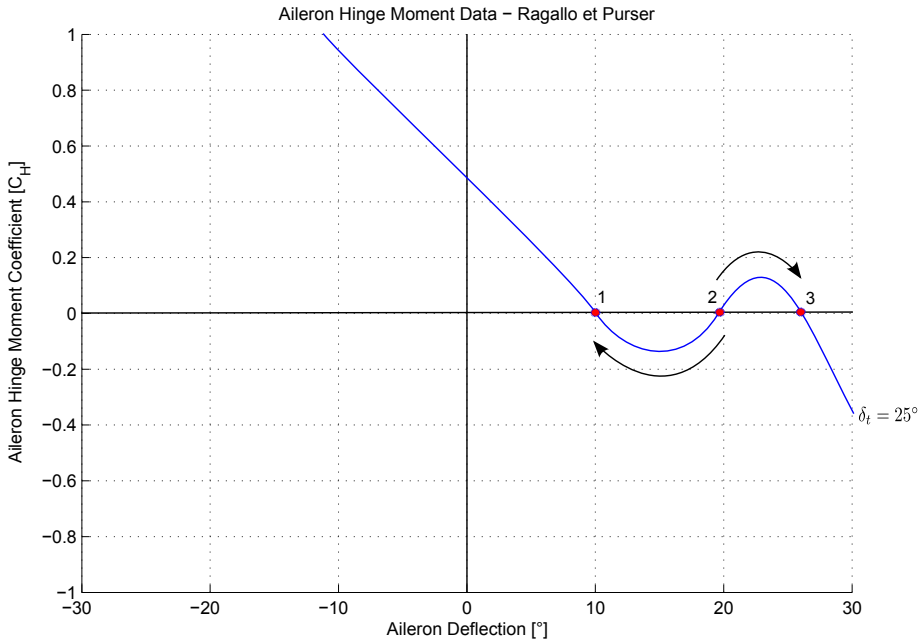

Figure 7.16 – Multiple Stable Aileron Positions

investigation of this effect would require a time history of the hinge moments, the tab deflection and the aileron deflection. The data is not available however the effect is noteworthy. Therefore, no further investigation into it is done at this point. Also, the linear model does not predict this effect since the hinge moment curve is linear and can therefore have only one equilibrium.

Continuing on the idea of change performance of the tab, the later datasets collected with the reconstructed model do not show the initial high tab effectiveness and then a sudden drop in effectiveness as with the initial model. There is a small chance that very early onset of the effects of the wing-aileron gap would mean that a marked decrease in tab effectiveness is not as apparent as in the first dataset but rather presents as gradual decrease in effectiveness. This would explain the much weaker overall performance of the tab and aileron combination. Further support for the early onset of this effect is driven by the appearance of a sudden decrease in the aileron deflection in the transient region at low angles, Figure 7.17. If enough momentum and tab effectiveness remains the aileron moves past the drop. In some cases however it results in a abrupt drop in the aileron deflection angle and stabilisation at a low angle. These two effects are shown in Figure 7.18 and Figure 7.17 respectively.

On a different note, it is found that natural frequency and gain is higher for the $0°$ and $5°$ responses than the $10°$ and $-5°$ responses. The reason why the theoretical linearised model does not show this is that the hinge moment coefficient derivative in theory does not vary significantly with angle of attack. Ragallo presents data for a NACA 230 aerofoil that shows little change in the the hinge moment coefficient derivatives with respect to angle of attack [28]. The variations are a possible result of aileron ventilation as demonstrated by Ragallo [28]. These effects are confirmed by [7].

Another aspect observed during wind tunnel testing is oscillation of the control surfaces

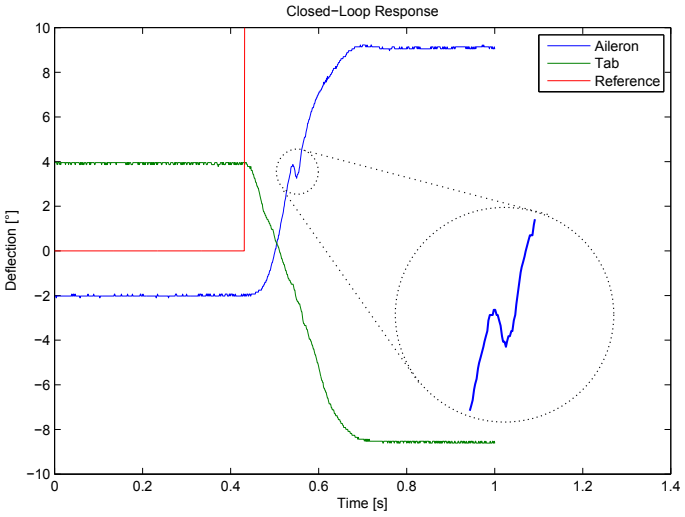

Figure 7.17 – Momentary Loss of Tab Effectiveness $\alpha = 5^\circ$ $V = 30ms^{-1}$

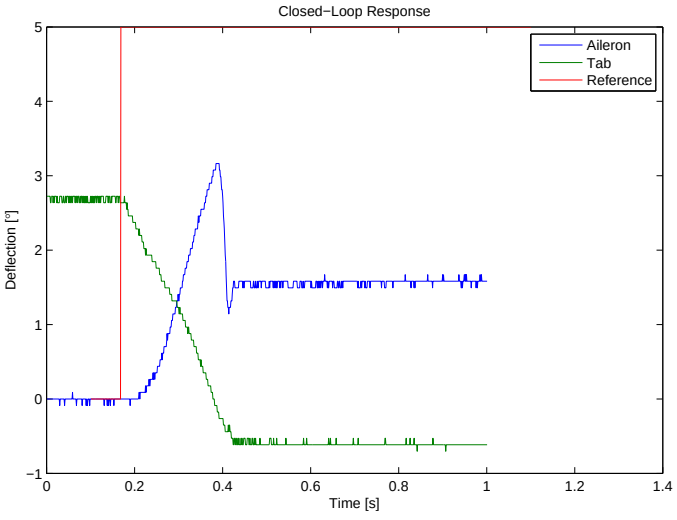

Figure 7.18 – Drastic Sudden Loss of Tab Effectiveness $\alpha = 5^\circ$ $V = 30ms^{-1}$

at velocities exceeding $40\ ms^{-1}$ at angle of attack of $10°$ and $-5°$. It was also observed at higher velocities, $60\ ms^{-1}$, at $0°$ and $5°$ angle of attack. The direct cause of this effect is not completely clear but there are possible causes. Firstly, it has to be considered whether the tab or aileron dynamics are causing the oscillations. Since the system is coupled, the eigenvalues considered in §2.4 does not provide a definitive answer. Looking a the response of the oscillation, it is found that the tab seems to be unstable since it oscillates the most vigorously. The frequency of oscillation is in the order of $29,4\ Hz$ or $185\ rads^{-1}$ at an airspeed of $60\ ms^{-1}$. The linear dynamics of the system only predicts aileron modes close to half this frequency at maximum and the estimation data confirms this. This is supported by the aileron response which seems insensitive to the tab response almost rejecting the tab input. The actuator poles are also at half and quarter of this frequency. However, in literature there is mention of similar phenomena of high frequency oscillation in spring tabs [8]. The effect has also been observed in rigid tabs where play as little as $0,6°$ results in tab oscillation [5]. The literature discerns between conventional flutter and single degree of freedom flutter or control surface buzz. The latter is shown to be caused by shock waves forming on the flap or in front of the hinge lines [32] which is quite impossible at the velocities at which tests were taking place. The cause of the oscillation must therefore be conventional flutter induced by the two degrees of freedom of the tab and aileron [33].

If, for the moment, it is assumed that the flutter is caused by linear behaviour of the system then the natural frequency trends observed during parameter estimation behaviour could predict the flutter frequency for the aileron. This is possible since the aileron in the open loop identification is a free surface only subject to some friction and the aerodynamic hinge moment coefficients. This predicts the aileron flutter frequency however the tab flutter observed is at a higher frequency. In §2.4 the highest frequency dynamics of the tab is well below the dynamics of this oscillation. A analogy can be drawn between the spring tab experiments done by Smith et al. [8] and the actuated tab. Consider the tab actuator with a zero load cut-off frequency of $25\ rads^{-1}$, beyond this point the actuator will no longer be able to reject the aerodynamic hinge moments and therefore sensitivity is approximately $0\ dB$ which means that a disturbance is not rejected at all. Since the tab hinge moment is considered a disturbance in the motor model, see §6.3.1, the tab servo would exert a hinge moment $180°$ out of phase with the tab deflection effectively becoming a spring. Therefore, it will not actively reject the tab aerodynamic hinge moment. The result is that the oscillation frequency of the tab is higher than the hinge moment coefficient and moment of inertia predicts. Under these conditions consider the tab actuator a spring in phase with the aerodynamic hinge moment. By considering the sum of the hinge moment coefficient derivatives, The restoring hinge moment derivative then becomes:

$$\frac{\partial M_t}{\partial \delta_t} = \frac{q\bar{c}^2}{I_t} C_{Ht_{\delta_t}} + \frac{\partial M_{actuator}}{\partial \delta_t} \tag{7.4.1}$$

The damping then determines whether the oscillation dies out. The shift of the frequency is then dependent on the ratio between the two right hand terms in the equation above assuming they remain in phase. To use this effect to predict the exact frequency of the oscillation will probably not be completely correct since the tab hinge moment coefficient derivative is probably not linear. However it does provide insight into why the tab oscillation frequency is much higher than its aerodynamic natural frequency related to the tab hinge moment coefficient derivative.

A possible reason for the excitation is the lack of mass balancing in the system. The use of mass balancing is debated since it has some disadvantages in the flutter scenario with a tab [34]. Mass balancing can reduce the chance of exciting the control surface oscillation however the added mass on the tab will increase combined moment of inertia lowering the flutter frequency [34]. It follows that an alternative option is to dampen the flutter. This can be easily achieved with hydraulic actuators which have inherently high damping characteristics when passive.

7.4.5 Model Overview

Up to this point the trends and non-ideal effects observed in parameter estimation was discussed. It might seem that the estimation results has many variations from the linear assumption. In reality this is often the case. The determining factor is what kind of variations are present and in which directions, stable or unstable, the variations occur.

A good way to compare the dynamics of the system for example is to look at the root locus of the system in term of a specific variable. For example, the velocity root locus of 10° steps for the estimated aileron parameters is displayed in Figure 7.19. The green indicates the theoretical and the red the actual pole position. The data from the 10° steps is displayed here since it contained the least outliers in its trends. It can however be seen that the root loci compare well. The actual model tend to have more damping than the theoretical model. However, this is due to in part friction and in part that the theoretical model uses the approximation method of induced angle of attack to approach damping in the system. It is convenient that the approximate model is very conservative in predicting damping. The natural frequency prediction is also of the same order. The distribution of all of the data of steps smaller than 20° is shown in Figure 7.20. Here red represents $10\ ms^{-1}$, blue $20\ ms^{-1}$, yellow $30\ ms^{-1}$, black $40\ ms^{-1}$ and magenta $50\ ms^{-1}$. Each velocity seems to form a cluster of poles of which it is associated with a theoretical pole, in green. It can also be seen that the poles become more spread out as velocity increases. The damping seems to show a band of variation nearly always to higher damping relative to the theoretical poles. The data for higher deflections, from 20° up, is shown in Figure 7.21. Here it can be seen that there is much less of a trend in velocity and that the higher deflections tend to be weakly damped compared to the small deflections. There is the additional effect of gain loss as the deflections become larger which is not visible on the pole plots.

The implication of the data presented is that in all probability the controller will be able to handle the pole variations for small step sizes up to 15°. However, some loss of performance will result if the controllers are designed for the theoretical model and applied to the actual model. The reason for this is that the damping is higher and therefore the bandwidth of the closed-loop response will tend to be lower. The major hurdle the controller will face is the variation in gain. It has been noted in the previous section that the data form the third run showed that the tab became ineffective at angles between 10° and 15°. The tab-only actuation controllers designed in §4 will therefore not be able to cope beyond these deflections for this specific model. The data from the second run showed greater than unity gain up to 25° aileron deflections therefore the servo tab controllers would have functioned over the complete range with that model. Sadly, the failure of the hinge meant that this cannot be proven practically. In the case where the tab becomes ineffective the bounded controller with tab and aileron reference would provide a simple structure for achieving the range of aileron deflections.

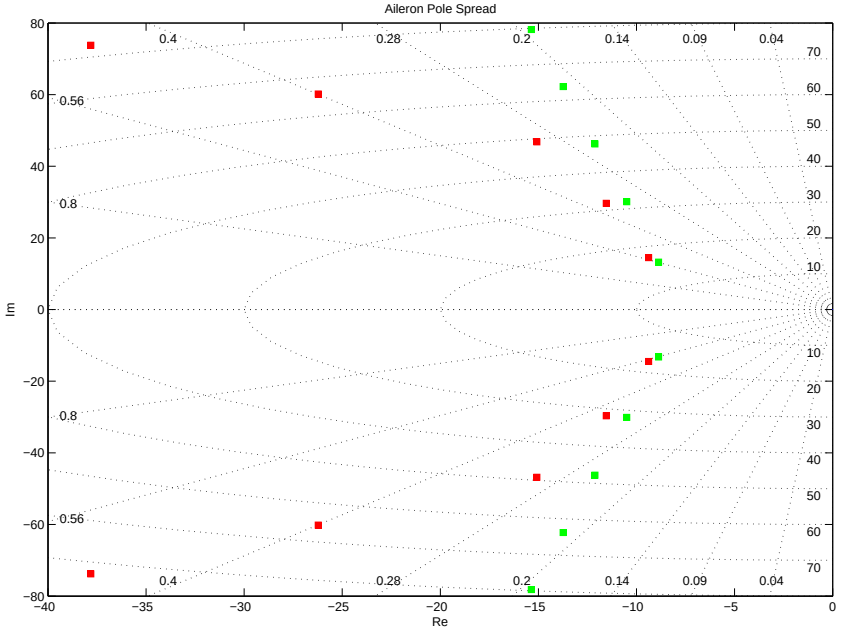

Figure 7.19 – Velocity Root Locus Comaprison

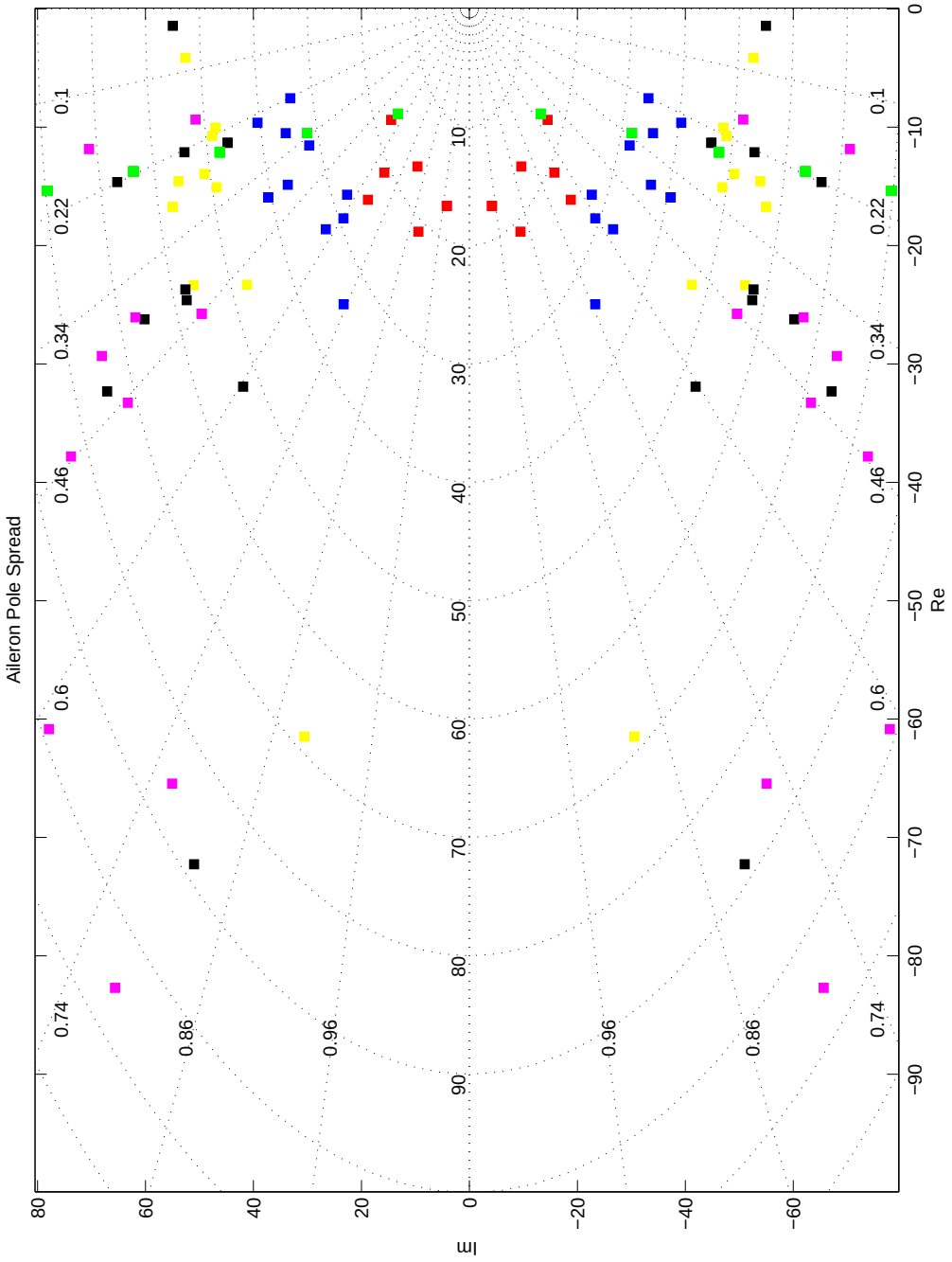

Figure 7.20 – Pole Spread Angles $\leq 15^{\circ}$

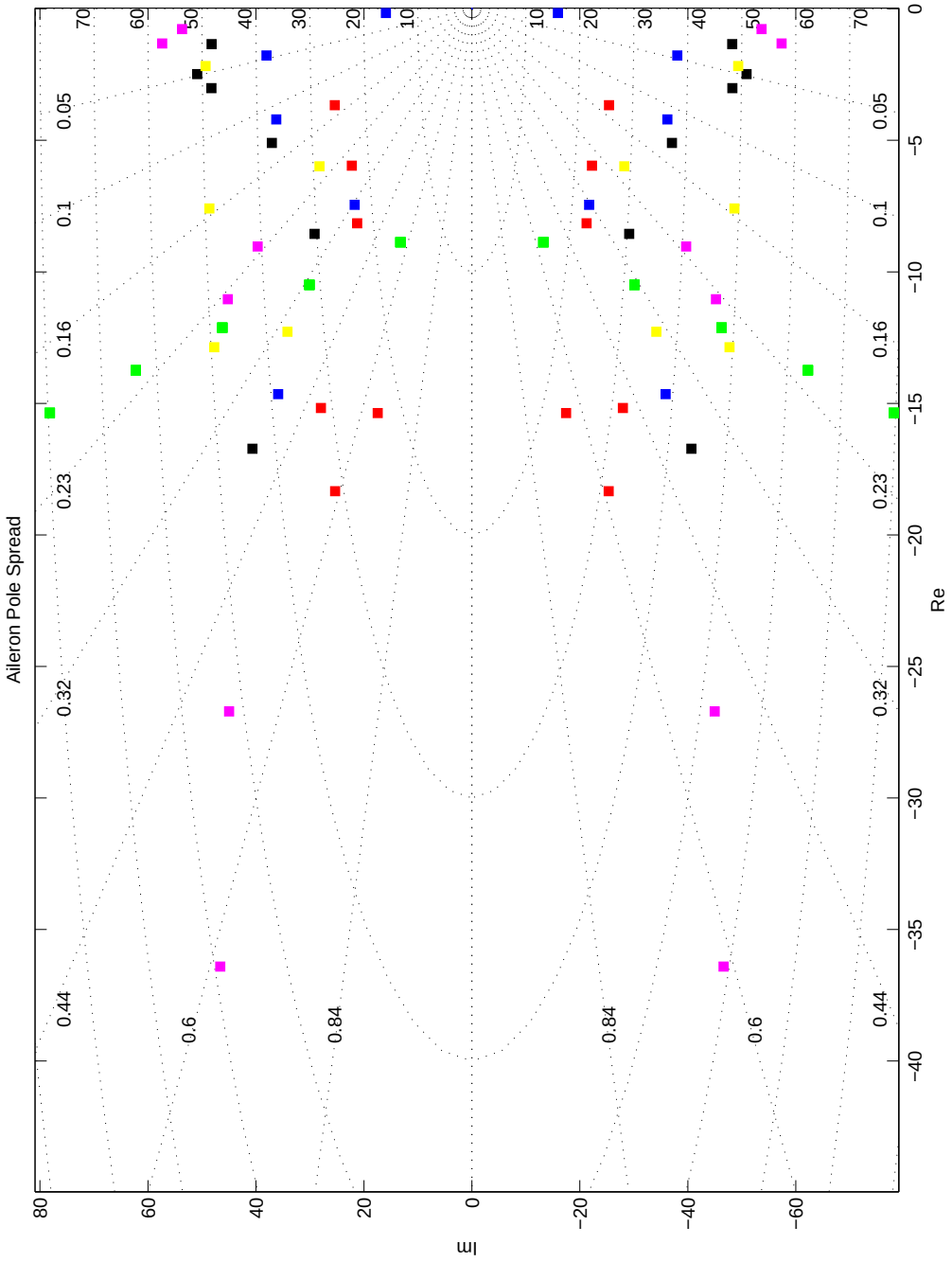

Figure 7.21 – Pole Spread Angles $\geq 20^{\circ}$

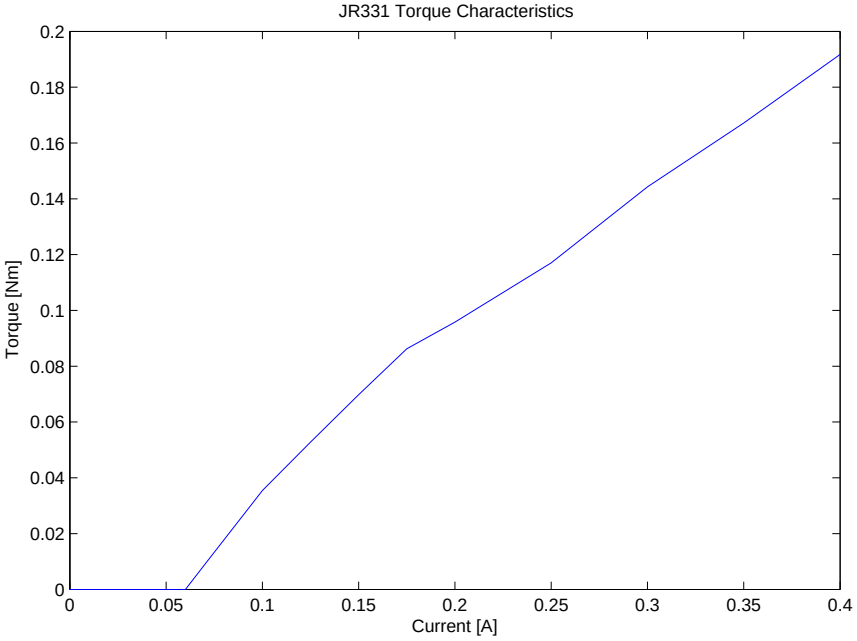

Figure 7.22 – Tab Actuator Torque Curve

7.5 Actuator Parameter Results

This section covers the necessary parameters of the two actuators used in the system identification and control implementation. The first parameters investigated is the motor torque constants for the tab and aileron servos. This is followed by the identification of the poles of the tab actuator in servo mode. The aileron actuator poles are not investigated since it is used only as a toque actuator with fast current control.

The method for determining the servo torque is through a simple rigid pendulum. Weights were attached to the pendulum and a current applied. The deflection angle of the pendulum was measured and the torque calculated. The slope of the line between the torque and current then becomes the torque constant K_T. The results are presented in Figure 7.22 for the tab actuator and Figure 7.23 for the aileron actuator. The torque constants are found to be:

$$K_{T_{JR331}} = 0.5289 \quad [NmA^{-1}] \tag{7.5.1}$$

$$K_{T_{HD1501MG}} = 0.5745 \quad [NmA^{-1}] \tag{7.5.2}$$

It can be seen from Figure 7.22 that there is a significant break-away current and therefore torque exhibited by the actuator. This initial torque must be overcome before any motion will occur. The effect of this torque also makes it extremely difficult to estimate the full-state moment input model as noted in §7.4.

In order to identify the tab servo actuator parameters, the position loop is closed around the rate actuator as shown in §4. The rate loop is the voltage controlled motor as

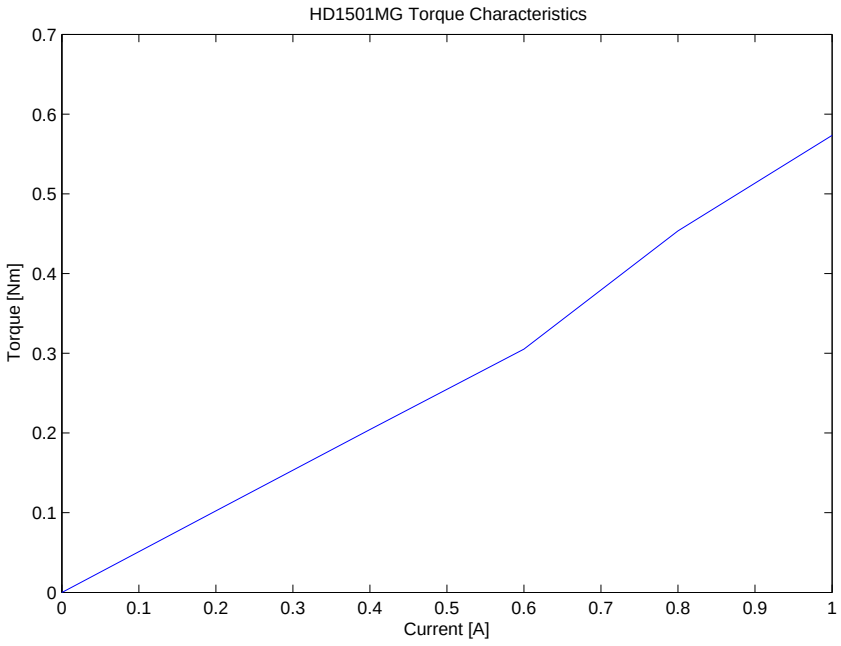

Figure 7.23 – Aileron Actuator Torque Curve

explained in §6.3.1. The feedback gain was then tuned to give approximately optimal damping. The response was then put through the parameter estimation as described in Equation 7.2.14 resulting in the fit presented in Figure 7.24. The resultant poles and gain were found to be:

$$p_1, p_2 = 29 \pm 20i \tag{7.5.3}$$

$$K_{IL} = 0.79 \tag{7.5.4}$$

In the implementation a feedforward gain correction is done. The poles and gain is then used in the control system design as the inner loop. Further, the torque constants are used for feedforward conversion from torque command to current command in the concurrent tab and aileron actuation scenario.

7.6 Scalability of Results

Up to this point all the parameter estimation and model evaluation has been done for the specific model setup. The aim in this section is to generalise some effects that will be observed in the predictable region of the model. The determining factors in control design is highlighted and the effect of aircraft scale and velocity is considered.

All analysis up to this point has shown that the predictable or linearisable region of the model varies with many extraneous factors. However, if the erratic extraneous effects were mitigated and accurate hinge moment data over the operating region acquired, the linearised model should provide a good indication of the dynamics of the aileron

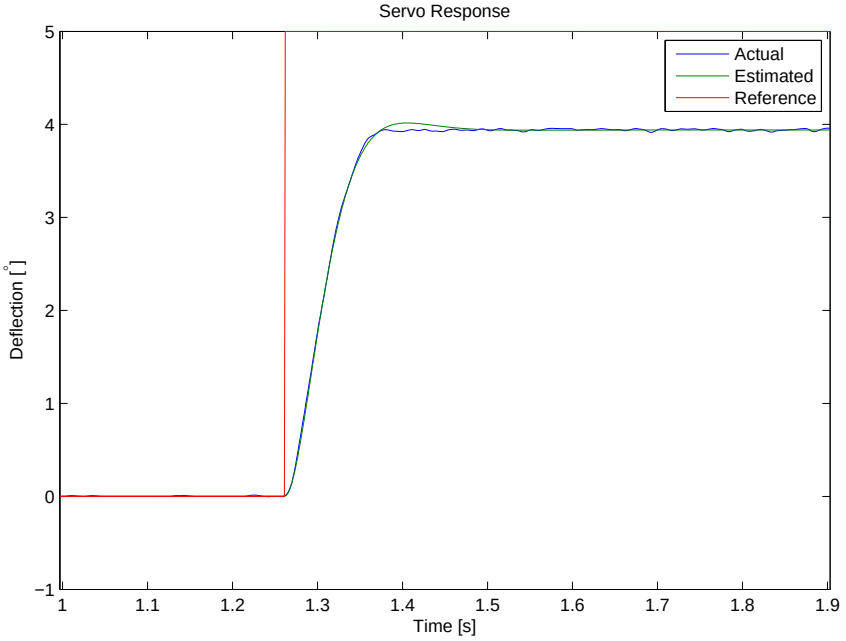

Figure 7.24 – Tab Pole Identification

as shown in §7.4.5. If data of of hinge moments under unsteady flow conditions were available the damping should also be more predictable by linearising at a unsteady-state.

It has been shown that the second order model structure can describe the tab-only actuated response over a limited region. It has also been shown that the natural frequency prediction of the aileron is within the correct ballpark. The damping approach has not provided conclusive evidence of being correct but has shown that it is definitely conservative. The model structure does not contain any scale dependent component and therefore it would not be expected that the structure should change with scale. However, individual parameters of the model would most definitely change as the scale changes and the velocity of the aircraft increases to the range of commercial liners such as the A330. In terms of scale, the important parameters are moment of inertia, chord and span each of which do not change for a fixed setup. If anything is learnt from the literature and previous analysis is that the behaviour of the system is not always predictable. It has been shown in §7.4 that most of the unpredictable behaviour is apparent in the static hinge moment coefficients as well. It follows that proper practical system identification of the specific configuration is very important.

There is one very obvious disadvantage of the tab and it is its tendency to flutter. This tendency is present mostly due to the addition of a badly damped second degree of freedom much more readily excitable than wing flexure and torsion [34]. §2.4 has shown that two of the coupled system poles are unstable. Following this, flutter was experienced in the experimental setup and failure resulted due to the actuator not being able to stabilise the tab dynamics. It is therefore imperative that flutter control is

undertaken. As noted by Boynton, mass balancing is not necessarily a option in a tab-aileron system since the secondary effects of increased mass negatively affect flutter immunity [34]. Generally flutter frequency would occur at higher frequencies than conventional actuator bandwidth meaning active flutter suppression is not necessarily feasible. The only option remaining is damping of flutter. The mechanical damping of flutter can have advantageous results for the control system performance as discussed in §4.4.

The implications of a fixed structure of the model means that the controller developed based on the model will be applicable to different scale system. All that is required is re-evaluation of controller parameters and insuring that the actuators can achieve the desired performance measures.

Chapter 8

Control Implementation Results

The controllers have been designed based on the models estimated in §7.4 and then practically tested in the wind tunnel. It was noted in §7.4.5 that a controller designed for a specific velocity will be able to handle the variation in dynamics of steps up to $15°$. However, it was also noted that the tab-only actuation controllers and the aileron reference FSF controller which is primarily dependent on tab performance will not function adequately if the tab becomes ineffective. This is why the concurrent tab and aileron reference controller was designed. This allows the tab to be limited to the point where it becomes ineffective and the aileron actuator then takes over and ensures aileron following.

The initial intent was to test all the controller but with the time constraints and the unforeseeable events, it resulted that only the tab-only actuation controllers and the aileron reference FSF controller could be tested. The controller gains were calculated based on one LTI model per velocity. The model for a $10°$ step was used to determine the gains at each velocity set point. The controllers were then also tested for robustness. Testing was done for some controllers at a lower velocity and a higher velocity as well as a lower angle of attack and a higher angle of attack than its design values. The testing matrix is presented in Table 8.1. The cell content shows the linearisation condition, the horizontal varies the velocity and the vertical varies the angle of attack.

	V $[ms^{-1}]$			
α	20	30	40	50
$0°$		$\alpha = 5° \; V = 30$		
$5°$	$\alpha = 5° \; V = 20$	$\alpha = 5° \; V = 10$ $\alpha = 5° \; V = 30$ $\alpha = 5° \; V = 50$	$\alpha = 5° \; V = 40$	$\alpha = 5° \; V = 50$

Table 8.1 – Testing Matrix for Controllers

8.1 Tab-Only Actuation Test

In this section the comparison between the two tab-only actuation controllers for a rate actuator is done and the overall performance evaluated. The dynamic performance

in terms of the rejection of higher frequency dynamics is also considered. Further, a qualitative comparison of the controller handling of non-idealities is given.

First consider the negative feedback controller implemented at the correct linearising condition. Recall, the approximate first order dynamics required is equivalent to a dominant pole at $p_{CL} = -15$ and unitary gain. This corresponds to a 98% settling time of $0,26\ s$ for the repsonse:

$$\delta_a = \left(1 - e^{\frac{-t}{\tau}}\right) \delta_{a_{ref}} \tag{8.1.1}$$

It was found that in the 2% settling time does not match the designed settling time of the system if the strict definition is followed. In most cases it can be seen that the response dynamics settles as it would for the ideal response however it usually has a steady-state error. At this stage it can be seen that the integrator kicks in and starts to correct for this error slowly by increasing the current, the rate of which is determined by the integrator gain. However, the presence of friction causes the integrator to wind-up a little before a response occurs this can be seen as steps in the response shown in Figure 8.1 in the time period between $5.5\ s$ and $7\ s$. This is typically also visible as a stepping around the zero command as seen in Figure 8.1 in the time period between $0\ s$ and $5\ s$. Additionally, the presense of friction can also be the cause of the gain error and the slowed performance. The result is that the rate controller is not effectively rejecting the frictional effects. By introducing a frictional model in the SISO system the effects of friction is reproduced as seen in Figure 8.2. There is however a small difference between the simulation and the measured effect. The tab oscillates as it attemps to counteract the aileron oscillation not seen in the actual result however the movement around the zero and the steady state values and the gain errors are represented quite well.

There is an additional effect also visible in nearly all responses to differing extents. There are sudden and erratic losses of aileron deflection. The extent of this is already covered in §7.4.4 and the effect on the controller is a degraded response and failure to achieve steady-state accuracy. This effect is considered most likely an side effect of flow leakage through the tab or aileron gaps as noted in §7.4.4.

A summary of the performance of the negative feedback controller is given in Table 8.2. The settling time is considered the time it takes for the dynamics to settle to 98% of the final value and not the reference. It can be seen that in most cases the steady-state error results. The addition of the integrator does mean the error is removed but a clear initial settling is visible. Steps larger than $10°$ was not considered since the responses showed that the tab alone could not push the aileron to those angles.

		V [ms^{-1}]		
Step		30	40	50
$5°$	Settling Time [s]	0,35	0,35	0,34
	Steady-State Error	-30%	-19%	-6.8%
$10°$	Settling Time [s]	0,31	0,29	0,30
	Steady-State Error	-15%	-14%	-6.8%

Table 8.2 – Negative Feedback Controller Performance

The same non-ideal effects were present with the positive feedback controller which once again impaired the performance of the system. A typical response resulting from

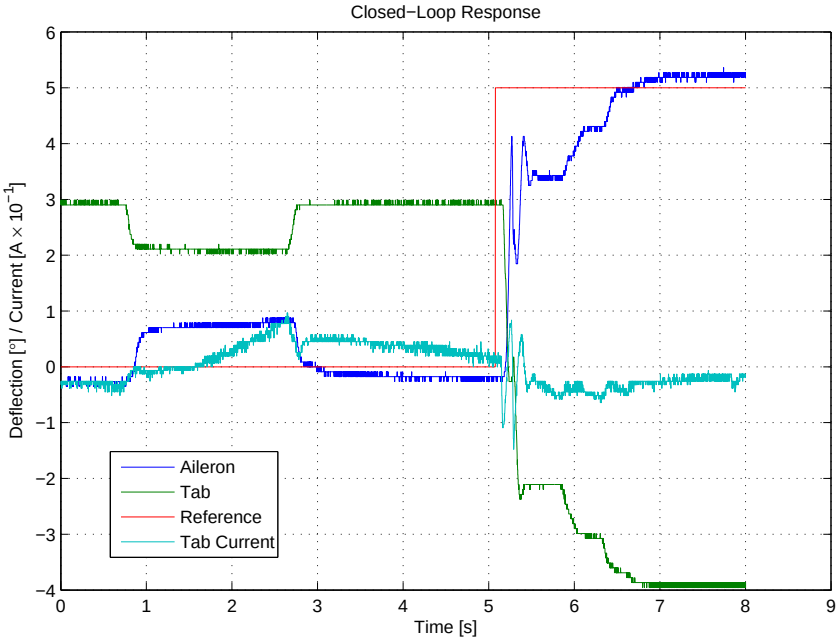

Figure 8.1 – Frictional Effect in Case of Steady-State Error and Around Zero Command at $\alpha = 5°$ and $V = 30\ ms^{-1}$

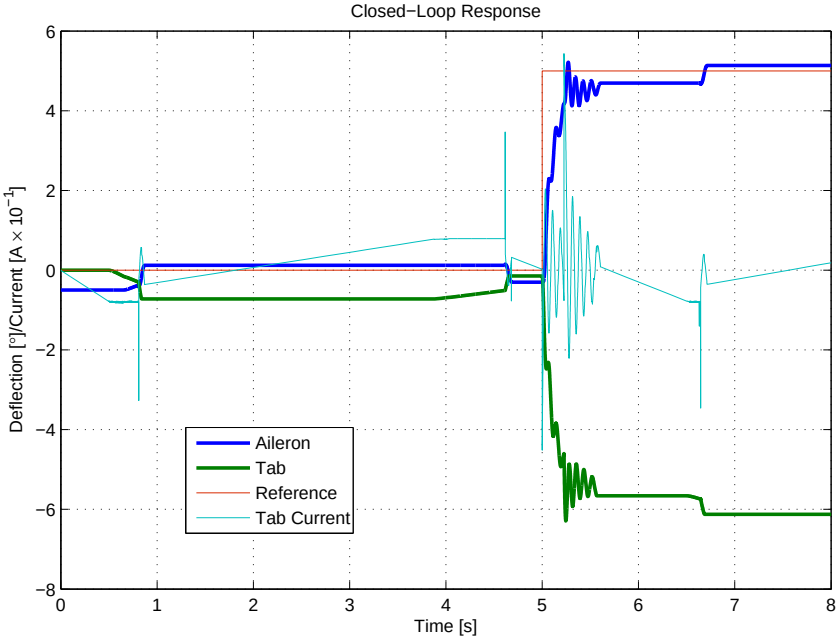

Figure 8.2 – Frictional Effect in Reproduced in Simulation

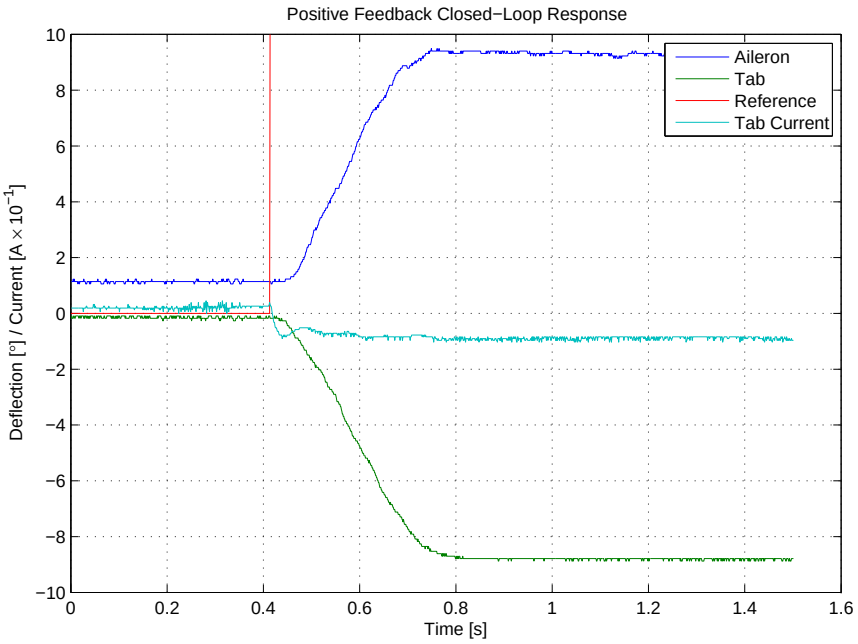

Figure 8.3 – Typical Positive Feedback Reponse

the positive feedback controller is shown in Figure 8.3. The summary of the performance data of the positive feedback controller is given in Table 8.3. The data for $5°$ steps are not included since consistent aileron deflection loss was experienced as noted before.

		V $[ms^{-1}]$		
Step		30	40	50
$5°$	Settling Time [s]	NA	NA	NA
	Steady-State Error	NA	NA	NA
$10°$	Settling Time [s]	0,25	0,26	0,29
	Steady-State Error	-8,6%	-12%	-6,8%

Table 8.3 – Positive Feedback Controller Performance

Another method to compare the response of the controller to the intended response is to consider the frequency domain response of the system. The frequency response of the system was attained through sequential sinusoidal excitation. Then the data was passed through the MATLAB fast-Fourier function, fft.m, to evaluate the amplitude of the response in the frequency domain by comparing the input spectrum with the output spectrum. The resultant frequency domain plots are shown in Figure 8.4. The bode diagrams tend to agree with the theoretical bode diagrams in terms of shape however it seems that the cut-off frequency is significantly lower than expected for the positive feedback controller. This is reflected in the poor dynamic performance of the controller. This could be the result of the non-idealities in the system and the inability of the positive feedback controller to deal with it. The negative feedback controller

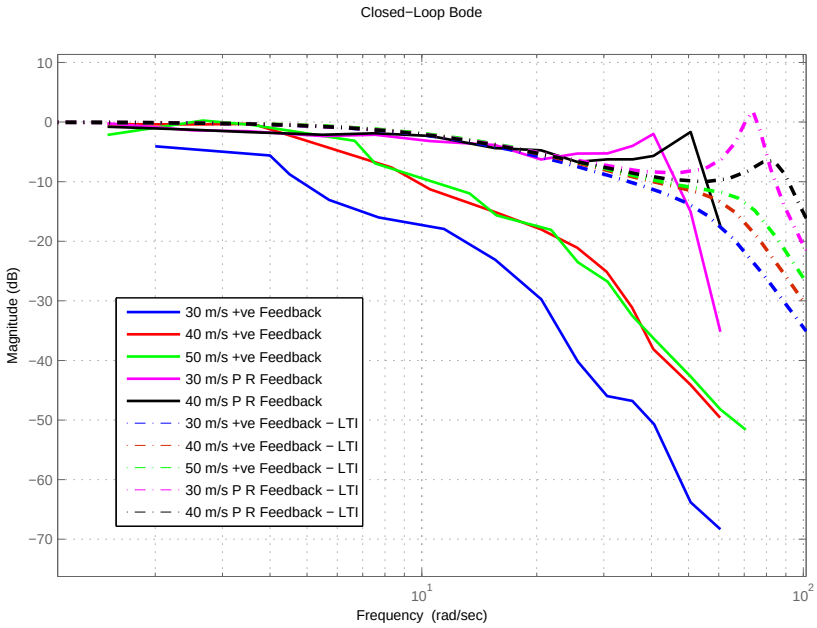

Figure 8.4 – Frequency Domain Response Comparison for Tab-Only Actuation Controllers

shows the correct initial cut-off frequency concluding that it deals much better with the non-idealities.

Furthermore, the aileron resonant dynamics are shown to be well rejected by the positive feedback controller but very weakly rejected by the negative feedback controller. This was correctly predicted by the original frequency response. However, the identified LTI model and negative feedback controller shows a significantly higher frequency for the resonant peak when compared to the experimental frequency response. A possible reason for this is that the inertial coupling between the tab and aileron is different under the sinusoidal and step excitation conditions. The high gain of the resonant peak would also mean that the negative feedback control will not be sufficient in suppressing control surface oscillation.

Finally, the evaluation of the controller performance outside the intended linearisation regions gives an good indication of the robustness of the controllers. The performance is once again summarised in Table 8.4. The positive feedback controller seems to be more robust in terms of steady-state accuracy whereas the negative feedback controller is more accurate in settling time. Both show very high sensitivity due to angle of attack. This is expected since it was noted in the system characterisation that the aileron dynamics vary to a large extent due to angle of attack, see §7.4.1. Further, the general characteristics in terms of aileron resonance rejection is maintained. The positive feedback controller once again results in better rejections of aileron dynamics.

	Conditions Controller	$\alpha = 5° \; V = 30$ $\alpha = 5° \; V = 10$	$\alpha = 5° \; V = 30$ $\alpha = 5° \; V = 50$	$\alpha = 0° \; V = 30$ $\alpha = 5° \; V = 30$
Positive Feedback Controller	Settling Time [s] Steady-State Error	0,40 -12%	0,29 2.0%	0,25 -38%
Neagtive Feedback Controller	Settling Time [s] Steady-State Error	0,31 -13%	0,36 -6%	0,31 -26%

Table 8.4 – Robust Performance $10°$ Steps

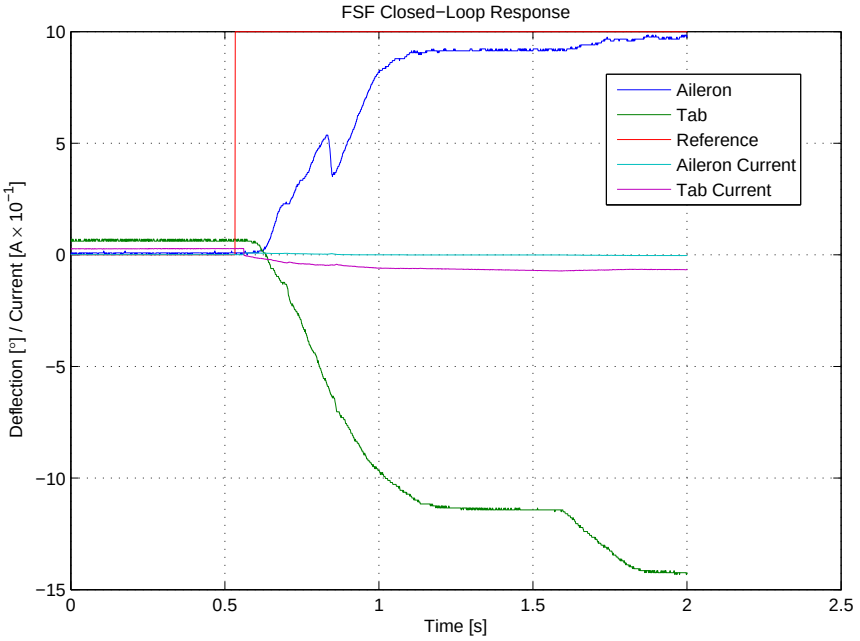

Figure 8.5 – Typical FSF LQR Controller Response

8.2 Aileron-Only Reference Concurrent Tab and Aileron Actuation Test

Much like the tab-only actuation controllers the full-state feedback controller was tested for their respective linearisation states and then a few robustness spot checks are done. The major difference between the tab-only actuation and the aileron-only reference FSF system is that the additional aileron actuator is being used. The weights on the inputs, described in §5.3, are still chosen to favour the tab actuator but the aileron actuator aids the response dynamics. However, even with the aileron actuator being used the controller will not be able to adjust to the tab becoming ineffective or saturating. The consequence is that the responses will also be limited to $10°$ aileron deflection.

The non-ideal effects are also visible as explained for the servo tab controllers. The sudden deflection loss and friction, as before, are all prevalent in the responses. A typical response indicative of the FSF LQR controller is provided in Figure 8.5.

The summary of the controller performance is given in Table 8.5. In this case there is no obvious initial settling of the dynamics as with the servo tab controllers. The settling

time is therefore measured to the final settling value. In theory the integrator should cause zero steady-state error however the addition of friction causes jumps in deflection around the final value. The loss of aileron deflection also observed in the servo tab controllers are present here and shows a major hindrance in the settling time of the responses since only the integrator gain could reject this disturbance. This rejection of the disturbance is therefore dependent on the integrator gain. It can be seen that the steady state performance of the system is greatly improved in the FSF controller when compared to the servo tab controllers however this is the result of the integrator gain being larger than in the servo tab controllers. This resulted from the augmented LQR controller. Further, the responses show good rejection of the aileron resonant dynamics as predicted by the design. This is confirmed by the experimental frequency response function of the system as shown in Figure 8.6. However, the experimental frequency response function has a significantly lower cut-off frequency which is again reflected by the poor dynamic performance of the controller. This is most certainly the effect of non-idealities unaccounted for in the linear model.

		V [ms^{-1}]		
Step		30	40	50
5°	Settling Time [s]	0,59	0,63	0,78
	Steady-State Error	5%	2%	-10%
10°	Settling Time [s]	0,63	0,49	0,51
	Steady-State Error	-9,5%	-4,0%	-8,6%

Table 8.5 – FSF Controller Performance

One effect of the addition of the second actuator is that there is more friction in the system. The additional friction is a result of the actuator internal gearing once again resulting in degraded dynamic performance. This is visible in all the settling times. The reason for the larger settling time is apparent from the investigation into the input to the tab and aileron actuator. It can be seen that the tab actuator current and therefore torque gives the initial step however there is little response from the tab. The integrator then takes over and increases the tab torque to a value about double that of the predicted torque value shown by the frictionless theoretical model. It is quite clear that this additional torque is the result of the additional torque required to overcome the internal tab gear friction. The effect is less visible in the aileron actuator since the aileron hinge moment input is not as strongly coupled to the integrator meaning it does not wind up as much as the tab. The initial torque command to the tab and aileron agrees in magnitude with that of the theoretical response. The solution to this problem would be giving a additional input command to overcome the detent torque of the servo. In hindsight this would have demonstrated the FSF controller more accurately if the effect were apparent during testing and mitigated at that stage.

The robustness is tested by varying the operating conditions. The performance data is presented in Table 8.6. It is concluded that dynamic characteristics tend to remain the same. The steady-state performance shows gain changes at velocities lower than the linearised velocities. This is most probably caused by the feedforward structure which is intended to improve dynamic response. However, the feedforward is designed for a larger velocity and therefore larger hinge moments which will cause the overshoot or larger gain if it is applied at a lower velocity. In this case, it presents as a smaller steady-state error.

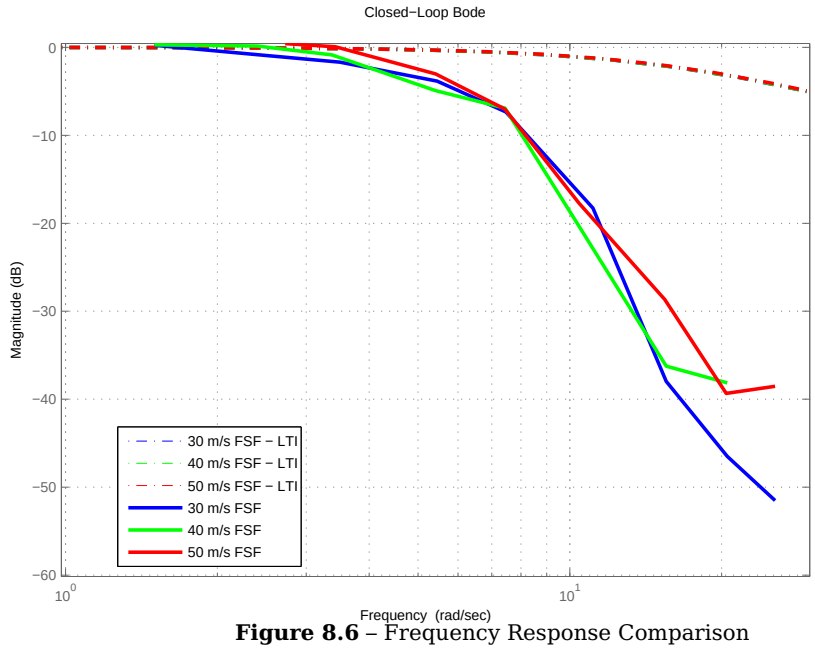

Figure 8.6 – Frequency Response Comparison

Consitions Controller	$\alpha = 5° \ V = 30$ $\alpha = 5° \ V = 10$	$\alpha = 5° \ V = 30$ $\alpha = 5° \ V = 50$
Settling Time [s]	0,69	0,61
Steady-State Error	-11%	-0,6%

Table 8.6 – Robust Performance of FSF LQR Controller

8.3 Results Overview

Considering the information gained in the practical tests and the conditions under which it was attained, the controllers tended to respond as expected. I was somewhat expected that the friction would affect dynamic performance and that the loss of tab effectiveness would limit these controllers. Further, the expectations that the positive feedback and FSF LQR controller would provide better rejection of the aileron dynamics is also confirmed. In terms of robustness, a clear comparative answer is not available but it can be said that the controllers performed consistently under the varied velocity conditions.

As a whole, it would not be a gross overstatement to say that the controllers do succeed in driving the system as intended and providing a reasonably dominant first order response. The controllers have therefore succeeded in pushing the dominant weakly damped poles to a less dominant region. Furthermore, the positive feedback controller and the FSF LQR controller provided exceptional rejection of aileron resonant dynamics safeguarding against possible oscillatory conditions of the aileron.

One aspect of the controllers that seems to perform dreadfully is the initial steady state accuracy. The steady-state accuracy is consistently in error between 5% and 15%. The slow integrator dynamics then tend to kick in and start correcting. The obvious solution to this would be to increase integrator gain however the risk remains that the integrator

interaction with the friction could start oscillations around the setpoint value. It has to be said however with this degree of friction and non-idealities in the aerodynamics one cannot expect the controllers to perform flawlessly. Therefore, the steady-state accuracy may not be a good indication of the controller performance in this case.

A common practice in this case would be to effectively make the integrator gain very large and effectively push through the integrator without cancelling it with a feed-forward term. This sadly limits the bandwith of the system due to the dominance of additional closed loop pole. This pole's location is dependent on the other closed loop poles. This is most apparent in the integrator loop root loci of the tab-only actuated controllers. The performance of a pure integral controller will however be very limited in its ability to reject aileron dynamics when the aileorn poles are dominant and badly damped.

Comparatively, the FSF LQR controller provided the most accurate response in steady-state. This, however, is a biased statement since the integrator action was faster due to a higher integrator gain. Here is is seen that rather than adding to the system the second actuator resulted in more friction and no real performance gain. It would lead to the conclusion that the addition of a second actuator is only a good option if the controller presented in §5.4 is used.

Chapter 9

Conclusion

9.1 Summary

This thesis has presented the development of a theoretical dynamic and static model of a tab assisted control surface. Both the static and dynamic models were derived for the general case where both the tab and the aileron are actuated. This resulted in a fully coupled model. The model was then decoupled to investigate the tab-only actuation concept. The predicted dynamics of both models was then presented.

The development of the theoretical model was accompanied with the development of a reduced size experimental model. The necessary hardware and software was designed to facilitate data collection and control of the experimental model. The experimental model was then tested in a low-speed wind tunnel and the data that was collected was correlated with the theoretical model. It was shown that the servo tab concept is capable of actuating a control surface. Many non-ideal effects were also observed. Some preliminary hypotheses were presented based on past research as discussion on the causes of these effects.

In conclusion, the available aerodynamic data is adequate for development of the linearised model. However, the model failed to predict the full extent of non-linear behaviour since the aerodynamic data is inherently not capable of predicting these effects.

Concerning controller development, the collected models were used in conjunction with the theoretical model to develop four control algorithms capable of achieving the target performance measures. This was then confirmed in simulation. Two of the algorithms were aimed at the tab-only actuation concept and two were aimed at the fully coupled concurrent tab and control actuated model. The algorithms were then evaluated in terms of disturbance rejection and noise sensitivity.

A second model check was run after the initial system identification. During this second run the model underwent violent control surface oscillations and failed. Considering the time and infrastructure availability limitations, it was decided to do a in-house reconstruction of the setup. However, due to the less than perfect nature of this model the original system identification data could not be reproduced. Despite this, it was decided to continue with the original project approach and verify the control algorithms.

The control algorithms were then implemented on the experimental model. The controllers' performance data was then analysed and evaluated against the controller design goals. It was found that there was significantly degraded controller performance.

After a detailed investigation, it is concluded that this is due to the degraded model and the non-idealities in the actuators. It is expected that if all the non-idealities specific to this experimental model is mitigated the controllers will perform as designed and predicted by simulation. In more general terms, it is apparent from all the tests done that active control of the tab-only or the concurrent tab and aileron actuation concept can be used to control the bandwidth of the tab assisted aileron and in so doing reject control surface oscillations.

With the available controller performance data, it was possible to then identify and confirm the weaknesses and strengths of each control algorithm as predicted in theory. Based on this, general recommendations were made in terms of actuator requirements.

In total, the goal of modelling the system, validating the model, designing control, simulation of control, implementation of control and identification of actuator requirements have been met to a large extent. It is believed that the theory and data presented in this thesis will serve as good ground work for future refinement and implementation of the tab assisted aileron concept.

9.2 Future Work and Recommendations

Some recommendations of how the models and control can be improved are made in this section. First, the development of a more accurate theoretical model will be very useful in identifying the severe non-linearities in the model.

The model can be improved obtaining more accurate aerodynamic hinge moment data to replace current thin aerofoil theory. This will allow one to predict the observed discontinuities in the model. The addition of rate dependent aerodynamic data would also be very useful for prediction the damping in the system. This data might originate from computational fluid dynamic methods or from experimentation and can be easily integrated into the model structure.

As a result of the testing done in the wind tunnel, it is highly recommended to investigate the effects of geometry on the lift coefficients. Specifically, the testing should focus on variation of the tab-aileron and tab-wing gap. Investigation into the effect of aerofoil shape and angle of attack on the tab and aileron hinge moments may be very useful since flow conditions over the tab might change drastically.

Concerning the application of the concept on commercial jetliners such as the Airbus A320 and A330, the effects of transonic flow should be investigated. At this point there is no available data for the tab assisted control surfaces under these flight conditions. Shock waves may result in unpredictable flutter behaviour as a result of unsteady flow.

Investigation into the three-dimensional flow around the tab sections will provide valuable insight into the practical performance of the surfaces when implemented on a aircraft lifting surface.

A dedicated flutter test model can be constructed to confirm the two degree of freedom control surface flutter frequencies of the tab and aileron combination. This would provide more insight into the accuracy of the theoretical model.

In future experimental setups, it is recommended to concentrate on the mitigation of frictional effects. It has been shown that the frictional effects can have a large effect on the dynamic and steady-state performance of the system. It follows that actuators with minimal detent torque needs to be used to avoid similar effects to friction.

A method of sealing the tab-aileron and aileron-wing gaps without introducing considerable extraneous forces to the system is also recommended. This should ensure more predictable aerodynamic performance.

Finally, the theoretical model of the tab and aileron should be implemented in the aircraft simulation provided by Airbus. This will provide valuable information about dynamic coupling between the control surface dynamics and aircraft dynamics.

Appendix A

A.1 Moment of Inertia Calculation

The moment of inertia of the tab and aileron was calculated by means of the a numerical integration of:

$$I_i = \int r^2 dm_i \tag{A.1.1}$$

with reference to Figure A.1. It can be seen that the skin and the core is considered independently due to the difference in density. For actuators and other components, the parallel axis theorem is used as follows [35]:

$$I_{H_i} = I_{cm} + m_i d^2 \tag{A.1.2}$$

This gives the moment of inertia of the object around its centre of mass, I_{cm}, around a parallel axis to the hinge axis which is located a perpendicular distance d from the hinge. The total moment of inertia about the hinge is then given by:

$$I = \sum I_i \tag{A.1.3}$$

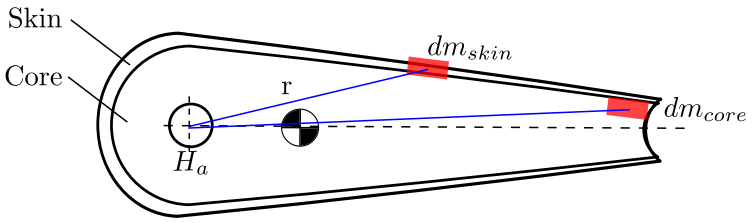

Figure A.1 – Representation of Moment of Inertia Calculation

A.2 Correction Factors

Some aspects of the wind tunnel are non-ideal since the flow is restricted to a limited cross section. The following section summarises the correction factors that could be used to correct for the most dominant effects [20]. However, this effect of horizontal buoyancy, otherwise known as solid blockage, is generally negligible when working with wing aerofoils [20]. Just for reference, the evaluation of the drag force due to this effect is estimated by:

$$D_B = -\frac{6h^2}{\pi}\Lambda\sigma p' \tag{A.2.1}$$

$$\sigma = \frac{\pi^2}{48}\left(\frac{c}{h}\right)^2 \tag{A.2.2}$$

$$\Lambda \sim \frac{t}{c} \tag{A.2.3}$$

The effect of solid blockage on drag is found by taking:

$$\epsilon_{sb} = \sigma\Lambda \tag{A.2.4}$$

the drag coefficient correction factor becomes

$$C'_{d0} = C_{d0}(1 - 3\epsilon_{sb}) \tag{A.2.5}$$

The relationship between Λ and $\frac{t}{c}$ has been determined and is represented graphical form [20].

The effect of solid blockage is seen as a change in velocity of the airflow due to the reduction in the cross section of the airflow when compared to free stream airflow. Correction of the measured velocity is given:

$$V' = V(1 + \epsilon_{sb}) \tag{A.2.6}$$

An additional effect of wake blockage is determined by correcting for the wake distortion with:

$$V' = V(1 + \epsilon_{wb}) \tag{A.2.7}$$

$$\epsilon_{wb} = \frac{c}{2h}C_d \tag{A.2.8}$$

The effect of the wake distortion can also be applied to the drag coefficient.

$$C'_{d0} = C_{d0}(1 - 2\epsilon_{wb}) \tag{A.2.9}$$

The total drag an velocity corrections can then be determined as follows:

$$V' = V(1 + \epsilon_{wb} + \epsilon_{sb}) \tag{A.2.10}$$

$$C'_{d0} = C_{d0}(1 - 3\epsilon_{sb} - 2\epsilon_{wb}) \tag{A.2.11}$$

Further correction of the angle of attack, lift and pitching moment can be made but requires the additional information of the actual lift and pitching moment coefficients. It is simpler to use a very small chord to height ratio of the aerofoil in order to maintain uncorrected effects as small as possible. By using rough estimates of solid blockage and wake blockage from lift and drag coefficient in the correct order of magnitude the velocity correction comes to around 1%. This is the convenient result of using a small wing chord removing the need for adjustment of the results.

A.3 Graphic User Interface

The graphic user interface is designed in Qt development environment in the C++ language. The user interface is has 8 tabs displaying various sets of information. The tabs are highlighted here to present an overview of the system functionality.

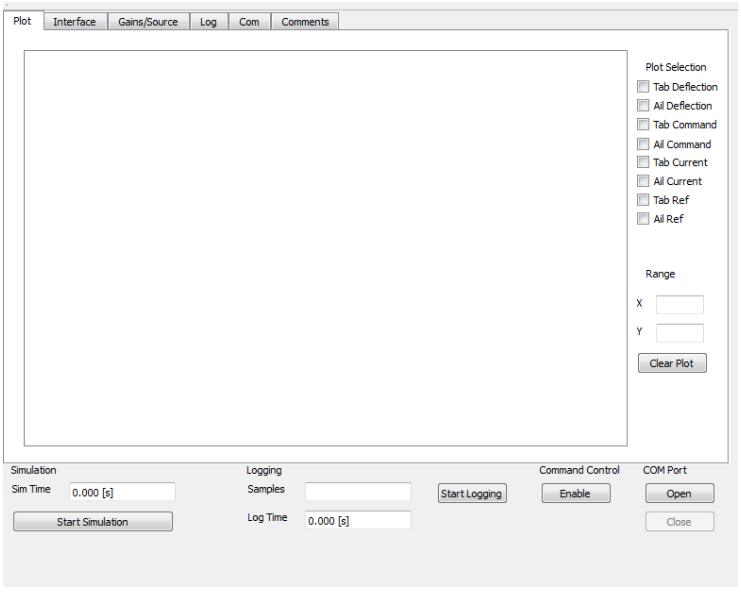

Figure A.2 – GUI Real-Time Plotting Window

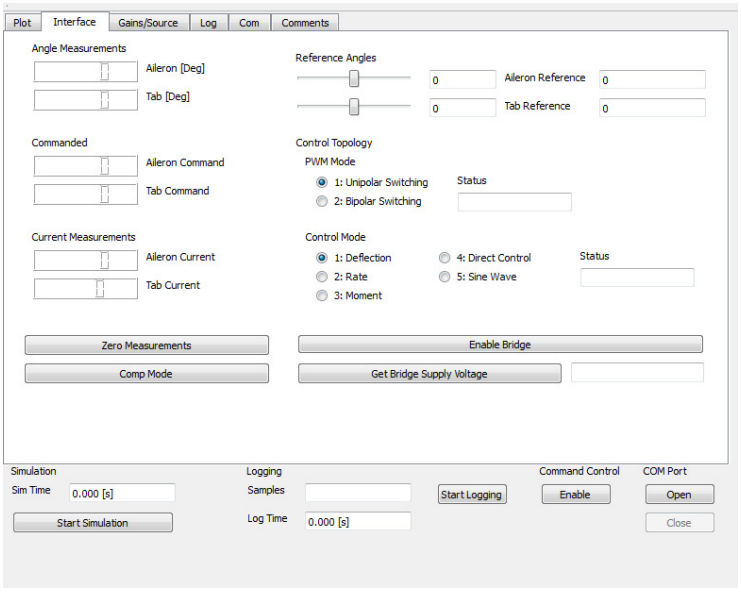

Figure A.3 – GUI Main Control and Interface Window

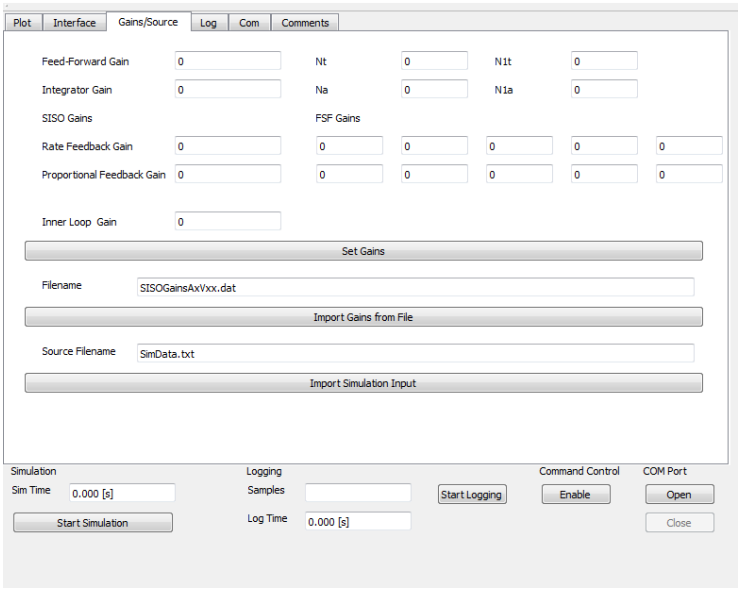

Figure A.4 – GUI Gain Import and Adjustment Window

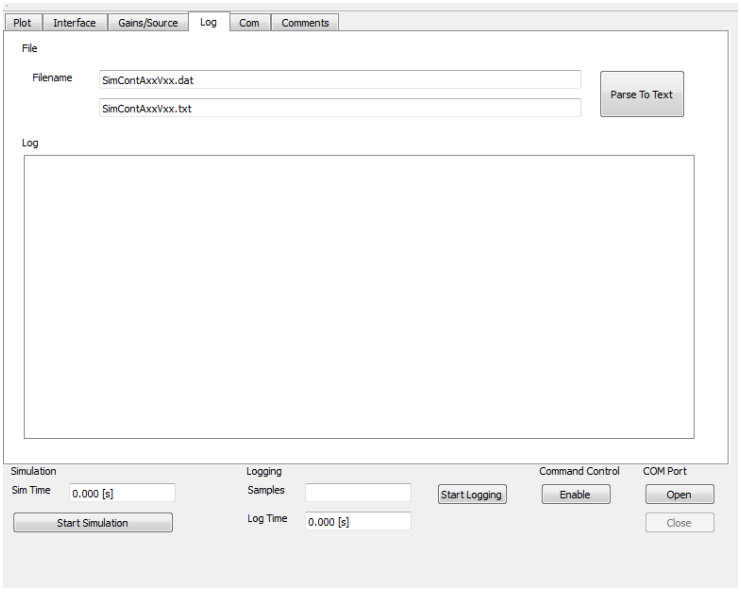

Figure A.5 – GUI Log and Debug Window

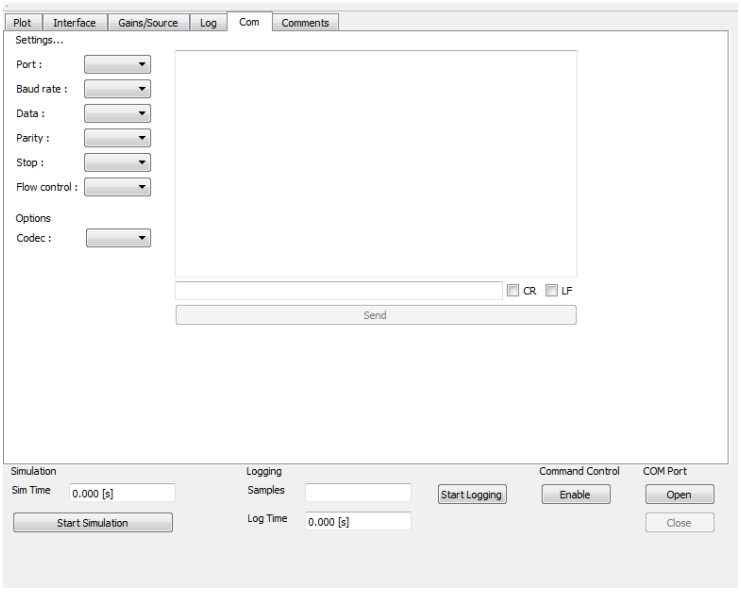

Figure A.6 – GUI Communication Settings

List of References

[1] Jaquet, C.: *Control Surfaces in Confined Spaces: The optimisation of trailing edge tabs to reduce control surface hinge moments*. Master's thesis, Stellenbosch University, 2010.

[2] Phillips, W.: Journey in aeronautical research: A career at nasa langley research center. Online.
Available at: `http://history.nasa.gov/monograph12/contents.htm`

[3] Jones, T.: Stellenbosch university research plan 2008 v2.0 for the airbus/nacoe/cput/stellenbosch research program, November 2007.

[4] Abzug, M. and Larrabee, E.: *Airplane Stability and Control: A History of the Technologies that Made Aviation Possible*. Cambridge University Press, 2002.

[5] Theodorsen, T. and Smith, N.: Flutter tests of b-34 fin-rudder-tab system. Tech. Rep., National Advisory Commitee for Aeronautics: Langley Memorial Aeronautical Laboritory, 1944.

[6] Smart maintenance of aviation hydraulic fluid using an onboard monitoring and reconditioning system. Online.
Available at: `http://ec.europa.eu/research/transport/projects/article_6533_en.html`

[7] Crandall, S. and Murray, H.: Analysis of available data on the effect of tabs on control-surface hinge moments. Tech. Rep., National Advisory Commitee for Aeronautics: Langley Memorial Aeronautical Laboritory, 1946.

[8] Smith, N., Clevenson, S. and Barmby, J.: Experimental investigation of a preloaded spring-tab flutter model. Tech. Rep., National Advisory Commitee for Aeronautics: Langley Memorial Aeronautical Laboritory, 1947.

[9] Soinne, E.: Aerodynamic and flight dynamic simulations of aileron characteristics. December 2000.

[10] Day, C.: Pablo script. Software, 2009.

[11] Waszak, M.: Modeling the benchmark active control technology wind-tunnel model for application to flutter suppression. In: *AIAA Atmospheric Flight Mechanics Conference*. 1996.

[12] Katz, J. and Plotkin, A.: *Low-Speed Aerodynamics*. 2nd edn. Cambridge University Press, 2001.

[13] Keuthe, A. and Chow, C.: *Foundations of Aerodynamics: Bases of Aerodynamic Design*. 3rd edn. John Wiley & Sons, Inc., 1976.

[14] Cook, M.: *Flight Dynamics Principles*. Elsevier Ltd., 2007.

[15] Cook, P.: *Nonlinear Dynamical System*. Prentice Hall Inc., 1994.

[16] Gopal, M.: *Control Systems: Principles and Design*. 2nd edn. McGraw-Hill, 2003.

[17] Boye, S.: Initial technical data for "control surfaces in confined spaces" project v2.0. April 2008.

[18] Franklin, G.F., Powell, D.J. and Workman, M.L.: *Digital Control of Dynamical Systems*. Addison-Wesley, 1998.

[19] Kwakernaak, H. and Sivan, R.: *Linear Optimal Control Systems*. Wiley-Interscience, 1972.

[20] Barlow, J., Rae, W. and Pope, A.: *Low-Speed Wind Tunnel Testing*. John Wiley & Sons, Inc., 1999.

[21] Mohan, N. and Undeland, T.: *Power electronics: converters, applications, and design*. Wiley India, 2007. ISBN 9788126510900.
Available at: `http://books.google.co.za/books?id=oxR8vB2XjgIC`

[22] Gopal, M.: *Digital Control and Sate Variable Methods*. 2nd edn. McGraw-Hill, 2004.

[23] Pintelon, R. and Shoukens, J.: *System Identification: A Frequency Domain Approach*. IEEE Press, 2001.

[24] Figliola, R. and Beasley, D.: *Theory and Design for Mechanical Measurements*. John Wiley & Sons, Inc., 2006.

[25] Phillips, C. and Nagle, H.: *Digital Control System Analysis and Design*. Prentice Hall Inc., 1995.

[26] Ljung, L.: *System Identification: Theory for the User*. Prentice Hall Inc., 1987.

[27] Madsen, K., Nielsen, H. and Tingleff, O.: *Methods for Non-Linear Least Squares*. Informatics and MAthematical Modelling: Technical Universiy of Denmark, 2004.

[28] Ragallo, F. and Purser, P.: Wind tunnel invetigation of plain aileron with various trailing-edge modifications on a tapered wing. Tech. Rep., National Advisory Commitee for Aeronautics: Langley Memorial Aeronautical Laboritory, 1943.

[29] Braslow, A.: Two-dimensional wind-tunnel invetigation of a 10.7-percent -thick symmetrical tail section with a 0.40 airfoil-chord control surface and a 0.20 control-surface-chord tab. Tech. Rep., National Advisory Commitee for Aeronautics: Langley Memorial Aeronautical Laboritory, 1947.

[30] Olsson, H., Astrom, K., Canudas de Wit, C., Gafvert, M. and Lischinsky, P.: Friction models and friction compensation. 1997.

[31] Brewer, J. and Queijo, M.: Wind-tunnel investigation of tab balance on tab and control-surface characteristics. Tech. Rep., National Advisory Commitee for Aeronautics: Langley Memorial Aeronautical Laboritory, 1947.

[32] Lambourne, N.: Control-surface buzz. Tech. Rep., Ministry of Aviation: Aeronautical Research Council, 1964.

[33] De Vries, G.: Safeguards against flutter of airplanes. Tech. Rep., National Advisory Commitee for Aeronautics, 1956.

[34] Boynton, R. and Wiener, K.: Measuring mass properties of aircraft control surfaces. Tech. Rep., S.A.W.E. Inc., 2000.

[35] Meriam, J. and Kraige, L.: *Engineering Mechanics: Dynamics*. John Wiley & Sons, Inc., 2003.